

Selective Atomic Layer Deposition and Etching of Oxides

PROEFSCHRIFT

ter verkrijging van de graad van doctor aan de Technische Universiteit Eindhoven,
op gezag van de rector magnificus prof.dr.ir. F.P.T. Baaijens, voor een commissie
aangewezen door het College voor Promoties, in het openbaar te verdedigen op
donderdag 5 juli 2018 om 11:00 uur

door

Alfredo Mameli

geboren te Barletta, Italië

Dit proefschrift is goedgekeurd door de promotoren en de samenstelling van de promotiecommissie is als volgt:

voorzitter: prof.dr.ir. G.M.W. Kroesen
1^e promotor: prof.dr. F. Roozeboom
2^e promotor: prof.dr.ir. W.M.M. Kessels
co-promotor: dr.ir. A.J.M. Mackus
leden: prof.dr. S. Barry (Carleton University)
prof.dr. S. De Gendt (Katholieke Universiteit Leuven)
dr. R. Luttge
dr. I. Swart (Universiteit Utrecht)

Het onderzoek dat in dit proefschrift wordt beschreven is uitgevoerd in overeenstemming met de TU/e Gegragscode Wetenschapsbeoefening.

The research project described in this dissertation has been supported by Holst Centre-TNO in Eindhoven, The Netherlands



Printed and bound by: Gildeprint Drukkerijen

Cover designed by: Alfredo Mameli

A catalogue record is available from the Eindhoven University of Technology Library

ISBN: 978-90-386-4531-5

Table of Contents

Chapter 1	Introduction	7
Chapter 2	Area-Selective ALD: an Overview	23
Chapter 3	Synopsis of Selective ALE	53
Chapter 4	Area-Selective Atomic Layer Deposition of In ₂ O ₃ :H Using a μ -Plasma Printer for Local Area-Activation Mameli, A.; Kuang, Y.; Aghaee, M.; Ande, C. K.; Karasulu, B.; Creatore, M.; Mackus, A. J. M.; Kessels, W. M. M.; Roozeboom, F. <i>Chem. Mater.</i> 2017 , <i>29</i> , 921–925.	67
Chapter 5	Area-Selective Atomic Layer Deposition of ZnO by Area-Activation Using Electron Beam Induced Deposition	85
Chapter 6	Area-Selective Atomic Layer Deposition of SiO ₂ Using Acetylacetone as a Chemoselective Inhibitor in an ABC-Type Cycle Mameli, A.; Merckx, M. J. M.; Karasulu, B.; Roozeboom, F.; Kessels, W. M. M.; Mackus, A. J. M. <i>ACS Nano</i> 2017 , <i>11</i> , 9303–9311.	103

Chapter 7	Isotropic Atomic Layer Etching of ZnO Using Acetylacetone and O ₂ Plasma	133
Chapter 8	Conclusions and Outlook	153
Summary		159
Contributions of the author		163
List of peer-reviewed publications		165
Acknowledgments		167
Curriculum Vitae		171

Chapter 1

Introduction

This chapter provides the background on today's worldwide developments in the field of selective atomic layer processing involving material deposition and etching. These techniques hold great potential in mitigating the process complexity and development costs currently faced by the semiconductor industry. In order to fully exploit the potential of these techniques in modern (three-dimensional) device fabrication, knowledge regarding challenges in state-of-the-art nanomanufacturing is a prerequisite.

In this chapter an outline of selective atomic layer processing techniques is given to provide a bird's eye perspective of nanomanufacturing and to guide the reader in comprehending the prospects of atomic layer processing.

It is important to note that the results of this dissertation are not solely aimed at specific applications in semiconductor manufacturing but more at investigating atomic layer processing techniques. The main objective was to develop area-selective deposition as well as selective etch processes using several materials as case studies. At the same time, this has shed light on the chemical and physical phenomena imparting selectivity in atomic layer processing. The insights thus obtained are expected to contribute towards the implementation of selective atomic layer processes not only in the field of semiconductor nanoelectronics but also in other application fields such as photovoltaics, displays, catalysis, etc.

1.1 Downscaling of electronic devices

Over the last six decades, the use of electronic devices has become prominent in our society. The downscaling of the single components (e.g., transistors) and the introduction of three-dimensional (3D) stacked integrated circuit designs have made every-day-use objects such as laptops and smartphones possible. It is exemplarily depicted by the fact that the first solid-state computer, the IBM 608 (shown in Figure 1a), commercialized in 1957, was sold for an equivalent of roughly 700 thousand dollars, whereas today smartphones (an example is given in Figure 1b) are typically 8 orders of magnitude smaller, 4 orders of magnitude faster, and 3 orders of magnitude cheaper.¹

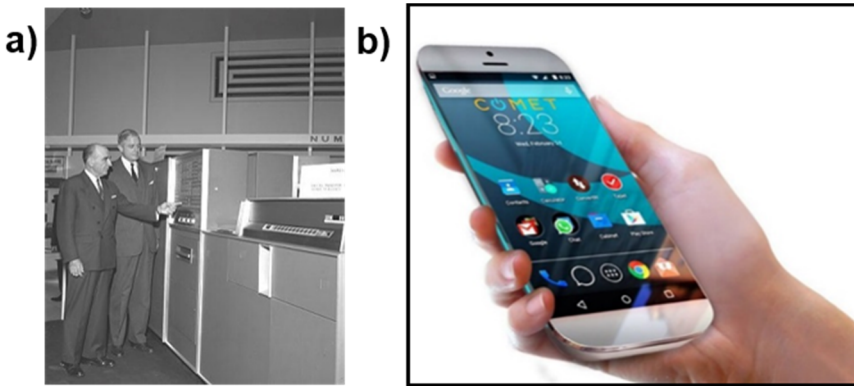


Figure 1.1: a) The first solid-state computer, the IBM 608 calculator, commercialized in 1957.² b) Today's common smartphone.

In 1965 Gordon Moore envisioned a rule of thumb for increasing computing power and cost efficiency that has been deliberately followed by chip manufacturers and has led to incommensurable innovations.^{1,3} The downscaling of transistors, which are the building blocks used to assemble complex electronic devices, has been following Moore's law which states that the transistor density doubles every two years. The benefits of this downscaling pace in terms of device performance are described by Dennard's relation: for a constant electric field, the reduction of the critical dimensions by a constant factor translates into a higher speed and a reduced power consumption for each transistor generation.^{4,5}

Nowadays, device manufacturing has become extremely complex because of the high density (with ever smaller dimensions) and the high aspect ratio (i.e., the length over the width of a 3D feature) of 3D features that compose a multi-layered structure, as shown in Figure 1.2. A large number of deposition, lithography and etching steps are required to fabricate and interconnect multiple levels of an integrated circuit. The key challenge in modern 3D device manufacturing is in building such a multi-layered device with every single feature perfectly aligned on top of the feature in the underlying layer, thus accurately located at the exact position required for the chip to operate correctly and with the highest possible efficiency.

To enable further downscaling, the pattern-to-pattern alignment between the various layers of the device, i.e., the so-called *overlay*, needs to be improved. These alignment issues originate from a complex combination of process variabilities during each fabrication step. The number of process steps required to realize advanced devices increases with every technology generation,⁶ and each step can introduce variations that may result in significant differences between the designed integrated circuit and the fabricated one. Solving the overlay issue warrants innovation in all areas, from lithography to deposition and etching.⁶⁻⁹

For the aforementioned reason, advanced deposition and etching techniques that can mitigate alignment issues are currently undergoing extensive research. The techniques that potentially enable *self-aligned* processing are area-selective atomic layer deposition (ALD) and selective atomic layer etching (ALE).

This dissertation focuses on the development of area-selective ALD and selective ALE processes for oxide materials and on the understanding of the underlying basic mechanism. The rest of this chapter is organized as follows. Firstly, in Section 1.2, the challenges in feature alignment currently faced in nanomanufacturing are described in greater detail. Next, the fundamentals of the atomic-level processing techniques (ALD, area-selective ALD and selective ALE) are briefly described in Section 1.3, together with their key advantages over conventional techniques. Two self-aligned processes that rely on area-selective ALD and selective ALE are also described. Finally, the research questions that outline this dissertation are presented in Section 1.4.

1.2 Challenges in manufacturing

The shrinking of feature sizes has been largely possible because of the continuous innovation in lithography. However, this downscaling is also accompanied by an increased complexity and cost factor in device fabrication.^{10,11} The overlay requirement typically has been $\frac{1}{4}$ of the minimum printable size (also referred to as *critical dimension*, CD). However, to successfully fabricate 7 or 5 nm technology nodes, the overlay must be between $\frac{1}{6}$ and $\frac{1}{10}$ of the CD.^{12,13} This means that the maximum misalignment of a few nanometers that can be tolerated at present, needs to be reduced to < 1 nm, i.e., < 5 silicon atoms wide. It can be understood how challenging that is and why techniques that allow for Ångström-level control over material deposition and removal will become a necessity.

A figure of merit commonly used to quantify the misalignment is the so-called *edge placement error* (EPE). The EPE can be thought of as the differences in position and in shape between the intended and the actual pattern on the sample accumulated after all the processing steps (deposition, lithography and etching).^{14–16} If severe EPEs show up during the manufacturing flow, these can lead to shorts or disconnections that result in poor device performance and yield, i.e., the cost per chip will dramatically increase. Therefore, controlling and minimizing the EPE represents the main bottleneck in further downscaling.

To illustrate the impact of EPEs on a real device structure and to comprehend the challenges involved in further downscaling, cross-sectional electron microscopy images of a 3D Xpoint memory device (commercialized by Intel in 2017) are shown in Figure 1.2. Briefly, the 3D Xpoint is a non-volatile memory device, consisting of different perpendicular metal lines (word lines and bit lines) that connect single memory cells

made of a selector and a phase-change material, where the information is stored. In this particular case, the two decks of the stacked memory cells share the bit line. What should be noted is that some of the bit line connections are not exactly aligned on top of each other, as highlighted by the dashed yellow lines in Figure 1.2b. It is likely that the most severe EPEs might cause local hot spots which can decrease the performance and lifetime of the memory cell, or lead to device yield loss due to misconnection.

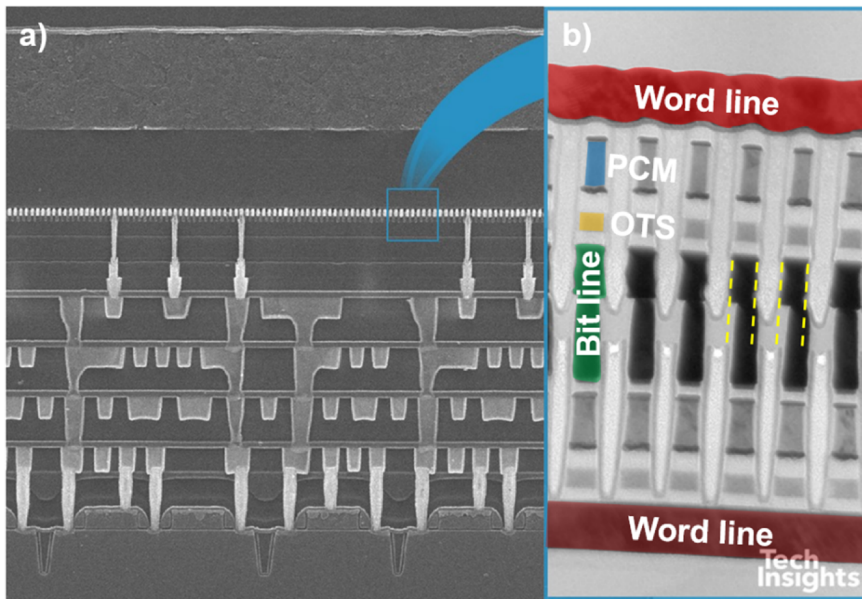


Figure 1.2: a) Cross-sectional SEM image of a 3D Xpoint memory device. b) Zoom-in TEM image of the actual double-deck memory, with a shared bit line (green), two word lines (red) and a series of single columns consisting of a so-called ovonic threshold switch (OTS, yellow) and a phase change material (PCM, blue). Scale bar not available. The width of the metal connection in the bit line is estimated to be ~ 20 nm, based on the dimensions of the transistors commonly used in memory devices. After Ref. 17.

In contrast, selective processing techniques, such as area-selective ALD as well as selective ALE, can intrinsically enable perfect overlap between the features present at the different levels of the device, or can be used to mitigate the alignment issues and therefore keep performance and yield as high as possible. Two examples of self-aligned processing, one relying on area-selective ALD and one on selective ALE are described below. Moreover, area-selective ALD allows for eliminating several processing steps as compared to conventional fabrication methods. Therefore, the *bottom-up* fabrication enabled by area-selective ALD also holds promise beyond the field of semiconductor nanoelectronics, e.g., for catalysis and for flexible electronics.^{18–23} For some of these applications, reducing the number of photolithography and etching steps can be highly beneficial, in terms of device performance and possible damage during etching steps. Bottom-up fabrication can be achieved by local activation or de-activation of a

substrate. When the activation step is performed using maskless techniques, the combined process (activation + area-selective ALD) is referred to as *direct-write* ALD (see Chapters 4 and 5). Before going into details, the basic principles of ALD, area-selective ALD and selective ALE, together with their key advantages over conventional techniques, are described in the next section.

1.3 Atomic-layer processing to the rescue!

Principle of ALD. ALD is a technique that enables layer-by-layer material deposition with atomic-level thickness control. As shown in Figure 1.3a, ALD relies on the cyclic and alternating exposure of a substrate to at least two vapor-phase reactants (typically a metalorganic or halide precursor and an oxidizing (e.g., H₂O, O₂, etc.) or reducing (e.g., H₂, NH₃, etc.) co-reactant that undergo subsequent and self-limiting surface reactions. These two half-reactions (A and B) are separated by purge steps in which excess of reactants and by-products are removed from the reaction chamber. Reactions do not take place in the gas-phase, thereby avoiding parasitic chemical vapor deposition (CVD) components. Figure 1.3b shows the thickness per cycle that is added every ALD cycle as a function of the exposures to precursor, purge, co-reactant and purge, respectively.

Conventional deposition techniques, like CVD, can lead to faster deposition at the entrance of a high aspect ratio (HAR) structure because the deposition rate depends on the local flux of chemical reagents on the surface. This dependence can lead to poor step coverage in HAR (Figure 1.3c). Conversely, since in ALD the deposition process is separated in two self-limiting half-reactions, the thickness deposited after each cycle is uniform even on HAR and controlled at the Ångström level (Figure 1.3d).²⁴ Another key advantage of ALD is that it typically allows for depositing materials at relatively low substrate temperature. This is particularly true in the case of plasma-based ALD processes where the co-reactant is replaced by a plasma step involving highly reactive radical species. Plasma co-reactants allow further reduction of the substrate temperatures. Furthermore, the use of plasma during ALD has been demonstrated to yield improved material properties, enable the use of more precursors and therefore more materials to be deposited (e.g., technologically relevant SiO₂ and SiN)²⁵ and allow for the use of temperature-sensitive substrates (e.g., polymer foils).

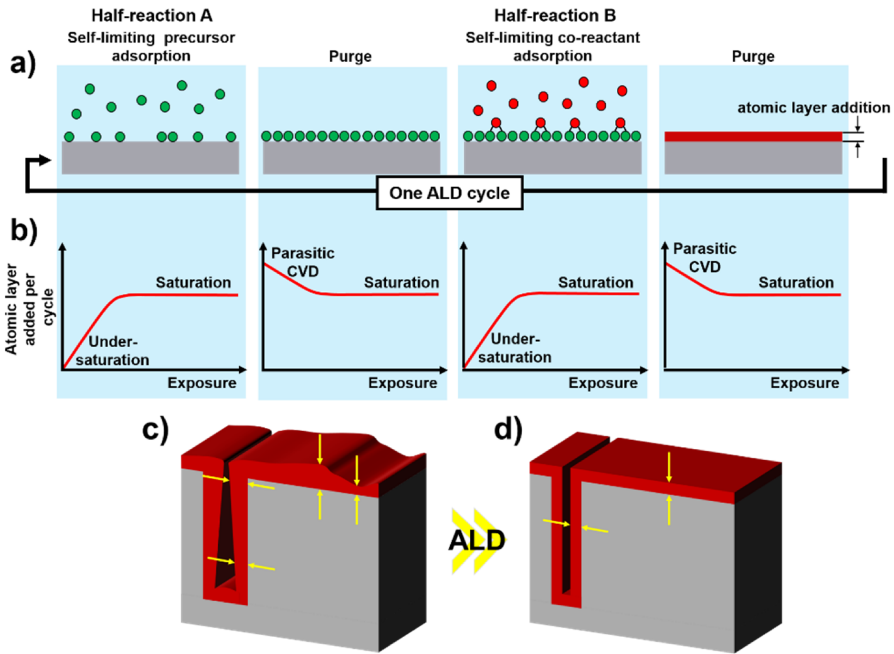


Figure 1.3: Schematic of **a)** one atomic layer deposition (ALD) cycle and **b)** the saturation curves for the various steps. The depicted processes consist of two self-limiting half-reactions A and B interleaved by purge steps. The cycles are repeated multiple times to achieve the desired thickness of material deposition. The saturation curves show that the exposure to precursor and co-reactant should be sufficiently long to reach self-limitation for each half-reaction (i.e., saturation). The purging in between these steps should be sufficiently long to avoid parasitic CVD reactions that compromise the ALD character of the processes. Comparison of thickness uniformity attainable on 3D substrates by **c)** conventional deposition techniques (e.g., CVD and PVD) and **d)** ALD. The arrows indicate the thickness of the deposited material. Thickness non-uniformity can be observed in the first case and conformal deposition (i.e., uniform thickness on a nanostructured sample) in the latter one.

Principle of area-selective ALD. In area-selective ALD, the chemical nature of the ALD technique is harnessed to control the locations where material deposition takes place, while ideally avoiding deposition where not needed. This is enabled by the fact that the extent to which the precursor or the co-reactant surface reactions occur depends on the specific chemistry of the substrate. A pre-requisite for area-selective ALD is that a substrate is pre-patterned with multiple areas, as depicted in Figure 1.4a. From a processing point-of-view, one area is active (referred to as *growth area*), and the other areas are passive (referred to as the *non-growth areas*) towards the specific ALD chemistry. In this way, by repeating the ALD cycles, material deposition occurs selectively on the *growth area*. Compared to other *top-down* patterning methods (involving deposition, lithography, etching) that suffer from alignment issues (Figure 1.4b), area-selective ALD can enable *bottom-up* growth with near-atomic scale precision alignment (Figure 1.4c).

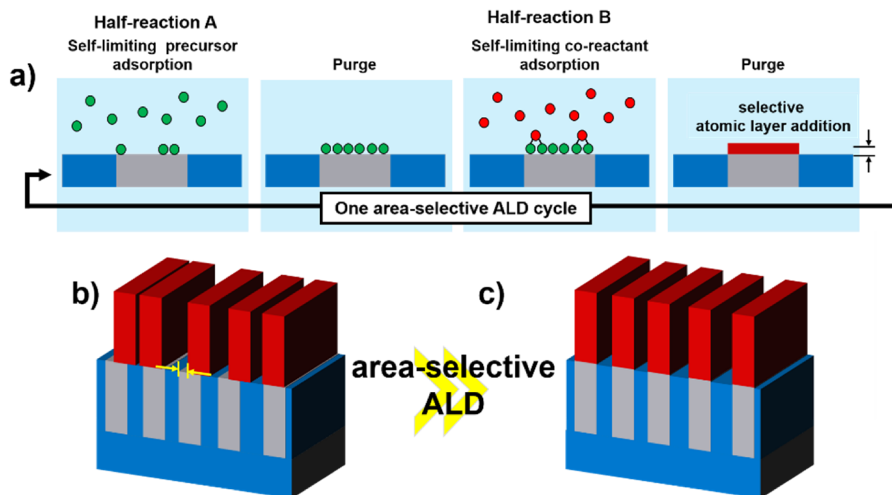


Figure 1.4: Schematic representation of **a)** one complete ALD cycle for area-selective deposition. Deposition occurs only on one area (*growth area*), because the half-reactions A and/or B are inhibited on the other surfaces (*non-growth areas*). Comparison of the resulting feature alignment for **b)** a conventional *top-down* and **c)** an ideal *bottom-up* fabrication process employing area-selective ALD. The arrows in Fig. 1.4b highlight the misalignment of the features in the case of *top-down* fabrication.

Principle of selective ALE. ALE is the etching counterpart of ALD, as it enables layer-by-layer material removal with atomic-level thickness control. Particularly relevant in ALE is the ability to selectively remove one material while, ideally, leaving the other as it is, as illustrated in Figure 1.5a. Although, many ALE processes have been reported in the literature so far, ‘selective’ ALE processes have not been as frequently described even though “selectivity” is an inherent component of etching processes. In this dissertation, we explicitly address the aspect of selectivity in ALE in Chapter 3, followed by an experimental example of selective ALE in Chapter 7. ALE relies on the cyclic exposure of a material to (typically) two reactants which undergo self-limiting half-reactions. In this case, unwanted etch reactions are avoided because of the interleaved purge steps that ensure a surface-controlled process. The self-limiting nature of the two half-reactions allows ALE to yield uniform film etching on large-area substrates. The main difference with ALD is that ALE can be either anisotropic/directional, if accelerated ions or neutral beams are used in the co-reactant step, or isotropic, if only thermal or radical-driven plasma reactions are employed (see Chapters 3 and 7). Figure 1.5b shows the thickness per cycle that is removed every ALE cycle as a function of the exposures to precursor, purge, co-reactant and again purge, respectively.

The etch rate in conventional dry etching techniques, such as reactive ion etching (RIE) is determined by the fluxes of radicals and ions at the surface of the target material. Their ratio can differ depending on the aspect ratio of the features to be etched since

ions are ballistically accelerated towards the target material, whereas radicals are transported by diffusion.^{6,26} The consequence of this flux-dependence is that the etch rate varies for different aspect ratio structures, which is referred to as aspect ratio dependent etching (ARDE), as depicted in Figure 1.5c. Another limitation of RIE is the ion-induced damage, which in some cases has been shown to impact the uppermost 20 nm of a material and affect the device performance.²⁷ Furthermore, RIE can suffer from bowing, microtrenching and other sorts of *non-fidelity* profiles.²⁸

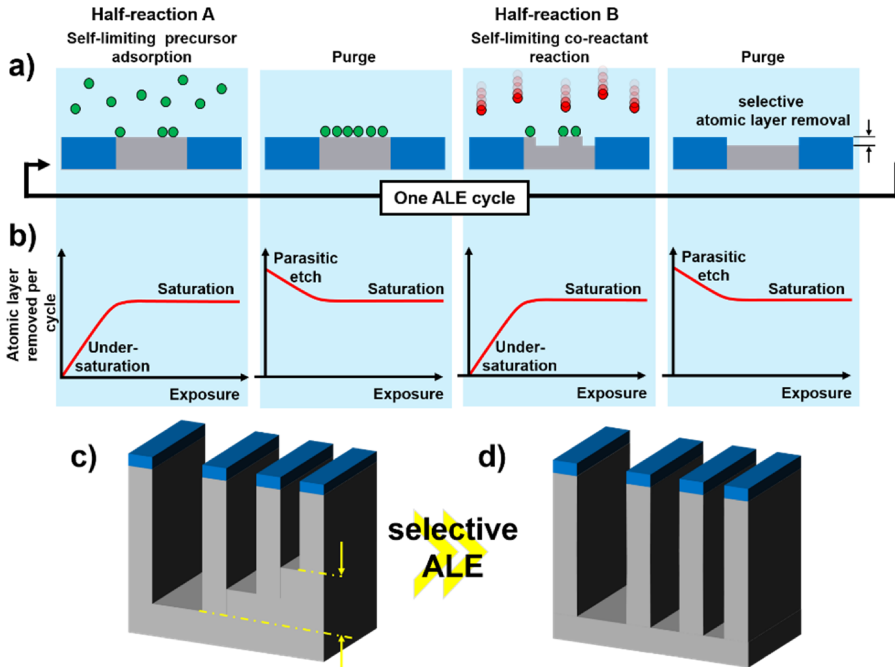


Figure 1.5: Schematics of **a)** one selective atomic layer etching (ALE) cycle and **b)** the saturation curves for the various steps. The depicted processes consist of two self-limiting half-reactions A and B interleaved by purge steps. The cycles are repeated multiple times to achieve the desired thickness of material removal. The saturation curves illustrate that the exposure to precursor and co-reactant should be sufficiently long to reach self-limitation for each half-reaction (i.e., saturation). The purging in between these steps should be sufficiently long to avoid parasitic etching reactions that compromise the ALE character of the processes. Selective removal of one material in the presence of another (hard mask) occurs, because the half-reactions A and/or B are inhibited on the hard mask material or a higher temperature (or ion energy) is required to form a volatile product with the hard mask material. Comparison of etch profiles that show **c)** aspect ratio dependent etching (ARDE) obtained after conventional reactive ion etching, and **d)** perfectly etched trenches using ALE through different mask openings. The arrows indicate the difference in trench depths.

Atomic layer etching (ALE) provides the opportunity to overcome the shortcomings of conventional etching techniques. The idea behind directional/anisotropic ALE is as simple as effective: the effect of ions and radicals can be decoupled into two time-separated and self-limiting steps, thereby allowing the etching to be flux independent and eliminating ARDE effects as well as produce high-fidelity profiles, as shown in Figure 1.5d. To ensure self-limiting behavior, the ion energy employed to provide directionality in ALE has to be well controlled and below the threshold for material sputtering, to avoid continuous material removal. This avoids ion-induced damage. Moreover, the precise control exerted on ion energy enables higher selectivity to be obtained, as compared to continuous etching. High selectivity can be obtained by operating with ion energies above the threshold required to remove a generic material A and below the threshold for removing a different material B.

Self-aligned processing enabled by area-selective ALD. Selective deposition may allow the reduction of the number of lithography and etch steps, thereby resulting in lower manufacturing costs. More importantly, area-selective ALD can ensure self-alignment of features and therefore rule out the issue of EPE. For this reason, area-selective ALD will play a key role in enabling further downscaling. In order to fully appreciate the potential of the technique, an example of an envisioned application is presented in Figure 1.6. Here, a conventional double damascene manufacturing flow for fabricating a generic metal layer ($Mx + 1$) that connects to the lower metal layer (Mx) is compared with a self-aligned process that makes use of area-selective ALD.²⁹

Figure 1.6a schematically represents a simplified double damascene process flow in which a via (i.e., a vertical interconnect access) first and then a trench next are etched in the interlayer dielectric (ILD) stack. The starting point is the metal layer Mx which consists of patterned metal lines and ILD lines. Due to the small metal pitch (distance between two adjacent metal lines) and the previously mentioned alignment issues, there is a high probability that the metal wire, i.e., the contact between Mx and $Mx + 1$, partially lands on the ILD. If so, the metal wire may be too close to the adjacent Mx line and this can cause shorts that result in device failure. Figure 1.6b represents a self-aligned via process flow, that can be used to mitigate the alignment issues.³⁰ During the metallization step the presence of a selectively deposited dielectric layer ‘guides’ the metal wire such that the latter lands exactly on the Mx line. At the bottom of Figure 1.6, the side views of the contacts created with either the double damascene process or with self-aligned via fabrication are compared in order to highlight the resulting alignment differences (panels a.5 and b.6).

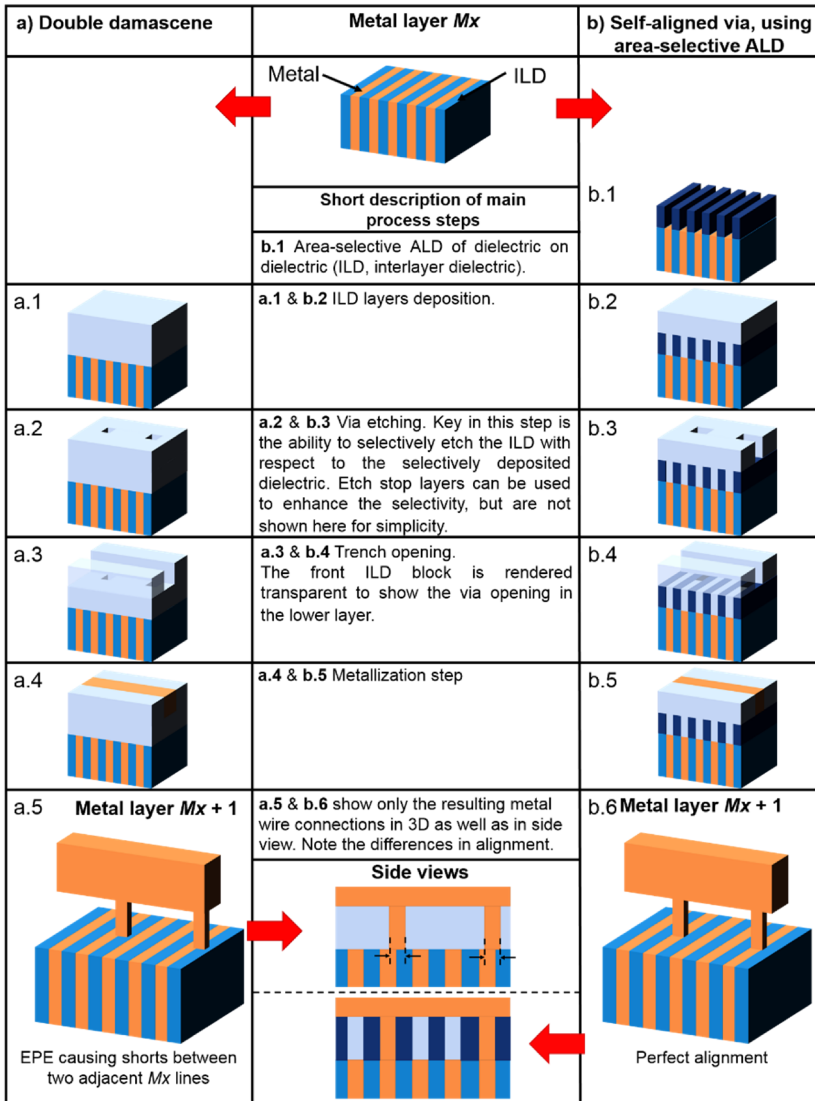


Figure 1.6: Simplified overview of the process flows for two different interconnects fabrication schemes **a)** traditional double damascene and **b)** self-aligned via using area-selective ALD. For simplicity only the most relevant steps to understand the process differences are included. Note that a more relaxed via size is possible in the self-aligned process (b.3). The misalignment in the damascene process is highlighted by the black arrows in the respective side view. In the self-aligned process, perfect alignment is ensured by the presence of the selectively deposited dielectric ‘guides’. Compiled from Refs. 31 and 30.

Self-aligned processing enabled by Atomic Layer Etching. Selective ALE can be employed to mitigate the issues in aligning the contacts at the transistor level. Figure 1.7 compares a conventional continuous etching process (RIE) with an ALE-based process. In the ALE-based process $C_4F_6/Ar/O_2$ plasma chemistry is alternated with Ar^+

bombardment. This etching process is used for the so-called self-aligned contact (SAC) process. The aim here is to etch SiO_2 with extreme selectivity over the SiN capping layer to create a slit that is used for the subsequent metal contacting at the transistor source and drain level. In order to facilitate the understanding of this process, Figures 1.7(a,b) provide a schematic representation of two gates and fins (a) before and (b) after SiO_2 filling. Although, SAC processes are already known in conventional etching, at very small dimensions, the etching process can fail because of unwanted etching of the SiN capping corners (due to poor selectivity), pinch-off of the slit (because of too thick CF_x -polymer deposition) and tapered etch profile (because of CF_x -polymer build-up at the SiN corners), as illustrated in Figures 1.7(c1, c2). The ion energy needs to be increased to be able to etch through the SiO_2 slit, however this significantly increases the chances of surface damage as well as SiN capping-layer overetching. The latter serves to insulate the gate from the subsequent metal contact to either source or drain, therefore it is necessary to keep it intact. Conversely, when using the ALE-based process, the SiO_2 slit is completely etched, as illustrated in Figures 1.7(d1, d2). The benefit of using ALE in this process is that a much higher etch selectivity (SiO_2 over SiN) can be achieved, as compared to the conventional etching process. The high etch selectivity stems from the fact that a lower ion energy can be used and a thinner and more controlled CF_x -polymer thickness is deposited every cycle. This enables the use of the SiN spacer as a protective ‘guide’ for the subsequent metal filling that will serve to contact the source or the drain of the transistor and to avoid possible shorting.

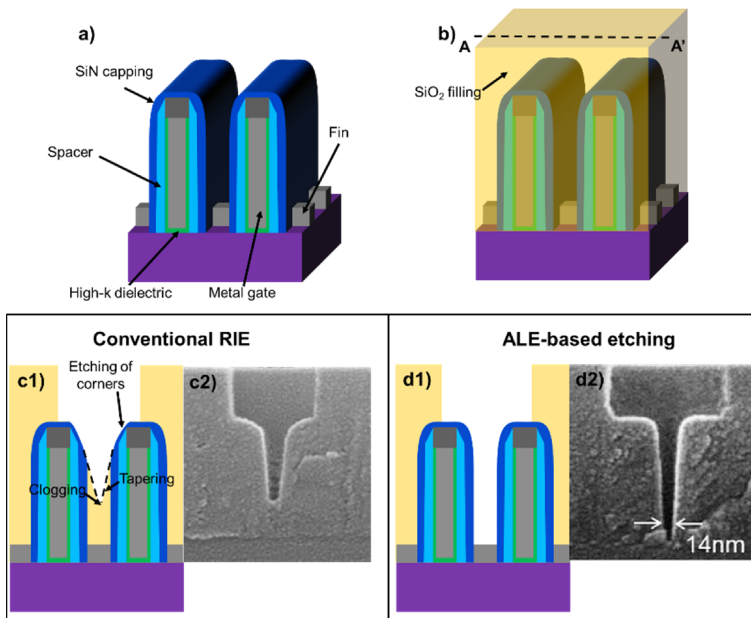


Figure 1.7: Transistor gates and fins **a)** before and **b)** after SiO_2 filling. Self-aligned contact (SAC) etch process using conventional reactive ion etching (RIE) that shows clogging of the slit in both schematic **c1)** and TEM image **c2)**. SAC etch process using ALE-based processing that enables slit opening shown in both schematic **d1)** and TEM image **d2)**. Figures c2 and d2 after Ref. 32.

1.4 Aim of the research project

The aim of the work described in this dissertation was three-fold, namely to: i) experimentally develop area-selective ALD processes and to define a novel route toward area-selective deposition using plasma-based ALD; ii) investigate the underlying mechanisms imparting selectivity, mostly from a theoretical point of view, using density functional theory (DFT) calculations, but also through experimental verification using *in-situ* infrared spectroscopy measurements; iii) develop a novel isotropic ALE process involving a plasma-based reaction step. The research questions that drove this work are formulated below. Each research question is followed by a short description to clarify how these questions have been addressed in the corresponding chapters.

Can we gain insights on the elemental reaction steps that impart selectivity in ALD and ALE?

Several area-selective ALD processes have been developed to allow for the selective deposition of various materials on patterned substrates. Nevertheless, many questions and challenges remain regarding how the selectivity of these processes can be improved to the point that it meets the stringent requirements necessary for industrial applications, where single-digit nanometer process control is imperative. Chapters 2 and 3 provide an overview of the recent advances in the field of area-selective ALD and selective ALE, respectively. A categorization of the area-selective ALD in terms of a *chemoselective precursor* or *chemoselective co-reactant* mechanisms is given. The basic understanding of the mechanisms underlying the selectivity is highlighted as a possible guide toward improving the selectivity of area-selective ALD processes. Examples of correction steps to improve the selectivity of the processes are also provided. Furthermore, optimization of the process parameter optimization as a means to improve selectivity of area-selective ALD is emphasized.

What patterning steps can be combined with area-selective ALD to achieve local substrate activation and therefore *bottom-up* fabrication at micro and nanoscale, in a direct-write fashion?

In Chapters 4 and 5, two processes for area-selective ALD of oxides are presented, i.e., $\text{In}_2\text{O}_3\text{:H}$ in Chapter 4 and ZnO in Chapter 5. These are so-called *direct-write* ALD approaches, since direct-write patterning techniques (i.e., maskless patterning) are employed to locally activate the substrate. In particular, the use of a microplasma printer to chemically activate the substrate could find applications in flexible electronics with pattern sizes of the order of hundreds of μm and beyond (Chapter 4). For smaller

patterning sizes, of typically hundreds of nm and below, the substrate activation step can be carried out using electron beam induced deposition (EBID) to deposit ultra-thin seed layers (Chapter 5). It is important to note that the combination of area-selective ALD with both activation techniques allow for obtaining patterns in a *bottom-up* fashion.

Can area-selective ALD be extended to plasma-based processes to enable selective deposition of more materials?

The use of plasma during ALD allows for a wider process parameter window and range of material properties compared with the conventional thermally driven ALD method. For instance, lower deposition temperatures can be employed when using highly reactive plasma-generated species. Moreover, several technologically relevant materials such as SiO_2 and SiN_x are typically deposited using plasma-assisted ALD. Plasma co-reactants are employed to facilitate reactions, whereas in area-selective ALD the aim is to block reactions on specific areas of a substrate. Therefore, achieving area-selective ALD, during plasma-assisted processes, represents a challenging problem. In Chapter 6, a novel approach for attaining area-selective ALD using plasma-based chemistry is demonstrated. This process utilizes inhibitor molecules that selectively de-activate the non-growth area, such that during the subsequent step, the precursor chemisorption is hindered on this surface. The ALD cycle is then completed by a plasma co-reactant step that removes the inhibitor as well as enables material deposition only on the growth area. The underlying mechanism was investigated using DFT and infrared spectroscopy methods.

Can we gain insights on the role of thermodynamics and kinetics of ALD reactions in imparting selectivity?

Besides demonstrating the feasibility of the *direct-write* area-selective ALD processes for $\text{In}_2\text{O}_3\text{:H}$ and ZnO , the surface chemistry enabling the processes was investigated by means of DFT calculations. These results are also presented in Chapters 4 and 5. The selectivity of the two processes was attributed to a chemoselective precursor mechanism that is thermodynamically controlled in the case of $\text{In}_2\text{O}_3\text{:H}$ and kinetically controlled in the case of ZnO . The effect of the deposition temperature was also investigated for the case of ZnO . The selectivity of this process was observed to increase with the deposition temperature. Physisorption of the precursor is suggested as a possible mechanism that reduces the selectivity at low deposition temperature.

Can plasma-based processing also lead to isotropic etch profiles?

Commonly, thermal ALE is typically associated with isotropic etch profiles and plasma-induced ALE with anisotropic etch profiles. However, when no bias is employed and the plasma parameters and chemistry are carefully chosen, also isotropic ALE profiles can be obtained by using a plasma co-reactant step. In Chapter 7, a plasma-based approach is demonstrated for the isotropic ALE of ZnO layers on 3D nanostructures, consisting of an array of vertical nanowires. Damage-free and isotropic etch profile was corroborated by high-resolution TEM inspections. A preliminary reaction mechanism is suggested on the basis of infrared spectroscopic measurements. This was used to provide a possible explanation of the high etch selectivity over SiO₂ and HfO₂.

REFERENCES

- (1) Waldrop, M. M. The Chips Are down for Moore's Law. *Nature* **2016**, *530*, 144–147.
- (2) Photographic Negative IBM 608 Transistor Calc c1956 <http://www.vintage-icl-computers.com/icl49cc>.
- (3) Borodovsky, Y. Marching to the Beat of Moore's Law. **2006**, *615301*, 615301.
- (4) Puers, Robert; Baldi, Livio; van Nooten, Sebastiaan E.; Van de Voorde, M. *Nanoelectronics: Materials, Devices, Applications*; Puers, Robert; Baldi, Livio; van Nooten, Sebastiaan E.; Van de Voorde, M., Ed.; Wiley-VCH Verlag GmbH & Co. KGaA: Weinheim, Germany, 2017.
- (5) Dennard, R. H.; Gaensslen, F. H.; Hwa-Nien, Y. U.; Leo Rideout, V.; Bassous, E.; Leblanc, A. R. Design of Ion-Implanted MOSFET's with Very Small Physical Dimensions. *IEEE J. Solid-State Circuits* **1974**, *SC-9(5)*, 256–268.
- (6) Lee, C. G. N.; Kanarik, K. J.; Gottscho, R. A. The Grand Challenges of Plasma Etching: A Manufacturing Perspective. *J. Phys. D. Appl. Phys.* **2014**, *47*, 273001.
- (7) Honda, M.; Katsunuma, T. Etch Challenges and Evolutions for Atomic - Order Control. *Proc. 16th Int. Conf. Nanotechnol.* **2016**, 448–451.
- (8) Horiguchi, N.; Milenin, A. P.; Tao, Z.; Hubert, H.; Altamirano-Sanchez, E.; Veloso, A.; Witters, L.; Waldron, N.; Ragnarsson, L.-Å.; Kim, M. S.; *et al.* Patterning Challenges in Advanced Device Architectures: FinFETs to Nanowires. **2016**, *9782*, 978209.
- (9) Radamson, H. H.; Zhang, Y.; He, X.; Cui, H.; Li, J.; Xiang, J.; Liu, J.; Gu, S.; Wang, G. The Challenges of Advanced CMOS Process from 2D to 3D. *Appl. Sci.* **2017**, *7*, 1047.
- (10) Pan, D. Z.; Liebmann, L.; Yu, B.; Xu, X.; Lin, Y. Pushing Multiple Patterning in Sub-10nm. *Proc. 52nd Annu. Des. Autom. Conf. - DAC '15* **2015**, 1–6.
- (11) Bristol, R.; Shykind, D.; Kim, S.; Borodovsky, Y.; Schwartz, E.; Turner, C.; Masson, G.; Min, K.; Esswein, K.; Blackwell, J.; *et al.* Double-Exposure Materials for Pitch Division with 193nm Lithography: Requirements, Results. *Adv. Resist Mater. Process. Technol. XXVI. Ed. by Henderson* **2009**, *7273*, 4.
- (12) Mulkens, J.; Hanna, M.; Wei, H.; Vaenkatesan, V.; Megens, H.; Slotboom, D. Overlay and Edge Placement Control Strategies for the 7nm Node Using EUV and ArF Lithography. *Proc. SPIE* **2015**, *9422*, 94221Q–1/13.
- (13) Borodovsky, Y. A. Overlay Improvement through Overlay Modeling. *Proc. SPIE* **2726**, *Opt. Microlithogr. IX* **1996**, 311–322.
- (14) Gupta, P.; Kahng, A. B.; Muddu, S. V.; Nakagawa, S. Modeling Edge Placement Error Distribution in Standard Cell Library. *Proc. SPIE Des. Process Integr. Microelectron. Manuf. IV* **2006**, *6156*, 61560S1–12.
- (15) Fang, C.; Graves, T.; Vaglio Pret, A.; Robertson, S.; Smith, M. Gaining Insight into Effective Metrology Height through the Use of a Compact CDSEM Model for Lithography Simulation. In *Metrology, Inspection, and Process Control for Microlithography XXX, Proc. of SPIE*; 2016; Vol. 9778, p. 97780B1–13.
- (16) Yildirim, O.; Buitrago, E.; Hoefnagels, R.; Meeuwissen, M.; Wuister, S.; Rispens, G.; van Oosten, A.; Derks, P.; Finders, J.; Vockenhuber, M.; *et al.* Improvements in Resist Performance towards EUV HVM. In *Extreme Ultraviolet (EUV) Lithography VIII, Proc. of SPIE*; 2017; p. 101430Q1–12.
- (17) Choe, J. Intel 3D XPoint Memory Die Removed from Intel Optane™ PCM (Phase Change Memory) <http://www.techinsights.com/about-techinsights/overview/blog/intel-3d-xpoint-memory-die-removed-from-intel-optane-pcm/>.
- (18) Park, J. C.; Lee, H.; Im, S. Self-Aligned Top-Gate Amorphous Indium Zinc Oxide Thin-Film Transistors Exceeding Low-Temperature Poly-Si Transistor Performance. **2013**.
- (19) Fan, C.; Shang, M.; Li, B.; Lin, Y.; Wang, S. A Self-Aligned a-IGZO Thin-Film Transistor Using a New Two-Photo-Mask Process with a Continuous Etching Scheme. **2014**, 5761–5768.
- (20) Xiao, S.; Fernandes, S. A.; Ostendorf, A. Selective Patterning of ITO on Flexible PET Substrate by 1064nm Picosecond Laser. *Phys. Procedia* **2011**, *12*, 125–132.
- (21) Pang, C. Efficiency Enhancement of Polymer Solar Cells. *J. Nanosci. Nanotechnol.* **2008**, *8*, 5279–5283.
- (22) Simon, A. H.; Bolom, T.; Niu, C.; Baumann, F. H.; Hu, C. K.; Parks, C.; Nag, J.; Kim, H.; Lee, J. Y.; Yang, C. C.; *et al.* Electromigration Comparison of Selective CVD Cobalt Capping with PVD Ta(N)

- and CVD Cobalt Liners on 22nm-Groundrule Dual-Damascene Cu Interconnects. *IEEE Int. Reliab. Phys. Symp. Proc.* **2013**, 1–6.
- (23) O'Neill, B. J.; Jackson, D. H. K.; Lee, J.; Canlas, C.; Stair, P. C.; Marshall, C. L.; Elam, J. W.; Kuech, T. F.; Dumesic, J. A.; Huber, G. W. Catalyst Design with Atomic Layer Deposition. *ACS Catal.* **2015**, *5*, 1804–1825.
- (24) George, S. M. Atomic Layer Deposition: An Overview. *Chem. Rev.* **2010**, *110*, 111–131.
- (25) Hwang, C. S.; Yoo, C. Y. *Atomic Layer Deposition for Semiconductors*; 2014.
- (26) Coburn, J. W.; Winters, H. F. Conductance Considerations in the Reactive Ion Etching of High Aspect Ratio Features. *Appl. Phys. Lett.* **1989**, *55*, 2730–2732.
- (27) Petit-Etienne, C.; Darnon, M.; Bodart, P.; Fouchier, M.; Cunge, G.; Pargon, E.; Vallier, L.; Joubert, O.; Banna, S. Atomic-Scale Silicon Etching Control Using Pulsed Cl₂ Plasma. *J. Vac. Sci. Technol. B, Nanotechnol. Microelectron. Mater. Process. Meas. Phenom.* **2013**, *31*, 11201.
- (28) Donnelly, V. M.; Kornblit, A. Plasma Etching: Yesterday, Today, and Tomorrow. *J. Vac. Sci. Technol. A Vacuum, Surfaces, Film.* **2013**, *31*, 50825.
- (29) Murdoch, G.; Bömmels, J.; Wilson, C. J.; Gavan, K. B.; Le, Q. T.; Tőkei, Z.; Clark, W. Feasibility Study of Fully Self Aligned Vias for 5nm Node BEOL. In *Interconnect Technology Conference (IITC), 2017 IEEE International*; 2017.
- (30) Smith, J.; DeVilliers, A. J. US 20170221760A1, 2017.
- (31) Nojiri, K. *Dry Etching Technology for Semiconductors*; 2015.
- (32) Honda, M.; Katsunuma, T.; Tabata, M.; Tsuji, A.; Oishi, T.; Hisamatsu, T.; Ogawa, S.; Kihara, Y. Benefits of Atomic-Level Processing by Quasi-ALE and ALD Technique. *J. Phys. D: Appl. Phys.* **2017**, *50*.

Chapter 2

Area-Selective ALD: an Overview

Semiconductor devices require the implementation of advanced process technologies with accurate position alignment and atomic scale fidelity. Deposition techniques such as area-selective atomic layer deposition (ALD) are needed in order to overcome the challenges in achieving near-atomic precision in the lateral alignment between different layers and to engineer innovative structures. Area-selective ALD is based on the initial differences in chemical reactivity of the precursor (or the co-reactant) and two diverse substrate areas. During the past decade, several area-selective ALD processes have been developed by taking advantage of chemoselective precursor/co-reactant reactions. Yet, there are fundamental difficulties in obtaining high selectivity. In this overview, we discuss the basic principles underlying area-selective ALD and emphasized on the important role of surface chemistry for understanding area-selective ALD processes. Next, we discuss how this knowledge can be used to account for non-idealities and as a guide for tuning the reaction conditions for improving the selectivity.

2.1 Introduction

As described in Chapter 1, area-selective atomic layer deposition (ALD) can allow *bottom-up* fabrication schemes. In such schemes, localized material deposition is obtained by exploiting differences in *chemical reactivity* of different substrate areas with respect to the precursor or the co-reactant (i.e. *chemoselectivity*). Area-selective ALD is envisioned as a potential technological solution in various applications among electronics, optoelectronics and catalysis.¹⁻³

Area-selective ALD is obtained on a pre-patterned substrate by making use of the differences in thin film nucleation on chemically different substrate areas, i.e. areas with diverse surface functional groups. Such surfaces can include self-assembled monolayers (SAMs), polymers, oxides, nitrides, metals, etc. As depicted in Figure 2.1, the patterned substrate is composed of multiple areas of two different materials and the aim is to deposit selectively on one of them (hereinafter referred to as the *growth area*), while preventing deposition from occurring on the remaining substrate surfaces (hereinafter referred to as the *non-growth areas*).

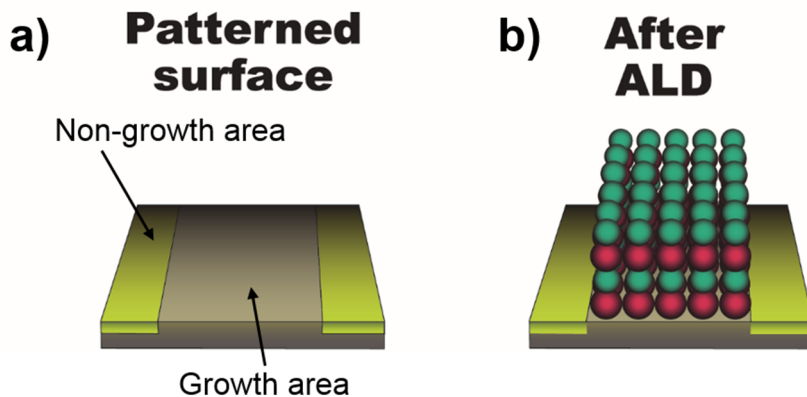


Figure 2.1: a) Starting patterned surface consisting of two different materials which represent the growth-area on which deposition is required, and the non-growth area onto which deposition is undesired. b) The same patterned surface after an ideal area-selective ALD process. Here, material deposition takes place exclusively on the growth-area. Adapted from Ref. 3.

To date, many area-selective ALD processes have been developed to allow for the selective deposition of several materials on different patterned substrates. Several reviews on ALD have included the topic of area-selective ALD.^{1,4-7} Recently, Cao *et al.* have reviewed the application possibilities of area-selective ALD for the fabrication of composite catalysts.⁷ They highlighted area-selective ALD as a unique method for tailoring interfaces, active sites and therefore, catalytic selectivity of the resulting composite catalysts. Mackus *et al.* distinguished two categories to achieve area-selective ALD:⁸

- *Area-deactivation*, when areas of a substrate are rendered inert towards the ALD chemistry (e.g., using SAMs or polymers)
- *Area-activation*, when a chemically inert surface is locally activated to enable material deposition (e.g., by local surface modification or deposition of seed layers)

Different ways of patterning result in a diverse number of steps and may be suitable for a specific application. That review categorizes area-selective ALD as based on the patterning step that defines two areas of a substrate with different chemical behaviour.

The content of this chapter is the following: in Section 2.2 we illustrate the concept of *nucleation delay*. This is then linked to the ALD surface chemistry and a general notion of thermodynamics and kinetics of surface reactions, discussed in Section 2.3. On the basis of these considerations, in Section 2.4, we attempt a classification of the area-selective ALD processes based on the mechanism that allows for attaining selectivity: *chemoselective precursor* or *chemoselective co-reactant mechanisms*. In Section 2.5, recent processing strategies

for improving the selectivity are reviewed and parallels with the literature for area-selective CVD are drawn. Finally, in Section 2.6 a short summary and outlook conclude the work.

2.2 Nucleation delay and selectivity window

Depending on the distinct chemical character of the substrate surface considered, as well as the reactivity between the latter and the chemicals involved in the deposition chemistry, the ALD process may experience a nucleation delay or trigger deposition.^{9,10} Figures 2.2(a-b) schematically depict the nucleation behavior of a generic ALD process on two chemically different starting surfaces (represented in the insets). In the first case (Figure 2.2a), immediate and linear thickness increase with the number of ALD cycles indicates fast film nucleation on the starting surface, resulting in a controlled layer-by-layer deposition of the desired material, as shown in Figures 2.2a1-a3. In the second case (Figure 2.2b), film deposition is delayed for several ALD cycles. During this nucleation delay, the starting surface ideally remains in its pristine non-reactive state, as depicted in Figure 2.2b1. However, such a nucleation delay typically does not last for a sufficiently large number of ALD cycles and film growth may start also on this surface, as shown in Figure 2.2b2. There can be several reasons for which deposition starts after a nucleation delay:

- a slow but gradual accumulation of deposited material
- uncontrolled changes of the starting surface during the ALD process (e.g., oxidation of the starting surface, or unwanted precursor or co-reactant physisorption)
- presence of defect sites on which the ALD reactions can take place.

After the nucleation delay, and once the surface is fully covered by the deposited material, the growth proceeds similarly to the case of Figure 2.2a and layer-by-layer deposition takes place also on this surface, as shown in Figure 2.2b3.

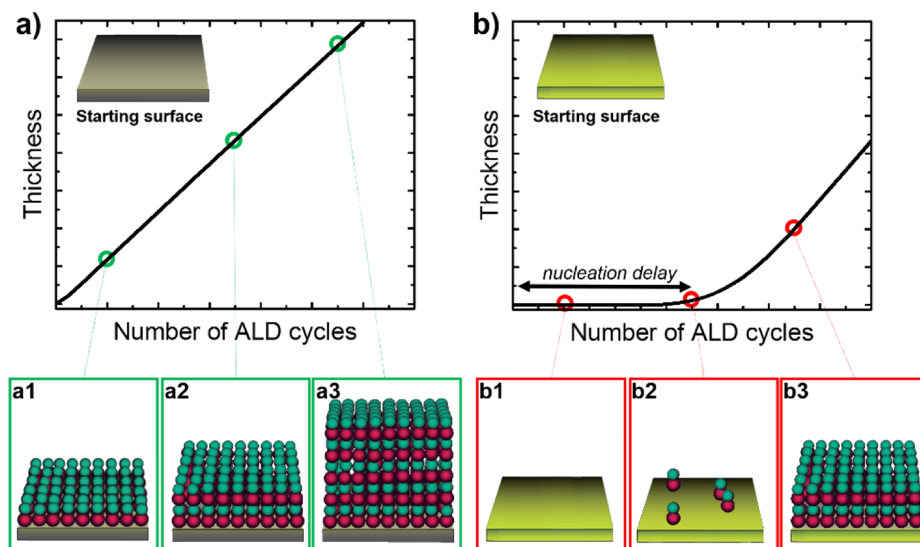


Figure 2.2: Film thickness as a function of the number of ALD cycles for two different starting surfaces. The cyclic dosage of precursor and co-reactant results in **a)** immediate and linear film thickness increase or **b)** a nucleation delay. Pictures **a1-a3)**, and **b1-b3)** schematically represent three different stages of the film deposition on the respective starting surface.

Such difference in nucleation behavior on diverse surfaces can be exploited (for a limited number of cycles) to achieve area-selective ALD by creating a substrate with a pattern of growth areas (Figure 2.2a) and non-growth areas (Figure 2.2b). To schematically illustrate this, in Figure 2.3 a patterned surface, consisting of a growth and two non-growth areas, is subjected to the same generic ALD process illustrated in Figures 2.2(a, b). During the nucleation delay, area-selective deposition is obtained on the growth area. After the nucleation delay, deposition starts also on the non-growth area, i.e. the selectivity is lost.

From Figure 2.2, it becomes also clear that, for the same process, a longer nucleation delay implies a larger selectivity. A *selectivity window* can be defined as the width (in number of cycles) of the nucleation delay (Figure 2.3). In such a selectivity window the amount of material non-intentionally deposited on the non-growth area remains (ideally) zero and concurrently material can be deposited on the growth area. Outside the selectivity window deposition take place also on the non-growth area, thus the selectivity will decrease and - eventually - will be lost.

Studies of the early stages in thin film nucleation on different surfaces are therefore extremely important to understand and develop area-selective ALD processes and often represent the first test in exploring possible area-selective ALD processes.

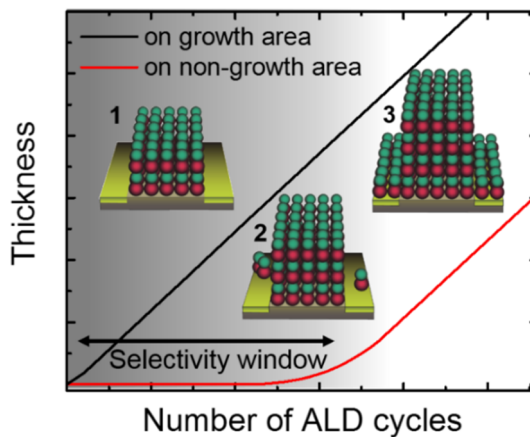


Figure 2.3: Schematic representation of film thickness on growth and non-growth areas during area-selective ALD on a patterned substrate. Three different stages are represented by the respective insets: **1)** no deposition on the non-growth area during the nucleation delay; this stage represents the selectivity window. **2)** At the edge of the selectivity window, deposition starts also on the non-growth area. **3)** Outside the selectivity window linear growth is observed on both areas.

At moderately low deposition temperature, the typical differences in nucleation delay on growth and non-growth areas in ALD can be explained by the differences in thermodynamics and/or kinetics of the surface reaction.¹¹ The width of the selectivity window is, therefore, governed by the ALD surface chemistry specific to the non-growth area.

2.3 Thermodynamics and kinetic aspects of surface reactions

It is instructive to describe concepts from thermodynamics and kinetics that are useful for the fields of area-selective CVD and area-selective ALD.

Thermodynamics. In the CVD literature, thermodynamic calculations have been extensively used to estimate whether a deposition reaction is feasible or not. In particular, if the change in Gibbs free energy is negative, $\Delta G < 0$, a reaction may occur because it is energetically favorable (exothermic), whereas if $\Delta G > 0$, the reaction does not occur because it is energetically unfavorable (endothermic).¹² By definition $\Delta G = \Delta H - T\Delta S$, where ΔH is the change in enthalpy of reaction and ΔS is the entropy change. Four possibilities are summarized in table I. If $\Delta H < 0$ (neglecting kinetics) and $\Delta S > 0$ the reaction take place spontaneously at all temperature, and if $\Delta H < 0$ and $\Delta S < 0$ only at low temperature (as low as ΔG becomes negative). If $\Delta H > 0$ and $\Delta S > 0$ the reaction is spontaneous only at high temperature (as high as ΔG becomes negative), and if $\Delta H > 0$ and $\Delta S < 0$ is thermodynamically forbidden. A first estimation of the sign of ΔS

can be obtained by considering the stoichiometry of a reaction (difference in number of moles of gas between products and reactants).¹³ In the area-selective ALD literature, the entropy term is typically neglected because at moderate low deposition temperatures it has a minor contribution. Therefore, the thermodynamic feasibility of a reaction is usually determined only by the sign of ΔH .

Table I: Four possibilities for enthalpy and entropy in determining the sign of the Gibbs free energy.

	$\Delta H < 0$	$\Delta H > 0$
$\Delta S > 0$	Always spontaneous	Spontaneous at high T
$\Delta S < 0$	Spontaneous at low T	Non-spontaneous

Thermodynamic calculations have been extensively applied to provide a theoretical explanatory background to area-selective CVD processes, and in some cases to predict how experimental parameters might affect the selectivity. Figure 2.4 shows the so called *selectivity parameter*, $R_{\Delta G}$, at different pressures and temperature, as a function of the molar ratio between H_2 and WF_6 for area-selective CVD of W. This parameter was introduced by Carlsson and co-workers and represents the ratio of the magnitude of the ΔG of reactions on growth and non-growth areas.¹⁴ $R_{\Delta G} > 1$ indicates the onset of selective deposition on the growth area in the presence of the non-growth area; for larger $R_{\Delta G}$, a larger selectivity can be expected. From this calculation it was concluded that lower temperature, lower total pressure and lower H_2 concentration will favor higher W selectivity, in agreement with experimental results.

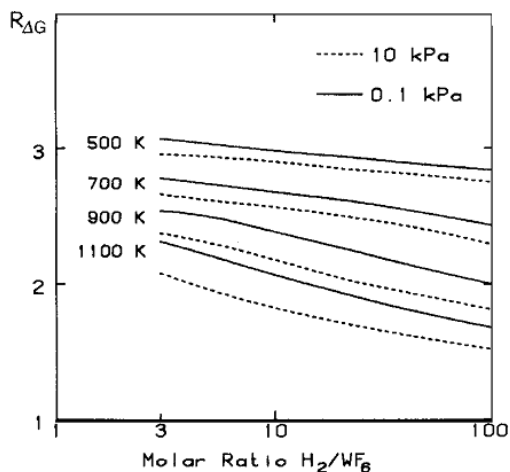


Figure 2.4: Selectivity parameter, $R_{\Delta G}$, for the W area-selective CVD on silicon in the presence of SiO_2 as a function of the H_2/WF_6 molar ratio for different temperatures and total pressure. After Ref. 14.

Kinetics. If a reaction is thermodynamically favored, it should be assessed whether it is also kinetically feasible. In the CVD literature, for a specific deposition system there can be several reaction pathways that are thermodynamically feasible, however in practice these are irrelevant for the deposition process when they proceed too slowly.¹⁵ Let us consider two reactions 1 and 2. The rate constant (k) of reaction 1 is given by $k_1 = A \exp(-E_a/RT)$, where A is the pre-exponential factor, E_a is the activation energy, R is the gas universal constant, and T is the absolute temperature. If k_1 is much larger than the rate constant of reaction 2, k_2 , then reaction 1 will proceed to completion in a considerably shorter time than reaction B. In Figure 2.5 we plotted the calculated *reaction half-life* (i.e. the amount of time required for a reaction to half the initial concentration of reactant) as a function of the activation energy and for two different temperatures. Assuming a pre-exponential factor of 10^{13} s^{-1} , first-order kinetics, and a temperature of 300 K, for an activation energies of 0.8 eV and 1 eV the reaction half-life are $\sim 2 \text{ s}$ and 1 h, respectively. For the same activation energies, increasing the temperature to 500 K decreases the reaction half-life to $\sim 8^{-6} \text{ s}$ and $\sim 8^{-4} \text{ s}$, respectively. Depending on the activation energy (and the temperature) a reaction may be defined as kinetically feasible if the half-time is in the range of seconds and kinetically hindered if the half-time is of the order of minutes or hours.

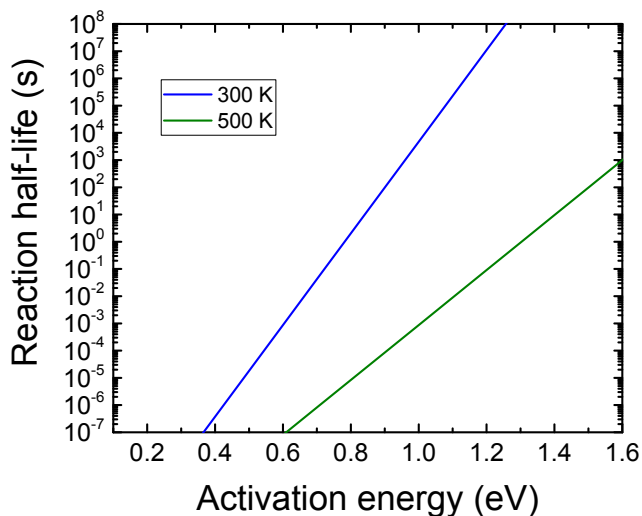


Figure 2.5: Reaction half-life as a function of the activation energy for 300 and 500 K.

Thermodynamic and kinetic considerations can be used as a guide for understanding nucleation delays. In short: if the deposition reactions are thermodynamically and kinetically feasible, nucleation and film growth is generally “immediate”. Conversely, if the reactions are either thermodynamically or kinetically hindered, the deposition can experience a nucleation delay.

2.4 Surface chemistry underlying area-selective ALD

This section focuses on how selectivity can be achieved on the basis of ALD surface reactions and provides an overview of the area-selective ALD processes reported in the literature. For the examples described in this section the area-selective ALD has been proved experimentally and the mechanism underlying the selectivity has been investigated using DFT calculations. A drawback of DFT simulations is that many alternative reaction pathways may be present in reality but not always considered during the modelling. For the same reaction pathway, there are differences in adsorption energies calculated using different DFT methods and adsorption energies experimentally determined (it should be also noted that the accuracy of experimentally determined values depends on experimental setup, calibrations and uncertainties in which reaction is exactly observed, among multiple that may happen at the same time).¹⁶ In addition, most of the time DFT models consider crystalline surfaces whereas amorphous surface are more frequently encountered during ALD experiments. Nevertheless, in relative terms the energy values of the same reaction on different surfaces can provide useful insights into the possible mechanism underlying selectivity in area-selective ALD.

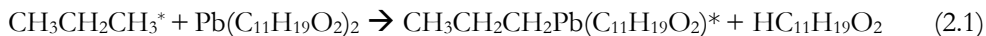
In ALD, the precursor and co-reactant are separated into two half-reactions that are alternated in a cyclic fashion, thus selectivity may stem from one of the two half-reactions. Depending on the substrate and on the chemistry of the process, area-selective ALD can therefore be controlled by a:

- *Chemoselective precursor mechanism, or*
- *Chemoselective co-reactant mechanism*

In the case of a *chemoselective precursor mechanism*, the precursor chemisorption on the non-growth area can be hindered for thermodynamic or kinetic reasons. As a result, deposition will be inhibited for at least a certain number of ALD cycles. In the case of a *chemoselective co-reactant mechanism*, the precursor chemisorbs on all areas, but area-selective ALD may be obtained when the co-reactant reactions are unfeasible or slow and therefore require a surface that can trigger such reactions, i.e. the growth area. Below, we describe several examples of area-selective ALD processes that fall in the two categories of chemoselective precursor or chemoselective co-reactant mechanisms, in Section 2.4.A and 2.4.B, respectively. A more comprehensive overview of these two categories is presented in Tables II and III, after which general considerations are drawn.

2.4.A. Chemoselective precursor mechanism

The differences in reactivity between surface groups with given precursors have been largely explored for achieving area-selective ALD of oxides, nitrides and metals. Commonly, the differences in reactivity of a precursor with SAM tail groups (-CH₃; -NH₂; -SH₂; -OH)^{5,17-19} or with different silicon substrate terminations (-OH; -H; -NH_x)²⁰⁻²³ are exploited as a means to control the precursor chemisorption step. For example, according to DFT calculations performed by Lee *et al.*, area-selective ALD of PbS was obtained because of the thermodynamically unfavorable reactions (2.1) between the lead precursor, Pb(tmhd)₂ (or Pb(C₁₁H₁₉O₂)₂), and the surface groups present on the non-growth area, i.e. CH₃-termination present on the tail of octadecyltrichlorosilane (ODTS) SAMs (Figure 2.6a).¹⁹ Conversely, the reaction (2.2) with OH-terminated silicon surfaces was calculated to be thermodynamically feasible (Figure 2.6b). These reactions, together with the associated activation energy, E_a , and the chemisorption enthalpy change, ΔH , are listed below:



$$\text{with } E_a = 2.39 \text{ eV}; \Delta H = 1.39 \text{ eV}$$



$$\text{with } E_a = 0.61 \text{ eV}; \Delta H = -0.60 \text{ eV}$$

where the asterisks represent the surface species. Consistent with the endothermic nature of the precursor chemisorption on a CH₃-terminated SAM surface, PbS deposition was inhibited for as long as 80 ALD cycles before a noticeable Pb 4f signal was detected by X-ray photoelectron spectroscopy (XPS) on the SAM-coated substrate.¹⁹

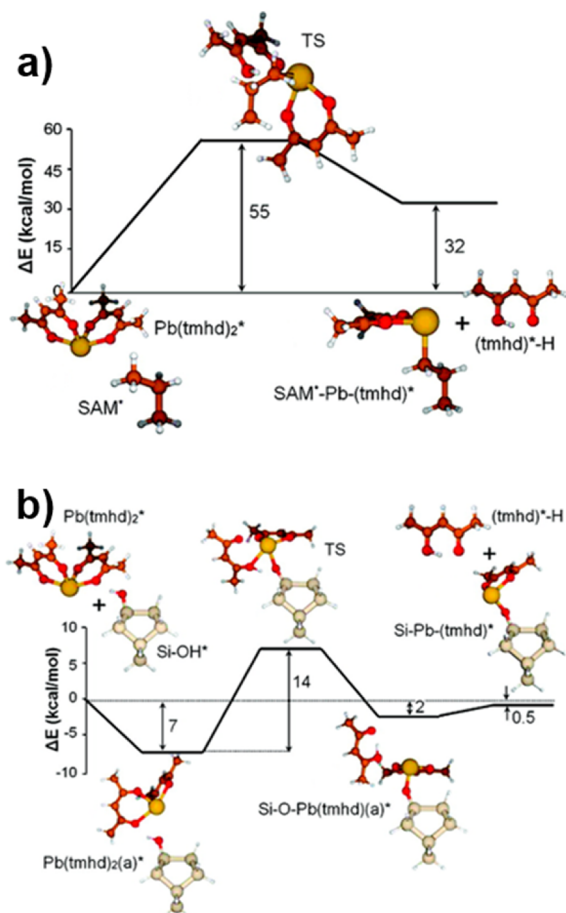


Figure 2.6: Energetics profile for the $\text{Pb}(\text{tmhd})_2$ reaction on: **a)** CH_3 -terminated alkane chain, representing the SAM-tail and **b)** hydroxylated silicon surface. The insets correspond to the static points of the energetic profile: physisorbed state, activated transition state (TS) complex, chemisorbed product, and desorbing by-product. Adapted from Ref. 19.

Besides SAMs, which are commonly used to inhibit precursor chemisorption, H-terminated Si or NH-terminated SiN_xH_y surfaces are also known for being relatively inert surfaces toward several ALD precursors.^{24–26} In the work presented in Chapters 4 and 5, we used these surface terminations to achieve area-selective ALD of In_2O_3 and ZnO on hydroxylated SiO_2 in the presence of H-terminated Si or NH-terminated SiN_xH_y .²⁷ Detailed descriptions of these processes are given in the respective Chapters.

An interesting example with reverse selectivity can be found for the case of the area-selective ALD of cobalt (Co) metal. Supported by DFT calculations and *in-situ* infrared spectroscopy measurements, Kwon *et al.* explained the substrate selectivity for Co ALD on H-terminated Si in the presence of SiO_2 , using ${}^t\text{Bu}$ -allyl- $\text{Co}(\text{CO})_3$ ($(\text{CH}_3)_3\text{C}=\text{CH}_2\text{CH}_2\text{Co}(\text{CO})_3$) as the precursor and dimethylhydrazine ($(\text{CH}_3)_2\text{N}_2$) as the reductant.

as the co-reactant.²⁸ Opposite to what is observed for the cases of In_2O_3 and ZnO , this precursor allows for Co deposition on H-terminated Si and not on SiO_2 . A model for a simplified precursor surface reactions underlying this process together with DFT-calculated reaction energies is listed below:



$$\text{with } E_a = 1.74 \text{ eV}; \Delta H = 0.65 \text{ eV}$$



$$\text{with } E_a = 0.91 \text{ eV}; \Delta H = -0.58 \text{ eV}$$

According to DFT calculations, the precursor chemisorption reaction (2.3) on hydroxylated SiO_2 was found to have a relatively high activation energy of 1.74 eV and to be 0.65 eV endothermic. Therefore, this reaction is assumed to be thermodynamically unfavorable. Conversely, reaction (2.4) on H-terminated Si was shown to have a lower activation energy of 0.91 eV and to be exothermic by -0.58 eV, making it more favorable thermodynamically.²⁸

In Table II we make an attempt to provide an overview of the area-selective ALD processes that are assumed to exploit a *chemoselective precursor mechanism*. This categorization includes published results for which the key role of the precursor in achieving selectivity has been explicitly suggested in the publication. For the ALD of W, the mechanism is derived from data reported in area-selective CVD literature.

TABLE II: Overview of area-selective ALD processes employing chemoselective precursor chemisorption. For each material, the precursor, co-reactant, growth and non-growth areas as well as the selectively grown thickness are listed. List of abbreviations: PVP = polyvinylpyrrolidone; ODPA = octadecylphosphonic acid; ODDC = n-octadecyldimethylchlorosilane; PMMA = poly(methyl methacrylate); OTS = octadecyltrichlorosilane; Ps-b-PVP = poly(styrene-block-2-vinylpyridine); DAT = dodecanethiol; FOTS = trichloro(perfluorooctyl)silane; HDMS = hexamethyldisilazane; ODS = octadecyltrimethoxysilane; ODTS = octadecyltrichlorosilane; dmamb = dimethylamido-2-methyl-2butoxide; acac = acetylacetonate; thd 2,2,6,6-tetramethylheptane-3,3-dionate; AMD = N,N'-diisopropylacetamidinate; EBECHE = ethylbenzyl(1-ethyl-1,4-cyclo-hexadienyl)

Material	Precursor	Co-reactant	Growth area	Non-growth area	Thickness selectively deposited (nm)	Reference
Al_2O_3	$(\text{CH}_3)_2\text{Al}(\text{OC}_3\text{H}_7)$	H_2O	SiO_2	PVP	85*	29
	$\text{Al}(\text{CH}_3)_3$	H_2O	SiO_2	ODPA on Cu	6	30
			SiO_2	ODPA on Cu + HCO_2H etching	60	30
			Ti	ODPA	60	31
AZO	$(\text{CH}_3)_2\text{Al}(\text{OC}_3\text{H}_7)$, $\text{Zn}(\text{C}_2\text{H}_5)_2$	H_2O	SiO_2	PVP	250*	29

TABLE II: continued

Material	Precursor	Co-reactant	Growth area	Non-growth area	Thickness selectively deposited (nm)	Reference
SiO ₂	H ₂ Si(NC ₄ H ₁₄) ₂	O ₂ plasma	SiO ₂ , Si ₃ N ₄ , etc.	Chemisorbed Hacac on Al ₂ O ₃ , HfO ₂ , etc.	~1	3 and Chapter 6
TiN	Ti[N(CH ₃) ₂] ₄	NH ₃	HfO ₂	ODDC on HfO ₂	30	32
TiO ₂	TiCl ₄	H ₂ O	SiO ₂	PMMA		33
	TiCl ₄	H ₂ O	SiO ₂	OTS on SiO ₂	7	34
	TiCl ₄	H ₂ O	SiO ₂	Si-H	3	22
	TiCl ₄	Ti[OCH(CH ₃) ₂] ₄	SiO ₂	Si-H	2	35
	Ti[OCH(CH ₃) ₂] ₄	H ₂ O	SiO ₂	PMMA	35	33
	Ti[OCH(CH ₃) ₂] ₄	H ₂ O	e-beam modified OTS	OTS on SiO ₂	20	36
	Ti(OCH ₃) ₄	H ₂ O	SiO ₂	PMMA	25	37
Co	Co(Pr-AMD) ₂	H ₂	Si	OTS	~45	38
	Co(Pr-AMD) ₂	NH ₃	Si	OTS	24	39
	^t BuAllylCo(CO) ₃	CH ₃ (NH) ₂ CH ₃	Si-H	SiO ₂	-	28
CoSi ₂	^t BuAllylCo(CO) ₃	Si ₃ H ₈	Si-H	SiO ₂	-	40
Ni	Ni(dmamb) ₂	NH ₃	SiO ₂	OTS on SiO ₂	55	41
ZnO	Zn(C ₂ H ₅) ₂	H ₂ O	SiO ₂	PVP	300*	29
	Zn(C ₂ H ₅) ₂	H ₂ O	SiO ₂	ODPA on Cu	36	42
	Zn(C ₂ H ₅) ₂	H ₂ O	SiO ₂	DAT on Au	30	43
	Zn(C ₂ H ₅) ₂	H ₂ O	SiO ₂	[CF ₃] _n	~15	44
	Zn(C ₂ H ₅) ₂	H ₂ O	SiO ₂	a-Si:H	7	Chapter 5
ZnO:N	Zn(C ₂ H ₅) ₂	H ₂ O + NH ₃	SiO ₂	PVP	200*	45
ZrO ₂	ZrCl ₄	H ₂ O	CNT	(C ₁₈ H ₃₅ NH ₂) on Pt	-	46
	ZrCl ₄	CH ₃ CH ₂ OH	SiO ₂	Cu	~3	47
Ru	RuCp ₂	air	Si	PMMA	41	37
	RuCp ₂	air	RuO _x	Si, SiO ₂	29	48
	EBECHRu	O ₂	H ₂ plasma treated SiCN and low-k dielectric	H ₂ plasma treated a-C:H	~3	49
Rh	Rh(acac) ₃	O ₂	SiO ₂	photoresist	~30	50
In ₂ O ₃	InCp	O ₂ + H ₂ O	SiO ₂	a-Si:H, Si, SiN _x :H	35	27 and Chapter 4

TABLE II: continued

Material	Precursor	Co-reactant	Growth area	Non-growth area	Thickness selectively deposited (nm)	Reference
HfO ₂	HfCl ₄	H ₂ O	SiO ₂	FOTS on SiO ₂	~4	51
	Hf[N(CH ₃) ₂] ₄	H ₂ O	SiO ₂	ODTS or HMDS	10	52
	Hf(NC ₂ H ₅) ₄	H ₂ O	SiO ₂	Cu	~3	53
Ta ₂ O ₅	(CH ₃) ₃ CNTa(N(CH ₃) ₂) ₃	O ₂ plasma	TiN	Si, SiO ₂	virtually infinite	54
W	WF ₆	SiH ₄	Si	SiO ₂ , TiO ₂ , Al ₂ O ₃ , ZnO	<14	55
	WF ₆ + H ₂	SiH ₄	Si	SiO ₂ , TiO ₂ , Al ₂ O ₃ , ZnO	~20	56
WS ₂	WF ₆	H ₂ S	a-Si	c-Al ₂ O ₃	~5	57
Ir	Ir(acac) ₃	O ₂	SiO ₂	ODS	22	58
	Ir(acac) ₃	O ₂	Si	PMMA	29	37
	Ir(acac) ₃	O ₂	Si	PVP	17	59
Pt	(CH ₃) ₃ CpPt(CH ₃) ₃	O ₂	Si	[CF ₃] _n	25	2
	(CH ₃) ₃ CpPt(CH ₃) ₃	O ₂	Si	PMMA	71	37
	(CH ₃) ₃ CpPt(CH ₃) ₃	O ₂	Si	PVP	24	59
PbS	Pb(tmhd) ₂	H ₂ S	SiO ₂	ODTS	~5	19
CeO _x	Ce(thd) ₄	O ₃	Pt(111)	Pt(100)	~2	60

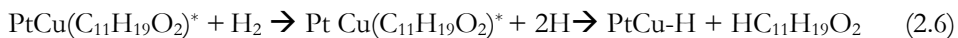
* Note that the extremely high selectivity exhibited for the Al₂O₃, AZO, ZnO and N:ZnO in combination with a PVP non-growth area is due to the large under-saturation conditions adopted during the respective spatial-ALD processes.

From the area-selective ALD processes listed in Table II, a few general observations can be made. The chemoselective precursor mechanism has been largely explored to achieve area-selective ALD, mostly for the selective deposition of oxides. This mechanism is common in combination with SAMs and polymers, because these surfaces generally lack the suitable reactive sites (e.g., OH-groups) for metalorganic precursor adsorption. H-terminated silicon substrates or, in a few cases, metallic surfaces can also be employed as effective non-growth areas in area-selective ALD. The exception is when H-terminated silicon surfaces act as the growth area by participating as an active reactant in the precursor half-reactions, during the deposition of some specific metals, e.g. W, Co and CoSi₂.^{28,40,61} For example, Si can reduce WF₆ through a highly exothermic reaction and thereby favor the deposition of W and likely the formation of HF by-products. Area-selective ALD of Co is thought to proceed through a reaction that parallels a catalytic hydrogenation reaction. Thus, it requires a surface that acts as an hydrogen donor (like H-terminated Si), instead of a surface that acts as a source of protons (like Si-OH).^{13,28}

From the values of selectively grown thicknesses reported in the literature (summarized in Table II) and comparative studies of precursor adsorption on different surfaces,³³ it can be speculated that halide-precursors are in general highly reactive and therefore inhibiting the precursor adsorption is more difficult. This indicates that when using halide precursors it is more difficult to achieve area-selective ALD,^{17,34,62} which is likely due to their high reactivity. An exception is the case of area-selective ALD of W using WF₆ as discussed above. Conversely, many cyclopentadienyl-based precursors have been reported to exhibit long nucleation delays on different surfaces and therefore are more suited for achieving area-selective ALD.^{37,63}

2.4.B. Chemoselective co-reactant mechanism

Area-selective ALD can also be achieved during the second half-reaction of the process by exploiting the differences in reaction energetics on different surfaces. This mechanism was found to be particularly useful for achieving area-selective ALD of noble metals. In this case the precursor chemisorbs on both growth and non-growth areas, however the commonly-used co-reactants such as O₂ and H₂ display low reactivity (particularly at low temperature) with the chemisorbed precursors.⁶⁴ Therefore, a substrate-catalyzed dissociation of the co-reactant is required to effectively remove the remaining precursor ligands and thereby allow deposition to take place. An example is the case of area-selective ALD of Cu on Pt/Pd in presence of SiO₂, ITO, TaO_x, FeO_x, NiO_x, TiN and Au.^{65–68} In this case, the Cu precursor, Cu(thd)₂ (or Cu(C₁₁H₁₉O₂)₂), chemisorbs on all surfaces giving stable chemisorbed Cu(C₁₁H₁₉O₂)^{*} and (C₁₁H₁₉O₂)^{*} species on the surface. However, the ability to remove the remaining ligand is dependent on the substrate on which the precursor has chemisorbed. Since H₂ dissociation is much less likely on an oxide substrates (reaction 2.5), this reaction requires high temperature or long co-reactant doses to take place.¹³ Conversely, in the case of a Pt substrate, the catalytic activity toward H₂ dissociation favours the elimination of the ligands (reaction 6), and therefore allows Cu growth to take place.⁶⁵ This mechanism for area-selective ALD is supported by infrared measurements performed by Sekine *et al.* who showed that Cu(C₇H₁₉O₂) adsorbs on oxides substrates, while the elimination of the Cu ligand is inhibited by the low reactivity of H₂.^{69,70} The general surface reactions are listed below:



where the asterisks represent the surface species and M the generic cation composing an oxide substrate. Unfortunately, the associated activation energy and enthalpy change of these reactions have not been calculated. However, the difference in the reaction rates for reactions (2.5) and (2.6) can be estimated by considering the activation energies reported in the literature for the H₂ dissociation. An activation energy of 2.50 eV has been reported for the dissociation of H₂ on SiO₂ and 0.06 to 0.40 eV on Pt(111).^{71,72}

These values suggest that it may be difficult to activate H_2 on oxides substrates in order to produce atomic hydrogen needed for the hydrogenation of the adsorbed ligands.⁷⁰ Using the Arrhenius equation and assuming the pre-exponential factors to be of the same magnitude, the different activation energies translate into a $\sim 10^{23}$ to $\sim 10^{20}$ times faster reactions on the Pt surface at 250 °C, thereby explaining the good selectivity of this process.

Mackus *et al.* demonstrated the area-selective ALD of Pt using $(MeCp)PtMe_3$ and O_2 on Pt, in the presence of Al_2O_3 and SiO_2 .⁸ In particular, the nucleation delay that allows for selective deposition, was studied as a function of the O_2 pressure. At O_2 pressures as low as 8 mTorr, no Pt deposition could be obtained on Al_2O_3 . However, when increasing the O_2 pressure to 800 mTorr the nucleation delay drastically decreased to 50 cycles. The nucleation delay is plotted as a function of the co-reactant pressure in Figure 2.7. Furthermore, the nucleation delay was also observed to be dependent on the dosing time of the co-reactant,⁷³ which suggests that the limiting step for nucleation is the co-reactant step. As a matter of fact, the chemisorption of $Pt(MeCp)Me_3$ has been demonstrated to take place on surface hydroxyl groups by several experimental and simulation studies,⁷³ and even at room temperature.⁷⁴ Also this area-selective ALD process can be explained by a kinetically hindered co-reactant reaction which is a function of both temperature and dose (pressure x time) of O_2 .⁷⁵ A similar dependence on the total co-reactant dose was also found for Ru ALD,⁷⁶ suggesting this effect to be common for noble metals.

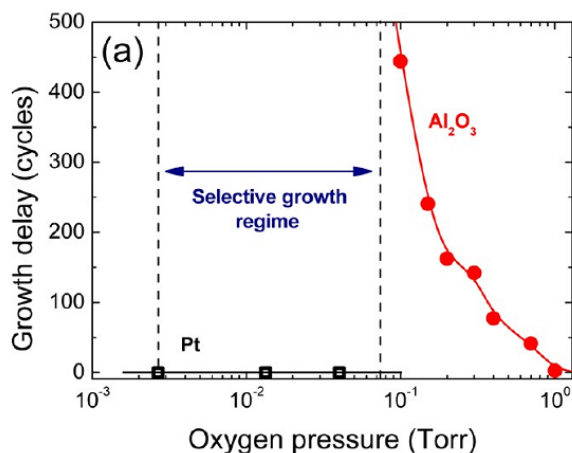


Figure 2.7: Growth delay of Pt ALD as a function of the O_2 pressure as measured by *in-situ* SE on Al_2O_3 and Pt starting surfaces. After Ref. 8.

In Table III we make an attempt to provide an overview of the area-selective ALD processes that are assumed to exploit a *chemoselective co-reactant mechanisms*. This categorization includes published results for which the key role of the co-reactant in achieving selectivity has been explicitly suggested in the publication.

TABLE III: Overview of area-selective ALD processes employing a chemoselective co-reactant reaction mechanism. For each material, the precursor, co-reactant growth area and non-growth area as well as the selectively deposited thickness are listed.

Material	Precursor	Co-reactant	Growth area	Non-growth area	Thickness selectively deposited (nm)	References
Fe ₂ O ₃	Fe(C ₅ H ₅)(C ₅ H ₄ C(CH ₃) ₃)	O ₂	Pt	SiO ₂	20	77
Cu	Cu(thd) ₂	H ₂	Pd/Pt	SiO ₂	-	64
			Pd	SiO ₂ , Au	14	65,67
Pd	Pd(hfac) ₂	H ₂	Pt	SiO ₂ , Al ₂ O ₃	-	78
Pt	(CH ₃) ₃ CpPt(CH ₃) ₃	O ₂	Pt	SiO ₂ , Al ₂ O ₃	19	79

From the area-selective ALD processes reported in Table III, a few general considerations can be drawn. Chemoselective co-reactant mechanisms are exploited mostly for noble metals and in combination with a growth area that acts as a catalyst for the co-reactant dissociation. The presence of a catalytically active growth area is fundamental in lowering the activation energies that may be involved during the co-reactant step. Fe₂O₃ is the only oxide material for which the area-selective ALD process may be explained by recurring to a chemoselective co-reactant mechanism. A drawback of this mechanism is that area-selective deposition can proceed only when the deposited material itself can catalyze the co-reactant dissociation or if the co-reactant can diffuse, reach the catalytic substrate, dissociate and effuse to the surface.

2.5. Processing conditions for improving the selectivity

As anticipated in Section 2.2, area-selective ALD usually does not retain its selectivity for an infinite number of cycles and material deposition can also start on the non-growth area, leading to selectivity loss. For example, in the case of kinetically-hindered surface reactions, although the rate of reaction on the non-growth area can be extremely slow, material may gradually deposit on this surface. In other cases, the precursor can strongly physisorb on the non-growth area and act as a reactive site for further reactions, or the co-reactant can chemically change the non-growth area, for instance H₂O may slowly oxidize H-terminated silicon surfaces. Finally, the presence of defect sites (dangling bonds, strained bonds, etc.) on the non-growth area can significantly affect the reaction energetics for instance by lowering the required activation energy.⁸⁰

Controlling the selectivity during an ALD process under these circumstances can be very challenging to achieve. First-level approximations can be derived from DFT calculations of the energetics involved in the surface reactions. During ALD reactions, the situation is typically very complex and alternative reaction pathways can have a

profound influence on the selectivity.^{80,81} In this respect, *in-situ* measurements can be used to identify secondary reaction mechanism and non-idealities.

If the mechanism for selectivity loss is understood, one way to tackle the challenging problem of retaining the selectivity for a large enough number of ALD cycles is tuning the processing conditions to avoid unwanted reaction pathways. Nevertheless, at a more pragmatic level, correction steps can be inserted to remove undesired deposition from the non-growth area(s) and possibly refresh the latter back into its pristine state such that the mechanism that leads to selectivity can be resumed.

In this section we describe different strategies that have been adopted to improve the selectivity of area-selective ALD processes. Figure 2.8 summarizes these approaches. As illustrated in Figure 2.8a, a lower precursor/co-reactant dose and/or a larger purge dose can widen the selectivity window (green arrows). The deposition temperature can be varied to expand the selectivity window (Figure 2.8b). Gas additives that can be co-injected with the precursor can promote side-reactions leading to *in-situ* passivation of the non-growth area (Figure 2.8c). High selectivity can be obtained by inserting etching as correction steps, which can be performed either *ex-situ* and selectively on the non-growth area (Figure 2.8d) or *in-situ* in a super-cycle fashion (Figure 2.8e). The main requirement is that the etching step does not change the surface chemistry of the non-growth area. Also, depending on the application, the correction step may or may not lead to etching of the non-growth area.

Below, we describe detailed examples for each approach and highlight the similarities with known area-selective CVD processes, when available.

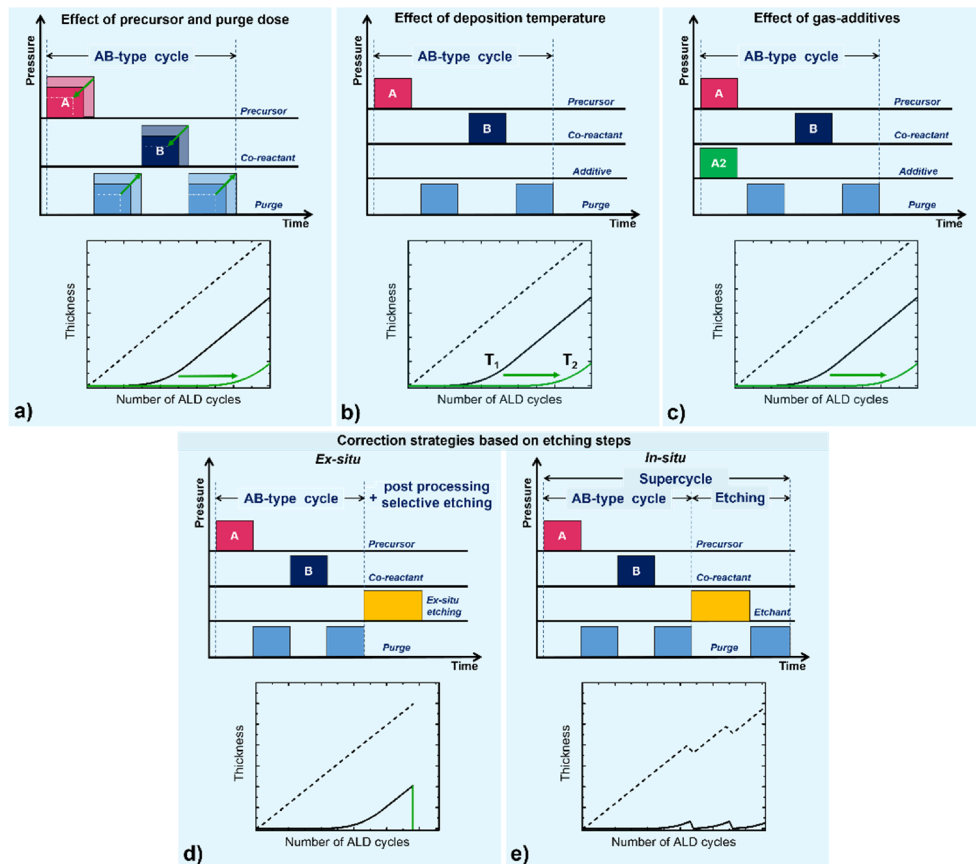


Figure 2.8: Schematics of various types of processing options for improving area-selective ALD: **a)** decreasing reactants (green arrow) and increasing purge doses (green arrow) may widen the selectivity window (green arrow) as illustrated in the corresponding nucleation curves (dashed line for the growth-area and solid lines for the non-growth area). However, decreasing the reactants dose below the saturation value can result in lower growth per cycle; **b)** variations of deposition temperature (T_1 and T_2) can also be exploited to widen the selectivity window; **c)** co-injection of gas additives may cause passivation of (or other side-reactions on) the non-growth area and thereby expand the selectivity window (green arrow); **d)** post-deposition selective etching of the non-growth area with the undesired material deposited atop yield higher selectivity; **e)** supercycles of deposition and interleaved etching steps can ideally lead to infinite selectivity.

2.5.A. Effect of precursor and purge dose (pressure \times time)

Recently, in-depth insights about how precursor and purge doses affect the selectivity were published by Seo *et al.*³⁰ They demonstrated the possibility of achieving highly selective ALD of Al_2O_3 using SAMs as the non-growth area by carefully tuning the $\text{Al}(\text{CH}_3)_3$ precursor and Ar purge dose. The water contact angle (WCA) was used as a figure of merit to evaluate the adsorption of TMA on the SAM-coated surfaces. In Figure 2.9 the observed change in WCA is shown as a function of TMA or Ar dose. Low-pressure and short TMA dose are required to effectively minimize TMA physisorption on the SAM-coated substrate. Furthermore, high doses of Ar during the purge step are also necessary to completely remove unwanted physisorbed TMA. Using DFT calculations Seo *et al.* found that the chemisorption of TMA on a CH_3 -terminated SAM is endothermic (+0.1 eV), however TMA strongly physisorbs (-0.66 eV) on the SAM surface. Starting from these energetic considerations, it was experimentally demonstrated that decreasing the TMA dose and increase the Ar purge dose enabled the selective deposition of 60 nm thick Al_2O_3 on Ti and not on ODPA-coated Ti areas. The drawback of too strong reduction of the precursor dose is that severe under-saturated ALD regimes can lead to non-conformal deposition on high aspect ratio and to poorer material properties.

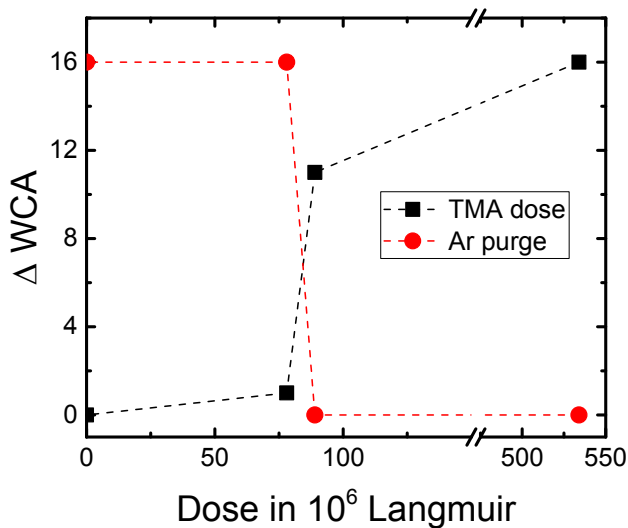


Figure 2.9: Differential water contact angle (WCA) of the SAM-coated surface as a function of the TMA, and Ar purge doses, expressed in Langmuir. The change in WCA is calculated with respect to the starting WCA measured on the as-deposited SAM. ΔWCA is, therefore, taken as a measure for the loss of selectivity, *i.e.* the deposition of Al_2O_3 . Small precursor doses and high purge doses lead to better selectivity. Compiled from Ref. 30.

2.5.B. Effect of deposition temperature

Besides dosing and purging strategies, the selectivity can also be improved by adjusting the deposition temperature. We recently developed such an approach for the case of ZnO area-selective ALD on SiO₂ in the presence of hydrogenated amorphous silicon (a-Si:H), which is discussed in more detail in Chapter 5. For a fixed number of cycles, the selectivity was observed to increase upon increasing the deposition temperature from 100 °C to 250 °C. We explained this effect by considering that for lower deposition temperatures a physisorbed precursor or co-reactant can cause undesired surface reactions. A similar effect of the temperature on the selectivity was also reported by McDonnell *et al.* for the area-selective ALD of TiO₂ on SiO₂ in the presence of H-terminated Si.⁴⁰ In their case, for temperatures as low as 30 °C, the selectivity was observed to be lowest as compared to those obtained at 100 °C and 150 °C. This effect was attributed to the physisorption of H₂O at low temperature, which causes parasitic surface reactions at the expenses of selectivity. The opposite behavior was observed by Lemaire *et al.* for the area-selective ALD process of W on Si-H in the presence of SiO₂, using WF₆ precursor with SiH₄ co-reactant.⁵⁴ Here, the selectivity was observed to decrease upon increasing the reaction temperature from 160 to 240 °C. The selectivity loss with increasing temperature can be attributed to the faster reaction kinetics of SiH₄ and WF₆ on both growth and non-growth areas.^{13,82}

2.5.C. Effect of gas-additives

The use of gas additives has been extensively explored in area-selective CVD. In many of these processes, exerting control over the partial pressure of gas additives allows one to modify the surface reaction kinetics,⁸³ or to promote etching reactions.^{84–86} This way the reaction equilibria are altered to favor deposition on the growth area, or to promote etching reactions on the non-growth area. As an example, in the selective epitaxial growth of Si in the presence of SiO₂, the selectivity can be optimized by co-injecting HCl which decreases the nucleation rate on SiO₂, as shown in Figure 2.10 a-b. The addition of HCl shifts the reaction equilibria to the reagents side, and therefore the nucleation rate is decreased.^{84,87} In the field of area-selective ALD, adding gas-additives is a somewhat less explored processing option. An example is the extension of the selectivity window for the area-selective ALD of W: Kalanyan *et al.* demonstrated an increased selectivity during ALD of W on Si in the presence of SiO₂ surfaces when co-dosing H₂ and WF₆, followed by SiH₄ as the co-reactant.⁵⁵ The addition of H₂ leads to the formation of HF, which was demonstrated by *in-situ* spectroscopic measurements. As shown in Figure 2.10 c-d, the HF may attack the SiO₂ surface and form SiF_x surface groups, with $x < 4$. From CVD literature on selective deposition of W, using the same chemistry, it is known that the SiF_x groups do not react with WF₆ (highly endothermic reaction with $\Delta G = +3.9$ eV).¹³ The authors suggest that the resulting fluorinate silicon surface inhibits also the SiH₄ co-reactant adsorption. In this way the thickness that can be selectively deposited was increased by ~6 nm. The absence of W nuclei on the non-

growth area (SiO_2) when using H_2 as a gas additive, demonstrates a higher selectivity as compared to the standard (without H_2) ALD recipe for W.

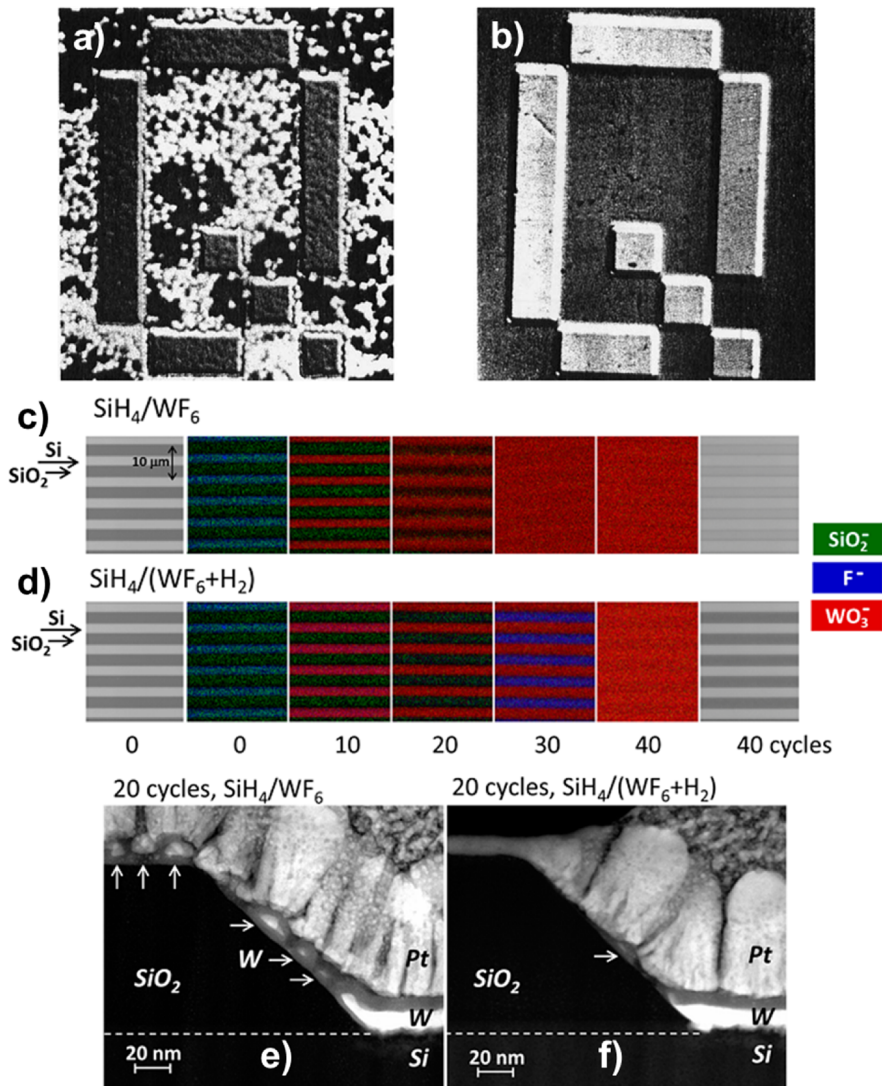


Figure 2.10: Two examples of gas-additives for area-selective CVD and area-selective ALD.

a-b) Selective Si epitaxial growth in the presence of SiO_2 using SiH_2Cl_2 as a single source precursor at 950 °C. Poor selectivity obtained without HCl **b)** high selectivity using HCl as a gas additive. After Ref. 84.

c-f) Time-of-flight secondary ion mass spectroscopy (TOF-SIMS) surface maps on patterned Si/SiO₂ surfaces after different numbers of W-ALD cycles: **c)** without H₂; and **d)** with H₂ gas additive during the precursor step. The transmission electron microscopy images are taken from the patterned substrate after 20 cycles of W area-selective ALD **e)** without H₂ and **f)** with H₂. See Ref. 55 for details.

2.5.D. Correction strategies based on etching steps

Hashemi *et al.* used a so-called self-correcting process to improve the selectivity of Al_2O_3 and ZnO area-selective ALD processes when using SAMs of octadecylphosphonic acid (ODPA) on Cu surfaces.²⁹ This process is schematically illustrated in Figure 2.11a. Instead of interrupting the ALD process at the onset of the selectivity loss, due to parasitic deposition on the SAM-coated Cu substrate, more cycles are applied. Similarly to a lift-off approach, an acetic acid post-etching process is then used to remove the uppermost oxidized Cu surface together with the SAMs and the material that has been deposited atop. By using this strategy, the selectivity was increased by a factor of 10. Furthermore, such process may be re-iterated several times to further increase the selectivity window.

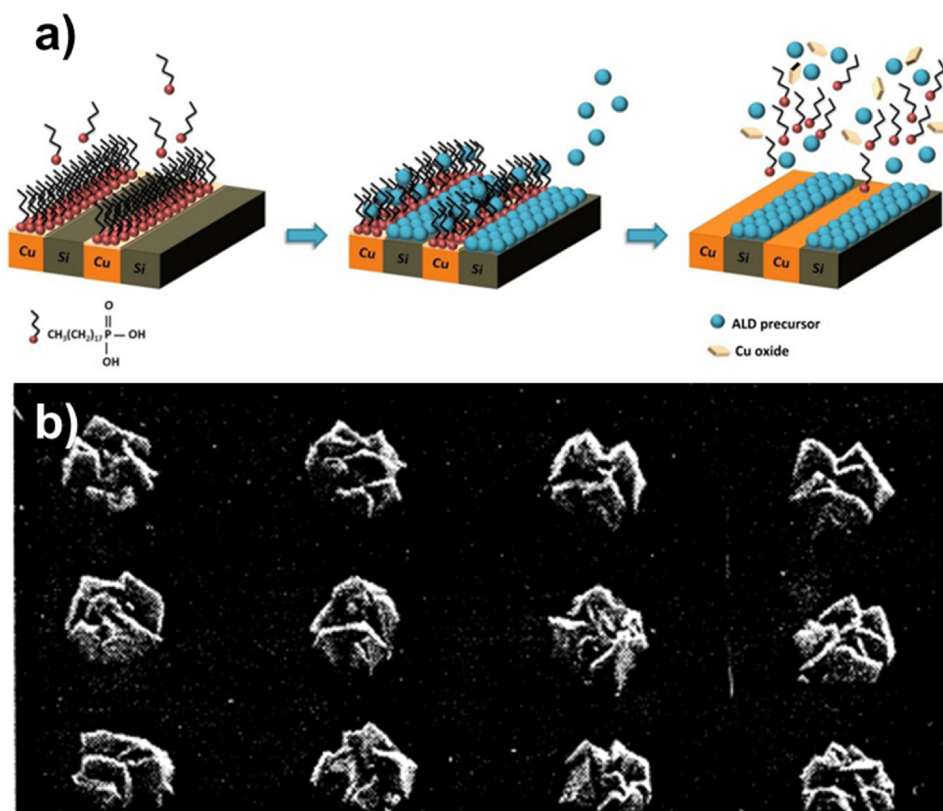


Figure 2.11: Two examples of etch-back correction steps for area-selective ALD and area-selective CVD. **a)** Schematic representation of the area-selective ALD process using a combination of selective deposition of ODPAs on copper in the presence of silicon and a selective post-process etching step. After Ref. 29. **b)** Top-view SEM of selective vertical interconnect aperture (via) W CVD filling, using 18 cycles of $\text{WF}_6 + \text{H}_2$ deposition and interleaved F_2 etch-back steps. The growth area is Si and the non-growth area is SiO_2 . The process resulted in $\sim 1 \mu\text{m}$ thick selectively deposited W. Without etch-back steps the selectivity was lost after 150 nm thick W deposit. After Ref. 88.

A similar approach involving etch-back correction steps is the one reported by Vallat *et al.* for the area-selective ALD of Ta₂O₅ on TiN in the presence of Si and SiO₂.⁵³ This has been achieved by using (CH₃)₃CNTa(N(CH₃)₂)₃ and O₂ plasma as the co-reactant. This process represents a particular case because a *plasma* co-reactant step was used here. Indeed, obtaining area-selective ALD using plasma co-reactants may be possible only in the case of a chemoselective precursor mechanism as the plasma co-reactant is typically highly reactive (Note: a novel approach to obtain area-selective ALD of SiO₂ using a plasma-assisted ALD process is described in detail in Chapter 6). The solution adopted by Vallat *et al.* is to exploit a short nucleation delay on Si and SiO₂ surfaces which is revived every 9 ALD cycles by a NF₃ plasma etch-back step that removes Ta₂O₅ nuclei from the non-growth areas, together with some of the Ta₂O₅ deposit on the growth area. After the etch-back step, the ALD process undergoes another nucleation delay on the non-growth area. Ideally, this process can be repeated as long as needed, in a supercycle fashion. A similar approach was also reported for the area-selective CVD of W. In this process NF₃ or F₂ thermal or plasma etching steps were demonstrated to selectively deposit W-films as thick as ~1 μm. This supercycle approach for area-selective CVD was tested for bottom-up *via* filling as shown in Figure 2.11b.⁸⁸

2.6. SUMMARY AND OUTLOOK

In this Chapter, we have discussed the basic principles underlying area-selective ALD and emphasized the crucial role of surface chemistry. As discussed in Section 2.2, area-selective ALD is obtained by exploiting the differences in nucleation delays of a deposition process on substrates with diverse chemical nature. The nucleation delay depends on the rate of the surface reactions involved and on the reaction conditions (temperature, dose, etc.). The most important challenge in area-selective ALD is selectively deposit sufficiently thick films on the growth area, while avoiding any deposition on the non-growth area.

Area-selective ALD can be accomplished with either a chemoselective precursor or co-reactant mechanism being the selectivity controlling half-reaction. In this respect *ab initio* methods such as DFT prove resourceful in gaining insights into the reaction mechanisms and the energetics (thermodynamics and kinetics) of the elemental steps involved in each half-reaction on the growth and non-growth areas. This knowledge can be used as a guide to understand the key factors that lead to area-selective ALD, and to make correlations to the field of area-selective CVD. The new insights can be utilized to improve the selectivity by carefully tuning the reaction conditions.

Possible experimental parameters to improve the selectivity and to eliminate unwanted side reactions are precursor and purge doses, deposition temperature and the use of gas-additives. Alternatively, selectivity can be increased by employing etch-back correction steps, as discussed in Section 2.5.D. Particularly effective are *in-situ* etch-back steps such

that the entire process can be carried out without breaking the vacuum. A requirement for this approach is that the etch step does not significantly affect the non-growth area.

We believe that the field of area-selective ALD will continue to grow, and find immediate application in advanced nanodevice fabrication flows, where novel and more complex atomic layer processing concepts are needed in the near-future (e.g., multi-step cycles, different temperature steps, insertion of etching reactions, etc.). This overview may provide the elements to advance, both theoretically and experimentally, the potential of area-selective ALD with the aim to improve the selectivity.

REFERENCES

- (1) Fang, M.; Ho, J. C. Area-Selective Atomic Layer Deposition: Conformal Coating, Subnanometer Thickness Control, and Smart Positioning. *ACS Nano* **2015**, *9*, 8651–8654.
- (2) Kim, W.-H.; Minaye Hashemi, F. S.; Mackus, A. J. M.; Singh, J.; Kim, Y.; Bobb-Semple, D.; Fan, Y.; Kaufman-Osborn, T.; Godet, L.; Bent, S. F. A Process for Topographically Selective Deposition on 3D Nanostructures by Ion Implantation. *ACS Nano* **2016**, *10*, 4451–4458.
- (3) Mamelii, A.; Merckx, M. J. M.; Karasulu, B.; Roozeboom, F.; Kessels, W. M. M.; Mackus, A. J. M. Area-Selective Atomic Layer Deposition of SiO₂ Using Acetylacetone as a Chemoselective Inhibitor in an ABC-Type Cycle. *ACS Nano* **2017**, *11*, 9303–9311.
- (4) George, S. M. Atomic Layer Deposition: An Overview. *Chem. Rev.* **2010**, *110*, 111–131.
- (5) Chen, R.; Bent, S. F. Chemistry for Positive Pattern Transfer Using Area-Selective Atomic Layer Deposition. *Adv Mater* **2006**, *18*, 1086–1090.
- (6) Lu, J.; Elam, J. W.; Stair, P. C. Synthesis and Stabilization of Supported Metal Catalysts by Atomic Layer Deposition. *Acc. Chem. Res.* **2013**, *46*, 1806–1815.
- (7) Cao, K.; Cai, J.; Liu, X.; Chen, R. Review Article: Catalysts Design and Synthesis via Selective Atomic Layer Deposition. *J. Vac. Sci. Technol. A Vacuum, Surfaces, Film.* **2018**, *36*, 10801.
- (8) Mackus, A. J. M.; Bol, A. A.; Kessels, W. M. M. The Use of Atomic Layer Deposition in Advanced Nanopatterning. *Nanoscale* **2014**, *6*, 10941–10960.
- (9) Hughes, K. J.; Engstrom, J. R. Nucleation Delay in Atomic Layer Deposition on a Thin Organic Layer and the Role of Reaction Thermochemistry. *J. Vac. Sci. Technol. A Vacuum, Surfaces, Film.* **2012**, *30*, 01A102.
- (10) Langerreis, E.; Heil, S. B. S.; Van De Sanden, M. C. M.; Kessels, W. M. M. In Situ Spectroscopic Ellipsometry Study on the Growth of Ultrathin TiN Films by Plasma-Assisted Atomic Layer Deposition. *J. Appl. Phys.* **2006**, *100*, 0235341-10.
- (11) Gates, S. M. Surface Chemistry in the Chemical Vapor Deposition of Electronic Materials. *Chem. Rev.* **1996**, *96*, 1519–1532.
- (12) Morosanu, C. E. Thermodynamics of CVD. *Thin Films by Chemical Vapour Deposition*, Elsevier, **1990**, pp. 91–100.
- (13) Creighton, J. R.; Parmeter, J. E. Metal CVD for Microelectronic Applications: An Examination of Surface Chemistry and Kinetics. *Solid State Mater. Sci.* **2006**, *18*, 175–237.
- (14) Carlsson, J.-O.; Boman, M. Selective Deposition of Tungsten—prediction of Selectivity. *J. Vac. Sci. Technol. A Vacuum, Surfaces, Film.* **1985**, *3*, 2298.
- (15) Morosanu, C. E. Kinetics of CVD. *Thin Films by Chemical Vapour Deposition*, Elsevier, **1990**, pp.101–140.
- (16) Haran, M.; Engstrom, J. R.; Clancy, P. Ab Initio Calculations of the Reaction Mechanisms for Metal-Nitride Deposition from Organo-Metallic Precursors onto Functionalized Self-Assembled Monolayers. *J. Am. Chem. Soc.* **2006**, *128*, 836–847.
- (17) Xu, Y.; Musgrave, C. B. A DFT Study of the Al₂O₃ Atomic Layer Deposition on SAMs: Effect of SAM Termination. *Chem. Mater.* **2004**, *16*, 646–653.
- (18) Lee, W.; Dasgupta, N. P.; Trejo, O.; Lee, J. R.; Hwang, J.; Usui, T.; Prinz, F. B. Area-Selective Atomic Layer Deposition of Lead Sulfide: Nanoscale Patterning and DFT Simulations. *Langmuir* **2010**, *26*, 6845–6852.
- (19) Fenno, R. D.; Halls, M. D.; Raghavachari, K. Hafnium Oxide and Zirconium Oxide Atomic Layer Deposition: Initial Precursor and Potential Side-Reaction Product Pathways with H/Si(100)-2×1. *J. Phys. Chem. B* **2005**, *109*, 4969–4976.
- (20) Longo, R. C.; McDonnell, S.; Dick, D.; Wallace, R. M.; Chabal, Y. J.; Owen, J. H. G.; Ballard, J. B.; Randall, J. N.; Cho, K. Selectivity of Metal Oxide Atomic Layer Deposition on Hydrogen Terminated and Oxidized Si(001)-(2×1) Surface. *J. Vac. Sci. Technol. B Microelectron. Nanom. Struct.* **2014**, *32*, 03D112.
- (21) McDonnell, S.; Longo, R. C.; Seitz, O.; Ballard, J. B.; Mordi, G.; Dick, D.; Owen, J. H. G.; Randall, J. N.; Kim, J.; Chabal, Y. J.; *et al.* Controlling the Atomic Layer Deposition of Titanium Dioxide on Silicon: Dependence on Surface Termination. *J. Phys. Chem. C* **2013**, *117*, 20250–20259.

- (22) Michalak, D. J.; Amy, S. R.; Aureau, D.; Dai, M.; Estève, A.; Chabal, Y. J. Nanopatterning Si(111) Surfaces as a Selective Surface-Chemistry Route. *Nat. Mater.* **2010**, *9*, 266–271.
- (23) Alam, M. A.; Green, M. L. Mathematical Description of Atomic Layer Deposition and Its Application to the Nucleation and Growth of HfO₂ Gate Dielectric Layers. *J. Appl. Phys.* **2003**, *94*, 3403–3413.
- (24) Copel, M.; Gribelyuk, M.; Gusev, E. Structure and Stability of Ultrathin Zirconium Oxide Layers on Si(001). *Appl. Phys. Lett.* **2000**, *76*, 436–438.
- (25) Kelly, M. J.; Han, J. H.; Musgrave, C. B.; Parsons, G. N. In-Situ Infrared Spectroscopy and Density Functional Theory Modeling of Hafnium Alkylamine Adsorption on Si-OH and Si-H Surfaces. *Chem. Mater.* **2005**, *17*, 5305–5314.
- (26) Mameli, A.; Kuang, Y.; Aghaee, M.; Ande, C. K.; Karasulu, B.; Creatore, M.; Mackus, A. J. M.; Kessels, W. M. M.; Roozeboom, F. Area-Selective Atomic Layer Deposition of In₂O₃:H Using a μ -Plasma Printer for Local Area Activation. *Chem. Mater.* **2017**, *29*, 921–925.
- (27) Kwon, J.; Saly, M.; Halls, M. D.; Kanjolia, R. K.; Chabal, Y. J. Substrate Selectivity of (^tBu-Allyl)Co(CO)₃ during Thermal Atomic Layer Deposition of Cobalt. *Chem. Mater.* **2012**, *24*, 1025–1030.
- (28) Ellinger, C. R.; Nelson, S. F. Selective Area Spatial Atomic Layer Deposition of ZnO, Al₂O₃, and Aluminum-Doped ZnO Using Poly(vinyl Pyrrolidone). *Chem. Mater.* **2014**, *26*, 1514–1522.
- (29) Minaye Hashemi, F. S.; Prasittichai, C.; Bent, S. F. Self-Correcting Process for High Quality Patterning by Atomic Layer Deposition. *ACS Nano* **2015**, *9*, 8710–8717.
- (30) Seo, S.; Oh, I.-K.; Yeo, B. C.; Han, S. S.; Yoon, C. M.; Yang, J. Y.; Yoon, J.; Yoo, C.; Kim, H.; Lee, Y.; *et al.* Reaction Mechanism of Area-Selective Atomic Layer Deposition for Al₂O₃ Nanopatterns. *ACS Appl. Mater. Interfaces* **2017**, acsami.7b13365.
- (31) Chopra, S. N.; Zhang, Z.; Kaihlanen, C.; Ekerdt, J. G. Selective Growth of Titanium Nitride on HfO₂ across Nanolines and Nanopillars. *Chem. Mater.* **2016**, *28*, 4928–4934.
- (32) Sinha, A.; Hess, D. W.; Henderson, C. L. Area Selective Atomic Layer Deposition of Titanium Dioxide: Effect of Precursor Chemistry. *J. Vac. Sci. Technol. B Microelectron. Nanom. Struct.* **2006**, *24*, 2523.
- (33) Färm, E.; Kemell, M.; Ritala, M.; Leskelä, M. Selective-Area Atomic Layer Deposition with Microcontact Printed Self-Assembled Octadecyltrichlorosilane Monolayers as Mask Layers. *Thin Solid Films* **2008**, *517*, 972–975.
- (34) Atanasov, S. E.; Kalanyan, B.; Parsons, G. N. Inherent Substrate-Dependent Growth Initiation and Selective-Area Atomic Layer Deposition of TiO₂ Using “water-free” Metal-Halide/metal Alkoxide Reactants. *J. Vac. Sci. Technol. A Vacuum, Surfaces, Film.* **2016**, *34*, 01A148.
- (35) Huang, J.; Lee, M.; Lucero, A.; Cheng, L.; Kim, J. Area-Selective ALD of TiO₂ Nanolines with Electron-Beam Lithography. *J. Phys. Chem. C* **2014**, *118*, 23306–23312.
- (36) Färm, E.; Kemell, M.; Ritala, M.; Leskela, M. Selective-Area Atomic Layer Deposition Using Poly (Methyl Methacrylate) Films as Mask Layers. *J. Phys. Chem.* **2008**, *112*, 15791–15795.
- (37) Lee, H.-B.-R.; Kim, H. Area Selective Atomic Layer Deposition of Cobalt Thin Films. *ECS Trans.* **2008**, *16*, 219–225.
- (38) Hyungjun, K.; Han-Bo-Ram, L.; Woo-Hee, K.; Jeong Won, L.; Jaemin, K.; Inchan, H. The Degradation of Deposition Blocking Layer during Area Selective Plasma Enhanced Atomic Layer Deposition of Cobalt. *J. Korean Phys. Soc.* **2010**, *56*, 104.
- (39) Bernal-Ramos, K.; Saly, M. J.; Kanjolia, R. K.; Chabal, Y. J. Atomic Layer Deposition of Cobalt Silicide Thin Films Studied by in Situ Infrared Spectroscopy. *Chem. Mater.* **2015**, *27*, 4943–4949.
- (40) Kim, W.; Lee, H.; Heo, K.; Lee, K.; Chung, T.; Kim, G.; Hong, S.; Heo, J.; Kim, H. Atomic Layer Deposition of Ni Thin Films and Application to Area-Selective Deposition. *J. Electrochem. Soc.* **2011**, *158*, D1–D5.
- (41) Sadat, F.; Hashemi, M.; Prasittichai, C.; Bent, S. F. A New Resist for Area Selective Atomic and Molecular Layer Deposition on Metal – Dielectric Patterns. *J. Phys. Chem. C* **2014**, *118*, 10957–10962.
- (42) Suresh, V.; Huang, M. S.; Srinivasan, M. P.; Krishnamoorthy, S. In Situ Synthesis of High Density Sub-50 Nm ZnO Nanopatterned Arrays Using Diblock Copolymer Templates. *ACS Appl. Mater.*

- Interfaces* **2013**, *5*, 5727–5732.
- (43) Dong, W.; Zhang, K.; Zhang, Y.; Wei, T.; Sun, Y.; Chen, X.; Dai, N. Application of Three-Dimensionally Area-Selective Atomic Layer Deposition for Selectively Coating the Vertical Surfaces of Standing Nanopillars. *Sci. Rep.* **2014**, *4*, 1–4.
- (44) Haider, A.; Deminskyi, P.; Khan, T. M.; Eren, H.; Biyikli, N. Area-Selective Atomic Layer Deposition Using Inductively Coupled Plasma Polymerized Fluorocarbon Layer: A Case Study for Metal-Oxides. *J. Phys. Chem. C* **2016**, *120*, 26393–26401.
- (45) Cheng, N.; Banis, M. N.; Liu, J.; Riese, A.; Li, X.; Li, R. Extremely Stable Platinum Nanoparticles Encapsulated in a Zirconia Nanocage by Area-Selective Atomic Layer Deposition for the Oxygen Reduction Reaction. **2015**, 277–281.
- (46) Kannan Selvaraj, S.; Parulekar, J.; Takoudis, C. G. Selective Atomic Layer Deposition of Zirconia on Copper Patterned Silicon Substrates Using Ethanol as Oxygen Source as Well as Copper Reductant. *J. Vac. Sci. Technol. A Vacuum, Surfaces, Film.* **2014**, *32*, 10601.
- (47) Färm, E. *Selective-Area Atomic Layer Deposition*; 2011, Ph.D. Thesis, Helsinki University.
- (48) Zyulkov, I.; Krishtab, M.; Gendt, S. De; Armini, S. Selective Ru ALD as a Catalyst for Sub-Seven-Nanometer Bottom-Up Metal Interconnects. *ACS Appl. Mater. Interfaces*, **2017**, *9*, 31031–31041.
- (49) Park, K. J.; Parsons, G. N. Selective Area Atomic Layer Deposition of Rhodium and Effective Work Function Characterization in Capacitor Structures. *Appl. Phys. Lett.* **2006**, *89*.
- (50) Chen, R.; Kim, H.; McIntyre, P. C.; Porter, D. W.; Bent, S. F. Achieving Area-Selective Atomic Layer Deposition on Patterned Substrates by Selective Surface Modification. *Appl. Phys. Lett.* **2005**, *86*, 1–3.
- (51) Guo, L.; Lee, I.; Zaera, F. Patterning of Solid Films via Selective Atomic Layer Deposition Based on Silylation and UV/Ozonolysis. *ACS Appl. Mater. Interfaces* **2016**, *8*, 19836–19841.
- (52) Tao, Q.; Jursich, G.; Takoudis, C. Selective Atomic Layer Deposition of HfO₂ on Copper Patterned Silicon Substrates. *Appl. Phys. Lett.* **2010**, *96*, 1921051-3.
- (53) Vallat, R.; Gassilloud, R.; Eychenne, B.; Vallée, C. Selective Deposition of Ta₂O₅ by Adding Plasma Etching Super-Cycles in Plasma Enhanced Atomic Layer Deposition Steps. *J. Vac. Sci. Technol. A Vacuum, Surfaces, Film.* **2017**, *35*, 01B104.
- (54) Lemaire, P. C.; King, M.; Parsons, G. N. Understanding Inherent Substrate Selectivity during Atomic Layer Deposition: Effect of Surface Preparation, Hydroxyl Density, and Metal Oxide Composition on Nucleation Mechanisms during Tungsten ALD. *J. Chem. Phys.* **2017**, *146*, 052811.
- (55) Kalanyan, B.; Lemaire, P. C.; Atanasov, S. E.; Ritz, M. J.; Parsons, G. N. Using Hydrogen to Expand the Inherent Substrate Selectivity Window during Tungsten Atomic Layer Deposition. *Chem. Mater.* **2016**, *28*, 117–126.
- (56) Heyne, M. H.; de Marneffe, J.-F.; Delabie, A.; Caymax, M.; Neyts, E. C.; Radu, I.; Huyghebaert, C.; De Gendt, S. Two-Dimensional WS₂ Nanoribbon Deposition by Conversion of Pre-Patterned Amorphous Silicon. *Nanotechnology* **2017**, *28*, 04LT01.
- (57) Färm, E.; Kemell, M.; Ritala, M.; Leskelä, M. Self-Assembled Octadecyltrimethoxysilane Monolayers Enabling Selective-Area Atomic Layer Deposition of Iridium. *Chem. Vap. Depos.* **2006**, *12*, 415–417.
- (58) Färm, E.; Kemell, M.; Santala, E.; Ritala, M.; Leskelä, M. Selective-Area Atomic Layer Deposition Using Poly(vinyl Pyrrolidone) as a Passivation Layer. *J. Electrochem. Soc.* **2010**, *157*, K10.
- (59) Cao, K.; Shi, L.; Gong, M.; Cai, J.; Liu, X.; Chu, S.; Lang, Y.; Shan, B.; Chen, R. Nanofence Stabilized Platinum Nanoparticles Catalyst via Facet-Selective Atomic Layer Deposition. *Small* **2017**, *13*, 1–7.
- (60) Lemaire, P. C.; King, M.; Parsons, G. N. Understanding Inherent Substrate Selectivity during Atomic Layer Deposition: Effect of Surface Preparation, Hydroxyl Density, and Metal Oxide Composition on Nucleation Mechanisms during Tungsten ALD. *J. Chem. Phys.* **2017**, *146*, 052811–1/9.
- (61) Hughes, K. J.; Engstrom, J. R. Nucleation Delay in Atomic Layer Deposition on a Thin Organic Layer and the Role of Reaction Thermochemistry. *J. Vac. Sci. Technol. A Vacuum, Surfaces, Film.* **2012**, *30*, 01A102.
- (62) Ramos, K. B.; Saly, M. J.; Chabal, Y. J. Precursor Design and Reaction Mechanisms for the Atomic

- Layer Deposition of Metal Film. *Coord. Chem. Rev.* **2013**, *257*, 3271–3281.
- (63) Knisley, T. J.; Kalutarage, L. C.; Winter, C. H. Precursors and Chemistry for the Atomic Layer Deposition of Metallic First Row Transition Metal Films. *Coord. Chem. Rev.* **2013**, *257*, 3222–3231.
- (64) Mårtensson, P.; Carlsson, J.-O. Atomic Layer Epitaxy of Copper. *J. Electrochem. Soc.* **1998**, *145*, 2926–2931.
- (65) B.G. Willis; Qi, J.; Jiang, X. Chen, J. Weisel, G.J.; Zimmerman D.T. Selective-Area Atomic Layer Deposition of Copper Nanostructures for Direct Electro-Optical Solar Energy Conversion. *ECS Trans.*, **2014**, *64*, 253–263.
- (66) Jiang, X.; Wang, H.; Qi, J.; Willis, B. G. *In-Situ* Spectroscopic Ellipsometry Study of Copper Selective-Area Atomic Layer Deposition on Palladium. *J. Vac. Sci. Technol. A Vacuum, Surfaces, Film.* **2014**, *32*, 41513.
- (67) Qi, J.; Zimmerman, D. T.; Weisel, G. J.; Willis, B. G. Nucleation and Growth of Copper Selective-Area Atomic Layer Deposition on Palladium Nanostructures. *J. Chem. Phys.* **2017**, *147*, 154702.
- (68) Sekine, R.; Kawai, M. Selective and Stoichiometric Reaction of Copper Dipivaloylmethanate [Cu(DPM)₂] with Surface Hydroxyls on SiO₂. *Appl. Phys. Lett.* **1990**, *56*, 1466–1468.
- (69) Zaera, F. Mechanisms of Surface Reactions in Thin Solid Film Chemical Deposition Processes. *Coord. Chem. Rev.* **2013**, *257*, 3177–3191.
- (70) Lopez, N.; Vitiello, M.; Illas, F.; Pacchioni, G. Interaction of H₂ with Strained Rings at the Silica Surface from Ab Initio Calculations. *J. Non. Cryst. Solids* **2000**, *271*, 56–63.
- (71) Nieto, P.; Pijper, E.; Barredo, D.; Laurent, G.; Olsen, R. A.; Baerends, E.-J.; Kroes, G.-J.; Farias, D. Reactive and Nonreactive Scattering of H₂ from a Metal Surface Is Electronically Adiabatic. *Science (80-.)*. **2006**, *312*, 86–89.
- (72) Mackus, A. J. M.; Verheijen, M. A.; Leick, N.; Bol, A. A.; Kessels, W. M. M. Influence of Oxygen Exposure on the Nucleation of Platinum Atomic Layer Deposition: Consequences for Film Growth, Nanopatterning, and Nanoparticle Synthesis. *Chem. Mater.* **2013**, *25*, 1905–1911.
- (73) Karasulu, B.; Vervuurt, R. H. J.; Kessels, W. M. M.; Bol, A. A. Continuous and Ultrathin Platinum Films on Graphene Using Atomic Layer Deposition: A Combined Computational and Experimental Study. *Nanoscale* **2016**, *8*, 19829–19845.
- (74) Takakusagi, S.; Fukui, K.; Tero, R.; Nariyuki, F.; Iwasawa, Y. Self-Limiting Growth of Pt Nanoparticles from MeCpPtMe₃ Adsorbed on TiO₂(110) Studied by Scanning Tunneling Microscopy. *Phys. Rev. Lett.* **2003**, *91*, 66102.
- (75) Grillo, F.; Van Bui, H.; Moulijn, J. A.; Kreutzer, M. T.; Van Ommen, J. R. Understanding and Controlling the Aggregative Growth of Platinum Nanoparticles in Atomic Layer Deposition: An Avenue to Size Selection. *J. Phys. Chem. Lett.* **2017**, *8*, 975–983.
- (76) Methaapanon, R.; Geyer, S. M.; Lee, H.-B.-R.; Bent, S. F. The Low Temperature Atomic Layer Deposition of Ruthenium and the Effect of Oxygen Exposure. *J. Mater. Chem.* **2012**, *22*, 25154.
- (77) Singh, J. A.; Thissen, N. F. W.; Kim, W.-H.; Johnson, H.; Kessels, W. M. M.; Bol, A. A.; Bent, S. F.; Mackus, A. J. M. Area-Selective Atomic Layer Deposition of Metal Oxides on Noble Metals through Catalytic Oxygen Activation. *Chem. Mater.* **2017**, acs.chemmater.7b03818.
- (78) Weber, M. J.; Mackus, A. J. M.; Verheijen, M. A.; van der Marel, C.; Kessels, W. M. M. Supported Core/shell Bimetallic Nanoparticles Synthesis by Atomic Layer Deposition. *Chem. Mater.* **2012**, *24*, 2973–2977.
- (79) Mackus, A. J. M.; Dielissen, S. A. F.; Mulders, J. J. L.; Kessels, W. M. M. Nanopatterning by Direct-Write Atomic Layer Deposition. *Nanoscale* **2012**, *4*, 4477–4480.
- (80) Lin, J. M.; Teplyakov, A. V.; Rodriguez-Reyes, J. C. F. Competing Reactions during Metalorganic Deposition: Ligand-Exchange versus Direct Reaction with the Substrate Surface. *J. Vac. Sci. Technol. A* **2013**, *31*, 21401.
- (81) Elliott, S. D.; Dey, G.; Maimaiti, Y.; Ablat, H.; Filatova, E. A.; Fomengia, G. N. Modeling Mechanism and Growth Reactions for New Nanofabrication Processes by Atomic Layer Deposition. *Adv. Mater.* **2016**, *28*, 5367–5380.
- (82) Elam, J. W.; Nelson, C. E.; Grubbs, R. K.; George, S. M. Kinetics of the WF₆ and Si₂H₆ Surface Reactions during Tungsten Atomic Layer Deposition. *Surf. Sci.* **2001**, *479*, 121–135.

- (83) Babar, S.; Mohimi, E.; Trinh, B.; Girolami, G. S.; Abelson, J. R. Surface-Selective Chemical Vapor Deposition of Copper Films through the Use of a Molecular Inhibitor. *ECS J. Solid State Sci. Technol.* **2015**, *4*, N60–N63.
- (84) Borland, J. O.; Drowley, C. I. Advanced Dielectric Isolation through Selective Epitaxial Growth Techniques. *Solid State Technol.* **1985**, *28*, 141–148.
- (85) Cheong, W.-S. Optimization of Selective Epitaxial Growth of Silicon in LPCVD. *ETRI J.* **2003**, *25*, 503–509.
- (86) Sammak, A.; De Boer, W.; Nanver, L. K. Large-Area Selective CVD Epitaxial Growth of Ge on Si Substrates. In *ICT.OPEN2011: Micro Technology and Micro Devices (SAFE 2011)*; 2011; pp. 1–4.
- (87) Carlsson, J. O. Selective Vapor-Phase Deposition on Patterned Substrates. *Crit. Rev. Solid State Mater. Sci.* **1990**, *16*, 161–212.
- (88) Fleming, J. G.; Omstead, T. R.; Dominguez, F. Sequential Deposition Etch Techniques for the Selective Deposition of Tungsten. In *Advanced Metallization for ULSI Applications*; Rana, V. V. S.; Joshi, R. V.; Ohdomari, I., Eds.; Materials Research Society: Pittsburgh, 1992; p. 233.

Chapter 3

Synopsis of Selective ALE

The continuous drive for shrinking device components requires innovations in both deposition and etching technologies. Atomic layer etching (ALE) holds potential to etch materials with atomic-scale control over etch profiles, virtually free of surface damage and with high etch selectivity. This synopsis provides a brief overview of the ALE processing options and discusses the mechanisms underlying selective ALE by means of examples from the literature. From a chemistry point-of-view diverse reaction pathways and the differences in reactivity of precursors or co-reactants with various materials can enable selective removal of a material in the presence of other materials. A comparison between selectivity in area-selective ALD and selective ALE concludes this Chapter.

3.1 Introduction

Dry etching techniques are ubiquitous in device fabrication as they allow for patterning nanometer-size features. There are four plasma-based dry etching types: 1) chemical etching, 2) physical etching (also called *sputtering*), and 3) reactive ion etching (RIE). Purely chemical etching is often *isotropic* in nature,¹ while the rest is *anisotropic* (or directional). Directional/anisotropic etching is caused by the trajectory of the ions that are accelerated perpendicularly to the substrate following the field lines in the so-called plasma sheath before impinging on the substrate surface. In RIE, the etching is accomplished by a synergetic effect of the plasma-generated reactive species that includes both radicals and ions.

Upon exposure to the plasma, reactive radicals diffusing towards the substrate react with and modify its surface. At the same time, owing to the negative bias applied to the substrate, ions are accelerated in the plasma sheath which leads to energetic ion bombardment. This weakens the atomic bonds in the surface and sub-surface regions of the substrate and makes those regions more prone to attack by the aforementioned reactive radicals. As a result the etch rate of the target material is significantly enhanced.^{2,3}

A key requirement in etching is the *etch selectivity* of the process, defined as the ratio of the etch rate of material A to that of another material B.

As discussed in Chapter 1, for conventional etching techniques there are several challenges associated with etching high aspect ratio structures, controlling the etch profile, and achieving high uniformity and high etch selectivity. Atomic layer etching (ALE) holds promise to overcome most of those shortcomings by dividing the etch process into two time-separated and self-limiting steps: half-reaction A and half-reaction B. Generally, during the first half-reaction the top surface of a material is

chemically modified. During the subsequent half-reaction, the modified top layer is removed through the formation of a volatile product which is purged or pumped off. In this chapter we will focus on the aspects of etch selectivity in ALE and describe the mechanisms underlying selective ALE through a few selected examples that have been reported in the literature. The content is organized as follows. In Section 3.2 various approaches for achieving ALE are briefly described. In Section 3.3 the concepts of *etch delay* and *etch selectivity* for a generic ALE process are discussed by drawing analogies with continuous etching techniques. In Section 3.4 the fundamental reasons underlying etch selectivity of selected ALE processes are discussed. Section 3.5 concludes the chapter with a comparison with the selectivity in area-selective ALD.

3.2 Approaches for ALE

Directional/anisotropic ALE is achieved by using accelerated ions (or neutral species), while *isotropic* ALE employs non-directional species (typically in thermochemical reactions). To ensure self-limiting behavior, the ion energy employed in directional/anisotropic ALE has to be well-controlled and below the threshold for material sputtering, thus avoiding continuous material removal. Furthermore, the use of low and precisely controlled ion energy can enable higher selectivity, as compared to continuous etching.⁴⁻⁶ Besides the mainstream concepts of directional plasma ALE and *isotropic* thermal ALE,⁷ hybrid approaches have been developed in order to expand the ALE toolbox. Such approaches involve the combination of half-reactions that exploit either radical-driven plasma reactions with thermochemical reactions or with annealing/cooling steps as reported by Shinoda *et al.*⁸

Figure 3.1 summarizes six possible ALE approaches, in which either plasma-based, or thermochemical reactions are used at least in one of the two half-reactions (A and B). In *directional/anisotropic* ALE, plasma-generated radicals (half-reaction A) can be used for isotropic surface modification, and ions (half-reaction B) for inducing directional removal of the modified layer (Figure 3.1a).⁵ Alternatively, thermochemical reactions with a vapor-phase precursor (half-reaction A) can be used in combination with accelerated ions/neutral species (half-reaction B); see Figure 3.1b. In Chapter 7 we introduce a novel concept for *isotropic* ALE, in which a thermochemical reaction (half-reaction A) is used to remove material. This reaction appears to be self-terminating due to the formation of a surface layer that inhibits further etching. A radical-driven O₂ plasma pulse (half-reaction B) is then used to reset the surface for the next ALE cycle (Figure 3.1c). Isotropic ALE can also be obtained by using a plasma-based process in which radicals modify the surface (half-reaction A) and an annealing step (half-reaction B) is used to desorb the modified layer (Figure 3.1 d)⁹⁻¹⁰. Precursor and co-reactant thermochemical reactions can be alternated in both half-reactions to achieve isotropic ALE (Figure 3.1e).^{11,12} Otherwise, a thermal annealing step (half-reaction B) can be used to desorb and etch the layer that was modified by a thermochemical reaction during half-reaction A (Figure 3.1 f).¹³

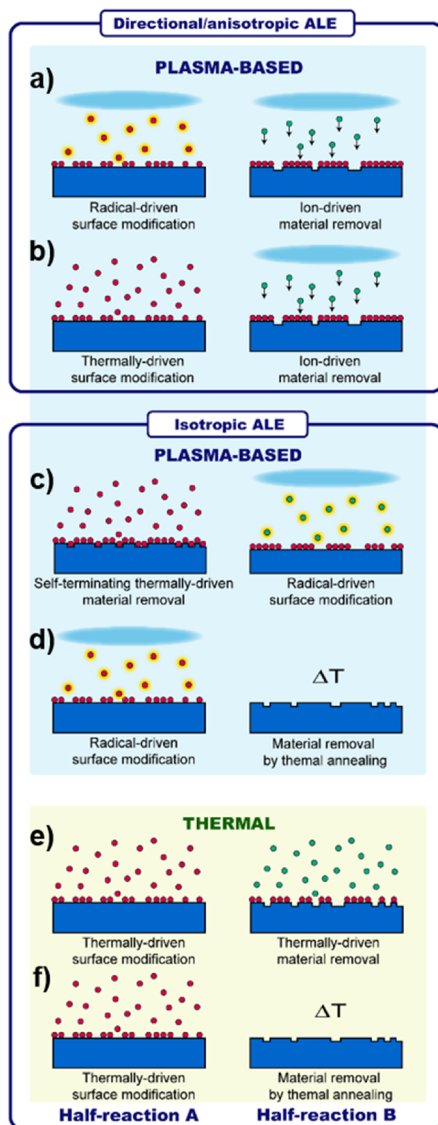


Figure 3.1: Schematic overview of several approaches of ALE. Directional/anisotropic ALE can be obtained by the alternated exposure to **a)** a plasma-generated radical precursor or **b)** a thermochemical precursor that modifies the material surface during the half-reaction A. In the subsequent half-reaction B, **a-b)** plasma-generated ions or neutral beams are used to remove the modified layer in a directional fashion.¹⁴ Isotropic ALE can be obtained using: **c)** a thermochemical reaction that removes the material in a self-terminating manner, during the half-reaction A, and a radically-driven plasma step that resets the surface during the half-reaction B (see Chapter 7 for more details); **d)** exposure to a plasma-generated radical precursor that modifies the material surface, during half-reaction A, and a subsequent thermal annealing step to desorb the modified layer, during half-reaction B;^{8–10} **e)** alternated exposure to a thermochemical precursor that modifies the surface and a co-reactant that removes the modified surface layer;^{7,12,15–18} or **f)** exposure to a thermochemical reaction with a precursor that modifies the surface and a thermal annealing step to desorb the modified layer.¹³

3.3 Selectivity and etch delay

In continuous etching, the etch selectivity is traditionally defined as the ratio between the etch rates of two different materials, A and B. Obviously, the same definition of etch selectivity applies for the case of ALE. An extreme case is when the chemistry utilized for etching material A does not form a volatile product containing B. In such case the etch rate of B is zero, resulting in a selectivity that is infinite by definition. In addition, a situation analogous to the phenomenon of nucleation delay that was discussed in Chapter 2 for deposition, has been observed in conventional etching processes (Figure 3.2). The so-called *dead time* that occurs between the beginning of an etch process and the onset of actual material removal can also be defined as the *etch delay*.¹⁹ The phenomenon of etch delay has not been explicitly reported in the ALE literature. However, the possibility of such delay taking place should not be excluded *a priori*. Actually, etch inhibition or etch enhancement in the early ALE cycles has been discussed by Lemaire *et al.*²⁰ They observed differences in the etch per cycle between the initial and the steady state of a thermal ALE process for TiO₂, using WF₆ as the precursor and BCl₃ as the co-reactant.

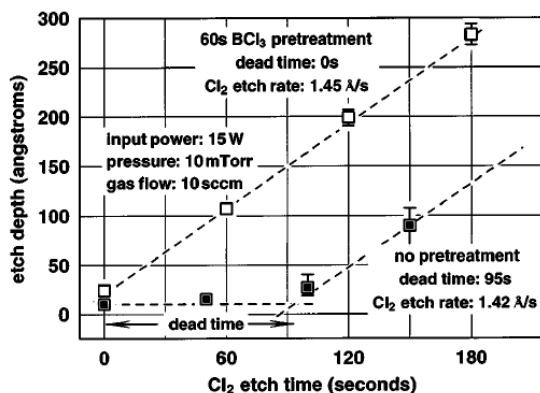


Figure 3.2: Etching depth for pristine and BCl₃-pre-treated AlGaN. The etch delay (also called *dead time*) observed for the pristine sample was attributed to the presence of a difficult-to-etch native oxide. A pretreatment with BCl₃ effectively removes the native oxide thereby eliminating the etch delay. After Ref. 19.

Figure 3.3 schematically depicts the etching behavior of a generic ALE process for two different materials, A and B. For material A (Figures 3.3a-3.3a3), an immediate and linear thickness decrease with the number of ALE cycles indicates controlled *layer-by-layer* etching accomplished by the cyclic exposure to a precursor and a co-reactant. In the case of material B (Figures 3.3b-3.3b2), the same ALE process initially results in no etching, thus the film thickness remains constant for several cycles. After this *etch delay*, the etching of material B starts (Figure 3.3b3). Here, a significant difference compared to area-selective ALD as discussed in Chapter 2 should be highlighted. When, after a transient growth regime in the case of area-selective ALD, deposition finally starts on

the non-growth area, the growth per cycle values are equal on both growth and non-growth area. This is because after the nucleation delay the material is deposited on itself. Once the etching starts for an ALE process, an etch delay may or may not exist and the etch rates of materials A and B will remain fundamentally different. For this reason, an analogous expression or parallel definition of the selectivity window as given for area-selective ALD (i.e. defined by the number of cycles, see Chapter 2) cannot be defined for the case of ALE.

The differences in etching behavior (in terms of etch delay or etch rate) can be exploited to achieve selective ALE, when materials A and B are present in a patterned fashion on a substrate, as depicted in Figure 3.3 c.

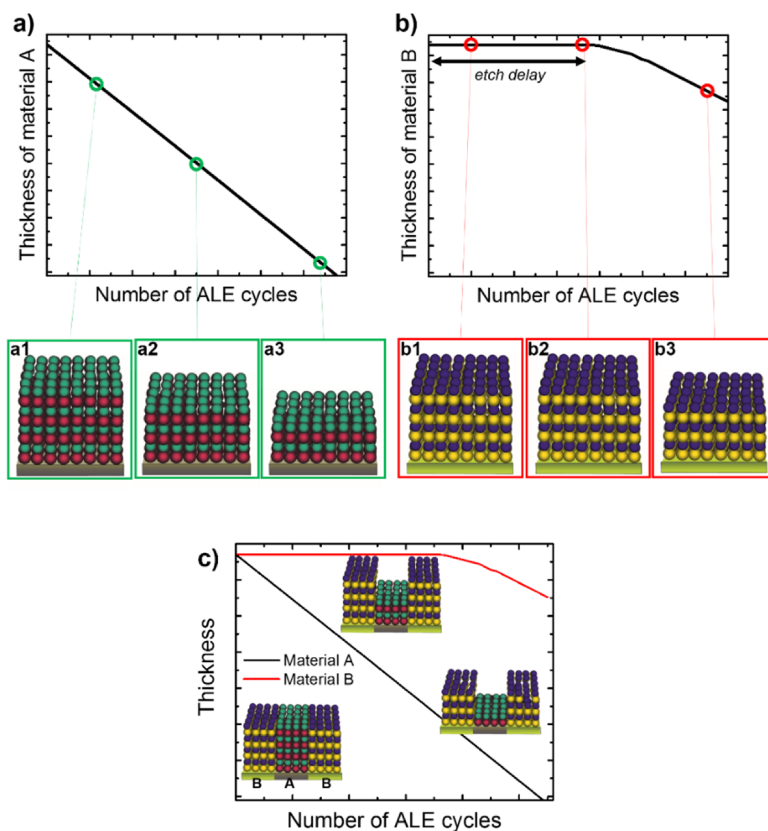


Figure 3.3: Film thickness as a function of the number of ALE cycles for two different starting (binary element) materials, A and B. The cyclic dosage of precursor and co-reactant results in **a)** an immediate and linear film thickness decrease for material A and **b)** a delayed decrease in film thickness (etch delay) for material B. Once the etching commences for material B, its etch rate (represented by the slope) is typically not identical to that of material A. **a1)** - **a3)**, and **b1)** - **b3)** schematically represent the different stages of the etching for the respective materials A and B. To clearly illustrate the concept of etch selectivity, a pattern consisting of **c)** materials A and B is subjected to ALE. The insets show the selective removal of material A in the presence of material B, for different numbers of ALE cycles.

3.4 Surface chemistry underlying selective ALE

Generally, etch selectivity with respect to a particular reference material may result from the fact that there is no suitable chemistry available to etch that material.^{21,22} This holds for both conventional etch processes and ALE. The key difference is that the etching reaction in ALE is divided into two half-reactions. High etch selectivity can therefore be imparted by differences in the thermodynamics or kinetics of each half-reaction (see Chapter 2 for clarification) for diverse materials. Therefore, depending on the choice of the substrate and chemistry of the ALE process, high etch selectivity can occur due to a:

- *chemoselective precursor mechanism, or*
- *chemoselective co-reactant mechanism*

Note that in the following sub-sections, we define the *precursor* step as the half-reaction that leads to material surface modification and the *co-reactant* step as the half-reaction that releases a volatile product containing the target material. By this definition, plasma radical-driven reactions or thermochemical reactions are considered as the precursor step, while ion-surface interactions, thermochemical reactions or annealing steps are considered as the co-reactant step.

3.4.A. Chemoselective precursor mechanism

Highly selective ALE of Si in the presence of SiO₂ was demonstrated by Tan *et al.*,²³ using a Cl₂ plasma step as the precursor and Ar⁺ ions in the co-reactant step, at a substrate temperature of -45 °C. As shown in Figure 3.4a, ‘infinite’ etch selectivity was obtained for low ion energies. Since Si and SiO₂ have similar Ar⁺ energy thresholds for commencing etching/sputtering (around 40 eV),^{23,24} the ion energy during the co-reactant step can play only a minor role in imparting selectivity. Thus, the authors ascribed the selectivity to the precursor step. The etch selectivity can be understood by considering the Si-O bond energy. When a Si-atom is backbonded to another oxygen atom ($E_{\text{OSi-O}} = 4.68$ eV) the Si-O bond energy is much larger than the Si-Cl bond energy for an O-backbonded Si ($E_{\text{OSi-Cl}} = 0.95$ eV).²⁵ Therefore, the chlorination of a SiO₂ surface from molecular Cl₂ is likely a thermodynamically unfavored process because the energy needed to dissociate a Cl₂ molecule and to break a OSi-O bond is much larger than the energy gained in forming an OSi-Cl bond. In agreement, Chang and Sawin demonstrated that for a continuous etch process at room temperature, molecular Cl₂ does not enhance the etch yield of SiO₂. However, Cl-radicals enhance the etching yield by a factor of 3-4, Figure 3.4b.²⁴ Based on these experimental results, it was concluded that when using Cl₂, the primary mechanism for etching SiO₂ is sputtering due to Ar⁺ which explains the decrease in selectivity at higher bias voltages shown in Figure 3.4a.²⁴ Another factor for the high selectivity could be the extremely low etching temperature

(-40 °C) that may sensibly slow down the kinetics of plasma surface chlorination on SiO₂.

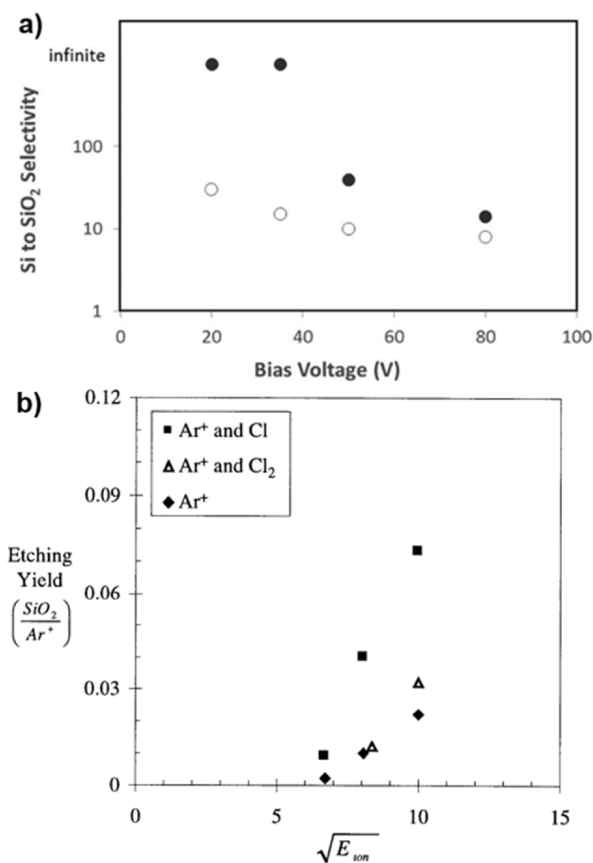


Figure 3.4: **a)** Etch selectivity (Si over SiO₂) as a function of the RF bias voltage for ALE (filled circles) and continuous etching (open circles). After Ref. 23. **b)** Etching yield of SiO₂ as a function of the square root of the ion energy for: Ar⁺(diamonds), Ar⁺ + Cl₂ mixture (triangles), and Ar⁺ + Cl (squares). The threshold for all processes is ~40 eV and the etching is enhanced significantly only when dosing Cl. After Ref. 24.

3.4.B. Chemoselective co-reactant mechanism

Etch selectivity in ALE can also be obtained by exploiting the differences in reaction energetics with different materials, during the co-reactant half-reaction of the process. Below, we discuss the role of three possible co-reactant steps: ion bombardment in directional ALE, thermochemical reaction in thermal ALE and thermal annealing in hybrid ALE approaches.

Directional ALE. Fine control over the ion energy can be exploited during the second half-reaction to achieve high etch selectivity, if the materials subjected to the ALE process have different bond energy. This is the case for ALE of Ge in the presence of Si. Here, a Cl_2 plasma is used to chlorinate both surfaces followed by an argon ion bombardment to remove the modified layer.²⁶ Etch selectivity of Ge over Si is obtained by tuning the applied RF bias voltage and thereby the Ar^+ ion energy. Ion energies of 20-30 eV are sufficient to remove the chlorinated Ge, whereas energies between 40-60 eV are required to achieve ALE of Si.²⁶ This can be explained by considering the bond energies in the bulk and at the surface for the two different materials. During the precursor step, the chlorination weakens the Ge-Ge and Si-Si bonds in the subsurface through the formation of strong surface bonds (> 4 eV), as schematically depicted in Figure 3.5. Due to the strong electronegativity of Cl, the bond energies of sub-surface Ge-GeCl and Si-SiCl are lower: < 2.7 eV and < 3.2 eV, respectively. As a result, the ion energy threshold required for breaking Ge-GeCl bonds is lower than the threshold needed to break the Si-SiCl bonds.²⁵ By controlling the ion energy below the threshold for silicon, etch selectivity of Ge over Si can be achieved in ALE.

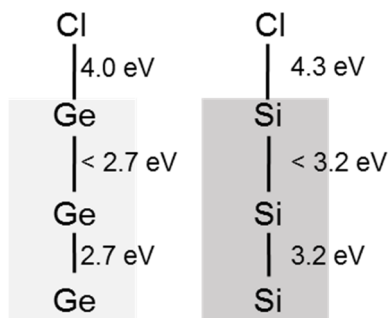
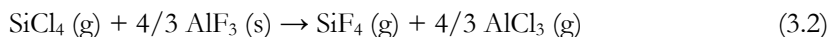


Figure 3.5: Schematic representation and bond energies for the chlorination of Ge and Si. Compiled from Ref. 25.

Thermal ALE. Etch selectivity during ALE may also result from the differences in reaction thermochemistry between the co-reactant and the modified substrate surfaces. This is the case for the selective ALE of HfO_2 in the presence of Al_2O_3 . Lee *et al.* demonstrated that, up to a temperature of 350 °C, no etching of Al_2O_3 occurs when using HF as the precursor and SiCl_4 as the co-reactant.²⁷ During the first half-reaction, HF fluorinates both HfO_2 and Al_2O_3 surfaces through a thermodynamically feasible reaction, i.e., a reaction with a negative change in Gibbs free energy ($\Delta G < 0$). In contrast, the ligand exchange reaction during the co-reactant step was calculated to be thermodynamically unfavored in the case of HfF_4 (reaction 3.1), and thermodynamically favored in the case of AlF_3 (reaction 3.2). The authors explained the etch selectivity by the proposed mechanism below:



$$\Delta G = -0.43 \text{ eV}$$



$$\Delta G = +1.13 \text{ eV}$$

The formation of AlCl_3 from AlF_3 and SiCl_4 requires a too high energy, therefore this process is unlikely to take place under the experimentally investigated conditions.

Hybrid ALE. When an annealing step is used it can be considered a ‘co-reactant’. High etch selectivity during ALE may then be obtained by controlling the annealing temperature such that the modified layer of one material is volatile enough to evaporate, whereas the modified layer of the other material is not. An example of this approach is the isotropic ALE process demonstrated by Ikeda *et al.* for Ge in the presence of Si.¹³ This hybrid ALE process involves the alternated chlorination of the Ge and Si surfaces by Cl_2 gas at room temperature. The chlorination step is followed by an annealing step at 400 °C, which enables the removal of the chlorinated germanium surface layer. Etch selectivity of Ge over Si can be achieved by controlling the annealing temperature well below 650 °C. Indeed, as calculated by Tang *et al.*, GeCl_2 is volatile (partial pressure of ~700 mTorr) at 600 K, while SiCl_2 requires temperatures above 800 K to be sufficiently volatile. This is shown for a system involving H_2 , Cl_2 , Ge and Si in Figure 3.6.²⁸ The same calculations also show that SiCl_4 has a high partial pressure even below 800 K, which has made SiCl_4 a very popular vapor phase silicon precursor in conventional CVD. Nevertheless, SiCl_4 (likewise GeCl_4) cannot be directly formed on the surface because the adsorption of Cl_2 on Si is known to form a chlorinated layer that inhibits further reactions.^{1,29} Hence, under the particular experimental conditions (thermochemical chlorination reaction) the formation of SiCl_4 (and GeCl_4) is a negligible process on the substrate surface and only the SiCl_2 and GeCl_2 species can be considered for the ALE process. In the light of these considerations, the temperature at which the ALE process for Ge is carried out imparts the selectivity by governing the volatility of the reaction products.

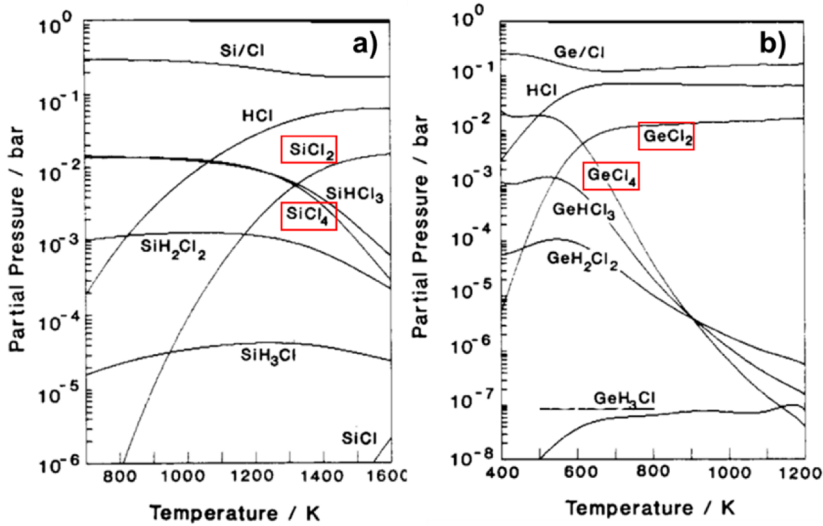


Figure 3.6: Variation of the gas phase partial pressures for the systems a) Si-Cl-H and b) Ge-Cl-H. The total pressure considered is 1 bar. From Tang *et al.*, Ref. 20.

3.4.C. Miscellaneous ALE selectivity mechanisms

We realize that the above classification of ALE selectivity mechanisms is sufficient but not exhaustive. A particular case not considered yet is the etch selectivity of SiN_x in the presence of SiO_2 demonstrated by Shinoda and co-workers.⁹ In this ALE-based process, high selectivity is obtained during the precursor step by using a hydrofluorocarbon plasma step (at 20 °C) that leads to modification of SiN_x (conversion to an ammonium fluorosilicate surface layer) and, at the same time, to fluorocarbon deposition on material SiO_2 . The ALE cycle is completed by a thermal annealing step (at 100 °C) that leads to the desorption of the ammonium fluorosilicate layer, i.e. etching of the modified SiN_x as shown in Figure 3.7, while a fluorocarbon protective layer remains the SiO_2 . Similar selective etch chemistry has also been demonstrated for the selective ALE of TiN in the presence of SiO_2 .⁸

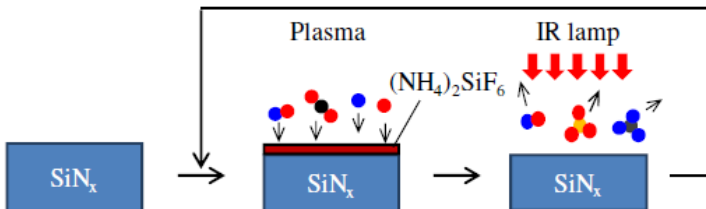


Figure 3.7: Schematic representation of a hybrid ALE approach for the etching of SiN_x . During the half-reaction A, a low temperature plasma step is used to convert the SiN_x surface into an ammonium fluorosilicate layer, $(\text{NH}_4)_2\text{SiF}_6$, which is subsequently desorbed in half-reaction B, by rapid thermal annealing with IR lamps. After Ref. 9.

3.5. Selectivity in ALE and in area-selective ALD

When comparing the fundamentals underlying the selectivity in ALD and ALE, many similarities can be found. The essence lies in controlling the relative reaction feasibilities and rates for the different materials at a substrate surface. To this end, thermodynamic and/or kinetic analyses can be useful in providing qualitative insights into the problem of selectivity and in facilitating the design of novel processes to be benchmarked with experimental results.

A major difference between selective ALE and area-selective ALD is that in the first case control over the energy of directional ions (or neutral beams)³⁰ is largely exploited to achieve selectivity. The role of ions influencing the chemical composition and film microstructure has only been recently investigated in-depth in the field of ALD.^{31,32} Inert ions and/or reactive ions might offer extra parameters to obtain or improve the selectivity also for the case of area-selective ALD. Ion-induced changes in microstructure (stress, damage) or chemically induced modification (e.g. surface dehydroxylation) may be used as a surface preparation step to manipulate the reactivity of a specific surface. Alternatively, so-called topographically selective processes can be obtained by depositing materials with different chemical or physical properties on planar and 3D vertical surfaces, as recently demonstrated by Karwal *et al.*³⁰ and Faraz *et al.*³¹

Another characteristic of ALE which does not have its direct counterpart in the field of area-selective ALD, is the use of simultaneous deposition on one material and etching of another material. If compatible with the specific fabrication step, a mirrored approach could be used to obtain high selectivity when the non-growth area is etched while material is deposited on the growth area. In this respect, it is also believed that ALD and ALE can be combined in more complex schemes to achieve high deposition selectivity and, *vice versa*, high etch selectivity.^{33,34}

REFERENCES

- (1) Flamm, D. Mechanisms of Silicon Etching in Fluorine-and Chlorine-Containing Plasmas. *Pure Appl. Chem.* **1990**, *62*, 1709–1720.
- (2) Kanarik, K. J.; Lill, T.; Hudson, E. A.; Sriraman, S.; Tan, S.; Marks, J.; Vahedi, V.; Gottscho, R. A. Overview of Atomic Layer Etching in the Semiconductor Industry. *J. Vac. Sci. Technol. A Vacuum, Surfaces, Film.* **2015**, *33*, 20802.
- (3) Lieberman, M. A.; Lichtenberg, A. J. *Principles of Plasma Discharges and Materials Processing*; Ed. II.; John Wiley & Sons: Hoboken, New Jersey, USA, 2005 page 590.
- (4) Carver, C. T.; Plombon, J. J.; Romero, P. E.; Suri, S.; Tronic, T. A.; Turkot, R. B. Jr. Atomic Layer Etching: An Industry Perspective. *ECS J. Solid State Sci. Technol.* **2015**, *4*, N5005–N5009.
- (5) Lill, T.; Kanarik, K. J.; Tan, S.; Shen, M.; Hudson, E.; Pan, Y.; Marks, J.; Vahedi, V.; Gottscho, R. A. Directional Atomic Layer Etching. *Encycl. Plasma Technol.* **2016**, 133–142.
- (6) Engelmann, S. U.; Bruce, R. L.; Nakamura, M.; Metzler, D.; Walton, S. G.; Joseph, E. A. Challenges of Tailoring Surface Chemistry and Plasma/Surface Interactions to Advance Atomic Layer Etching. *ECS J. Solid State Sci. Technol.* **2015**, *4*, N5054–N5060.
- (7) George, S. M.; Lee, Y. Prospects for Thermal Atomic Layer Etching Using Sequential, Self-Limiting Fluorination and Ligand-Exchange Reactions. *ACS Nano* **2016**, *10*, 4889–4894.
- (8) Shinoda, K.; Miyoshi, N.; Kobayashi, H.; Kurihara, M.; Izawa, M.; Ishikawa, K.; Hori, M. Thermal Cyclic Atomic-Level Etching of Nitride Films: A Novel Way for Atomic-Scale Nanofabrication K. Shinoda. *ECS Trans.* **2017**, *80*, 3–14.
- (9) Shinoda, K.; Izawa, M.; Kanekiyo, T.; Ishikawa, K.; Hori, M. Thermal Cyclic Etching of Silicon Nitride Using Formation and Desorption of Ammonium Fluorosilicate. *Appl. Phys. Express* **2016**, *9*, 1062011–3.
- (10) Shinoda, K.; Miyoshi, N.; Kobayashi, H.; Miura, M.; Kurihara, M.; Maeda, K.; Negishi, N.; Sonoda, Y.; Tanaka, M.; Yasui, N.; *et al.* Selective Atomic-Level Etching Using Two Heating Procedures, Infrared Irradiation and Ion Bombardment, for next-Generation Semiconductor Device Manufacturing. *J. Phys. D. Appl. Phys.* **2017**, *50*, 194001–13.
- (11) Lee, Y.; George, S. M. Atomic Layer Etching of Al₂O₃ Using Sequential, Self-Limiting Thermal Reactions with Sn(acac)₂. *ACS Nano* **2015**, *9*, 2061–2070.
- (12) Lee, Y.; Dumont, J. W.; George, S. M. Trimethylaluminum as the Metal Precursor for the Atomic Layer Etching of Al₂O₃ Using Sequential, Self-Limiting Thermal Reactions. *Chem. Mater.* **2016**, *28*, 2994–3003.
- (13) Ikeda, K.; Imai, S.; Matsumura, M. Atomic Layer Etching of Germanium. *Appl. Surf. Sci.* **1997**, *112*, 87–91.
- (14) Yoder, M. N. US Pat. 4,756,794 A **1988**.
- (15) Lee, Y.; DuMont, J. W.; George, S. M. Atomic Layer Etching of HfO₂ Using Sequential, Self-Limiting Thermal Reactions with Sn(acac)₂ and HF. *ECS J. Solid State Sci. Technol.* **2015**, *4*, N5013–N5022.
- (16) Zywojtko, D. R.; George, S. M. Thermal Atomic Layer Etching of ZnO by a “Conversion-Etch” Mechanism Using Sequential Exposures of Hydrogen Fluoride and Trimethylaluminum. *Chem. Mater.* **2017**, *29*, 1183–1191.
- (17) Johnson, N. R.; Sun, H.; Sharma, K.; George, S. M. Thermal Atomic Layer Etching of Crystalline Aluminum Nitride Using Sequential, Self-Limiting Hydrogen Fluoride and Sn(acac)₂ Reactions and Enhancement by H₂ and Ar Plasmas. *J. Vac. Sci. Technol. A Vacuum, Surfaces, Film.* **2016**, *34*, 50603.
- (18) Lee, Y.; Dumont, J. W.; George, S. M. Atomic Layer Etching of AlF₃ Using Sequential, Self-Limiting Thermal Reactions with Sn(acac)₂ and Hydrogen Fluoride. *J. Phys. Chem. C* **2015**, *119*, 25385–25393.
- (19) Buttari, D.; Chini, A.; Palacios, T.; Coffie, R.; Shen, L.; Xing, H.; Heikman, S.; McCarthy, L.; Chakraborty, A.; Keller, S.; *et al.* Origin of Etch Delay Time in Cl₂ Dry Etching of AlGaIn/GaN Structures. *Appl. Phys. Lett.* **2003**, *83*, 4779–4781.
- (20) Lemaire, P. C.; Parsons, G. N. Thermal Selective Vapor Etching of TiO₂: Chemical Vapor Etching via WF₆ and Self-Limiting Atomic Layer Etching Using WF₆ and BCl₃. *Chem. Mater.* **2017**, *29*, 6653–6665.
- (21) Patel, V. Handbook of Vacuum Science and Technology. In *Handbook of vacuum science and technology*; Hoffman, Dorothy M.; Singh, Bawa; Thomas, J. H., Ed.; Academic Press: San Diego, CA; pp. 628–671.

- (22) *Fundamentals of Microfabrication and Nanotechnology Vol. II*; Madou, M. J., Ed.; CRC Press: Boca Raton, USA, 2011, Ch.5.2.
- (23) Tan, S.; Yang, W.; Kanarik, K. J.; Lill, T.; Vahedi, V.; Marks, J.; Gottscho, R. A. Highly Selective Directional Atomic Layer Etching of Silicon. *ECS J. Solid State Sci. Technol.* **2015**, *4*, N5010–N5012.
- (24) Chang, J. P.; Sawin, H. H. Molecular-Beam Study of the Plasma-Surface Kinetics of Silicon Dioxide and Photoresist Etching with Chlorine. *J. Vac. Sci. Technol. B Microelectron. Nanom. Struct.* **2001**, *19*, 1319.
- (25) Luo, Y.-R. Bond Dissociation Energies. In *CRC Handbook of Chemistry and Physics 89th ed.*; CRC Press: Boca Raton, USA, 2009.
- (26) Matsuura, T.; Sugiyama, T.; Murota, J. Atomic-Layer Surface Reaction of Chlorine on Si and Ge Assisted by an Ultraclean ECR Plasma. *Surf. Sci.* **1998**, *402–404*, 202–205.
- (27) Lee, Y.; Huffman, C.; George, S. M. Selectivity in Thermal Atomic Layer Etching Using Sequential, Self-Limiting Fluorination and Ligand-Exchange Reactions. *Chem. Mater.* **2016**, *28*, 7657–7665.
- (28) Tang, H. P.; Vescan, L.; Lüth, H. Equilibrium Thermodynamic Analysis of the Si-Ge-Cl-H System for Atmospheric and Low Pressure CVD of Si_{1-x}Ge_x. *J. Cryst. Growth* **1992**, *116*, 1–14.
- (29) Aldao, C. M.; Weaver, J. H. Halogen Etching of Si via Atomic-Scale Processes. *Prog. Surf. Sci.* **2001**, *68*, 189–230.
- (30) Park, S. D.; Oh, C. K.; Bae, J. W.; Yeom, G. Y.; Kim, T. W.; Song, J. I.; Jang, J. H. Atomic Layer Etching of InP Using a Low Angle Forward Reflected Ne Neutral Beam. *Appl. Phys. Lett.* **2006**, *89*, 0431091-3
- (31) Karwal, S.; Verheijen, M. A.; Williams, B. L.; Faraz, T.; Kessels, W. M. M.; Creatore, M. Low Resistivity HfN_x Grown by Plasma-Assisted ALD with External Rf Substrate Biasing. *J. Mater. Chem. C*, **2018**, *6*, 3917-3926
- (32) Faraz, T.; Knoops, H. C. M.; Verheijen, M. A.; van Helvoirt, C. A. A.; Karwal, S.; Sharma, A.; Beladiya, V.; Szeghalmi, A.; Hausmann, D. M.; Henri, J.; *et al.* Tuning Material Properties of Oxides and Nitrides by Substrate Biasing during Plasma-Enhanced Atomic Layer Deposition on Planar and 3D Substrate Topographies. *ACS Appl. Mater. Interfaces* **2018**, *10*, 13158-13180
- (33) Roozeboom, F.; van den Bruele, F.; Creyghton, Y.; Poodt, P.; Kessels, W. M. M. A Spatial ALD Oxide Passivation Module in an All-Spatial Etch-Passivation Cluster Concept. *ECS J. Solid State Sci. Technol.* **2015**, *4*, N5067-N5076.
- (34) Kanarik, K. J.; Marks, J.; Singh, H.; Kabansky, A.; Yang, W.; Kim, T.; Hausmann, D. M.; T., L. Integrating Atomic Scale Processes: ALD (Atomic Layer Deposition) and ALE (Atomic Layer Etch). US009576811B2, 2017.

Chapter 4

Area-Selective Atomic Layer Deposition of $\text{In}_2\text{O}_3\text{:H}$ Using a μ -plasma Printer for Local Area-Activation*

Area-selective atomic layer deposition of $\text{In}_2\text{O}_3\text{:H}$ was achieved using a μ -plasma printer by locally activating the surface of various H-terminated silicon-based materials (HF-last $\text{Si}(100)$, $a\text{-Si:H}$ and $a\text{-SiN}_x\text{:H}$) before initializing the ALD cycles. With this direct write ALD technique, $\text{In}_2\text{O}_3\text{:H}$ patterns ranging from 0.6 to 3 mm in width were prepared at 100 °C, from indium cyclopentadienyl (InCp) and a mixture of H_2O and O_2 . The selectivity of the ALD process was demonstrated by X-ray photoelectron spectroscopy. A resistivity value of 0.59 m Ω cm was obtained on patterns grown using 780 ALD cycles (~75 nm thick). Density Functional Theory (DFT) calculations provided a quantitative understanding of the surface chemistry that lies at the basis of the high selectivity.

4.1 Introduction

Electronic device fabrication generally requires several lithographic steps to obtain well-aligned features. This is becoming ever more challenging in the semiconductor industry as feature dimensions of state-of-the-art devices keep shrinking.¹⁻⁴ It is, however, not only the semiconductor industry that faces such challenges. Some of the challenges in patterning for nanoelectronics share common ground with those of microscale patterning as used in large-area electronics. Furthermore, removing material by etching can be detrimental in terms of materials damage and contamination.⁵ Moreover, for large-area electronics cost per unit and throughput considerations also limit the use of expensive and iterative ‘litho-etch’ steps. This holds for example for patterned transparent conductive oxides (TCOs).⁶⁻⁸ TCO films are ubiquitous in many devices such as displays,⁹⁻¹² solar cells,¹³ solid state lighting and sensors,^{7,8} including those based on emerging organic light-emitting devices (OLEDs)¹⁴ and on halide perovskite materials. To date, methods used for patterning TCOs such as such as rapid laser patterning¹⁵ often have limited uniformity and resolution or suffer from material degradation during the etch processes.⁶ Furthermore, more than six steps are typically required to fabricate patterned TCOs.^{6-8,16} Hence, several applications that require millimeter and sub-millimeter patterned TCO films would benefit from the availability of alternative patterning methods.⁹⁻¹²

*Published as: Mameli, A.; Kuang, Y.; Aghaee, M.; Ande, C. K.; Karasulu, B.; Creatore, M.; Mackus, A. J. M.; Kessels, W. M. M.; Roozeboom, F. *Chem. Mater.* **2017**, *29*, 921–925.

Area-selective atomic layer deposition has emerged as a promising solution to push device manufacturing towards new frontiers. Significant efforts, in academia and industry, are currently devoted towards the development of area-selective ALD techniques that can be incorporated within existing fabrication schemes. To date, most of these efforts have been inspired by the need to prepare nanoscale features in the semiconductor industry as an alternative or a possible solution for extremely complex lithography schemes. Although the number of viable methods is still very limited, the approaches for achieving area-selective ALD can be categorized as: (1) area deactivation, in which a part of the surface is rendered inert towards a specific ALD process; and (2) area activation, where conversely, an inert surface is locally activated for a specific type of ALD chemistry.^{17–19} A prototype example of the first case is area deactivation of a surface by blocking it with self-assembled monolayers.^{2,20,21} A particular case of the latter approach is the direct activation of a surface region without any subtractive steps. This can be referred to as *direct-write* ALD,^{2,18,22} and it enables patterning and ALD to be combined into a truly bottom-up process drastically reducing the number of required fabrication steps. One embodiment of *direct-write* ALD was developed by Mackus et al. by exploiting the catalytic activity of a Pt seed layer grown locally using electron beam induced deposition (EBID). After EBID, ALD was applied for selectively thickening the Pt seed layers into high-quality Pt nanostructures.^{2,18,22}

In this work, we present a novel method for area-selective ALD which targets the preparation of microscale features relevant in large-area electronics. It is a *direct-write* ALD process of $\text{In}_2\text{O}_3\text{:H}$, a highly promising and relevant TCO material,²³ which makes use of printing technology for surface activation. As schematically depicted in Figure 4.1, first the surface of H-terminated silicon materials is locally activated by a μ -plasma printer in air or O_2 ,²⁴ and subsequently $\text{In}_2\text{O}_3\text{:H}$ is deposited selectively on the activated areas. The selectivity stems from the fact that ALD $\text{In}_2\text{O}_3\text{:H}$ leads to very long nucleation delays on H-terminated silicon materials.²⁵ In this work it is demonstrated that this method allows for preparing microscale $\text{In}_2\text{O}_3\text{:H}$ features in a true bottom-up approach on surfaces of H-terminated Si(100), a-Si:H or a-SiN_x:H with the $\text{In}_2\text{O}_3\text{:H}$ material quality being as high as for blanket films.²⁶ This novel approach for *direct-write* ALD of $\text{In}_2\text{O}_3\text{:H}$ holds therefore potential for applications in large-area electronics which make use of patterned TCOs such as displays and solar cells.

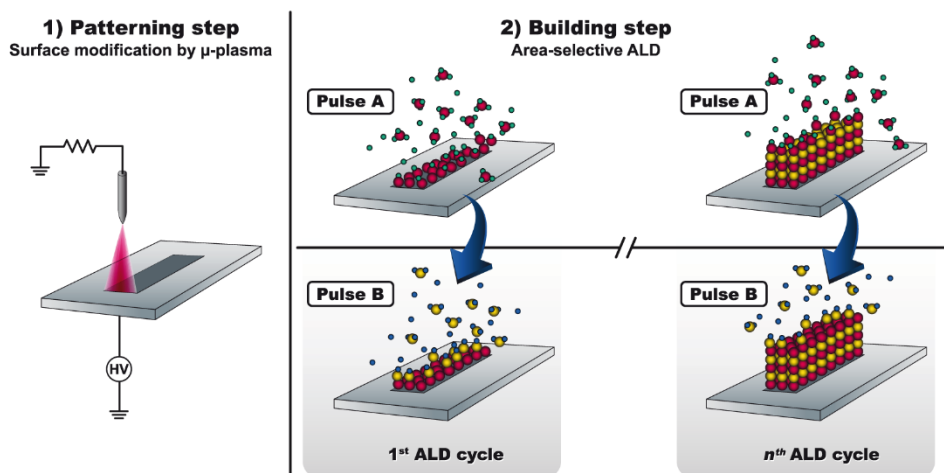


Figure 4.1. Schematic representation of the area-selective ALD process of $\text{In}_2\text{O}_3\text{:H}$ on H-terminated silicon materials. In the first step (1) microscale patterns are defined by activating the surface with a μ -plasma operated in air or O_2 . In the second step (2) the $\text{In}_2\text{O}_3\text{:H}$ is deposited selectively on the activated areas in a building step. The ALD process consists of two alternating half reactions: InCp precursor dosing in pulse A and a mixture of O_2 and H_2O dosing in pulse B. Note that in the case that conductive substrates are used, a thin dielectric membrane (Al_2O_3) is positioned between the needles and the substrate, as shown in Figure 4.A1 (a).

4.2 Experimental methods

For the experiments an Oxford Instruments Opal™ ALD reactor was used to deposit the $\text{In}_2\text{O}_3\text{:H}$ films. Indium cyclopentadienyl (InCp) served as indium precursor and a mixture of H_2O and O_2 as co-reactants.²⁷ A standard recipe was employed as detailed elsewhere.^{23,27} The reactor pressure was ~ 150 mTorr throughout the cycle with a pressure spike of ~ 200 mTorr during the 20 ms H_2O dose. All samples prepared in this study were deposited at 100°C .

Films of a-Si:H and a-SiN_x:H on p-type Si(100) served as substrates. These 10 nm thick films were prepared by inductively coupled plasma chemical vapor deposition (ICP-CVD) from SiH_4 and Ar at 50°C and from SiH_4 and NH_3 at 80°C for a-Si:H and a-SiN_x:H, respectively. Alternatively, H-terminated Si(100) was prepared by dipping the wafer in diluted (1% vol.) hydrofluoric acid (HF) for 2-3 minutes.²⁸ Furthermore, a 400 μm thick stainless steel foil with 20 nm of a-Si:H on top was used as a flexible substrate. After preparation, the surfaces were locally activated by a μ -plasma printer developed by the company InnoPhysics. The print-head of this μ -plasma printer consists of actuated needle electrodes in a multi needle-to-plate dielectric barrier discharge configuration.²⁴ It allows varying the patterning width by setting the number of actuated

needles and achieving high throughput (1 cm² in less than 5 s). For this study air and O₂ plasmas at atmospheric pressure were used to locally activate the surface of the silicon based materials.

4.3 Results and discussion

By carrying out the sequence of local plasma activation and the ALD cycles as illustrated in Figure 4.1, the area-selective deposition was demonstrated for a macroscopic pattern on a large area. Figure 4.2a shows a 4-inch wafer covered with 10 nm a-Si:H onto which the Eindhoven University of Technology (TU/e) logo was prepared by μ -plasma patterning and 400 ALD cycles. This resulted in \sim 35 nm thick In₂O₃:H locally deposited as measured by *ex-situ* spectroscopic ellipsometry (SE) at two different angles (65 and 75 degrees, using an M-2000D system from J. Woollam Co. with photon energy range: 1.2 to 6.5 eV). The selectivity of the process was confirmed by XPS measurements using a Thermo Scientific K-Alpha system probing distinctive points inside and outside the patterned area. The In3d_{3/2} and In3d_{5/2} signals for two of such points are shown in Figure 4.2b. High signals were collected on the patterned area whereas a negligible signal was measured outside the pattern. This demonstrates the excellent selectivity reached, even after 400 ALD cycles. This finding was substantiated by I-V measurements within and between the different letters of the logo in Figure 4.2a (see the Appendix, Figure 4.A3).

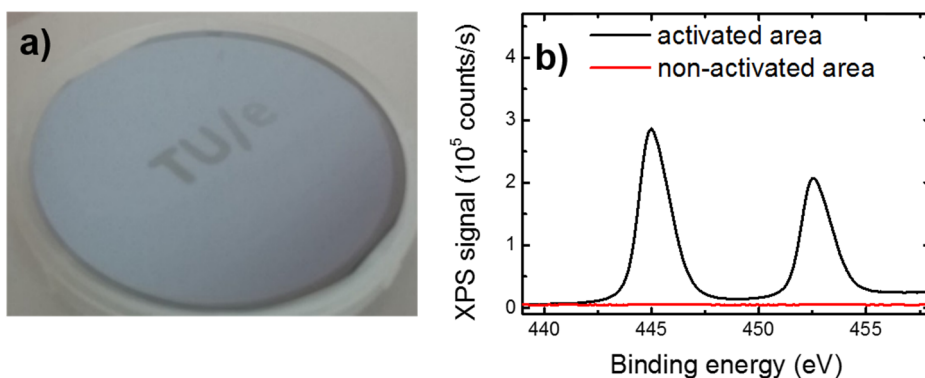


Figure 4.2. **a)** Photograph of a 4-inch Si(100) wafer covered with 10 nm of a-Si:H on which the logo of the Eindhoven University of Technology (TU/e) was deposited using the *direct-write* ALD process of In₂O₃:H. The number of ALD cycles was 400 and the thickness of the In₂O₃:H was \sim 35 nm. **b)** XPS signals for the In3d_{5/2} and In3d_{3/2} binding energy measured for two distinctive points: black, inside and red, outside the patterned area.

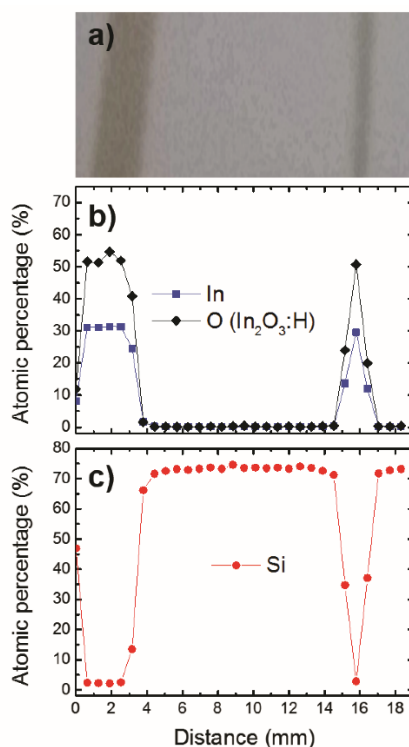


Figure 4.3. a) Photograph of $\text{In}_2\text{O}_3:\text{H}$ lines being 3.0 and 0.8 mm wide as prepared by the direct-write ALD process with 400 cycles. XPS line scans for the patterns depicted in a) showing the atomic percentages related to b) In_2O_3 (In $3d_{5/2}$ and O $1s$) and c) the Si substrate (Si $2p$).

The patterning capabilities of the μ -plasma printer were subsequently investigated using three active needle combinations to pattern lines which were 3.0, 0.8 and 0.6 mm in width. This is done by actuating 12, 4 and 3 needles, respectively, yielding the result in Figure 4.3a. All three patterns are shown in Figure 4.A1 (b) in the Appendix. The material at the surface was probed by XPS through line scans across the 3.0 and 0.8 mm wide lines. The XPS spot size was $400\ \mu\text{m}$ and the distance between successive sampling points was $600\ \mu\text{m}$. For clarity, only the atomic percentages of In and O bonded to In (Figure 4.3b) and Si (Figure 4.3c) are reported. The complete XPS data, together with the results on $\text{a-SiN}_x:\text{H}$, are shown in Figure 4.A2 of the Appendix. The XPS line scans reproduce the patterns in Figure 4.3a as atomic percentages of In and O, while the Si atomic percentage was observed to be complementary to the $\text{In}_2\text{O}_3:\text{H}$ signals. The In atomic percentage decreased from a maximum of $\sim 30\%$ inside the pattern area towards 0% in between the patterns, again demonstrating the high selectivity of the ALD process. The result also demonstrate the capability of the μ -plasma printer to pattern microscale features on a large-area substrate. In the current μ -plasma printer

configuration, the smallest achievable feature size is $\sim 200 \mu\text{m}$. This limitation is caused by the tip radius/shape of each of the actuating needles (for an impression of the μ -plasma printer configuration see the Appendix). It was also verified that the area-selective processing does not affect the material properties as compared to full blanket films. The resistivity of the $\text{In}_2\text{O}_3\text{:H}$ patterns was measured using a four-point probe station on 3 mm wide patterns. In this case the patterns were prepared on a wafer with 450 nm thick thermal SiO_2 and 10 nm a-Si:H. The $\text{In}_2\text{O}_3\text{:H}$ prepared by the *direct-write* ALD process had a resistivity of $0.59 \text{ m}\Omega\cdot\text{cm}$, which corresponds well with results obtained for blanket films.²⁵ In addition the microstructure of the films probed by cross-sectional SEM was found to be comparable to what obtained for blanket films (Figure 4.A4).

As mentioned in the introduction, the selectivity of the $\text{In}_2\text{O}_3\text{:H}$ ALD process is stemming from the fact that very long nucleation delays are obtained on H-terminated surfaces of silicon materials whereas the nucleation delay on oxide surfaces is considerably shorter as shown in Figure 4.4.²⁵

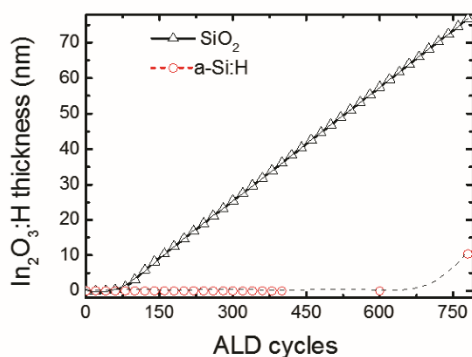
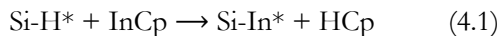


Figure 4.4. Film thickness measured by *in situ* SE as a function of the $\text{In}_2\text{O}_3\text{:H}$ ALD cycles on SiO_2 (open triangles) and on a-Si:H (open circles). *Ex-situ* SE measurements were taken only for 600 and 780 ALD cycles on a-Si:H. Above 600 ALD cycles the selectivity of the process appears to degrade.

To elucidate the role of the surface groups during ALD of $\text{In}_2\text{O}_3\text{:H}$, first-principle calculations have been carried out using density functional theory (DFT)^{29,30} with the Perdew–Burke–Ernzerhof (PBE) exchange correlation functional.^{31,32} Van der Waals interactions were also accounted for on an empirical basis.³³ Additional computational details can be found in the Appendix section 4.A4. The structures and associated relative energies have been calculated for the stationary points along the anticipated reaction pathways for the chemisorption of the InCp precursor and proton transfer from the substrate to the Cp ligand of the precursor. This was done for: (1) hydrogenated silicon and (2) hydroxylated silicon oxide surfaces, as these are expected to represent the H-terminated and plasma activated surfaces to a good approximation.

The reactions considered are therefore:



where the asterisks indicate the surface species involved in the reactions.

Figure 4.5 shows the corresponding energies obtained by the DFT calculations. The results reveal that reaction (4.1) is endothermic and requires an energy input of 0.31 eV to proceed, with associated activation energy of 0.36 eV. For reaction (4.2) the activation energy of 0.28 eV is slightly lower and in contrast to reaction (4.1), the overall process is exothermic.

Based on the Arrhenius equation, assuming the pre-factor is similar in magnitude for both surface reactions, this difference in activation energies translates into a ~ 13 -fold higher rate for reaction (4.2) in comparison to reaction (4.1) at the ALD temperature of 100 °C. Moreover, the proton transfer reaction for reaction (4.2) is exothermic and releases energy (0.30 eV). By contrast, reaction (4.1) requires an energy intake of 0.31 eV to take place, such that reaction (4.2) likely proceeds with a much higher probability.³⁴

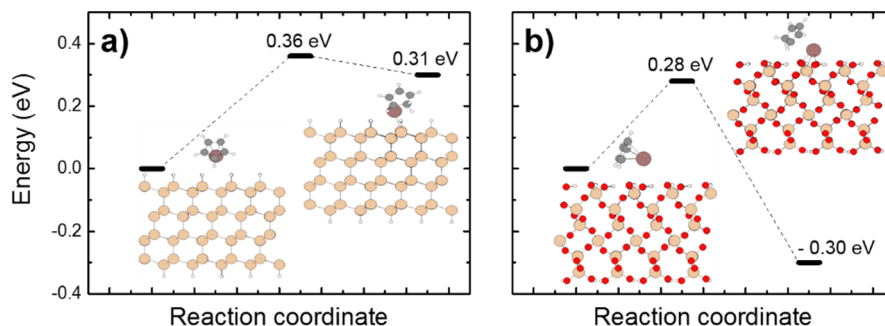


Figure 4.5. Energy profiles computed by DFT method (PBE-D3) for the chemisorption of InCp on **a)** hydrogenated silicon (Si-H termination) and **b)** on hydroxylated silicon oxide (Si-OH termination).

The predicted reaction energies therefore point to the thermodynamically favored nature of InCp binding on the hydroxylated SiO₂ surface as opposed to the H-terminated silicon. This can explain the high selectivity that can be reached for the area-selective ALD process of In₂O₃:H on activated and non-activated surfaces of H-terminated silicon materials.

4.4 Conclusions

In conclusion, a novel *direct-write* ALD process has been demonstrated for $\text{In}_2\text{O}_3:\text{H}$, a highly relevant TCO material. By combining local activation of H-terminated surfaces of silicon materials by a μ -plasma printer and area-selective ALD of $\text{In}_2\text{O}_3:\text{H}$, microscale patterns can be generated in a true bottom-up process. Excellent selectivity and low resistivity of the $\text{In}_2\text{O}_3:\text{H}$ were demonstrated. The method therefore provides bright prospects for large-area applications because both the μ -plasma printing and the area-selective ALD process are scalable. Large-area applications employing flexible substrates such as OLED displays and flexible photovoltaics are of particular interest due to the current trend towards printing technology and roll-to-roll ALD processes.^{35–37} Therefore, as a first demonstrator, the *direct-write* ALD process was employed on a flexible stainless steel foil with 20 nm thick a-Si:H as is shown in Figure 4.6. Transferring the technology to printing on flexible substrates combined with spatial ALD processes will be the next steps. Also the extension of the process to other substrate materials and ALD materials systems will be considered. Other ALD precursors that undergo similar surface reactions can possibly also be used to develop area-selective ALD in a few cases.^{28,34,38} Finally, we note that preliminary investigations using a focused electron beam have yielded promising results with respect to the extension of the current *direct-write* ALD process of $\text{In}_2\text{O}_3:\text{H}$ towards nanoscale dimensions.

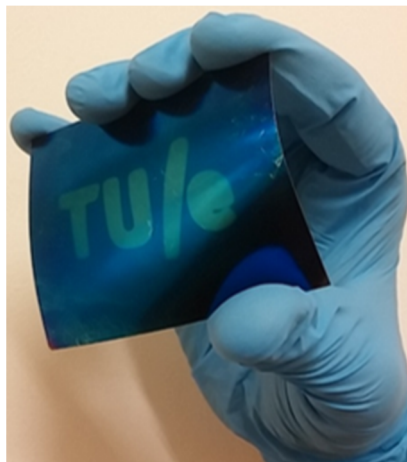


Figure 4.6. Eindhoven University of Technology (TU/e) logo created by *direct-write* ALD of a 35 nm thick $\text{In}_2\text{O}_3:\text{H}$ film on a flexible stainless steel foil covered with 20 nm of a-Si:H. This serves as a first demonstrator of the capability of the *direct-write* ALD process for large-area and flexible electronics.

REFERENCES

- (1) Hua, Y.; King, W. P.; Henderson, C. L. Nanopatterning Materials Using Area Selective Atomic Layer Deposition in Conjunction with Thermochemical Surface Modification via Heated AFM Cantilever Probe Lithography. *Microelectron. Eng.* **2008**, *85*, 934–936.
- (2) Mackus, A. J. M.; Bol, A. A.; Kessels, W. M. M. The Use of Atomic Layer Deposition in Advanced Nanopatterning. *Nanoscale* **2014**, (2011), 10941–10960.
- (3) Kim, W.; Lee, H.; Heo, K.; Lee, K.; Chung, T.; Kim, G.; Hong, S.; Heo, J.; Kim, H. Atomic Layer Deposition of Ni Thin Films and Application to Area-Selective Deposition. *J. Electrochem. Soc.* **2011**, *158*, D1–D5.
- (4) Kim, W.-H.; Minaye Hashemi, F. S.; Mackus, A. J. M.; Singh, J.; Kim, Y.; Bobb-Semple, D.; Fan, Y.; Kaufman-Osborn, T.; Godet, L.; Bent, S. F. A Process for Topographically Selective Deposition on 3D Nanostructures by Ion Implantation. *ACS Nano* **2016**, *10*, 4451–4458.
- (5) Sinha, A.; Hess, D. W.; Henderson, C. L. Area-Selective ALD of Titanium Dioxide Using Lithographically Defined Poly(methyl Methacrylate) Films. *J. Electrochem. Soc.* **2006**, *153*, G465–G469.
- (6) Jeong, H. S.; Jeon, H.-J.; Kim, Y. H.; Oh, M. B.; Kumar, P.; Kang, S.-W.; Jung, H.-T. Bifunctional ITO Layer with a High Resolution, Surface Nano-Pattern for Alignment and Switching of LCs in Device Applications. *NPG Asia Mater.* **2012**, *4*, e7.
- (7) Tandon, N.; Marsano, A.; Maidhof, R.; Numata, K.; Montouri-Sorrentino, C.; Cannizzaro, C.; Voldman, J.; Vunjak-Novakovic, G. Surface-Patterned Electrode Bioreactor for Electrical Stimulation. *Lab Chip* **2010**, *10*, 692–700.
- (8) Kim, S. H.; Yamamoto, T.; Fourmy, D.; Fujii, T. Electroactive Microwell Arrays for Highly Efficient Single-Cell Trapping and Analysis. *Small* **2011**, *7*, 3239–3247.
- (9) Xiao, S.; Fernandes, S. A.; Ostendorf, A. Selective Patterning of ITO on Flexible PET Substrate by 1064nm Picosecond Laser. *Phys. Procedia* **2011**, *12*, 125–132.
- (10) Breen, T. L.; Fryer, P. M.; Nunes, R. W.; Rothwell, M. E. Patterning Indium Tin Oxide and Indium Zinc Oxide Using Microcontact Printing and Wet Etching. *Langmuir* **2002**, *18*, 194–197.
- (11) Chae, J.; Jang, L.; Jain, K. High-Resolution, Resistless Patterning of Indium-Tin-Oxide Thin Films Using Excimer Laser Projection Annealing Process. *Mater. Lett.* **2010**, *64*, 948–950.
- (12) Choi, H. W.; Farson, D. F.; Bovatsek, J.; Arai, a; Ashkenasi, D. Direct Write Patterning of Indium-Tin-Oxide Film by High Pulse Repetition Frequency Femtosecond Laser Ablation. *Appl. Opt.* **2007**, *46*, 5792–5799.
- (13) Pang, C. Efficiency Enhancement of Polymer Solar Cells. *J. Nanosci. Nanotechnol.* **2008**, *8*, 5279–5283.
- (14) Wang, J.; Li, W.; Wang, C. Improving Light Outcoupling Efficiency for OLEDs with Microlens Array Fabricated on Transparent Substrate. *J. Nanomater.* **2014**, 289752.
- (15) Chae, J.; Appasamy, S.; Jain, K. Patterning of Indium Tin Oxide by Projection Photoablation and Lift-off Process for Fabrication of Flat-Panel Displays. *Appl. Phys. Lett.* **2007**, *90*, 1–3.
- (16) Harrison, P. M.; Wendland, J.; Henry, M. Innovative Laser Patterning of Black Matrix for LCD Manufacture Top Ablation Air. *Proc. SID Int. Symp. Dig. Tech. Pap. Soc. Inf. Disp.* **2008**, *39*, 737–739.
- (17) Faraz, T.; Roozeboom, F.; Knoops, H. C. M.; Kessels, W. M. M. Atomic Layer Etching: What Can We Learn from Atomic Layer Deposition? *ECS J. Solid State Sci. Technol.* **2015**, *4*, N5023–N5032.
- (18) Mackus, A. J. M.; Dielissen, S. A. F.; Mulders, J. J. L.; Kessels, W. M. M. Nanoscale Nanopatterning by Direct write Atomic Layer Deposition. *Nanoscale* **2012**, *4*, 4477–4480.
- (19) Färm, E.; Lindroos, S.; Ritala, M.; Leskelä, M. Microcontact Printed RuOx Film as an Activation Layer for Selective-Area Atomic Layer Deposition of Ruthenium. *Chem. Mater.* **2011**, *24*, 275–278.
- (20) Chen, R.; Bent, S. F. Chemistry for Positive Pattern Transfer Using Area-Selective Atomic Layer Deposition. *Adv Mater* **2006**, *18*, 1086–1090.
- (21) Chen, R.; Kim, H.; McIntyre, P. C.; Porter, D. W.; Bent, S. F. Achieving Area-Selective Atomic Layer Deposition on Patterned Substrates by Selective Surface Modification. *Appl. Phys. Lett.* **2005**, *86*, 1–3.
- (22) Mackus, A. J. M.; Mulders, J. J. L.; Van De Sanden, M. C. M.; Kessels, W. M. M. Local Deposition of High-Purity Pt Nanostructures by Combining Electron Beam Induced Deposition and Atomic Layer

- Deposition. *J. Appl. Phys.* **2010**, *107*, 107–109.
- (23) Macco, B.; Wu, Y.; Vanhemel, D.; Kessels, W. M. M. High Mobility In₂O₃:H Transparent Conductive Oxides Prepared by Atomic Layer Deposition and Solid Phase Crystallization. *Phys. Status Solidi - Rapid Res. Lett.* **2014**, *8*, 987–990.
- (24) Schalken, J. R. G.; Creatore, M.; Verhoeven, P.; Stevens, A. Micro-PlasmaPrinting Deposition of Amine-Containing Organo-Silane Polymers by Means of 3-Aminopropyl Trimethoxysilane. *Nanosci. Nanotechnol. Lett.* **2015**, *7*, 62–66.
- (25) Kuang, Y.; Macco, B.; Karasulu, B.; Ande, C. K.; Bronsveld, P. C. P.; Verheijen, M. A.; Wu, Y.; Kessels, W. M. M.; Schropp, R. Towards the Implementation of Atomic Layer Deposition In₂O₃:H in Silicon Heterojunction Solar Cells. *Sol. Energy Mater. Sol. Cells* **2017**, *163*, 43–50.
- (26) Macco, B.; Knoops, H. C. M.; Kessels, W. M. M. Electron Scattering and Doping Mechanisms in Solid-Phase-Crystallized In₂O₃:H Prepared by Atomic Layer Deposition. *ACS Appl. Mater. Interfaces* **2015**, *7*, 16723–16729.
- (27) Libera, J. A.; Hryn, J. N.; Elam, J. W. Indium Oxide Atomic Layer Deposition Facilitated by the Synergy between Oxygen and Water. *Chem. Mater.* **2011**, *23*, 2150–2158.
- (28) Michalak, D. J.; Amy, S. R.; Aureau, D.; Dai, M.; Estève, A.; Chabal, Y. J. Nanopatterning Si(111) Surfaces as a Selective Surface-Chemistry Route. *Nat. Mater.* **2010**, *9*, 266–271.
- (29) Hohenberg, P. Inhomogeneous Electron Gas. *Phys. Rev.* **1964**, *136*, B864–B871.
- (30) Kohn, W.; Sham, L. J. Self-Consistent Equations Including Exchange and Correlation Effects. *Phys. Rev.* **1965**, *140*, A1133–A1138.
- (31) Perdew, J. P.; Burke, K.; Ernzerhof, M. Generalized Gradient Approximation Made Simple. *Phys. Rev. Lett.* **1996**, *77*, 3865–3868.
- (32) Perdew, J. P.; Burke, K.; Ernzerhof, M. Generalized Gradient Approximation Made Simple. *Phys. Rev. Lett.* **1997**, *78*, 1396–1396.
- (33) Grimme, S.; Antony, J.; Ehrlich, S.; Krieg, H. A Consistent and Accurate Ab Initio Parametrization of Density Functional Dispersion Correction (DFT-D) for the 94 Elements H-Pu. *J. Chem. Phys.* **2010**, *132*, 154104.
- (34) Longo, R. C.; McDonnell, S.; Dick, D.; Wallace, R. M.; Chabal, Y. J.; Owen, J. H. G.; Ballard, J. B.; Randall, J. N.; Cho, K. Selectivity of Metal Oxide Atomic Layer Deposition on Hydrogen Terminated and Oxidized Si(001)-(2×1) Surface. *J. Vac. Sci. Technol. B Microelectron. Nanom. Struct.* **2014**, *32*, 03D112.
- (35) Wong, W. S.; Chabinyc, M. L.; Ng, T.-N.; Salleo, A. *Materials and Novel Patterning Methods for Flexible Electronics*; Wong, W. S., Salleo, A., Eds; Springer: New York, **2009**.
- (36) Kessels, W. M. M.; Putkonen, M. Advanced Process Technologies: Plasma, Direct-Write, Atmospheric Pressure, and Roll-to-Roll ALD. *MRS Bull.* **2011**, *36*, 907–913.
- (37) Petti, L.; Munzenrieder, N.; Vogt, C.; Faber, H.; Buthe, L.; Cantarella, G.; Bottacchi, F.; Anthopoulos, T. D.; Troster, G. Metal Oxide Semiconductor Thin-Film Transistors for Flexible Electronics. *Appl. Phys. Rev.* **2016**, *3*, 1–53.
- (38) Thissen, P.; Peixoto, T.; Longo, R. C.; Peng, W.; Schmidt, W. G.; Cho, K.; Chabal, Y. J. Activation of Surface Hydroxyl Groups by Modification of H-Terminated Si(111) Surfaces. *J. Am. Chem. Soc.* **2012**, *134*, 8869–8874.

Appendix

Area-Selective Atomic Layer Deposition of $\text{In}_2\text{O}_3\text{:H}$ Using a μ -Plasma Printer for Local Area-Activation

4.A1 Patterning Capabilities of the μ -Plasma Printer

The μ -plasma printer consists of two rows of twelve needles that can be individually actuated on the substrate. The substrate holder is kept at high voltage and the plasma is ignited as one or more needles pass a certain threshold distance when moving down to the substrate. This distance is defined by the Paschen curve, for a specific voltage and feeding gas.¹ As shown in Figure 4.A1 (a), in case of conductive substrates, a 260 μm thick Al_2O_3 dielectric membrane layer is used between the needles and the substrate. The patterning capabilities of the μ -plasma printer were investigated using three active needle combinations to pattern lines which are 3.0, 0.8 and 0.6 mm in width. This is done by actuating 12, 4 and 3 needles for each row, respectively, yielding the result in Figure 4.A1 (b). Since the size of single plasma filament generated from one needle is approximately 200 μm , the smallest pattern achievable in the current configuration of the μ -plasma printer is of approximately this dimension.^{2,3}

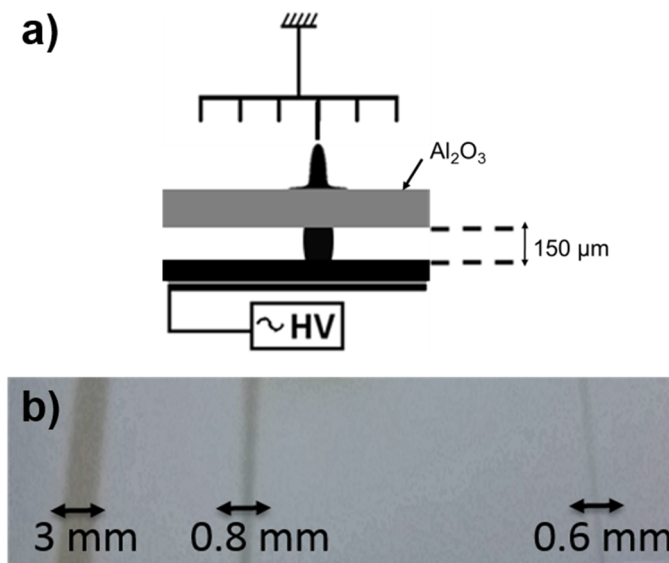


Figure 4.A1: a) Schematic of the μ -plasma printer head working principle. When a needle is actuated a μ -discharge is ignited. For conductive substrates, a thin Al_2O_3 membrane is placed at $150\ \mu\text{m}$ from the substrate. b) Photograph of $\text{In}_2\text{O}_3\text{:H}$ lines of 3.0, 0.8 and 0.6 mm wide prepared by the *direct-write* ALD process using 400 cycles.

The ultimate patterning resolution of the μ -plasma printer was found to be dependent on the gas supply composition and the number of passes (print repeats). In particular, the latter was found to have an influence on the pattern width and on the $\text{In}_2\text{O}_3\text{:H}$ nucleation as well. The width of the patterns was found to increase nonlinearly with the number of print repeats. It is believed that this effect is related to the diffusion and the lifetime of the radical species produced during the discharge. Furthermore, the resolution can be influenced by the applied voltage and the distances between the μ -plasma printer head, the substrate and dielectric membrane layer. More information can be found in reference 24 of Chapter 4.

4.A2 Selectivity of $\text{In}_2\text{O}_3\text{:H}$ on a-Si:H and a-SiN_x:H

A large part of the study presented here has been carried out on a-Si:H starting surfaces for which the selectivity of the *direct-write* process has been investigated by XPS line scan measurements (XPS spot size is $400\ \mu\text{m}$). For completeness, Figure 4.A2 (a) shows the atomic percentages of all species present on the surface after 400 cycles of area-selective ALD $\text{In}_2\text{O}_3\text{:H}$ on a-Si:H surface. We also investigated the suitability of a-SiN_x:H as a

substrate for achieving area-selective ALD of $\text{In}_2\text{O}_3\text{:H}$. In this case 200 ALD cycles were used to grow $\text{In}_2\text{O}_3\text{:H}$ on the area activated using an O_2 μ -plasma printer. An XPS line scan from the $\text{In}_2\text{O}_3\text{:H}$ pattern to the non-treated a- $\text{SiN}_x\text{:H}$ area was conducted to evaluate the selectivity. Figure 4.A2 (b) shows that $\text{In}_2\text{O}_3\text{:H}$ was deposited only on the activated area, whereas moving away from the pattern an increase in Si and N signals confirms that on the non-activated area no $\text{In}_2\text{O}_3\text{:H}$ can be detected after 200 ALD cycles. This confirms that area-selective ALD of $\text{In}_2\text{O}_3\text{:H}$ can also be carried out on a- $\text{SiN}_x\text{:H}$ starting surfaces.

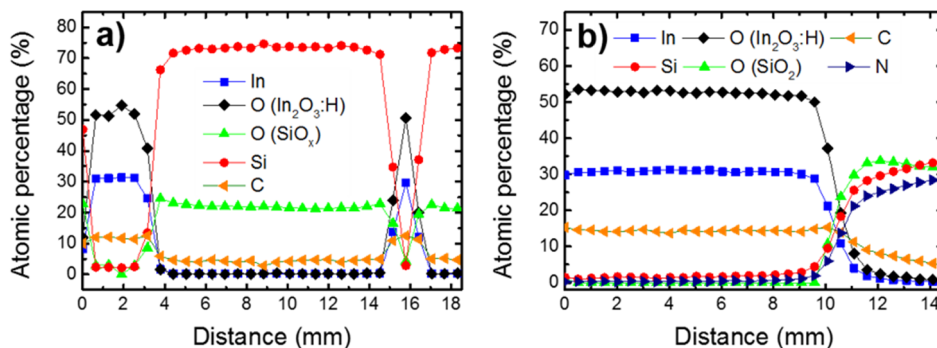


Figure 4.A2: XPS surface line scans for area-selective ALD of $\text{In}_2\text{O}_3\text{:H}$ prepared by the *direct-write* ALD process. Different starting surfaces and numbers of ALD cycles were used: **a)** 10 nm of a- Si:H on $\text{Si}(100)$ and 400 ALD cycles; **b)** 20 nm a- $\text{SiN}_x\text{:H}$ on $\text{Si}(100)$ and 200 ALD cycles. Being a surface scan, the carbon (C) is mostly adventitious.

The selectivity was corroborated by current-voltage (I-V) measurements between the letters 'T' and the 'U' of the area-selective ALD grown pattern, which is shown in Figure 4.2a of Chapter 4, and compared with the I-V curve measured within the letter 'U'. The conductivity data represent a good figure of merit for the selectivity and demonstrate the electrical isolation between the patterns, hence the excellent selectivity.

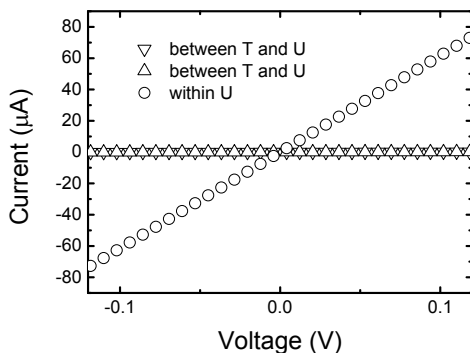


Figure 4.A3: I-V measurements of area-selective ALD $\text{In}_2\text{O}_3\text{:H}$ within the ‘U’ (open circles) and between the ‘T’ and the ‘U’ letters (open triangles) of the pattern reported in Figure 4.2a of Chapter 4. The measurement between the separated patterns was done twice to verify reproducibility.

4.A3 $\text{In}_2\text{O}_3\text{:H}$ crystallinity

In our earlier work it has been shown that the substrate material influences the crystallinity and nuclei formation of In_2O_3 ALD films.⁴ We found that the $\text{In}_2\text{O}_3\text{:H}$ is polycrystalline when prepared at 100 °C on a blank a-Si:H surface after O_2 plasma activation. Consistently, polycrystalline $\text{In}_2\text{O}_3\text{:H}$ was also observed in the case of the area-selective process, as shown in Figure 4.A4.

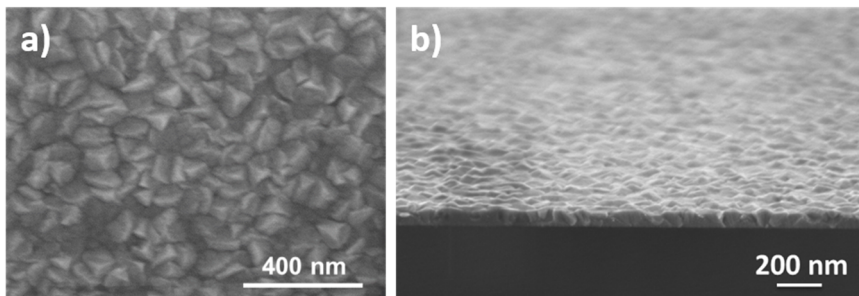


Figure 4.A4: a) Plan view and b) cross-sectional SEM images of 75 nm thick $\text{In}_2\text{O}_3\text{:H}$ prepared by the *direct-write* ALD process using 780 ALD cycles. The $\text{In}_2\text{O}_3\text{:H}$ pattern was 3 mm wide and was prepared on Si(100) with 10 nm a-Si:H on top.

4.A4 Computational Methods

All electronic structure calculations were done using the projector augmented wavefunction (PAW)^{5,6} as implemented in Vienna Ab Initio Simulation Package (VASP v.5.3.5).^{7–10} We used the generalized gradient approximation (GGA) to density functional theory (DFT)^{11,12} jointly with a plane-wave basis having a kinetic energy cutoff of 400 eV. We employed the Perdew–Burke–Ernzerhof (PBE) exchange correlation functional^{13,14} along with the Grimme’s DFT(PBE)-D3 method including Becke-Jonson damping¹⁵ to account for Van der Waals interactions on an empirical basis. We note that a non-local density functional that explicitly treats the pairwise non-bonded interactions (e.g. optB88-VdW, VdW-DF/2, etc.) is expected to predict more accurate binding energies for aromatic systems like InCp, as previously demonstrated for graphene.¹⁶ However, detailed benchmarks show that the empirical method (e.g. DFT-D3) can successfully reproduce the qualitative picture predicted by VdW-DF for a lower computational cost.^{17,18} We also considered the spin-polarized formalism to account for the possible radical pairs created during the detachment of Cp. Structural relaxations were carried out using the conjugate gradient algorithm, where they were considered converged once all forces deviate less than 0.01 eV Å⁻¹ in two consecutive ionic steps. Besides, we used the default accuracy parameters for the FFT grid and real space projectors alongside a Gaussian smearing of 0.1 eV. Minimum energy paths (MEPs) along the predefined reaction pathways connecting a reactant-product pair were computed by optimizing several geometries collectively with the climbing-image nudge elastic band (CI-NEB) method.¹⁹ CI-NEB optimizations were done with a looser convergence criterion on forces (0.1 eV Å⁻¹) utilizing the Hessian-based (G)-LBFGS²⁰ and FIRE²¹ algorithms as implemented in VTST tool set.²² In order to accommodate an InCp precursor on a given surface and to minimize the resulting interactions via periodic boundary conditions, supercells were kept rather large in the xy plane. Likewise, for avoiding the image interactions, the slabs in each prepared model system were separated along the z-axis by a vacuum thickness of 15 Å or more. We considered the 18 layer model for the hydroxylated SiO₂ as suggested in a previous study.²³ Due to their large size, the supercells could be integrated in reciprocal-space with only one k-point centered on the Γ -point. Relevantly, all of the supercells considered here are optimized in terms of size and shape using a rather large kinetic energy cutoff of 520 eV, only containing the silicon or SiO₂ surfaces. Optimized supercells are later used in the simulations of InCp binding on the relevant surfaces. We computed the binding energies of InCp on various silicon surfaces through physisorption (ΔE_p) or chemisorption (ΔE_c) using Eqn. 4.A1.

$$\Delta E_{p/c} = E_{PS} - E_P - E_S \quad (4.A1)$$

where E_{pS} is the total energy of the physisorbed/chemisorbed substrate-precursor complex, E_p and E_S are the total energies of an isolated InCp precursor and a given substrate surface. Here, physisorption can be described as the weak physical (non-covalent) binding of the InCp precursor onto a given silicon surface, whereas the chemisorption requires the chemical (covalent) binding of indium that is likely accompanied by the decomposition of InCp.

REFERENCES

- (1) Paschen, F. Ueber Die Zum Funkenübergang in Luft, Wasserstoff Und Kohlensäure Bei Verschiedenen Drucken Erforderliche Potentialdifferenz. *Ann. Phys.* **1889**, *273*, 69–75.
- (2) Dongen, M.A.H. van, μ Plasma Patterning and Inkjet Printing to Enhance Localized Wetting and Mixing Behaviour, Ph.D. Dissertation, Eindhoven University of Technology, Twente University, 2014.
- (3) Dongen, M. van; Bernards, J.; Niewenhuis, E.; Verkuijlen, R.; Verbraeken, L. μ Plasma Printing of Hydrophobic and Hydrophilic Patterns to Improve Wetting Behaviour for Printed Electronics. *LOPEC Proc. 2012* **2012**, 1–5.
- (4) Wu, Y. Growth, Phase and Doping Control in ZnO and In₂O₃ Thin Films Prepared by Atomic Layer Deposition, Ph.D. Dissertation, Eindhoven University of Technology, 2016.
- (5) Blöchl, P. E. Projector Augmented-Wave Method. *Phys. Rev. B* **1994**, *50*, 17953–17979.
- (6) Kresse, G. From Ultrasoft Pseudopotentials to the Projector Augmented-Wave Method. *Phys. Rev. B* **1999**, *59*, 1758–1775.
- (7) Kresse, G.; Hafner, J. Ab Initio Molecular Dynamics for Liquid Metals. *Phys. Rev. B* **1993**, *47*, 558–561.
- (8) Kresse, G.; Hafner, J. Ab Initio Molecular-Dynamics Simulation of the Liquid-Metal–amorphous-Semiconductor Transition in Germanium. *Phys. Rev. B* **1994**, *49*, 14251–14269.
- (9) Kresse, G.; Furthmüller, J. Efficiency of Ab-Initio Total Energy Calculations for Metals and Semiconductors Using a Plane-Wave Basis Set. *Comput. Mater. Sci.* **1996**, *6*, 15–50.
- (10) Kresse, G. Efficient Iterative Schemes for Ab Initio Total-Energy Calculations Using a Plane-Wave Basis Set. *Phys. Rev. B* **1996**, *54*, 11169–11186.
- (11) Hohenberg, P. Inhomogeneous Electron Gas. *Phys. Rev.* **1964**, *136*, B864–B871.
- (12) Kohn, W.; Sham, L. J. Self-Consistent Equations Including Exchange and Correlation Effects. *Phys. Rev.* **1965**, *140*, A1133–A1138.
- (13) Perdew, J. P.; Burke, K.; Ernzerhof, M. Generalized Gradient Approximation Made Simple. *Phys. Rev. Lett.* **1996**, *77*, 3865–3868.
- (14) Perdew, J. P.; Burke, K.; Ernzerhof, M. Generalized Gradient Approximation Made Simple. *Phys. Rev. Lett.* **1997**, *78*, 1396–1396.
- (15) Grimme, S.; Antony, J.; Ehrlich, S.; Krieg, H. A Consistent and Accurate Ab Initio Parametrization of Density Functional Dispersion Correction (DFT-D) for the 94 Elements H–Pu. *J. Chem. Phys.* **2010**, *132*, 154104.
- (16) Björk, J.; Hanke, F.; Palma, C.-A.; Samori, P.; Cecchini, M.; Persson, M. Adsorption of Aromatic and Anti-Aromatic Systems on Graphene through Π – π Stacking. *J. Phys. Chem. Lett.* **2010**, *1*, 3407–3412.
- (17) Grimme, S. Density Functional Theory with London Dispersion Corrections. *Wiley Interdiscip. Rev. Comput. Mol. Sci.* **2011**, *1*, 211–228.
- (18) Hu, X.; Schuster, J.; Schulz, S. E.; Gessner, T. Simulation of ALD Chemistry of (nBu₃P)₂Cu(acac) and Cu(acac)₂ Precursors on Ta(110) Surface. *Microelectron. Eng.* **2015**, *137*, 23–31.
- (19) Henkelman, G.; Uberuaga, B. P.; Jónsson, H. A Climbing Image Nudged Elastic Band Method for Finding Saddle Points and Minimum Energy Paths. *J. Chem. Phys.* **2000**, *113*, 9901.
- (20) Nocedal, J. Updating Quasi-Newton Matrices with Limited Storage. *Math. Comput.* **1980**, *35*, 773–773.
- (21) Bitzek, E.; Koskinen, P.; Gähler, F.; Moseler, M.; Gumbsch, P. Structural Relaxation Made Simple. *Phys. Rev. Lett.* **2006**, *97*, 1–4.
- (22) VTST tool set for VASP.
- (23) Goumans, T. P. M.; Wander, A.; Brown, W. A.; Catlow, C. R. A. Structure and Stability of the (001) α -Quartz Surface. *Phys. Chem. Chem. Phys.* **2007**, *9*, 2146–2152.

Chapter 5

Area-Selective Atomic Layer Deposition of ZnO by Area-Activation using Electron Beam Induced Deposition*

Area-selective atomic layer deposition (ALD) of ZnO was achieved on SiO₂ seed layer patterns on H-terminated Si substrates, using diethylzinc (DEZ) as the Zn precursor and H₂O as the co-reactant. The selectivity of the ALD process was studied using in-situ spectroscopic ellipsometry (SE) and scanning electron microscopy (SEM) for different deposition temperatures, between 100 and 250 °C. Density functional theory (DFT) calculations were performed to corroborate the experimental results obtained and to provide atomic-level understanding of the underlying surface chemistry. A kinetically hindered proton transfer reaction from the H-terminated Si was conceived to underpin the selectivity exhibited by the ALD process. By independent SE and SEM measurements, the selectivity of the process was found to improve with increasing the deposition temperature. The selectivity was investigated further using transmission electron microscopy and energy dispersive X-ray spectroscopy. We suggest that this trend in selectivity may be due to a strong DEZ or H₂O physisorption on the H-terminated Si at low deposition temperature, which highlights the temperature as an extra knob to improve the selectivity.

5.1 Introduction

The scaling in state-of-the-art device nanofabrication requires ever finer lithographic steps with increasing demands on feature alignment. This scaling poses serious challenges as the features become smaller than what can be patterned with conventional top-down fabrication.¹ Nanopatterning involving area-selective deposition, in particular area-selective atomic layer deposition (ALD), has been identified as a potential solution to aid nano-scale device manufacturing.¹⁻⁴

ALD relies on the self-limiting surface reactions that take place between surface functional groups and vapor-phase precursors. The chemospecific nature of the technique allows precise control of the location where these reactions take place by tailoring the surface chemistry. From a patterning point of view, two main approaches for achieving area-selective ALD can be distinguished:

- (1) area-deactivation, in which a part of the surface is rendered inert toward the ALD process chemistry;⁵ and
- (2) area-activation, where conversely, an inert surface is locally activated to enable a specific ALD chemistry.^{6,7}

*Mameli, A.; Karasulu, B.; Verheijen, M.A.; Barcones, B.; Mackus, A. J. M.; Kessels, W. M. M.; Roozeboom, F. *in preparation for publication*

When no subtractive steps are employed, the latter approach is referred to as direct-write ALD.^{4,7–9} This specifically combines patterning and ALD into a *bottom-up* (i.e. additive) approach. Recently, we have demonstrated an area-selective ALD approach for $\text{In}_2\text{O}_3\text{:H}$ with micrometer scale pattern dimensions, consisting of area-activation using a μ -plasma printer, followed by thermal ALD of $\text{In}_2\text{O}_3\text{:H}$.⁹ This approach relies on the long nucleation delay observed for $\text{In}_2\text{O}_3\text{:H}$ ALD on H- and NH_x -terminated silicon substrate surfaces, when using indium cyclopentadienyl (InCp) precursor and a combination of H_2O and O_2 as co-reactants. Conversely, deposition takes place almost directly on OH-terminated silicon surfaces.¹⁰ High selectivity was demonstrated for this process, and the material properties were shown to be similar to those of the $\text{In}_2\text{O}_3\text{:H}$ deposited on blanket silicon substrates. The high selectivity could be attributed to the thermodynamically unfavorable chemisorption of the precursor, InCp, on the H-terminated surfaces.

In this work, we extend the approach to another metal oxide, i.e. ZnO, which can be considered as a model system for a class of oxides that are technologically relevant for applications in sensing, optoelectronic and memory devices.^{12–15} ZnO was deposited from diethylzinc (DEZ) and H_2O . In this case, the area-activation step has been performed at nanoscale dimensions which aligns with the aforementioned search for new nanopatterning approaches. The combination of the direct-write activation step with the subsequent ALD building step is schematically illustrated in Figure 5.1. In the patterning step, an ultra-thin SiO_2 seed layer is locally deposited using electron beam induced deposition (EBID).¹¹ In this way, nanoscale OH-terminated regions are defined that are reactive toward the ZnO ALD chemistry, as opposed to the H-termination of the starting surface. In the building step, ZnO is grown with digital thickness control on the activated area by alternating the two ALD half-reactions (pulses A and B) in a cyclic fashion.

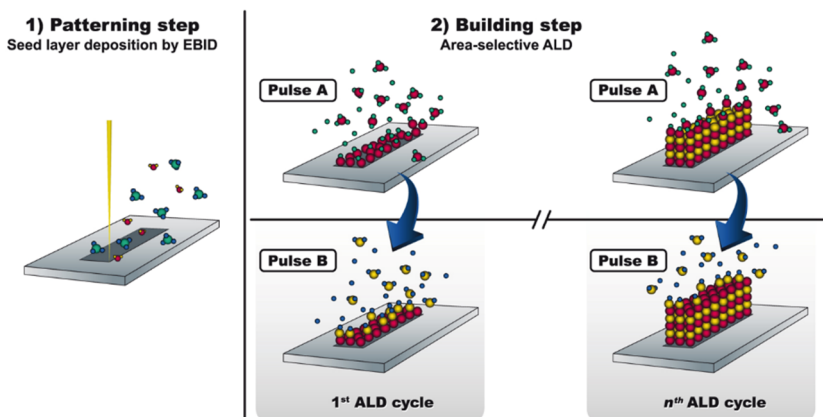


Figure 5.1: Schematic representation of the area-selective ALD approach of ZnO on an H-terminated amorphous silicon layer. First, nanoscale patterns are defined by depositing a SiO_2 seed layer using EBID (patterning step 1). Next, ZnO is deposited selectively on the activated areas (i.e. SiO_2 seed layer patterns) by area-selective ALD (building step 2). This ALD process consists of cycles of two alternating half-reactions: precursor dosing in pulse A and co-reactant dosing in pulse B.

Due to its ability to directly deposit nanostructures with sub-10 nm lateral dimensions without shape constraints, the EBID technique allows to meet the stringent requirements of modern and future device manufacturing in terms of resolution.^{19,20} Furthermore, the EBID technique enables deposition of materials in a direct-write (i.e. no subtractive steps) fashion on various substrates, including polymers.²¹ This unique capability makes it a suitable technique for high-resolution bottom-up patterning of areas consisting of different materials having specific chemical functionalities.

In this Chapter, the key factors that impart selectivity to the ALD process for ZnO are discussed in terms of nucleation delay, as measured by *in-situ* spectroscopic ellipsometry (SE). The selectivity is further elaborated on a molecular-scale level, as corroborated by density functional theory (DFT) calculations. Furthermore, the area-selective ALD was experimentally demonstrated using scanning electron microscopy (SEM) and for the most illustrative sample, using transmission electron microscopy (TEM) cross-section inspection combined with energy dispersive x-ray spectroscopy (EDX) performed in scanning TEM mode. The effect of the deposition temperature on the selectivity (for which a definition is reported in section 5.3.B) between 100 and 200 °C is also studied through a combination of *in-situ* SE and scanning electron microscopy (SEM). The selectivity is found to be higher at high deposition temperatures. Several mechanisms that may play a role in the selectivity loss at lower temperatures will be described.

5.2. Experimental section

5.2.A. Substrate Preparation Method

10 nm thick a-Si:H films were deposited on bare p-type c-Si(100) coupons with native oxide, using inductively-coupled plasma chemical vapor deposition (ICP-CVD) from SiH₄ and Ar at 50 °C.

5.2.B. Patterning Step

After deposition of the a-Si:H starting surfaces, the samples were quickly transferred to the SEM system. Here, localized activation was achieved by depositing an ultra-thin seed layer of SiO₂ using EBID. The nanoscale patterns were generated in an FEI Nova 600 NanoLab DualBeam™ SEM. Tetraethyl orthosilicate (TEOS) was used as the Si-precursor, together with H₂O to generate SiO₂ (with ~26% C impurities) patterns. Both gases were simultaneously fed into the SEM chamber through a Gas Injection System (GIS) at a pressure of 2.5 · 10⁻⁵ mbar. The SiO₂ nanoscale patterns were generated by scanning an electron beam with 2, 5, 10, 15 or 30 kV acceleration voltages and currents between ~0.04 to ~0.14 nA. The volume per dose (i.e. the yield of SiO₂ EBID) was calculated for both 30 and 5 kV by depositing test structures and measuring their volume by SEM inspections. The values thus calculated were used to select settings for deposition of SiO₂ seed layers as thin as ~1 nm for all the accelerating voltages described

above. The best spatial resolution of the seed layer was obtained for acceleration voltages of 15 kV and currents of 0.14 nA, which were therefore used in this work. Right after the patterning step, the samples were transferred to the ALD reactor. The transfer was done within a few minutes in order to minimize possible oxidation and degradation of the H-termination of non-treated the surface of the substrates, due to their exposure to the ambient atmosphere.

5.2.C. ALD Process

For this study a commercial ALD reactor (OpAL™, Oxford Instruments) was used for depositing intrinsic ZnO. Diethylzinc (DEZ) was employed as the zinc precursor and H₂O as the co-reactant. A standard recipe was employed, for which the details can be found elsewhere.²³ The patterned ZnO samples described in this study were prepared using 80 ALD cycles at temperatures ranging from 100 to 250 °C. Deposition temperatures higher than 250 °C were not investigated as the H-termination of the a-Si:H is expected to be stable only for temperatures below 300 °C.⁴¹

The chamber pressure during the ALD process was ~170 mTorr during the 50 ms DEZ pulses and the Ar purges, with a spike of 250 mTorr during the 100 ms H₂O pulses.

5.2.D. Analytical Methods

Nucleation studies were carried out using in-situ spectroscopic ellipsometry (SE), performed with a J.A. Woollam M2000D ellipsometer. Morphology and surface coverage analyses of the ZnO structures prepared by area-selective ALD were carried out in an FEI Nova 600 Nanolab DualBeam™ SEM system using 10 kV and 0.54 nA. The same SEM system was used to prepare a cross-sectional lamella by means of focused ion beam milling. Before the lamella preparation, a protective layer of Al₂O₃ was deposited by thermal ALD using trimethylaluminum and H₂O as the precursor and co-reactant, respectively. Cross-sectional TEM studies were performed in high-angle annular dark-field (HAADF) STEM and in bright-field TEM modes using a probe-corrected TEM system (JEOL JEM ARM 200F) equipped with a 100 mm² Centurio SDD Energy dispersive X-ray spectroscopy (EDX) detector for chemical analysis. TEM studies were employed to assess the selectivity of the process.

5.2.E. Density Functional Theory Methods

All electronic structure calculations were performed using the projector augmented wave function (PAW)^{24,25} as implemented in Vienna *Ab Initio* Simulation Package (VASP v.5.3.5).^{26–28} First-principles calculations were carried out using the generalized gradient approximation (GGA) to the DFT.^{29,30} Perdew–Burke–Ernzerhof (PBE) exchange correlation functional³¹ were employed and the Van der Waals interactions were also accounted for on an empirical basis (PBE-D3).³² Hydroxylated α -SiO₂ clusters were used as approximations of the EBID SiO₂ seed layers and c-Si with native oxide

utilized in the experiments. Accordingly, H-terminated c-Si clusters were employed as approximations of the a-Si:H used in the experiments.⁹ These simulation models of the α -SiO₂ and H-terminated c-Si surfaces have been utilized for studying the precursor adsorption step in similar ALD processes.^{9,10,33} Minimum energy pathways (MEPs) for the chemisorption of a single DEZ precursor molecule on each surface were computed using the climbing-image nudged elastic band (NEB) method,³⁴ as implemented in VASP-VTST tools.³⁵ The same method was used to study the chemisorption of a H₂O molecule on a H-terminated c-Si surface. Further details on model preparations and computations can be found in our previous reports.^{9,10} Binding energies of DEZ or H₂O on various silicon surfaces through physisorption or chemisorption ($\Delta E_{p/c}$) were evaluated using Eqn. 5.1.

$$\Delta E_{p/c} = E_{PS} - E_P - E_S \quad (5.1)$$

where E_{PS} is the total energy of the physisorbed/chemisorbed substrate-precursor complex, E_P and E_S are the total energies of an isolated DEZ precursor and a given substrate surface. Here, physisorption can be described as the weak physical (non-covalent) binding of the DEZ precursor on a given surface, whereas the chemisorption requires the chemical (covalent) bonding of the precursor (or the co-reactant), accompanied by the loss of one of the ligands.

5.3. Results and discussion

5.3.A. ALD of ZnO: nucleation on SiO₂ and a-Si:H

Figure 5.2 shows the ZnO film thickness as a function of the number of ALD cycles, as measured by *in-situ* SE, for a deposition temperature of 100 °C. The nucleation behavior was measured on a freshly deposited ~10 nm a-Si:H film or on c-Si coupons with native oxide (hereinafter referred to as SiO₂), which can be considered as representative for the SiO₂ EBID seed-layers. A relatively long nucleation delay of ~80 cycles was observed on the a-Si:H substrate. After a transient regime,³⁶ linear growth starts with a growth per cycle (GPC) of ~1.6 Å/cycle. Conversely, a very short nucleation delay is observed on SiO₂ before the film growth becomes linear with a GPC of ~1.6 Å/cycle. The results of Figure 5.2 represent a first indication that area-selective ALD of ZnO can be obtained by exploiting the difference in nucleation delays on the two surfaces. Furthermore, the nucleation curves suggest a selectivity window (expressed as the number of ALD cycles for which no deposition is obtained on the a-Si:H) of about 80 ALD cycles before deposition occurs on both surfaces and the selectivity is lost.

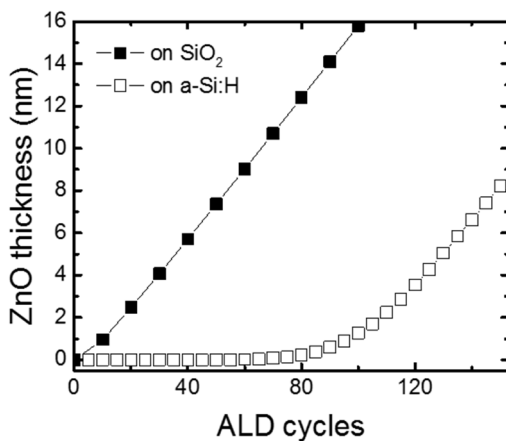
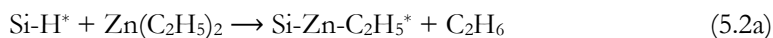


Figure 5.2: ZnO film thickness measured by *in-situ* SE as a function of the number of ALD cycles performed on substrates with a native SiO₂ surface (closed squares) and with a ~10 nm-thick a-Si:H layer (open squares). The ZnO film thickness increases linearly after a short delay of a few cycles on SiO₂, whereas the ZnO deposition experiences a relatively long nucleation delay on a-Si:H. Only after 80 ALD cycles the growth also starts on the a-Si:H and enters a linear regime at about 120 cycles. Both depositions were carried out at 100 °C.

The key reason for the difference in nucleation delay lies in the surface chemistry, because dissimilar surface groups have distinct kinetic barriers towards various thermodynamically favorable end states. Two reaction pathways were proposed to investigate the chemisorption of DEZ on the different surfaces from a theoretical point of view. Using DFT methods, activation and chemisorption energies were therefore calculated for the following reactions:



where the asterisks indicate the relevant surface groups.

DFT calculations indicate that the physisorption of DEZ on both surfaces is exothermic with similar energy gains ($\Delta E_p = -0.37$ eV vs. -0.34 eV, see Figure 5.A1). Figure 5.3 shows the corresponding DFT-based energy profiles connecting the physisorbed and chemisorbed species given in reactions 5.2a and 5.2b. Both reactions are thermodynamically favored, with chemisorption energies of -0.98 and -1.25 eV, respectively. However, an activation energy of 1.16 eV was calculated for reaction 5.2a and 0.81 eV for reaction 5.2b. The difference in energy barriers points toward a more kinetically hindered surface reaction in the case of DEZ on an H-terminated surface. This may explain the difference in nucleation delay observed in Figure 5.2. Assuming the pre-exponential factors in the Arrhenius equation to be similar in magnitude for the

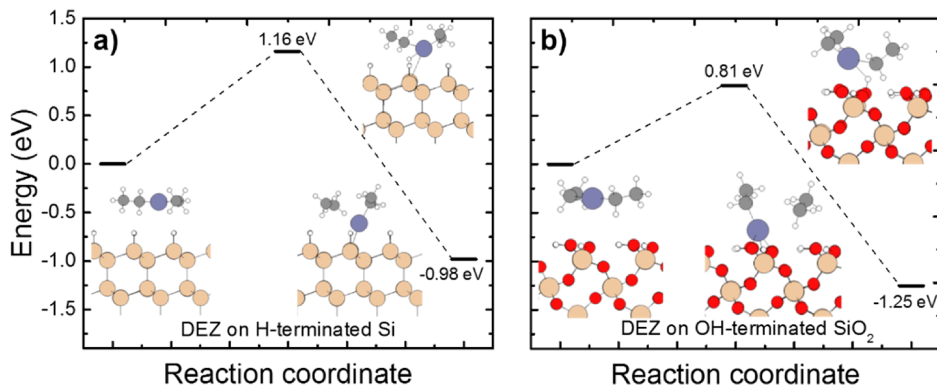


Figure 5.3: DFT/PBE-D3-level energy profiles for the chemisorption of DEZ on **a)** H-terminated Si and **b)** OH-terminated SiO₂. The zero corresponds to the physisorbed states: DEZ on H-terminated Si, $\Delta E_p = -0.37$ eV and on OH-terminated SiO₂ surface, $\Delta E_p = -0.34$ eV, respectively. Color code: light gray: carbon; light orange: silicon; red: oxygen; white: hydrogen; blue: zinc.

two reactions, at 100 °C the difference in kinetic barrier translates into a rate constant $5.4 \cdot 10^4$ times higher on SiO₂ than on a-Si:H.

Since either DEZ or H₂O surface reactions can play a role in the loss of selectivity after a prolonged number of ALD cycles (as shown in Figure 5.2), the reaction energetics of the co-reactant with the H-terminated c-Si was also investigated (see Appendix, Figure 5.A2). H₂O exposure might cause uncontrolled surface activation through parasitic oxidation reactions of the a-Si:H. Figure 5.A2 shows the corresponding DFT energy profile. The oxidation of H-terminated surface by H₂O was found to be a slower process (with an activation energy of 1.49 eV), as compared to the DEZ chemisorption (reaction 5.2a). These findings are in agreement with the well-known stability of H-terminated surfaces towards mild oxidants.^{37–39} Based on these considerations and neglecting other possible effects that in reality may affect the deposition process (e.g., presence of: multiple reaction pathways, surface defects, or impurities), the DFT results suggest that reaction 5.2a forms the limiting step eventually leading to selectivity loss and therefore to the nucleation of ZnO on a-Si:H.

5.3.B. Selectivity at 100 °C

To demonstrate the feasibility of the area-selective ALD method, ALD was performed to deposit ZnO on 500 x 500 nm² SiO₂ EBID patterns that were created on a ~10 nm a-Si:H-coated substrate. Figures 5.4(a,b) show 35 SiO₂ EBID patterns before and after 80 ALD cycles of ZnO at a deposition temperature of 100 °C. ZnO deposition occurred predominantly on the SiO₂ EBID patterns, although some ZnO nucleation was observed outside the patterns, as will be discussed below.

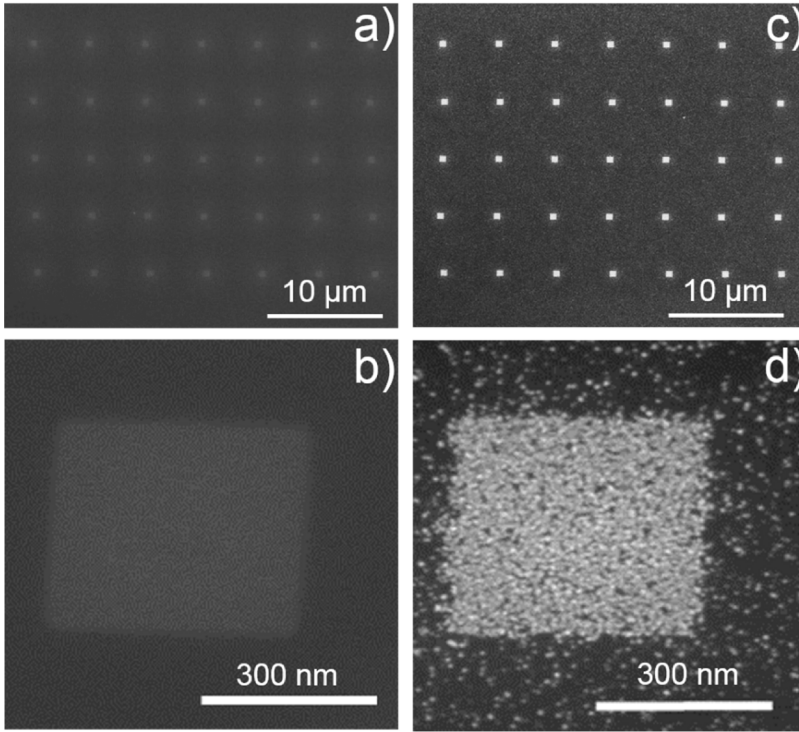


Figure 5.4: a, b) Top-view SEM image of 35 EBID SiO_2 seed layers with an area of $500 \times 500 \text{ nm}^2$ and $\sim 1 \text{ nm}$ thick. The high magnification image in b) shows a single pattern. **c, d)** Top-view SEM image of a similar sample after 80 ALD cycles of ZnO, deposited at $100 \text{ }^\circ\text{C}$. The high magnification image in d) shows a single pattern on which the polycrystalline ZnO is clearly visible.

The selectivity, S , was defined by Gladfelter in the field of area-selective CVD as:⁴⁰

$$S = \frac{N_{GA} - N_{NGA}}{N_{GA} + N_{NGA}} \quad \text{with } 0 \leq S \leq 1 \quad (5.3)$$

Here, N_{GA} is the amount of material deposited (*i.e.* in terms of thickness, coverage, *etc.*) on the surface on which growth should take place, referred to as the growth area (GA). N_{NGA} is the amount of material on the surface on which growth should be inhibited, referred to as the non-growth area (NGA). We note, that the same surface areas (or area-normalized measurements) should be considered when calculating the selectivity. By definition, $S = 1$ for perfectly selective processes and $S = 0$ for non-selective processes.

Using the definition above, the selectivity of the ZnO ALD process was calculated using the thickness as measured by the SE data shown in Figure 5.2 or the coverage as imaged by the SEM in Figure 5.4d. After 80 ALD cycles of ZnO at a deposition temperature of $100 \text{ }^\circ\text{C}$, the selectivity was measured to be 0.96 by SE and 0.83 by SEM.

This difference in selectivity indicates that the SE data can overestimate the selectivity, which might be due to optical modelling as well as to difficulties in modelling a non-continuous film. Nevertheless, SE provides a good first indication of the selectivity and of its changes with the number of ALD cycles. These aspects will be elaborated more in detail below. Furthermore, it should be noted that the EBID grown SiO₂ and the c-Si native oxide may also behave differently, since a high concentration of carbon impurities (~26%) was measured for the SiO₂ deposited by EBID (see Appendix, Figure 5.A3).^{43,44} Such high carbon contents might lead to slightly longer nucleation delays.

5.3.C. Effect of the deposition temperature on selectivity

The temperature dependence of the selectivity was assessed by *in-situ* SE measurements and further corroborated by SEM inspections. This dependence can provide additional insights into the mechanisms leading to selectivity loss after a certain number of ALD cycles. Figure 5.5a shows the evolution of the ZnO thickness as a function of the number of ALD cycles on blanket SiO₂ and a-Si:H samples for deposition temperatures of 100 and 250 °C. A larger nucleation delay is observed for deposition at 250 °C. Figure 5.5b shows the corresponding selectivity as a function of the number of ALD cycles, for 100 and 250 °C. The selectivity was calculated by combining the datasets shown in Figure 5.5a. For a deposition temperature of 100 °C, the selectivity decreases from 1.0 to 0.96 at 80 ALD cycles. By further increasing the number of cycles, the selectivity drops to 0.85 (at 100 cycles), which corresponds to a ZnO thickness of ~1 nm on the non-growth area. For a deposition temperature of 250 °C, the selectivity, S , remains 1 until 110 cycles and then decreases to 0.95 at 140 ALD cycles.

These results clearly show an important aspect concerning the selectivity of this process: the selectivity window can be extended by tuning the deposition temperature. According to the idealized kinetic model described by DFT-calculations in **Section 5.3A**, one would expect the selectivity to increase with decreasing temperature since the chemisorption of DEZ on H-terminated Si surface would be even slower. In contrast, the experimental results demonstrate that selectivity increases with the deposition temperature, thereby highlighting that several other factors may play a role in causing selectivity loss, as discussed below.

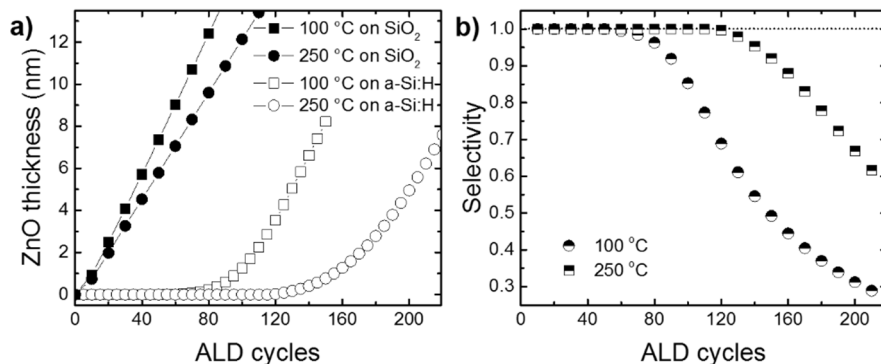


Figure 5.5: a) ZnO nucleation curves on SiO₂ (closed symbols) and a-Si:H (open symbols) as measured by *in-situ* SE for two different temperatures: 100 (square) and 250 °C (circle). b) Selectivity as a function of the number of ALD cycles, for deposition temperatures of 100 °C (square) and 250 °C (circles). The horizontal dotted line at $S = 1$ indicates perfect selectivity.

To further investigate the effect of the temperature, the selectivity was measured for different deposition temperatures, while keeping the number of ALD cycles fixed at 80. In this case, the selectivity was calculated using the ZnO surface coverage in and outside the patterned area, as measured by top-view SEM. Figure 5.6 shows the selectivity after 80 ALD cycles as a function of the deposition temperature, together with the SEM top-view images of the patterns deposited at 100, 150 and 250 °C as insets. The selectivity increases from 0.83 (at 100 °C) to 0.97 (at 150 °C) and 0.99 (at 200 and 250 °C). In other words, the SEM-measured selectivity data confirmed the results obtained with SE: the selectivity increases with the deposition temperature up to 250 °C.

The effect of the temperature on the selectivity has been also reported by McDonnell *et al.* for area-selective ALD of TiO₂ on SiO₂ in presence of H-terminated Si.⁴¹ In their case, for temperatures as low as 30 °C, the selectivity was much lower as compared to those at 100 °C and 150 °C. This was attributed to the presence of physisorbed H₂O, which causes parasitic surface reactions and therefore drastically reduces the selectivity. Recently, trimethylaluminum physisorption has also been identified as the cause of selectivity loss using SAMs as the non-growth area and titanium as the growth area.⁴² Likewise, at decreasing temperature DEZ (or H₂O) molecules may remain physisorbed on the surface and cause undesired (CVD-regime) side reactions. This may also explain our experimentally observed selectivity shift with deposition temperature.

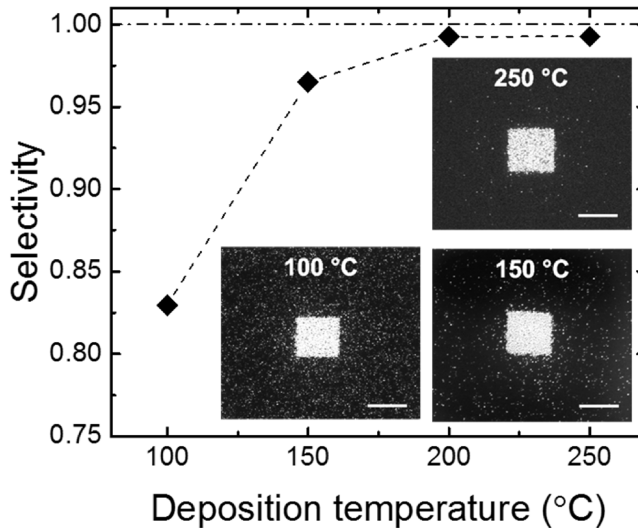


Figure 5.6: Selectivity for 80 ZnO ALD cycles as a function of the deposition temperature. The insets show the top view SEM images of patterns realized using the same EBID parameters and number of ALD cycles, but different ZnO growth temperatures (100, 150 and 250 °C); scale bars are 500 nm. The horizontal dotted line at $S = 1$ indicates perfect selectivity.

5.3.D. Evidence of area-selective ALD by cross-sectional TEM analysis

Area-selective deposition was further investigated by cross-sectional TEM analysis of a pattern similar to those shown in the insets of Figure 5.6. Figure 5.7a shows an HAADF-STEM cross-section image of a ~ 1 nm thick SiO_2 EBID layer with a ~ 7 nm thick ZnO layer deposited by area-selective ALD using 80 ALD cycles at a deposition temperature of 250 °C. In Figures 5.7 a-b, low magnification images clearly show that ZnO deposition took place only on the activated area, *i.e.* the SiO_2 seed layer. To further prove this, high-magnification images were taken from the central area of the pattern, and from the region 250 nm away from this area (Figures 5.7c-d). Figures 5.7(e-f) present the EDX elemental mappings of the pattern shown in the corresponding TEM images, which confirm the presence of Zn on the activated area. No Zn could be detected in the regions outside the SiO_2 EBID pattern, clearly demonstrating the good selectivity of the ALD process.

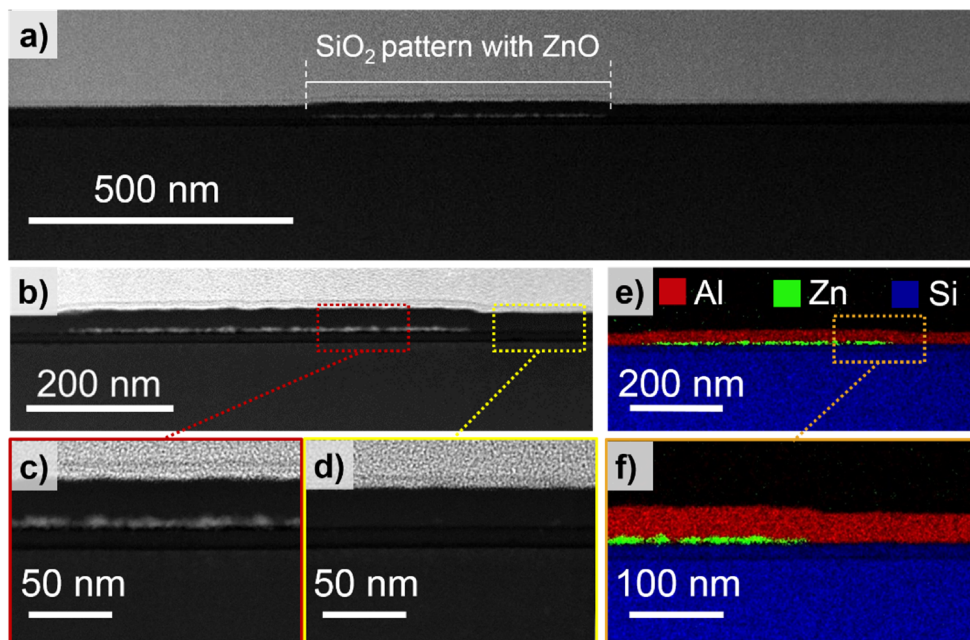


Figure 5.7: a-b) Cross-sectional TEM images of a ZnO thin film that was selectively deposited (using 80 ALD cycles) on a ~ 1 nm thick SiO_2 EBID pattern with a width of ~ 500 nm. The images show a pristine non-growth area outside the patterned growth area, indicating that no ZnO deposition occurred on these surfaces. **c)** High magnification images showing the patterned growth area and **d)** a region 250 nm away from the pattern, confirming the selectivity of the process. **e-f)** EDX elemental mappings of the same pattern at two different magnifications also show the presence of ZnO on the SiO_2 growth area and the absence of ZnO on the a-Si:H non-growth area.

5.4. Conclusions

We demonstrated a *bottom-up* patterning process at the nanoscale involving area-selective ALD of ZnO with good selectivity on SiO_2 with respect to H-terminated silicon. This process exploits the direct-write patterning capabilities of EBID to locally activate H-terminated surfaces, by the deposition of SiO_2 seed layers. Considering a defect-free H-terminated c-Si surface model, the energetics of the surface reactions were calculated by DFT methods. The results suggest that the selectivity originates from a kinetically-limited surface reaction between the DEZ precursor and an H-terminated Si surface, with respect to the same reaction on an OH-terminated SiO_2 surface.

Based on this model, the chemisorption of the H_2O co-reactant was calculated to be a much slower process. Thus it can be inferred that, at a fixed deposition temperature, the limiting step that causes selectivity loss is the DEZ precursor chemisorption on H-terminated Si. From these modelling results it can be stressed that reaction kinetics play a key role in controlling selectivity during ALD.

Experimentally, we observed that increasing the deposition temperature plays a significant role in improving the selectivity of the process. Here, we suggest that

physisorption of DEZ or H₂O at low temperatures can contribute in hampering high selectivity. Improving the selectivity remains a challenging problem since multiple processes (kinetics, physisorption, etc.) can cause effects in opposite directions. These results demonstrate that opposite effects can play a role in determining the selectivity and more detailed investigations are required to find the optimum deposition conditions for achieving high selectivity.

REFERENCES

- (1) Fang, M.; Ho, J. C. Area-Selective Atomic Layer Deposition: Conformal Coating, Subnanometer Thickness Control, and Smart Positioning. *ACS Nano* **2015**, *9*, 8651–8654.
- (2) Minaye Hashemi, F. S.; Prasittichai, C.; Bent, S. F. Self-Correcting Process for High Quality Patterning by Atomic Layer Deposition. *ACS Nano* **2015**, *9*, 8710–8717.
- (3) Kim, W.-H.; Minaye Hashemi, F. S.; Mackus, A. J. M.; Singh, J.; Kim, Y.; Bobb-Semple, D.; Fan, Y.; Kaufman-Osborn, T.; Godet, L.; Bent, S. F. A Process for Topographically Selective Deposition on 3D Nanostructures by Ion Implantation. *ACS Nano* **2016**, *10*, 4451–4458.
- (4) Mackus, A. J. M.; Bol, A. A.; Kessels, W. M. M. The Use of Atomic Layer Deposition in Advanced Nanopatterning. *Nanoscale* **2014**, *6*, 10941–10960.
- (5) Chen, R.; Bent, S. F. Chemistry for Positive Pattern Transfer Using Area-Selective Atomic Layer Deposition. *Adv Mater* **2006**, *18*, 1086–1090.
- (6) Färm, E.; Lindroos, S.; Ritala, M.; Leskelä, M. Microcontact Printed RuO_x Film as an Activation Layer for Selective-Area Atomic Layer Deposition of Ruthenium. *Chem. Mater.* **2011**, *24*, 275–278.
- (7) Mackus, A. J. M.; Mulders, J. J. L.; Van De Sanden, M. C. M.; Kessels, W. M. M. Local Deposition of High-Purity Pt Nanostructures by Combining Electron Beam Induced Deposition and Atomic Layer Deposition. *J. Appl. Phys.* **2010**, *107*, 107–109.
- (8) Mackus, A. J. M.; Dielissen, S. A. F.; Mulders, J. J. L.; Kessels, W. M. M. Nanopatterning by Direct-Write Atomic Layer Deposition. *Nanoscale* **2012**, *4*, 4477–4480.
- (9) Mamei, A.; Kuang, Y.; Aghaee, M.; Ande, C. K.; Karasulu, B.; Creatore, M.; Mackus, A. J. M.; Kessels, W. (Erwin) M. M.; Roozeboom, F. Area-Selective Atomic Layer Deposition of In₂O₃:H Using a μ -Plasma Printer for Local Area Activation. *Chem. Mater.* **2017**, *29*, 921–925.
- (10) Kuang, Y.; Bart, M.; Karasulu, B.; Ande, C. K.; Bronsveld, P.; Verheijen, M. A.; Wu, Y.; Kessels, W. M. M.; Schropp, R. Towards the Implementation of Atomic Layer Deposition In₂O₃:H in Silicon Heterojunction Solar Cells. *Sol. Energy Mater. Sol. Cells* **2017**, *163*, 43–50.
- (11) Utke, I.; Hoffmann, P.; Melngailis, J. Gas-Assisted Focused Electron Beam and Ion Beam Processing and Fabrication. *J. Vac. Sci. Technol. B Microelectron. Nanom. Struct.* **2008**, *26*, 1197.
- (12) Sun, K.; Zeimpekis, I.; Hu, C.; Ditshego, N. M. J.; Thomas, O.; De Planque, M. R. R.; Chong, H. M. H.; Morgan, H.; Ashburn, P. Low-Cost Top-down Zinc Oxide Nanowire Sensors through a Highly Transferable Ion Beam Etching for Healthcare Applications. *Microelectron. Eng.* **2016**, *153*, 96–100.
- (13) Suresh, V.; Huang, M. S.; Srinivasan, M. P.; Krishnamoorthy, S. In Situ Synthesis of High Density Sub-50 Nm ZnO Nanopatterned Arrays Using Diblock Copolymer Templates. *ACS Appl. Mater. Interfaces* **2013**, *5*, 5727–5732.
- (14) Bauermann, L. P.; Gerstel, P.; Bill, J.; Walheim, S.; Huang, C.; Pfeifer, J.; Schimmel, T. Templated Self-Assembly of ZnO Films on Monolayer Patterns with Nanoscale Resolution. *Langmuir* **2010**, *26*, 3774–3778.
- (15) Chevalier-César, C.; Nomenyo, K.; Romyantseva, A.; Gokarna, A.; Gwiazda, A.; Léronnel, G. Direct Holographic Patterning of ZnO. *Adv. Funct. Mater.* **2016**, *26*, 1787–1792.
- (16) Sadat, F.; Hashemi, M.; Prasittichai, C.; Bent, S. F. A New Resist for Area Selective Atomic and Molecular Layer Deposition on Metal – Dielectric Patterns. *J. Phys. Chem. C* **2014**, *118*, 10957–10962.
- (17) Haider, A.; Deminskyi, P.; Khan, T. M.; Eren, H.; Biyikli, N. Area-Selective Atomic Layer Deposition Using Inductively Coupled Plasma Polymerized Fluorocarbon Layer: A Case Study for Metal-Oxides. *J. Phys. Chem. C* **2016**, *120*, 26393–26401.
- (18) Ober, C. K. Directed Self-Assembly: A Dress Code for Block Copolymers. *Nat. Nanotechnol.* **2017**, *12*, 507–508.
- (19) Jesse, S.; Borisevich, A. Y.; Fowlkes, J. D.; Lupini, A. R.; Rack, P. D.; Unocic, R. R.; Sumpter, B. G.; Kalinin, S. V.; Belianinov, A.; Ovchinnikova, O. S. Directing Matter: Toward Atomic-Scale 3D Nanofabrication. *ACS Nano* **2016**, *10*, 5600–5618.
- (20) van Dorp, W. F. Sub-10 Nm Writing: Focused Electron Beam-Induced Deposition in Perspective. *Appl. Phys. A Mater. Sci. Process.* **2014**, *117*, 1615–1622.
- (21) Peinado, P.; Sangiao, S.; De Teresa, J. M. Focused Electron and Ion Beam Induced Deposition on Flexible and Transparent Polycarbonate Substrates. *ACS Nano* **2015**, *9*, 6139–6146.

- (22) Silvis-Cividjian, N.; Hagen, C. W.; Kruit, P. Spatial Resolution Limits in Electron-Beam-Induced Deposition. *J. Appl. Phys.* **2005**, *98*.
- (23) Wu, Y.; Potts, S. E.; Hermkens, P. M.; Knoop, H. C. M.; Roozeboom, F.; Kessels, W. M. M. Enhanced Doping Efficiency of Al-Doped ZnO by Atomic Layer Deposition Using Dimethylaluminum Isopropoxide as an Alternative Aluminum Precursor. *Chem. Mater.* **2013**, *25*, 4619–4622.
- (24) Blöchl, P. E. Projector Augmented-Wave Method. *Phys. Rev. B* **1994**, *50*, 17953–17979.
- (25) Kresse, G. From ultrasoft pseudopotentials to the projector augmented-wave method. *Phys. Rev. B* **1999**, *59*, 1758–1775.
- (26) Kresse, G.; Hafner, J. *Ab Initio* Molecular Dynamics for Liquid Metals. *Phys. Rev. B* **1993**, *47*, 558–561.
- (27) Kresse, G.; Hafner, J. *Ab Initio* Molecular-Dynamics Simulation of the Liquid-Metal–amorphous-Semiconductor Transition in Germanium. *Phys. Rev. B* **1994**, *49*, 14251–14269.
- (28) Kresse, G.; Furthmüller, J. Efficiency of *Ab-Initio* Total Energy Calculations for Metals and Semiconductors Using a Plane-Wave Basis Set. *Comput. Mater. Sci.* **1996**, *6*, 15–50.
- (29) Hohenberg, P. Inhomogeneous Electron Gas. *Phys. Rev.* **1964**, *136*, B864–B871.
- (30) Kohn, W.; Sham, L. J. Self-consistent equations including exchange and correlation effects. *Phys. Rev.* **1965**, *140*, A1133–A1138.
- (31) Perdew, J. P.; Burke, K.; Ernzerhof, M. Generalized Gradient Approximation Made Simple. *Phys. Rev. Lett.* **1997**, *78*, 1396–1396.
- (32) Grimme, S.; Antony, J.; Ehrlich, S.; Krieg, H. A consistent and accurate *ab initio* parametrization of density functional dispersion correction (DFT-D) for the 94 elements H–Pu. *J. Chem. Phys.* **2010**, *132*, 154104.
- (33) Marnett, A.; Merckx, M. J. M.; Karasulu, B.; Roozeboom, F.; Kessels, W. M. M.; Mackus, A. J. M. Area-Selective Atomic Layer Deposition of SiO₂ Using Acetylacetone as a Chemoselective Inhibitor in an ABC-Type Cycle. *ACS Nano* **2017**, *11*, 9303–9311.
- (34) Henkelman, G.; Uberuaga, B. P.; Jonsson, H. A climbing image nudged elastic band method for finding saddle points and minimum energy paths. *J. Chem. Phys.* **2000**, *113*, 9901.
- (35) VTST tool set for VASP.
- (36) Puurunen, R. L.; Vandervorst, W. Island Growth as a Growth Mode in Atomic Layer Deposition: A Phenomenological Model. *J. Appl. Phys.* **2004**, *96*, 7686–7695.
- (37) Michalak, D. J.; Amy, S. R.; Aureau, D.; Dai, M.; Estève, A.; Chabal, Y. J. Nanopatterning Si(111) Surfaces as a Selective Surface-Chemistry Route. *Nat. Mater.* **2010**, *9*, 266–271.
- (38) Kramer, N.; Jorritsma, J.; Birk, H.; Schoenenberger, C. Nanometer Lithography on Silicon and Hydrogenated Amorphous-Silicon with Low-Energy Electrons. *Microelectron. Eng.* **1995**, *27*, 47–50.
- (39) Ikeda, H.; Hotta, K.; Yamada, T.; Zaima, S.; Iwano, H.; Yasuda, Y. Oxidation of H-Terminated Si(100) Surfaces Studied by High-Resolution Electron Energy Loss Spectroscopy. *J. Appl. Phys.* **1995**, *77*, 5125–5129.
- (40) Gladfelter, W. L. Selective Metallization by Chemical-Vapor-Deposition. *Chem. Mater.* **1993**, *5*, 1372–1388.
- (41) McDonnell, S.; Longo, R. C.; Seitz, O.; Ballard, J. B.; Mordt, G.; Dick, D.; Owen, J. H. G.; Randall, J. N.; Kim, J.; Chabal, Y. J.; *et al.* Controlling the Atomic Layer Deposition of Titanium Dioxide on Silicon: Dependence on Surface Termination. *J. Phys. Chem. C* **2013**, *117*, 20250–20259.
- (42) Seo, S.; Oh, I.-K.; Yeo, B. C.; Han, S. S.; Yoon, C. M.; Yang, J. Y.; Yoon, J.; Yoo, C.; Kim, H.; Lee, Y.; *et al.* Reaction Mechanism of Area-Selective Atomic Layer Deposition for Al₂O₃ Nanopatterns. *ACS Appl. Mater. Interfaces* **2017**, *9*, 41607–41617.
- (43) Sánchez, E. J.; Krug, J. T.; Xie, X. S. Ion and Electron Beam Assisted Growth of Nanometric SimOn Structures for near-Field Microscopy. *Rev. Sci. Instrum.* **2002**, *73*, 3901.
- (44) Frabboni, S.; Gazzadi, G. C.; Spessot, A. Transmission Electron Microscopy Characterization and Sculpting of Sub-1 nm Si-O-C Freestanding Nanowires Grown by Electron Beam Induced Deposition. *Appl. Phys. Lett.* **2006**, *89*, 1–4.

Appendix

Area-Selective Atomic Layer Deposition of ZnO by Area-Activation using Electron Beam Induced Deposition

5.A1. Diethylzinc physisorption energetics

Figure 5.A1 shows the physisorption energies of diethylzinc (DEZ) on H-terminated Si and OH-terminated SiO₂, as calculated by DFT. It should be noted that Van der Waals interactions were accounted for on an empirical basis, which decreases the accuracy of the physisorbed state. Furthermore, the DFT models consider crystalline surfaces whereas amorphous surfaces are employed for the ALD experiments.

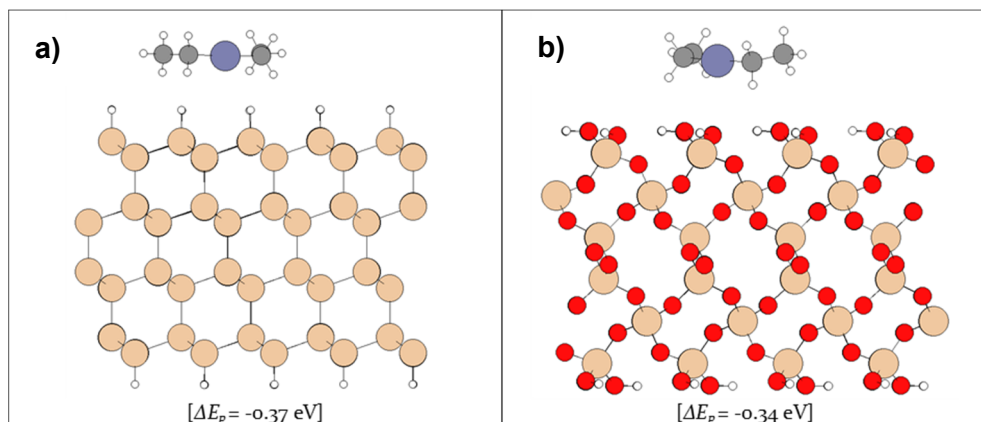
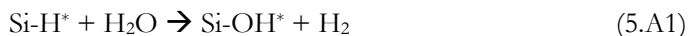


Figure 5.A1: DFT/PBE-D3 level optimized geometries of the physisorbed DEZ on a) Si or b) SiO₂ surfaces. Corresponding physisorption energies (ΔE_p) are also given in brackets. Color codes: grey, carbon; pink, silicon; red, oxygen; white, hydrogen; violet, zinc.

5.A2. Effect of the Co-reactant Exposure on H-Terminated Silicon oxidation

Since H₂O exposure during the co-reactant pulse can cause oxidation of the a-Si:H surface, *i.e.* uncontrolled surface activation, the energetics for the reaction between H₂O and H-terminated silicon were calculated. Figure 5.A2 shows the energetics of H₂O chemisorption on H-terminated silicon, as calculated by density functional theory (DFT/PBE-D3) simulations (see **SECTION 5.2.E**). It was found that the hydroxylation of an H-terminated silicon surface is an exothermic process with an energy gain of 0.44 eV. However, an extremely high kinetic barrier is predicted to be associated (1.49 eV) with the reaction:



This confirms the relative stability of the a-Si:H surface toward oxidation, which has been documented also experimentally.^{1–3} The DFT prediction that the activation energy for the hydroxylation is higher than the activation energy for the reaction between DEZ and H-terminated silicon suggests that, considering perfect surfaces, the rate-limiting step, causing a loss of selectivity is the chemisorption reaction of DEZ. Note, that the presence of defects on experimental substrate surfaces can significantly affect the energetics of both reactions.

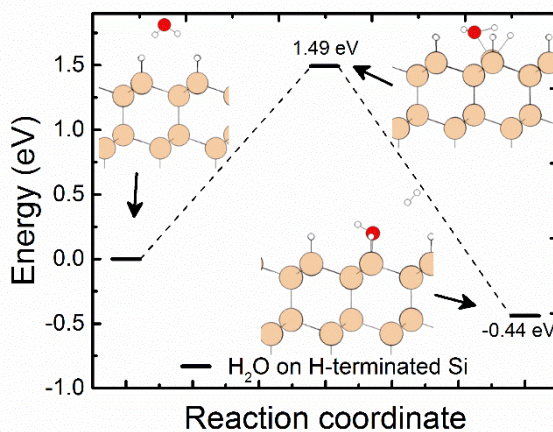


Figure 5.A2: Energy profiles computed by DFT method (PBE-D3) for the chemisorption of H₂O on H-terminated Si. The overall reaction was found to be exothermic (-0.44 eV) but with a high energy barrier (1.49 eV), which points to a kinetically hindered reaction. Color codes: pink, silicon; red, oxygen; white, hydrogen.

5.A3. Elemental Analysis of EBID SiO₂

A SiO₂ pattern with 1 x 1 μm² size and 500 nm thickness was deposited and analyzed *in-situ* for its elemental composition by energy dispersive X-ray spectroscopy (EDX) performed in the same vacuum chamber as where the EBID was conducted. An acceleration voltage of 5 kV was employed during EDX analysis. This gives an interaction depth of ~300 nm, thereby ensuring that the signal is collected only from the EBID SiO₂ and not from the substrate. From the EDX spectrum shown in Figure 5.A3 an O/Si ratio of ~1.8 was calculated from the integrated area of the EDX signals for oxygen and silicon. Moreover, a high level of carbon contamination, 26 % was detected. This amount of carbon impurities is in agreement with previous reports utilizing TEOS and H₂O for SiO₂ EBID.^{4,5}

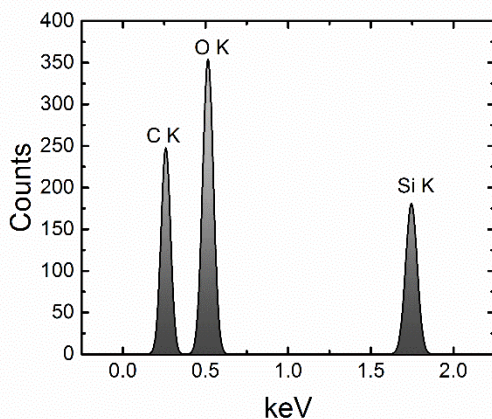


Figure 5.A3: Energy dispersive X-ray spectroscopy spectrum of a 1 x 1 x 0.5 μm³ SiO₂ EBID pattern. The atomic percentages were calculated to be O = 48 at. %, Si= 26 at. %, and C= 26 at. %.

REFERENCES

- (1) Ikeda, H.; Hotta, K.; Yamada, T.; Zaima, S.; Iwano, H.; Yasuda, Y. Oxidation of H-Terminated Si(100) Surfaces Studied by High-Resolution Electron Energy Loss Spectroscopy. *J. Appl. Phys.* **1995**, *77*, 5125–5129.
- (2) Kramer, N.; Jorritsma, J.; Birk, H.; Schoenenberger, C. Nanometer Lithography on Silicon and Hydrogenated Amorphous-Silicon with Low-Energy Electrons. *Microelectron. Eng.* **1995**, *27*, 47–50.
- (3) Michalak, D. J.; Amy, S. R.; Aureau, D.; Dai, M.; Estève, A.; Chabal, Y. J. Nanopatterning Si(111) Surfaces as a Selective Surface-Chemistry Route. *Nat. Mater.* **2010**, *9*, 266–271.
- (4) Sánchez, E. J.; Krug, J. T.; Xie, X. S. Ion and Electron Beam Assisted Growth of Nanometric SimOn Structures for near-Field Microscopy. *Rev. Sci. Instrum.* **2002**, *73*, 3901.
- (5) Frabboni, S.; Gazzadi, G. C.; Spessot, A. Transmission Electron Microscopy Characterization and Sculpting of Sub-1 Nm Si-O-C Freestanding Nanowires Grown by Electron Beam Induced Deposition. *Appl. Phys. Lett.* **2006**, *89*, 1–4.

Chapter 6

Area-Selective Atomic Layer Deposition of SiO₂ Using Acetylacetone as a Chemoselective Inhibitor in an ABC-Type Cycle*

Area-selective atomic layer deposition (ALD) is rapidly gaining interest because of its potential application in self-aligned fabrication schemes for next-generation nanoelectronics. Here, we introduce an approach for area-selective ALD that relies on the use of chemoselective inhibitor molecules in a three-step (ABC-type) ALD cycle. A process for area-selective ALD of SiO₂ was developed comprising acetylacetone inhibitor (step A), bis(diethylamino)silane precursor (step B), and O₂ plasma reactant (step C) pulses. Our results show that this process allows for selective deposition of SiO₂ on GeO₂, SiN_x, SiO₂ and WO₃, in the presence of Al₂O₃, TiO₂, and HfO₂ surfaces. In-situ Fourier transform infrared spectroscopy experiments and density functional theory calculations underline that the selectivity of the approach stems from the chemoselective adsorption of the inhibitor. The selectivity between different oxide starting surfaces as well as the compatibility with plasma-assisted or ozone-based ALD are distinct features of this approach. Furthermore, the approach offers the opportunity of tuning the substrate-selectivity by proper selection of inhibitor molecules.

6.1 Introduction

Directing matter to create structures with atomic level control of physical and chemical properties is a long sought-after goal in nanotechnology. The deposition of atoms at specific locations on a surface can boost advances in catalysis,^{1–3} energy harvesting⁴ and semiconductor device fabrication.⁵ Today, the semiconductor industry is one of the main driving forces that pushes for advancing the field of area-selective deposition.^{6,7} As the state-of-the-art technology is entering the sub-10 nm scale, the conventional patterning of thin-films is becoming extremely challenging in terms of atomic scale precision and reliable processing. Current semiconductor manufacturing requires many lithography and etching steps to fabricate multi-layered 3D devices with perfectly aligned features.⁸ Especially alignment issues leading to the so-called edge placement errors (EPE) have become the prime bottleneck for continued downscaling.⁹ Therefore, innovative *bottom-up* techniques are required to replace or complement *top-down* fabrication schemes.

*Published as: Mamei, A.; Merx, M. J. M.; Karasulu, B.; Roozeboom, F.; Kessels, W. M. M.; Mackus, A. J. M. *ACS Nano* **2017**, *11*, 9303–9311

One of the main emerging solutions is to implement self-aligned fabrication schemes, in which a material is deposited on a pre-determined area in a selective manner. Area-selective deposition will reduce the number of photolithography and etching steps and thereby enable cost-effective options to create these structures in a *bottom-up* approach. Hence, a significant effort is underway in both industry and academia to develop robust area-selective deposition techniques.¹⁰

Atomic layer deposition (ALD) enables layer-by-layer growth with atomic-level thickness control. The technique relies on the cycle-wise and alternate exposure of a substrate to various vapor-phase precursors that undergo self-limiting surface reactions, thereby allowing for uniform and 3D-conformal film deposition.¹¹ However, ALD typically leads to deposition on the entire surface, and therefore the process needs to be adapted to enable area-selective deposition.^{7,12–15} To date, most of the efforts in the field of area-selective ALD include substrate patterning steps before the area-selective ALD.^{12,16,17} On the other hand, in self-aligned fabrication, a partially-processed device architecture is taken as starting point, where patterning has been performed in a previous processing step. Thus, the sample surface consists of several different materials, and the challenge is to selectively deposit on the surface of only one or a subset of these materials. The area-selective ALD processes developed so far often concern metal-on-metal or oxide-on-oxide deposition.^{18–21} However, self-aligned fabrication can also require other material combinations to be deposited in an area-selective manner. For example, some applications might demand area-selective ALD on a specific metal oxide in the presence of other oxide surfaces.

In this work, an approach for area-selective ALD is introduced. It is based on a three-step (ABC-type) ALD cycle, where step A is the exposure of the surface to inhibitor molecules and B and C are the steps of a regular ALD process. Earlier investigations in chemical vapor deposition illustrate some of the advantages of using inhibitors for achieving area-selective deposition.²² Our approach is inspired by the work of Yanguas-Gil *et al.* who used inhibitor molecules (*e.g.* ethanol, acetone, hexane) in ABC-type ALD cycles to improve the doping efficiency in ALD grown materials.²³ Instead of reducing the growth per cycle by partial blocking of the adsorption sites for the precursor molecule,²³ we intend to completely block precursor adsorption on specific starting materials.

Our approach for achieving area-selective ALD is illustrated in Figure 6.1. In step A, we use an inhibitor molecule that selectively adsorbs on certain materials on which no deposition is desired (referred to as the non-growth area). The inhibitor blocks the precursor adsorption during the subsequent step B. The cycle is completed in step C by removing the precursor ligands together with the inhibitor molecules, and by activating the surface for the next cycle. This approach should ideally allow for area-selective ALD on surfaces where the inhibitor does not adsorb (referred to as the growth area).

A pronounced benefit of this approach is that the selectivity does no longer rely solely on the chemoselective adsorption of an ALD precursor on a specific surface. Chemoselective adsorption is decoupled from the precursor by inserting an inhibitor step, and this will therefore yield more freedom for developing area-selective ALD processes. Similar to previous work on the application of self-assembled monolayers

(SAMs) for area-selective ALD, this approach relies on the blocking of surface sites for precursor adsorption. However, the main difference is that the inhibitor molecules are re-applied every single cycle, which can potentially lead to a more robust approach that does not suffer from a gradual degradation of the blocking layer.¹³ Another advantage of re-applying the inhibitor every cycle is that it renders area-selective deposition compatible with (or accessible to) more types of ALD processes, including plasma-assisted or ozone-based ALD. This will therefore extend the set of materials that can be deposited by ALD in an area-selective manner.

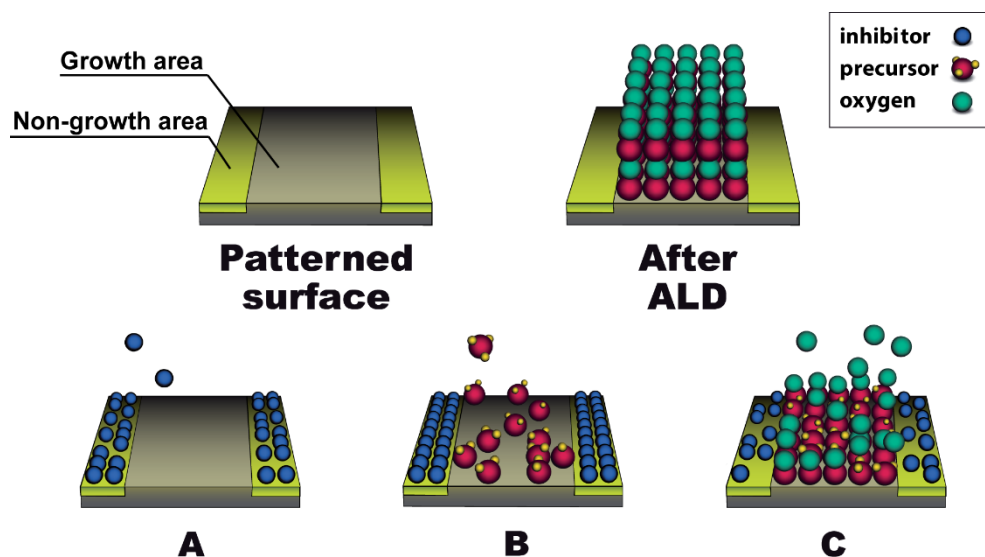


Figure 6.1: Schematic illustration of an ideal area-selective ALD using ABC-type ALD cycles with inhibitor molecules. The starting point is a patterned surface with two different materials: the growth area on which selective deposition is desired, and the non-growth area on which deposition should not occur. In step A, the inhibitor molecules selectively adsorb on the non-growth area. These inhibitor molecules block the precursor adsorption in step B, such that precursor molecules only adsorb on the growth area. This results in area-selective deposition on the growth area after removal of the precursor ligands and inhibitor molecules in step C. By repeating the cycles, material can be deposited by ALD area-selectively. It should be noted that in reality some inhibitor adsorption could still be allowed on the growth area, provided the growth rate and/or material properties of the deposited film are not significantly affected.

In this article, we demonstrate a proof-of-concept for using ABC-type ALD cycles to achieve area-selective ALD of SiO_2 , a low- κ material that is ubiquitous in many devices. The process consists of acetylacetone (abbreviated in the literature as Hacac) as the inhibitor, bis(diethylamino)silane (BDEAS) as the Si precursor, and O_2 plasma as the co-reactant. In contrast to previous area-selective ALD studies in which typically only two surfaces were considered, the nucleation behavior of this ABC-type ALD process is investigated here on as many as 14 different starting surfaces. As a proof-of-concept,

the process was tested on patterned $\text{Al}_2\text{O}_3/\text{GeO}_2$ samples, and the selectivity was probed using surface analysis techniques. Theoretical calculations as well as *in-situ* studies were performed to determine the mechanistic aspects of the chemoselective inhibitor adsorption and the precursor blocking. The basic understanding obtained this way can be used to further improve the selectivity of the current approach. Finally, the opportunities enabled by this area-selective ALD approach will be discussed.

6.2. Results and discussion

6.2.A. Impact of Hacac adsorption on SiO_2 nucleation

Saturation curves for the ABC-type ALD cycle, included in the Appendix (Figure 6.A1), demonstrate that the saturation behavior and the growth per cycle are not influenced by the addition of the Hacac step. ABC-type ALD cycles of SiO_2 were carried out on various starting surfaces to identify on which surfaces deposition of SiO_2 is obtained, and on which ones it is blocked. Figure 6.2 depicts the nucleation curves as measured by *in-situ* spectroscopic ellipsometry (SE). The graph shows that SiO_2 grows without any nucleation delay on GeO_2 , SiO_2 , WO_3 , and SiN_x . On these substrates a growth per cycle of approximately 0.09 nm/cycle was obtained. This is comparable to the growth per cycle of the regular two-step ALD process, consisting of BDEAS precursor and O_2 plasma pulses (referred to as the BC process).²⁴ Figure 6.2 also shows that growth delays for ABC-type ALD of SiO_2 are observed on Al_2O_3 (15 cycles), TiO_2 and HfO_2 (both 10 cycles). The growth delay of 15 cycles that is obtained when using the ABC-type cycles on Al_2O_3 means that a SiO_2 film of ~ 1 nm in thickness can be selectively deposited on GeO_2 in the presence of Al_2O_3 . Nucleation curves for the BC process are shown in Figure 6.A2, demonstrating that there is no nucleation delay for the regular ALD process on these starting materials. Additional data for ABC-type ALD cycles of SiO_2 on Pd, Pt, Ru, ZnO, FeO_x , MoO_x and CoO_x starting surfaces, presented in Figure 6.A3a, show immediate deposition on Pd, short nucleation delays (of ~ 5 cycles) on Ru, ZnO, FeO_x , and Pt, and longer delays (of ~ 8 -12 cycles) on MoO_x and CoO_x . Figure 6.A3b depicts that the deposition temperature also plays a role in determining the extent of the nucleation delay, slightly better results were obtained at 200 °C.

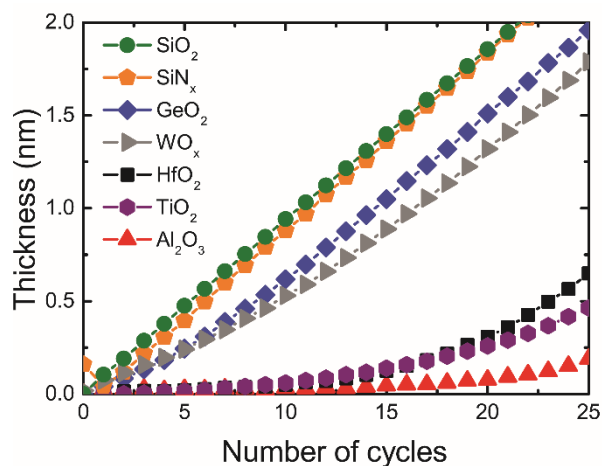


Figure 6.2: Nucleation curves for ABC-type ALD of SiO₂ on different starting surfaces. The graphs show the thickness as a function of the number of ALD cycles as measured by *in-situ* SE. We note that due to the use of an O₂ plasma as the co-reactant, the topmost layer of the starting surfaces can be oxidized during the first few ALD cycles, which was accounted for in the SE modelling of SiN_x.

To gain insights into the inhibited deposition on Al₂O₃ and the immediate deposition on SiO₂, SE measurements were conducted after every individual sub-cycle. Figures 6.3(a-b) show the results for a sequence of AC, ABC, and BC cycles on Al₂O₃ and SiO₂ starting surfaces. Similar data are presented for other starting surfaces like TiO₂, GeO₂ and HfO₂ in Figure 6.A4. The data for the AC cycles on Al₂O₃ in Figure 6.3a show a thickness increase after each A step, and a decrease after every subsequent C step. This suggests that Hacac adsorbs on Al₂O₃, and can be removed by an O₂ plasma pulse. The thickness increase does not correspond directly to the thickness of the Hacac monolayer, because its dielectric function is unknown and not taken into account in the SE modelling. However, the thickness increase can be considered as a measure for the amount of adsorbed material, and is therefore represented as an *apparent thickness*.²⁵ Pulse C removes the adsorbed Hacac by combustion reactions and prepares the surface for the subsequent cycle. The thickness does not decrease completely to zero during the first O₂ plasma step, which is attributed to a slight change of the optical response of the underlying Al₂O₃ film affecting the ellipsometry modelling. The middle part of Figure 6.3a representing the ABC cycles indicates that after exposing the Al₂O₃ surface to Hacac (A), no significant amount of BDEAS adsorption takes place (B). Conversely, when exposing the Al₂O₃ surface to BDEAS (B) and O₂ plasma (C), as shown at the right-hand in the graph, there is a net thickness increase indicating deposition of SiO₂ with a growth per cycle of ~0.09 nm/cycle.

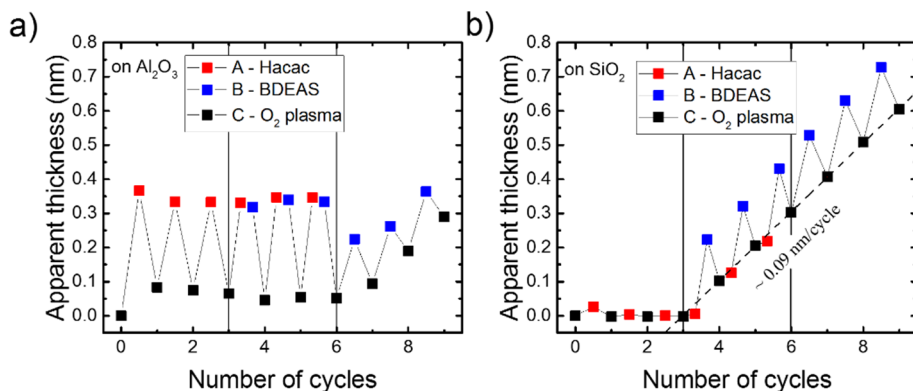


Figure 6.3: Apparent thickness as measured after every reactant dosing pulse on **a)** Al_2O_3 and **b)** SiO_2 . The left-hand part of the figure represents 3 AC cycles with Hacac (A) and O_2 plasma (C) pulses, the middle part 3 ABC cycles with Hacac (A), BDEAS precursor (B), and O_2 plasma (C) pulses, and the right-hand part 3 BC cycles with BDEAS precursor (B), and O_2 plasma (C) pulses. The apparent thickness is used to reflect that the SE modelling did not take into account the dielectric function of the surface groups such that the thickness after step A might not correspond to the physical thickness.²⁵ The starting surfaces were prepared by regular ALD.

Marked differences are observed when performing AC, and ABC cycles on a SiO_2 substrate (Figure 6.3b). There is virtually no change in apparent thickness during AC cycles on SiO_2 , which indicates that Hacac adsorbs, at most, in minute and ineffective amounts on a SiO_2 surface. Consequently, ABC-type cycles on SiO_2 result in the same growth per cycle (~ 0.09 nm/cycle) as observed for regular ALD using BC cycles. This demonstrates that the addition of Hacac does not significantly influence the SiO_2 deposition on SiO_2 starting surfaces. To conclude, Figure 6.3 suggests that the selectivity of the ABC-type process stems from the chemoselective adsorption of Hacac, and that Hacac - once adsorbed - effectively blocks the precursor adsorption.

6.2.B Proof-of-concept of area-selective deposition

ABC-type ALD of SiO_2 was performed on Al_2O_3 and GeO_2 surfaces. GeO_2 was selected as a starting surface because it shows similar behavior to SiO_2 , *i.e.* the addition of an Hacac pulse to the cycle does not significantly affect the deposition of SiO_2 on this surface. Moreover, the GeO_2 surface allows for quantification of the amount of SiO_2 deposited using X-ray photoelectron spectroscopy (XPS) and time-of-flight secondary ion mass spectroscopy (TOF-SIMS). Figure 6.A5 shows the Si 2p signals for SiO_2 after 12, 15 and 21 ABC-type ALD cycles of SiO_2 on both GeO_2 and Al_2O_3 starting surfaces. After 15 ABC-type ALD cycles the ratio of the Si 2p integrated peak areas on Al_2O_3 and GeO_2 is ~ 0.11 . Consistent with the SE data, the integrated peak areas for the Si 2p peak confirm the blocking effect of Hacac.

The selectivity was further investigated on a patterned $\text{Al}_2\text{O}_3/\text{GeO}_2$ sample. To this end, an ALD-prepared Al_2O_3 layer was patterned on a GeO_2 surface using a regular lift-off method. Figures 6.4a-c show the TOF-SIMS elemental mapping images for the Ge^+ , Al^+ and Si^+ secondary ions for the patterned sample after 15 ABC-type ALD cycles of SiO_2 . The mappings confirm that ALD of SiO_2 occurred predominantly on the GeO_2 regions. The line scans, presented in Figure 6.4d, show a high Si^+ signal in the regions not covered by Al_2O_3 , indicating area-selective deposition of SiO_2 on GeO_2 . Only a very small amount of Si is also present on Al_2O_3 , which was quantified to correspond to a 0.01 nm thick SiO_2 layer, as derived from calibration measurements (see the Methods section). Also, lateral broadening of ~ 1 nm, the so-called *mushrooming effect*, is expected to take place given the nature of the ALD technique. This will mainly impact (and be observable for) nanoscale patterns and the effect will be investigated on such samples in future work.

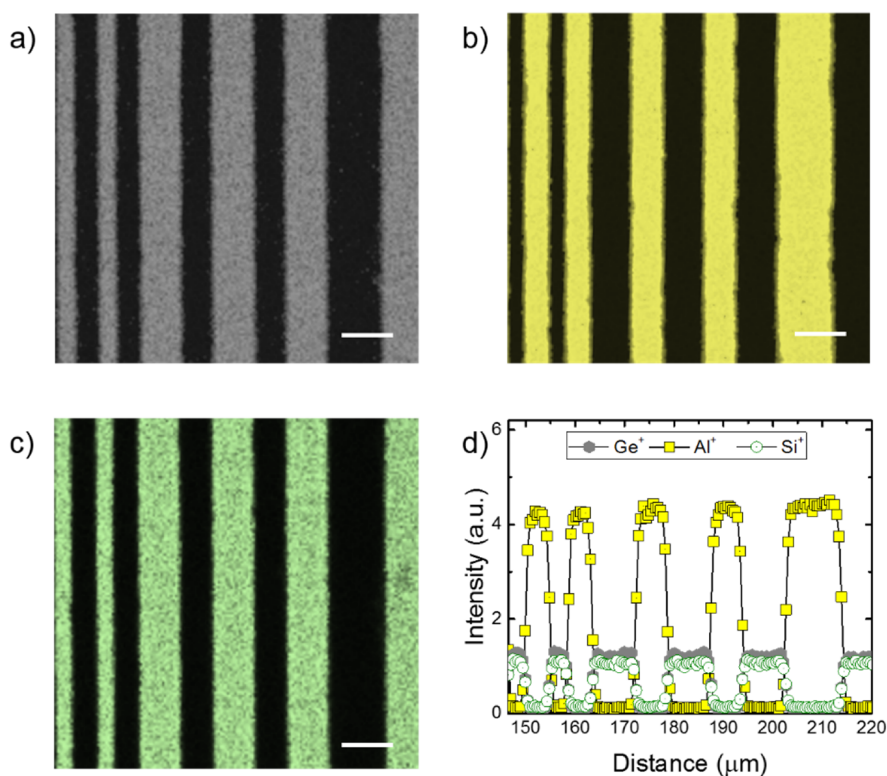


Figure 6.4: Elemental TOF-SIMS mappings showing a) Ge^+ in grey b) Al^+ in yellow, c) Si^+ in green, after 15 SiO_2 ABC-type ALD cycles using Hacac as inhibitor; scale bar is $10 \mu\text{m}$. d) Corresponding line scans for Ge^+ , Al^+ and Si^+ of the sample.

6.2.C. Surface chemistry of the ABC SiO₂ ALD process

In order to investigate the Hacac and BDEAS adsorption on SiO₂ and Al₂O₃ starting surfaces, *in-situ* infrared absorption spectroscopy experiments were performed on pellet-pressed SiO₂ powder using a Fourier transformed spectrometer (FTIR). To this end, the SiO₂ powder was first coated using 30 ALD cycles of SiO₂ or Al₂O₃, respectively. FTIR spectra were collected after coating the powder, and after the subsequent Hacac and the BDEAS dosing steps. Figure 6.5a shows the results on Al₂O₃ as difference spectra, using the spectrum collected after Al₂O₃ coating as the reference. The results confirm that Hacac adsorbs on Al₂O₃, as indicated by the absorption peaks in the wavenumber range 1300 – 1650 cm⁻¹.^{26,27} Subsequent dosing of BDEAS precursor causes only a minor change in the spectrum, which confirms that the pre-adsorbed Hacac molecules act as inhibitors and block the impinging BDEAS molecules from chemisorbing onto the Al₂O₃ surface. It is estimated that the minor change corresponds to a fraction of ~ 8% of the amount of BDEAS molecules adsorbed on bare Al₂O₃. This indicates that Hacac is not fully effective in blocking the precursor adsorption.

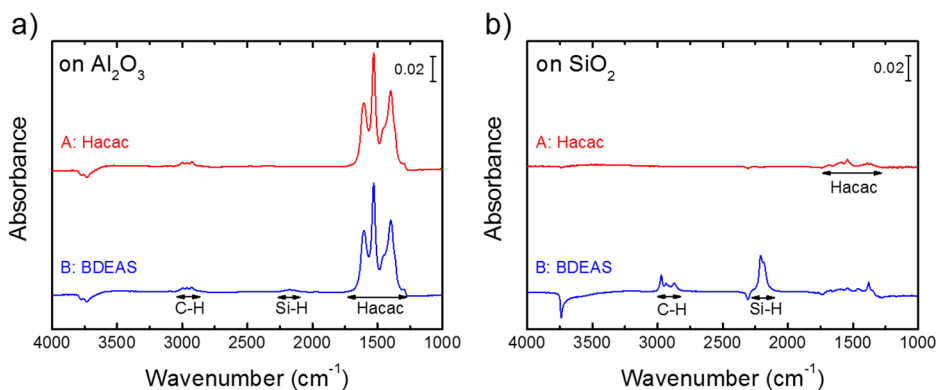


Figure 6.5: *In-situ* infrared absorption spectra recorded after Hacac dosing (step A) and BDEAS precursor dosing (step B) during ABC-type ALD of SiO₂ on **a)** an Al₂O₃-coated substrate, **b)** a SiO₂-coated substrate. The graph for Al₂O₃ shows the adsorption of a large amount of Hacac, and the blocking of BDEAS precursor adsorption during the subsequent pulse. The graph for SiO₂ reveals that only a small amount of Hacac adsorbs on SiO₂, which does not significantly affect the adsorption of the BDEAS precursor. The spectra collected after step A and B are both referenced to the starting surface (*i.e.* Al₂O₃ and SiO₂).

A similar experiment on the SiO₂-coated sample, using identical Hacac and BDEAS dosing times, revealed a distinctly different behavior, as shown in Figure 6.5b. Now, only 8% of Hacac adsorbs on SiO₂ as compared to the amount that adsorbs on the Al₂O₃-coated surface. Consequently, the adsorption of BDEAS is not significantly affected on this surface, as shown by the large (positive) absorption peaks. BDEAS adsorption results in positive peaks in the wavenumber ranges 2800 - 3000 cm⁻¹ and 2130 - 2240 cm⁻¹, originating from the C-H and Si-H stretching vibrations of the

adsorbed BDEAS molecules.^{28,29} Concurrently, there is a loss of absorbance around 3740 cm^{-1} , characteristic for the O-H stretching vibrations of the surface hydroxyl groups that are consumed during BDEAS precursor adsorption.^{28,30}

In conclusion, the FTIR studies confirms that Hacac selectively adsorbs on Al_2O_3 , and subsequently inhibits the BDEAS adsorption. Yet, the studies also provide insights for further improvement of the process that will be discussed below.

6.2.D. Mechanism underpinning the chemoselective adsorption of the Hacac inhibitor

Density functional theory (DFT) calculations were performed to better understand the mechanism of the chemoselective Hacac adsorption at a molecular level. Hydroxylated surfaces of $\alpha\text{-Al}_2\text{O}_3$ (0001) and $\alpha\text{-SiO}_2$ (0001) were employed to represent the experimentally used Al_2O_3 and SiO_2 surfaces. The calculations revealed that Hacac prefers to bind in a chelate configuration on both surfaces, with both of its oxygen atoms bonded to $\text{Al}^{3+}/\text{Si}^{4+}$ surface sites. Alternative binding configurations were also found, as discussed below. Concertedly, H_2O is predicted to form as a by-product on both surfaces through a proton transfer to a hydroxyl surface group. The H_2O by-product is expected to stick to the surface, where it plays an important role in stabilizing the chemisorbed acac^- product through H-bond interactions (see Appendix, Figure 6.A7 and the accompanying discussion).

The structures and associated relative energies were calculated for the stationary points along the suitable reaction pathways (*i.e.* minimum energy paths, MEPs) for the adsorption of the Hacac inhibitor on Al_2O_3 and SiO_2 (Figure 6.6). For the first step in Hacac binding, *i.e.* physisorption, two distinctive binding orientations were identified by the DFT calculations (horizontal and vertical, see Figure 6.A6 and detailed description in the Appendix). As evident from Figure 6.6a, the dissociative binding of Hacac on Al_2O_3 is associated with an overall exothermic reaction with an energy gain of 0.49 eV. The chemisorption involves the formation of an intermediate complex through a slightly-exothermic ($\Delta E = -0.07$ eV) process with near-to-zero barrier ($E_a \approx 0.01$ eV). The intermediate complex comprises Hacac that is bonded to the Al^{3+} -site through one of its oxygen atoms (Figure 6.A7a). This intermediate species is predicted to lose its hydroxyl-proton through a kinetically-accessible process ($E_a = 0.25$ eV), producing a monodentate adduct (Type A, Figure 6.A7b) alongside H_2O . However, this adduct corresponds to a transition-state species on the energetically-downhill path that yields the chelate end-product (Type B, Figure 6.A7c) through binding of acac^- *via* its second oxygen to the same surface Al^{3+} -site. Considering that the Hacac would have already gained sufficient kinetic energy by physisorbing on the Al_2O_3 surface (*i.e.* $\Delta E_p = -0.75$ eV, physisorption energy), it would readily overcome the overall barrier of 0.25 eV and be converted to the chelate (Type B) end-product. Therefore, none of the monodentate (Type A) species (intermediate or adduct) are expected to accumulate on the Al_2O_3 surface.

Similar to the Al_2O_3 case, a chelate (Type B, Figure 6.A7d) species is the end-product of Hacac adsorption on SiO_2 , whereas the monodentate (Type A) complex is only a transition state (Figure 6.6b). More importantly, the overall chemisorption reaction on SiO_2 is calculated to be endothermic and to require an energy of 0.98 eV, accompanied by an extremely high kinetic barrier ($E_a = 2.35$ eV). In accordance with the SE and FTIR results, these DFT findings suggest that Hacac binds readily on hydroxylated Al_2O_3 , while the overall reaction on hydroxylated SiO_2 is both thermodynamically and kinetically hindered. This explains the selectivity of Hacac adsorption on Al_2O_3 as opposed to SiO_2 during the ABC-type ALD of SiO_2 .

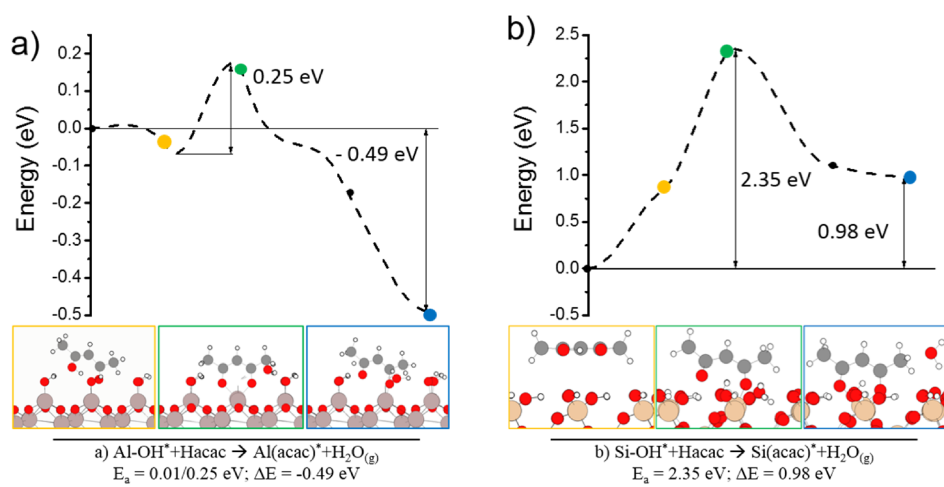
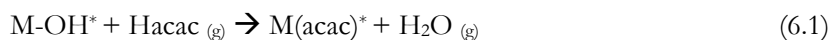


Figure 6.6: DFT (GGA/PBE-D3) level minimum energy paths (MEPs) for the Hacac adsorption on **a)** Al_2O_3 and **b)** SiO_2 surfaces, as described by the corresponding chemical equations. Minimum energy structures of the important steps are also shown (yellow, green and blue dots and corresponding insets), where some oxygen and hydrogen atoms are hidden for clarity. First points of the energy profiles correspond to the Hacac species physisorbed on each surface, and have $\Delta E_p = -0.75$ and -0.37 eV with respect to the separated Hacac gas phase and $\text{Al}_2\text{O}_3/\text{SiO}_2$ surfaces. These are taken as reference points (0 eV) to calculate the activation and final state energies. Color code for atoms: silicon, pink; aluminum, light gray hydrogen, white; oxygen, red; carbon, gray.

6.2.E Role of surface acidity on Hacac adsorption

The chemoselective adsorption of Hacac on various starting surfaces can also be interpreted in terms of surface acidity.³¹ This allows to explain the results obtained on the experimentally used starting surfaces. Hacac has a pK_a value of 9.0 in aqueous solution at 25 °C, and therefore it should behave as a weak acid.³² A reaction with Hacac is not likely to occur with the hydroxyl groups that possess an acidic character (*e.g.* SiO₂).³³ Conversely, hydroxyl groups with more basic character can react with Hacac. In this framework, an acid/base surface reaction between Hacac and the surface hydroxyl groups of a given oxide (*e.g.* Al₂O₃) can be written as:



where M is a generic atom of the oxide (either metal or non-metal) and the asterisks represent the surface species. A generalization can be made in order to explain which surfaces allow for the chemoselective adsorption of the Hacac inhibitor (and potential blocking of the precursor), and which surfaces will lead to immediate deposition instead. The acidity of an oxide can be predicted from the electronegativity of the cation element, M.³⁴ The relative acidity of several oxide surfaces was calculated using Sanderson's electronegativity scale and the electronegativity equalization principle, in order to explain the data of Figures 6.2 and 6.A3, as presented in Figure 6.A8. The agreement of the calculated values with the experimental data underlines that the distinct acidic/basic behavior of different oxide compounds governs the chemoselective adsorption of Hacac. Therefore, this provides a framework for predicting the area-selectivity on different starting surfaces.

6.2.F. Merits and opportunities provided by the approach

The approach introduced in this article shows similarities with recent work by Engstrom and co-workers in which inhibitor molecules are co-injected into the reactor together with the precursor.³⁵ Also that approach relies on influencing the precursor adsorption by an inhibitor molecule. The benefit of dividing the inhibitor and precursor exposure over two different dosing steps is that the adsorption of both molecules can reach saturation independently, without suffering from competitive adsorption effects. Consequently, similar to regular two-step ALD processes, an ABC-type ALD process should allow for the deposition of conformal films on nanostructured surfaces.

A more natural approach for achieving area-selective ALD would be to design dedicated ALD precursors to enable chemoselective adsorption on materials on which deposition should occur. However, in practice this is extremely challenging because the precursor molecule has to contain the atom to be deposited, while also satisfying other requirements to behave as an effective ALD precursor (in terms of stability, volatility, and self-limiting adsorption). By using two different molecules in an ABC-type ALD

cycle, the inhibitor provides the selectivity in step A, without compromising the properties of the precursor dosed in step B.

When the ABC-type ALD approach is compared to other area-selective ALD approaches, several distinctive aspects can be identified. As discussed in the introduction, re-applying the inhibitor molecules every cycle can be beneficial from a reliability point-of-view, while it also makes the approach compatible with plasma-assisted or ozone-based ALD. Moreover, an important merit of this approach is that it distinguishes between the growth on different oxide surfaces (*e.g.* GeO₂/SiO₂ *versus* Al₂O₃/HfO₂/TiO₂).

The FTIR studies revealed that the selectivity of the Hacac adsorption is not perfect, since some adsorption was also observed on SiO₂. However, the amount of Hacac on SiO₂ is sufficiently small such that it does not influence the deposition on the growth area, as we concluded from the *in-situ* SE measurements (Figures 6.2 and 6.A1). Moreover, a small amount of BDEAS adsorption was detectable on Al₂O₃ after dosing the Hacac inhibitor. *Ex-situ* XPS and TOF-SIMS also confirmed that a minor amount of SiO₂ was deposited on Al₂O₃ after 15 cycles suggesting that the adsorbed Hacac does not completely block the precursor adsorption. This incomplete precursor blocking can occur most likely due to the presence of: (i) surface defects or impurities that can negatively influence the ideal inhibitor adsorption behavior; (ii) surface reactive sites that remain accessible to the precursor; and (iii) physisorbed water molecules on the surface that can compete with the Hacac chemisorption, as discussed in the DFT calculations in the Appendix, Figure 6.A7. This implies that the selectivity of the ABC-type ALD process can be further improved by exploring different surface preparation procedures and by optimizing the deposition conditions. In addition, alternative inhibitors, different inhibitor dosing strategies, or co-dosing two or more inhibitor molecules can be considered for improving the selectivity. All these parameters offer physico-chemical pathways to enhance the inhibitor surface coverage and, therefore, maximize the blocking effect during the precursor dose step. For these reasons, we foresee that it should be possible to significantly improve the selectivity to the extent it meets the requirements of semiconductor manufacturing.

The ABC approach provides the opportunity of tailoring the substrate-selectivity of an ALD process by selection of the chemoselective inhibitor molecule. There is a wealth of information in surface science and catalysis literature about the adsorption of organic molecules on inorganic surfaces,^{36,37} which can serve as a good starting point for selecting suitable inhibitor molecules.²³ The ideal case would be to use an inhibitor molecule that adsorbs on all surfaces, except for the particular surface on which deposition is needed. Additional research is required to investigate whether such selectivity is achievable, and to further explore the toolbox of using inhibitor molecules for area-selective ALD. We expect that this approach can enable area-selective ALD for different materials by using other precursors and for example H₂ or NH₃ plasmas co-reactants. To this end, the interaction of the inhibitor with the material to be deposited and with the plasma needs to be studied. In view of the large set of possibilities, this will be the subject of a follow-up study.

6.3 Conclusions

We have demonstrated the use of chemoselective inhibitors in ABC-type ALD cycles as a route for area-selective ALD. Area-selective ALD of SiO_2 was achieved using a process consisting of alternated Hacac inhibitor, BDEAS precursor, and O_2 plasma pulses on a GeO_2 substrate with patterned Al_2O_3 features. SiO_2 is an extremely relevant and widely employed low- κ material, for which no area-selective ALD process is available. *In-situ* SE studies revealed that area-selective (*i.e.* non-inhibited) growth can also be obtained on WO_x , SiO_2 , SiN_x , and Pd, while there are nucleation delays of 10-15 cycles on TiO_2 , HfO_2 , CoO_x , and MoO_x . The selectivity originates from the chemoselective adsorption of the Hacac inhibitor molecule. This was corroborated in detail by *in-situ* SE and FTIR experiments, as well as by DFT calculations, and generalized by correlating the Hacac adsorption to the acidity of the starting surface. SE and FTIR experiments confirmed that adsorbed Hacac blocks the subsequent BDEAS precursor adsorption, thereby resulting in area-selective deposition of SiO_2 on those surfaces on which Hacac does not adsorb.

The presented results establish a proof-of-concept for the introduced approach, and provide insight into how the selectivity can be further improved. The SiO_2 ABC-type process offers an exceptional substrate-selectivity, by distinguishing between different oxide starting surfaces. We expect that the compatibility of the approach with ozone-based or plasma-assisted ALD, as well as the ability to tune the substrate-selectivity by selection of the inhibitor molecule, will extend the portfolio of materials that can be deposited by ALD in an area-selective manner.

6.4 Methods

ALD Processes. The depositions were carried out in an Oxford Instruments FlexAL reactor, which is described in detail in Ref. 38. In short, it is a vacuum vessel equipped with a remote inductively-coupled plasma (ICP) source, a 200 mm substrate table, a turbo-molecular pump and a loadlock. The SiO₂ plasma-assisted ALD recipe with BDEAS (H₂Si[N(C₂H₅)₂]₂) precursor (also known as SAM.24) and O₂ plasma pulses, characterized by Dingemans *et al.*,²⁴ was used as the starting point. The recipe was changed to an ABC-type ALD process by adding a step of Hacac dosing before the precursor step. The Hacac ($\geq 99\%$ ReagentPlus®; CAS 123-54-6) was purchased from Sigma Aldrich and it was employed without further purification. The Hacac has a vapor pressure of 6 Torr at 25 °C and it exists in two tautomeric forms: keto and enol. In gas phase, the tautomeric equilibrium is shifted toward the enol form,³⁹ which was the form considered in the DFT calculations. The Hacac inhibitor was kept at room temperature in a stainless steel container and vapor drawn into the chamber using 3 pulses of 5 seconds each. All experiments were carried out at a substrate temperature of 150 °C.

Substrate Preparation Methods. A set of 14 different materials was investigated as starting surfaces in this study. Al₂O₃, HfO₂, TiO₂, WO_x, CoO_x, MoO_x, FeO_x, ZnO, Pt, Pd, Ru, and SiN_x samples were prepared by ALD in our lab using standard ALD recipes. In addition, crystalline Si and Ge substrates were used. All these substrates were cleaned by 5 minutes O₂ plasma exposure (8 mtorr O₂, 200 W) prior to the deposition, exception made for SiN_x. Because of this O₂ plasma cleaning step, the Si and Ge substrates are referred to as SiO₂ and GeO₂, respectively, in this article.

Analytical Methods. *In-situ* SE was performed using a J.A. Woollam M2000D ellipsometer as the main diagnostic technique to characterize the process and to measure the nucleation curves, using a Cauchy parametrization to model the data. In the case of SiN_x, O₂ plasma oxidation occurs during the SiO₂ deposition, which was taken into account in the modelling of the data of Figure 6.2. The nucleation delay was defined as the number of cycles until the first data point that showed a measurable increase in thickness. The dielectric function of a monolayer of adsorbed Hacac molecules was not taken into account and the same Cauchy parametrization as used to describe the deposited SiO₂ was employed to model the sub-cycle SE data of Figures 6.3 and 6.A4. In these results, the thickness obtained from modeling the data after Hacac exposure is therefore represented as an ‘apparent thickness’.

XPS measurements were performed using a K-Alpha system from Thermo Scientific. TOF-SIMS analysis was performed at Philips Innovation Labs using an Ion-ToF TOF-SIMS IV instrument, which was operated in positive mode to measure Al⁺ ($m/z=27$), Si⁺ ($m/z=28$), and Ge⁺ (sum of $m/z=70, 72$ representing the most abundant isotopes of Ge). In addition, TOF-SIMS mapping was performed on patterned GeO₂/Al₂O₃ samples by applying burst-alignment with long pulses of 200 ns, resulting in high lateral resolution ($\sim 0.3 \mu\text{m}$), but low mass resolution ($\sim 1 m/z$). A series of 2, 5, and 10 regular ALD cycles for SiO₂ deposition was performed on Ge substrates to

calibrate the TOF-SIMS signals for thickness quantification. These samples were probed using the high-current bunched mode that allows for measurement with high mass-resolution. Note, that the thickness of the deposited SiO₂ on the GeO₂ regions is already beyond the linearity limit of TOF-SIMS, meaning that the ratio of the Si⁺ intensity of the GeO₂ and Al₂O₃ regions in the line scans underestimates the selectivity.

In-situ FTIR experiments were carried in a home-built ALD setup, which is very similar to the FlexAL reactor in terms of the plasma source and pumping system. This home-built setup is equipped with a Bruker Vector FTIR spectrometer with a mid-infrared light source (Globar ~10000 – 50 cm⁻¹) and a liquid N₂ cooled mercury cadmium tellurium (MCT) detector with a spectral range of 12000 – 550 cm⁻¹, a translational and rotational sample manipulator, and KBr windows that can be isolated from the chamber with gate valves. FTIR measurements were performed on Aerosil OX50 SiO₂ powder that was pellet-pressed on a tungsten mesh. The powder was heated to 150 °C by passing a current through the mesh. To account for the accessible surface area of the powder, the spectra were normalized to the peak intensities of regular saturated TMA or BDEAS adsorption on the same sample before the Hacac dosing.

Computational Methods. All electronic structure calculations were performed using the projector augmented wave function (PAW)^{40,41} as implemented in Vienna *Ab Initio* Simulation Package (VASP v.5.3.5).^{42–44} First-principles calculations were carried out using the generalized gradient approximation (GGA) to the density functional theory (DFT).^{45,46} Perdew–Burke–Ernzerhof (PBE) exchange correlation functional⁴⁷ were employed and the Van der Waals interactions were also accounted for on an empirical basis (PBE-D3).⁴⁸ Hydroxylated α -Al₂O₃ and α -SiO₂ clusters were used as approximations of the amorphous hydroxylated Al₂O₃ and SiO₂ used in the experiments. Additional computational details including the model system preparation can be found in the Appendix and also elsewhere.^{17,49}

REFERENCES

- (1) Cheng, N.; Banis, M. N.; Liu, J.; Riese, A.; Li, X.; Li, R.; Ye, S.; Knights, S.; Sun, X. Extremely Stable Platinum Nanoparticles Encapsulated in a Zirconia Nanocage by Area-Selective Atomic Layer Deposition for the Oxygen Reduction Reaction. *Adv. Mater.* **2015**, *27*, 277–281.
- (2) Xie, J.; Yang, X.; Han, B.; Shao-Horn, Y.; Wang, D. Site-Selective Deposition of Twinned Pt Nanoparticles on TiSi_2 Nanonets by Atomic Layer Deposition and Their Oxygen Reduction Activities. *ACS Nano* **2013**, *7*, 6337–6345.
- (3) Lee, H. B. R.; Baeck, S. H.; Jaramillo, T. F.; Bent, S. F. Growth of Pt Nanowires by Atomic Layer Deposition on Highly Ordered Pyrolytic Graphite. *Nano Lett.* **2013**, *13*, 457–463.
- (4) Li, R.; Zhang, F.; Wang, D.; Yang, J.; Li, M.; Zhu, J.; Zhou, X.; Han, H.; Li, C. Spatial Separation of Photogenerated Electrons and Holes among $\{010\}$ and $\{110\}$ Crystal Facets of BiVO_4 . *Nat. Commun.* **2013**, *4*, 1432.
- (5) Elko-Hansen, T. D.-M.; Dolocan, A.; Ekerdt, J. G. Atomic Interdiffusion and Diffusive Stabilization of Cobalt by Copper During Atomic Layer Deposition from Bis(N-Tert-Butyl-N'-Ethylpropionamidinato) Cobalt(II). *J. Phys. Chem. Lett.* **2014**, *5*, 1091–1095.
- (6) Fang, Ming; Ho, J. C. Area-Selective Atomic Layer Deposition: Conformal Coating, Subnanometer Thickness Control, and Smart Positioning. *ACS Nano* **2015**, *9*, 8651–8654.
- (7) Kim, W.-H.; Minaye Hashemi, F. S.; Mackus, A. J. M.; Singh, J.; Kim, Y.; Bobb-Semple, D.; Fan, Y.; Kaufman-Osborn, T.; Godet, L.; Bent, S. F. A Process for Topographically Selective Deposition on 3D Nanostructures by Ion Implantation. *ACS Nano* **2016**, *10*, 4451–4458.
- (8) Pan, D. Z.; Liebmann, L.; Yu, B.; Xu, X.; Lin, Y. Pushing Multiple Patterning in Sub-10nm. *Proc. 52nd Annu. Des. Autom. Conf. - DAC '15* **2015**, 1–6.
- (9) Mulkens, J.; Hanna, M.; Wei, H.; Vaenkatesan, V.; Megens, H.; Slotboom, D. Overlay and Edge Placement Control Strategies for the 7nm Node Using EUV and ArF Lithography. *Proc. SPIE* **2015**, *9422*, 94221Q–1/13.
- (10) Liddle, J. A.; Gallatin, G. M. Nanomanufacturing: A Perspective. *ACS Nano* **2016**, *10*, 2995–3014.
- (11) George, S. M. Atomic Layer Deposition: An Overview. *Chem. Rev.* **2010**, *110*, 111–131.
- (12) Mackus, A. J. M.; Bol, A. A.; Kessels, W. M. M. The Use of Atomic Layer Deposition in Advanced Nanopatterning. *Nanoscale* **2014**, *6*, 10941–10960.
- (13) Minaye Hashemi, F. S.; Prasittichai, C.; Bent, S. F. Self-Correcting Process for High Quality Patterning by Atomic Layer Deposition. *ACS Nano* **2015**, *9*, 8710–8717.
- (14) Heyne, M. H.; de Marneffe, J.-F.; Delabie, A.; Caymax, M.; Neyts, E. C.; Radu, I.; Huyghebaert, C.; De Gendt, S. Two-Dimensional WS_2 Nanoribbon Deposition by Conversion of Pre-Patterned Amorphous Silicon. *Nanotechnology* **2017**, *28*, 04LT01.
- (15) Lemaire, P. C.; King, M.; Parsons, G. N. Understanding Inherent Substrate Selectivity during Atomic Layer Deposition: Effect of Surface Preparation, Hydroxyl Density, and Metal Oxide Composition on Nucleation Mechanisms during Tungsten ALD. *J. Chem. Phys.* **2017**, *146*, 052811–1/9.
- (16) Chen, R.; Bent, S. F. Chemistry for Positive Pattern Transfer Using Area-Selective Atomic Layer Deposition. *Adv Mater* **2006**, *18*, 1086–1090.
- (17) Marnett, A.; Kuang, Y.; Aghaee, M.; Ande, C. K.; Karasulu, B.; Creatore, M.; Mackus, A. J. M.; Kessels, W. M. M.; Roozeboom, F. Area-Selective Atomic Layer Deposition of In_2O_3 :H Using a μ -Plasma Printer for Local Area Activation. *Chem. Mater.* **2017**, *29*, 921–925.
- (18) Mayberry, M. ALD: Essential but Not Sufficient. *15th International Conference on Atomic Layer Deposition*, 2015.
- (19) Haider, A.; Yilmaz, M.; Deminskyi, P.; Eren, H.; Biyikli, N. Nanoscale Selective Area Atomic Layer Deposition of TiO_2 Using E-Beam Patterned Polymers. *RSC Adv.* **2016**, *6*, 106109–106119.
- (20) Kamcev, J.; Germack, D. S.; Nykypanchuk, D.; Grubbs, R. B.; Nam, C. Y.; Black, C. T. Chemically Enhancing Block Copolymers for Block-Selective Synthesis of Self-Assembled Metal Oxide Nanostructures. *ACS Nano* **2013**, *7*, 339–346.
- (21) Lee, H.-B.-R.; Kim, H. Area Selective Atomic Layer Deposition of Cobalt Thin Films. *ECS Trans.* **2008**, *16*, 219–225.
- (22) Babar, S.; Mohimi, E.; Trinh, B.; Girolami, G. S.; Abelson, J. R. Surface-Selective Chemical Vapor Deposition of Copper Films through the Use of a Molecular Inhibitor. *ECS J. Solid State Sci. Technol.*

- 2015, 4, N60–N63.
- (23) Yanguas-Gil, A.; Libera, J. A.; Elam, J. W. Modulation of the Growth Per Cycle in Atomic Layer Deposition Using Reversible Surface Functionalization. *Chem. Mater.* **2013**, *25*, 4849–4860.
- (24) Dingemans, G.; van Helvoirt, C. A. A.; Pierreux, D.; Keuning, W.; Kessels, W. M. M. Plasma-Assisted ALD for the Conformal Deposition of SiO₂: Process, Material and Electronic Properties. *J. Electrochem. Soc.* **2012**, *159*, H277–H285.
- (25) Langereis, Erik; Heil, S. B. S.; Knoops, H. C. M.; Keuning, W. van de Sanden, M. C. M.; Kessels, W. M. M. *In Situ* Spectroscopic Ellipsometry as a Versatile Tool for Studying Atomic Layer Deposition. *J. Appl. Phys. D Appl. Phys.* **2009**, *42*, 073001–1/19.
- (26) van Veen, J. A. R.; Jonkers, G.; Hesselink, W. H. Interaction of Transition-Metal Acetylacetonates with γ -Al₂O₃ Surfaces. *J. Chem. Soc. Faraday Trans. 1* **1989**, *85*, 389–413.
- (27) Slabzhennikov, S. N.; Ryabchenko, O. B.; Kuarton, L. A. Interpretation of the IR Spectra of Aluminum, Gallium, and Indium Tris(acetylacetonates). *Russ. J. Coord. Chem.* **2006**, *32*, 545–551.
- (28) Stuart, B. H. *Infrared Spectroscopy: Fundamentals and Applications*; Ande, D. J., Ed.; Wiley: Dartford, Kent, UK, 2004.
- (29) Bugaev, K. O.; Zelenina, A. A.; Volodin, V. A. Vibrational Spectroscopy of Chemical Species in Silicon and Silicon-Rich Nitride Thin Films. *Int. J. Spectrosc.* **2012**, *2012*, 1–5.
- (30) Morrow, B. A.; Cody, I. A. Infrared Spectra of the Isolated Hydroxyl Groups on Silica. *J. Phys. Chem.* **1973**, *77*, 1465–1469.
- (31) Kytokivi, A.; Rautiainen, A.; Root, A. Reaction of Acetylacetone Vapour with γ -Alumina. *J. Chem. Soc. Faraday Trans.* **1997**, *93*, 4079–4084.
- (32) The IUPAC Stability Constants Database, SC-Database and Mini-SCDatabase.
- (33) *Semiconductor Device-Based Sensors for Gas, Chemical, and Biomedical Applications*; Ren, Fan; Pearton, S. J., Ed.; CRC Press: Boca Raton, USA, 2011.
- (34) Jeong, N. C.; Lee, J. S.; Tae, E. L.; Lee, Y. J.; Yoon, K. B. Acidity Scale for Metal Oxides and Sanderson's Electronegativities of Lanthanide Elements. *Angew. Chem. Int. Ed.* **2008**, *47*, 10128–10132.
- (35) J.R. Engstrom. Examination of the Mechanisms Involved in Self-Aligned, Selective Area Atomic Layer Deposition Using Surface Sensitive Probes. In *Area Selective Deposition Workshop*; Leuven (BL), 2016.
- (36) Ma, Z.; Zaera, F. Organic Chemistry on Solid Surfaces. *Surf. Sci. Rep.* **2006**, *61*, 229–281.
- (37) Barteau, M. A. Organic Reactions at Well-Defined Oxide Surfaces. *Chem. Rev.* **1996**, *96*, 1413–1430.
- (38) Heil, S. B. S.; van Hemmen, J. L.; Hodson, C. J.; Singh, N.; Klootwijk, J. H.; Roozeboom, F.; van de Sanden, M. C. M.; Kessels, W. M. M. Deposition of TiN and HfO₂ in a Commercial 200mm Remote Plasma Atomic Layer Deposition Reactor. *J. Vac. Sci. Technol. A* **2007**, *25*, 1357–1366.
- (39) Fokendt, M. M.; Weiss-Lopez, B. E.; Chauvel, J. P.; True, N. S. Gas-Phase ¹H Studies of Keto-Enol Tautomerism of Acetylacetone, Methyl Acetoacetate, and Ethyl Acetoacetate. *J. Phys. Chem.* **1985**, *89*, 3347–3352.
- (40) Blöchl, P. E. Projector Augmented-Wave Method. *Phys. Rev. B* **1994**, *50*, 17953–17979.
- (41) Kresse, G. From Ultrasoft Pseudopotentials to the Projector Augmented-Wave Method. *Phys. Rev. B* **1999**, *59*, 1758–1775.
- (42) Kresse, G.; Hafner, J. *Ab Initio* Molecular Dynamics for Liquid Metals. *Phys. Rev. B* **1993**, *47*, 558–561.
- (43) Kresse, G.; Hafner, J. *Ab Initio* Molecular-Dynamics Simulation of the Liquid-Metal–amorphous-Semiconductor Transition in Germanium. *Phys. Rev. B* **1994**, *49*, 14251–14269.
- (44) Kresse, G.; Furthmüller, J. Efficiency of *Ab-Initio* Total Energy Calculations for Metals and Semiconductors Using a Plane-Wave Basis Set. *Comput. Mater. Sci.* **1996**, *6*, 15–50.
- (45) Hohenberg, P. Inhomogeneous Electron Gas. *Phys. Rev.* **1964**, *136*, B864–B871.
- (46) Kohn, W.; Sham, L. J. Self-Consistent Equations Including Exchange and Correlation Effects. *Phys. Rev.* **1965**, *140*, A1133–A1138.
- (47) Perdew, J. P.; Burke, K.; Ernzerhof, M. Generalized Gradient Approximation Made Simple. *Phys. Rev. Lett.* **1997**, *78*, 1396–1396.
- (48) Grimme, S.; Antony, J.; Ehrlich, S.; Krieg, H. A Consistent and Accurate *Ab Initio* Parametrization of Density Functional Dispersion Correction (DF-T-D) for the 94 Elements H–Pu. *J. Chem. Phys.* **2010**, *132*, 154104.

- (49) Kuang, Y.; Macco, B.; Karasulu, B.; Ande, C. K.; Bronsveld, P. C. P.; Verheijen, M. A.; Wu, Y.; Kessels, W. M. M.; Schropp, R. E. I. Towards the Implementation of Atomic Layer Deposited $\text{In}_2\text{O}_3\text{:H}$ in Silicon Heterojunction Solar Cells. *Sol. Energy Mater. Sol. Cells* **2017**, *163*, 43–50.

Appendix

Area-Selective Atomic Layer Deposition of SiO_2 Using Acetylacetone as a Chemoselective Inhibitor in an ABC-Type Cycle

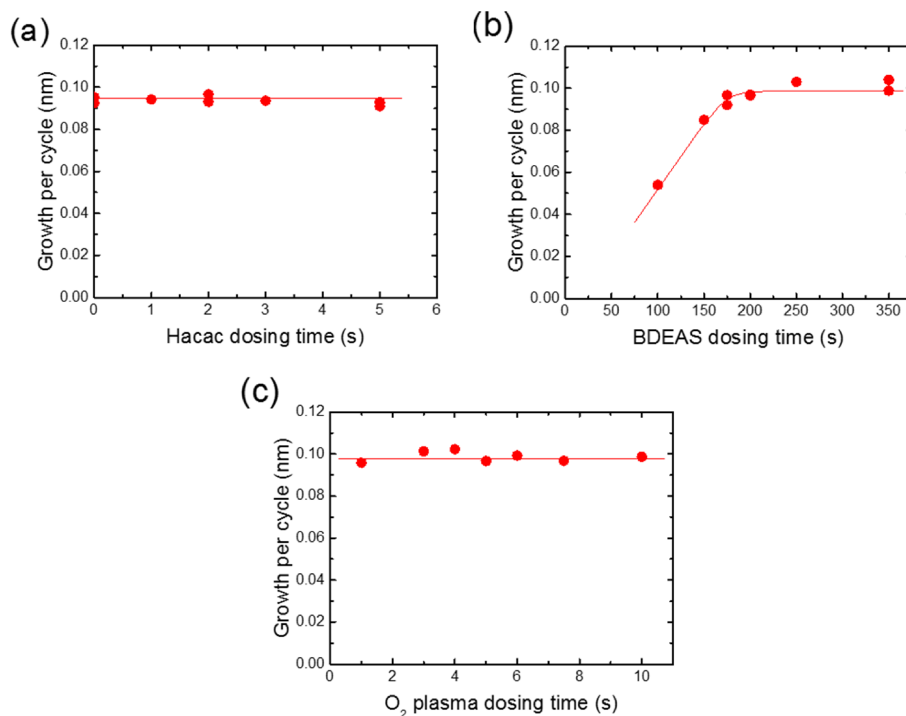


Figure 6.A1: Saturation curves showing the growth per cycle for SiO_2 as a function of the (a) Hacac dosing time, (b) BDEAS and (c) O_2 plasma dosing time as measured by *in-situ* spectroscopic ellipsometry (SE). The starting surface is SiO_2 deposited by ALD. The lines serve as guides to the eye. From (a), it can be concluded that even if some Hacac adsorption on SiO_2 takes place (see FTIR results and discussion), the growth per cycle of SiO_2 on a SiO_2 starting surface is not affected by the addition of a Hacac dose to the ALD cycle.

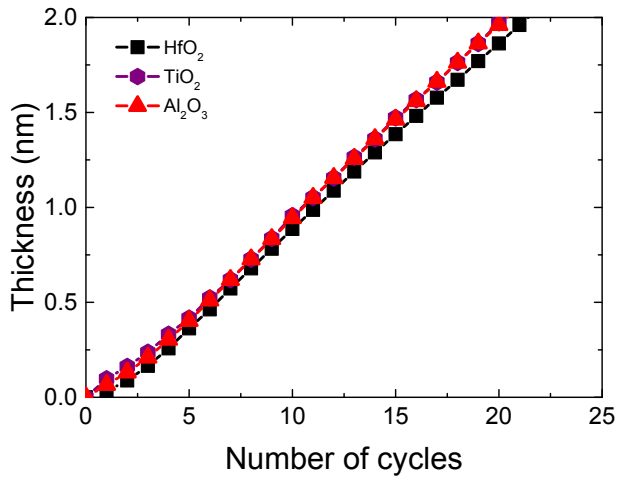


Figure 6.A2: Nucleation curves for the regular BC-type ALD process of SiO₂ on different starting surfaces. The graphs show the thickness as a function of the number of ALD cycles as measured by *in-situ* SE. The figure demonstrates that there is no nucleation delay for SiO₂ ALD on HfO₂, TiO₂, or Al₂O₃ when the cycle does not include an additional Hacac dosing step.

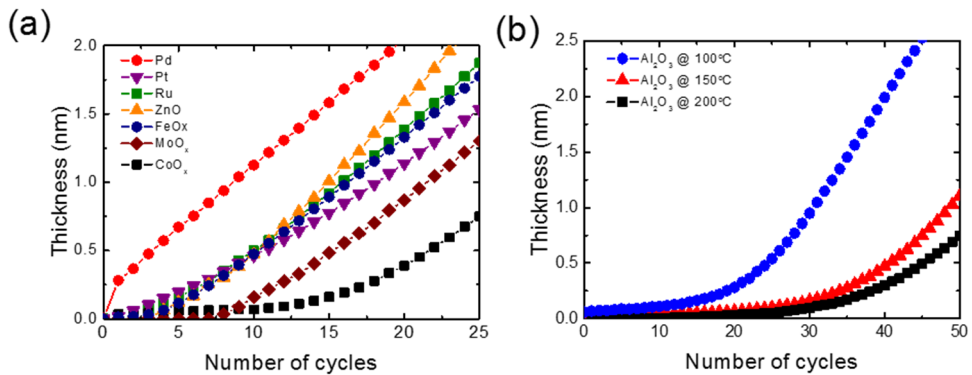


Figure 6.A3: Nucleation curves for SiO₂ deposited by ABC-type ALD **a)** on different starting surfaces and **b)** at two different temperatures on Al₂O₃. The graphs show the SiO₂ thickness as a function of the number of ALD cycles as measured by *in-situ* SE. A slightly longer nucleation delay was observed at 200 °C.

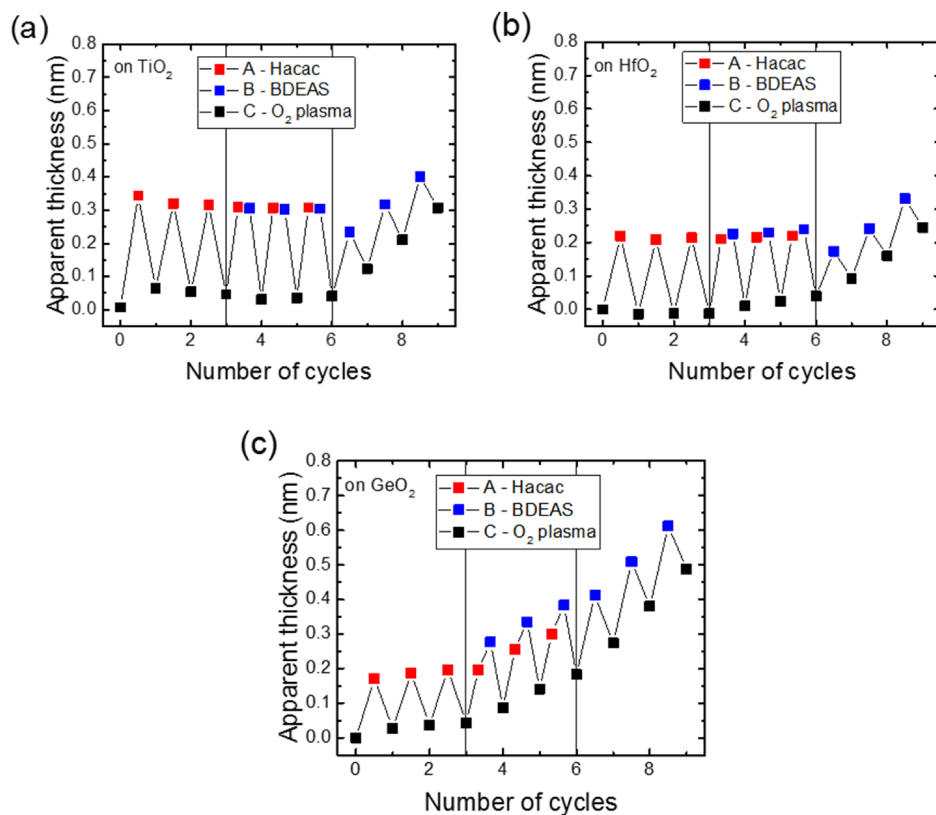


Figure 6.A4: Apparent thickness as measured after every reactant dosing pulse on **a)** TiO_2 , **b)** HfO_2 and **c)** GeO_2 starting surfaces. The left-hand parts of the figures represent 3 cycles with Hacac (A) and O_2 plasma (B) pulses, the middle parts 3 cycles with Hacac (A), BDEAS precursor (B), and O_2 plasma (C) pulses, and the right-hand parts 3 cycles with BDEAS precursor (B), and O_2 plasma (C) pulses. Figures (a) and (b) demonstrate that Hacac adsorbs on TiO_2 and HfO_2 , and is subsequently able to block BDEAS adsorption. On HfO_2 , the increase of the apparent thickness caused by Hacac adsorption is lower, suggesting that the coverage of Hacac is lower on HfO_2 as compared to Al_2O_3 or TiO_2 . Correspondingly, there is a small thickness increase when dosing BDEAS during the ABC cycles. Figure (c) shows that, in contrast to the SiO_2 data of Figure 6.3b, Hacac molecules adsorb on GeO_2 . However, the amount of Hacac appears to be insufficient to prevent adsorption of the BDEAS precursor, as revealed by the ABC-type ALD cycles.

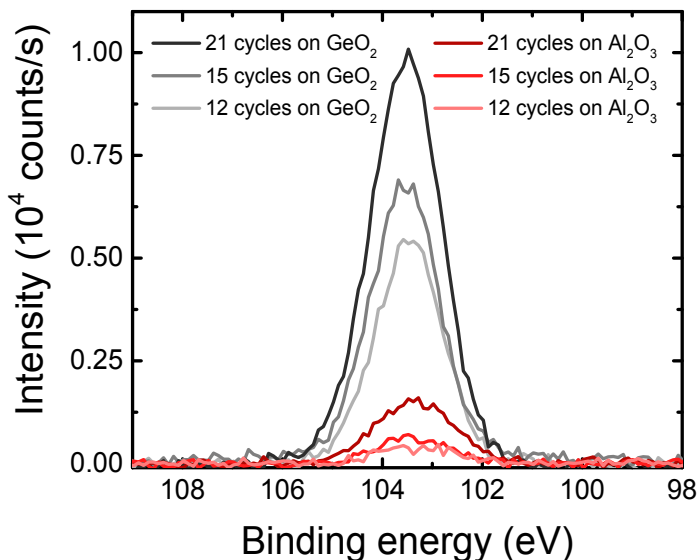


Figure 6.A5: Si 2p signal related to SiO₂ on GeO₂ and Al₂O₃ starting surfaces for 12, 15 and 21 ABC-type ALD cycles, as measured by XPS. The ratio of the integrated peak areas of Si 2p on Al₂O₃ and GeO₂ starting surfaces after 15 cycles is ~ 0.11 . This confirms that the precursor blocking is not fully effective.

6.A1. Computational Details

All electronic structure calculations were performed using the projector augmented wave function (PAW)^{1,2} as implemented in Vienna *Ab Initio* Simulation Package (VASP v.5.3.5).^{3–6} We used the generalized gradient approximation (GGA) to density functional theory (DFT)^{7,8} jointly with a plane-wave basis having a kinetic energy cut-off of 400 eV. We employed the Perdew–Burke–Ernzerhof (PBE) exchange correlation functional^{9,10} along with the Grimme’s DFT(PBE)-D3 method including Becke-Jonson damping¹¹ to account for Van der Waals interactions on an empirical basis. Structural relaxations were carried out using the conjugate gradient algorithm, where they were considered converged once all forces deviate less than 0.01 eV Å⁻¹ in two consecutive ionic steps. Besides, we used the default accuracy parameters for the FFT grid and real space projectors alongside a Gaussian smearing of 0.1 eV. No constraints have been applied on any atoms during the optimizations. Minimum energy paths (MEPs) along the predefined reaction pathways connecting a reactant-product pair were computed by optimizing several geometries collectively with the climbing-image nudge elastic band (CI-NEB) method.¹² CI-NEB optimizations were done with a looser convergence criterion on forces (0.1 eV Å⁻¹) utilizing the Hessian-based (G)-LBFGS¹³ algorithm as implemented in the VTST tool set.¹⁴

Due to their rather large size, the supercells (see **Selection of the Simulation Models**) could be integrated in reciprocal space with only one *K*-point coinciding with the Γ -

point. Relevantly, all of the supercells considered here were optimized in terms of size and shape using a rather large kinetic energy cut-off of 520 eV, only containing the Al_2O_3 or SiO_2 surfaces. Optimized supercells were later used in the simulations of Hacac binding on the relevant surfaces.

We computed the binding energies of Hacac on diverse hydroxylated surfaces (*i.e.* $\alpha\text{-Al}_2\text{O}_3$ and $\alpha\text{-SiO}_2$) through physisorption (ΔE_p) or chemisorption (ΔE_c) using Eqn. 6.A1.

$$\Delta E_{p/c} = E_{IS} - E_I - E_S \quad (6.A1)$$

where E_{IS} is the total energy of the physisorbed/chemisorbed substrate-inhibitor complex, E_I and E_S are the total energies of an isolated Hacac inhibitor and a given substrate surface. Here, physisorption can be described as the weak physical (non-covalent) binding of the Hacac inhibitor on a given silicon surface, whereas the chemisorption requires the chemical (covalent) binding of Hacac-oxygen that is likely accompanied by proton transfer to the target surface.

6.A2. Selection of the Simulation Models

ALD procedures used for preparing the starting surfaces of alumina and silica lead to deposition of amorphous layers of these oxides on a given substrate. Since the amorphous structures are challenging for DFT methods, we have adopted the most stable crystalline structures of alumina and silica following a common practice in the literature.

Starting from a bulk corundum structure, we created a surface slab of sapphire comprising the $\alpha\text{-Al}_2\text{O}_3(0001)$ crystalline structure with Al termination. This specific surface slab was previously shown to be the most stable phase in numerous experimental and theoretical studies (see for instance Refs. 15–24). Having ample under-coordinated sites, a freshly-cut (*i.e.* bare) $\alpha\text{-Al}_2\text{O}_3(0001)$ surface readily gets hydroxylated upon contact with moisture. Among two distinctive models of hydroxylated $\alpha\text{-Al}_2\text{O}_3(0001)$ surface, the partially-hydroxylated one formed by the dissociative binding of water molecules on adjacent surface sites,¹⁹ was shown to be the most relevant by reproducing the observed surface hydroxyl group coverage (theory:²⁵ $16 \mu\text{mol m}^{-2}$ vs. experiment:²⁶ $15 \mu\text{mol m}^{-2}$). The other fully-hydroxylated surface model (*i.e.* Gibbsite-like, constructed by replacing the top-most aluminum atoms) is therefore not included in this study, yet it has been subject of previous theoretical studies as to the Al_2O_3 ALD process.^{25,27–31} Starting from the bulk α -quartz structure,³² we constructed the $\alpha\text{-SiO}_2(0001)$ surface slab, while we fully hydroxylated the two surfaces, as the freshly-cleaved $\alpha\text{-SiO}_2$ surface has a high surface energy (like $\alpha\text{-Al}_2\text{O}_3$).³³ This hydroxylated $\alpha\text{-SiO}_2(0001)$ model has been used with success for investigating other similar ALD nucleation processes.^{34–38}

In order to accommodate an Hacac inhibitor on a given surface and to minimize the resulting interactions *via* periodic boundary conditions, supercells were kept rather large in the xy plane. Specifically, a 4×4 supercell of $\alpha\text{-Al}_2\text{O}_3$ (with the optimized dimensions

of $19.03 \times 19.03 \text{ \AA}^2$, covering 3.6 nm^2 surface, 383 atoms) and a 4×4 supercell of $\alpha\text{-SiO}_2$ ($19.42 \times 19.42 \text{ \AA}^2$, 3.8 nm^2 surface, 384 atoms). To limit the computational efforts, we have reduced the thickness of the $\alpha\text{-Al}_2\text{O}_3$ slab to 4 layers in our model, which turned out to yield binding energies within 2 meV of the commonly-used 6-layer model. For the hydroxylated $\alpha\text{-SiO}_2$, we used the model including 18-layers as suggested in Ref. 33, without further truncations. For minimizing the image interactions, the surface slabs in each prepared model were separated along the z axis by a vacuum thickness of 15 \AA or more.

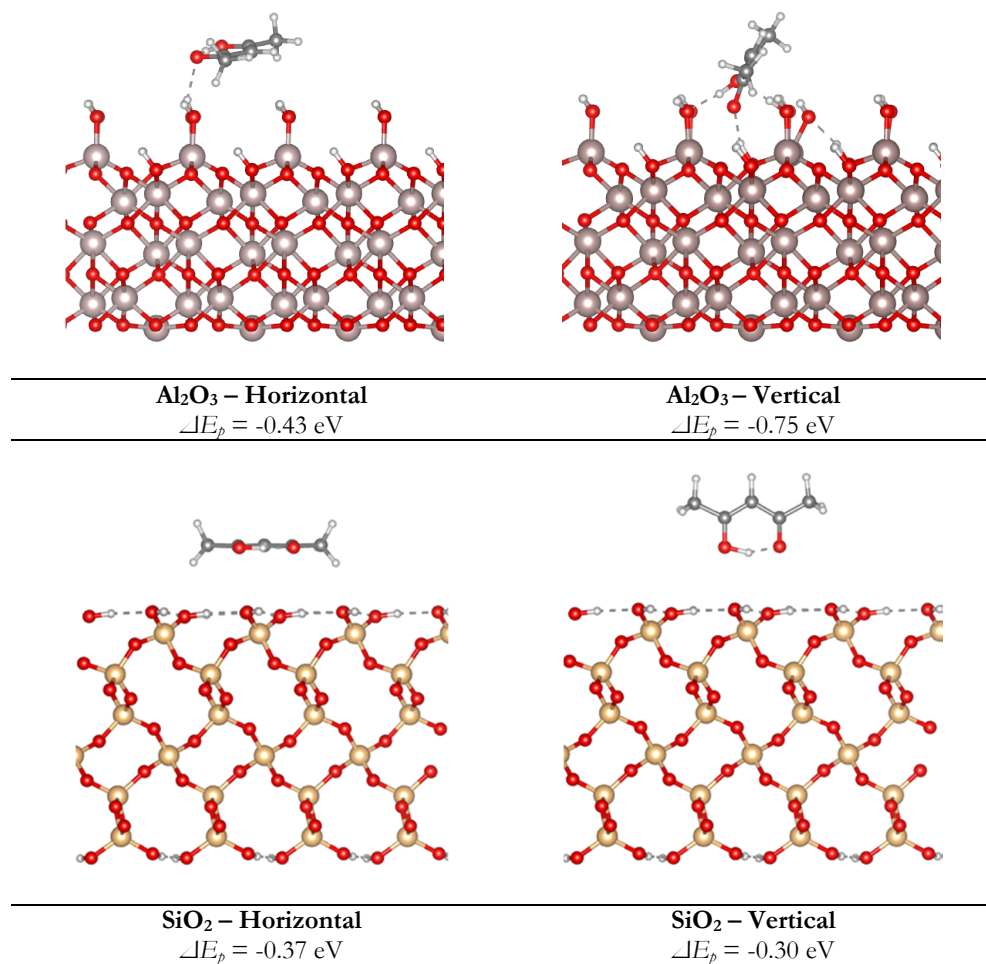
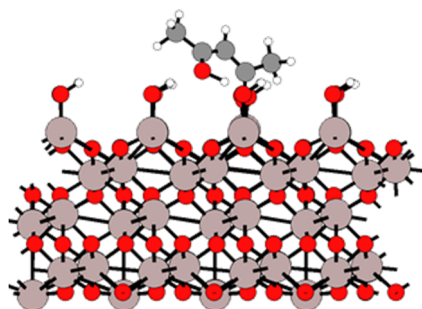


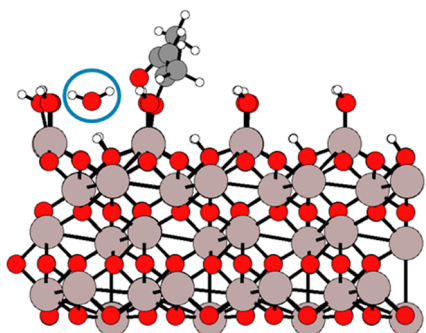
Figure 6.A6: DFT-based minimum-energy structures of the physisorbed Hacac species on (top) $\alpha\text{-Al}_2\text{O}_3(0001)$ and on (bottom) $\alpha\text{-SiO}_2(0001)$ surfaces. Two distinctive binding orientations are noted for the Hacac physisorption on both surfaces: (left) horizontal and (right) vertical. H-bonding interactions are also depicted with pale, dashed lines. Color code: silicon, pink; aluminum, light gray; hydrogen, white; oxygen, red; carbon, gray.

Vertical orientation of the Hacac adsorbate leads to a stronger physisorption on Al_2O_3 ($\Delta E_p = -0.75$ vs. -0.43 eV) due to an enhanced H-bonding network between the Hacac and the surface hydroxyl groups compared to horizontal alignment. On the contrary, the Hacac orientation has a less prominent effect on the binding energies on the SiO_2 surface ($\Delta E_p = -0.37$ vs. -0.30 eV for two orientations). The latter can be due to the alignment of surface hydroxyl sites, namely the Al_2O_3 surface has hydroxyl groups extending out of plane that render the surface more susceptible to hydrogen bonding with the Hacac adsorbate. In any binding orientation, though, physisorption on Al_2O_3 is stronger than SiO_2 , increasing the sticking probability of Hacac on Al_2O_3 and thus facilitating the subsequent chemisorption steps.

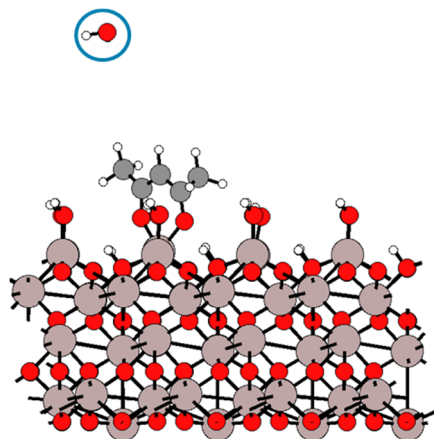


(a1) Al_2O_3 – Intermediate
 $\Delta E_c = -0.97$ eV

(a2) H_2O taken away
 Not-applicable as no H_2O is formed yet.



(b1) Al_2O_3 - Type A (Monodentate)
 $\Delta E_c = -0.91$ eV



(b2) H_2O taken away
 $\Delta E_c = -0.98$ eV

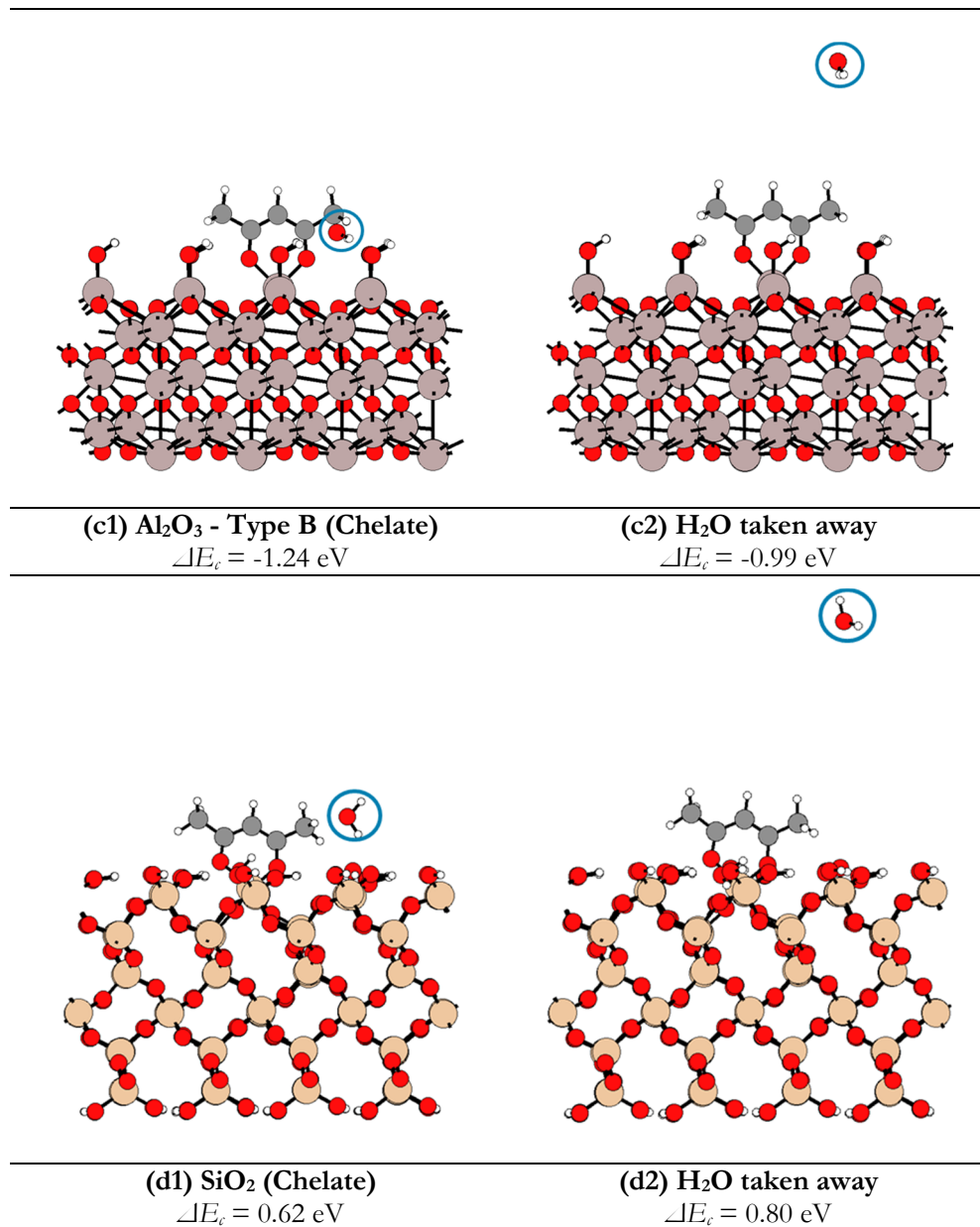


Figure 6.A7: DFT-based minimum-energy structures of (left panel) chemisorbed Hacac species on α -Al₂O₃(0001) and on α -SiO₂(0001) surfaces and (right panel) their variants where the H₂O by-product is taken away for probing the stabilizing effect of the byproduct. Chemisorption energies (ΔE_c) of each species are also given. Color code: silicon, pink; aluminum, light gray; hydrogen, white; oxygen, red; carbon, gray.

A metastable intermediate (a) is formed following the physisorption of Hacac on the Al_2O_3 surface, which is then converted to two distinctive chemisorbed products through a proton transfer to the surface: (b) Type A (monodentate) and (c) Type B (chelate). For SiO_2 , only a chelate product (d) could be located, whereas the designated monodentate product structures were readily converted to the chelate form.

The H_2O byproduct, which is predicted to form during the Hacac adsorption on both Al_2O_3 and SiO_2 surfaces, has a stabilizing effect on the final chemisorbed product, as revealed by increased relative energies (see energies of the b1-d1 vs. b2-d2 structures). This is mainly due to the enhanced H-bonding network the H_2O byproduct forms with the surface hydroxyl groups. One should also note that the monodentate (Type A) chemisorbed product could not be obtained -despite our efforts- when the byproduct H_2O is taken away from the surface, as this Type A product was readily converted to the chelate (Type B) product (b1 and b2). This point underlines once again that monodentate chemisorbed products are metastable and readily converted to the chelate form. Accumulating H_2O by-products could be competing with the Hacac adsorption by partly blocking available sites, and removal of these side products would enhance the Hacac inhibition power.

Considering that the Hacac would have already gained sufficient kinetic energy by physisorbing on the Al_2O_3 surface (*i.e.* $\Delta E_p = -0.75$ eV, Figure 6.A7a), it would readily overcome the overall barrier of 0.25 eV and be converted to the chelate (Type B) end-product. Nevertheless, to investigate the unlikely case where the monodentate intermediate was given enough time to relax, an unconstrained geometry optimization was carried out for this Type A intermediate, starting from point #2 on the MEP (Figure 6.A7a). During this optimization, which is free from nudge-elastic-band constraints, the intermediate further relaxed to a geometry (see Figure 6.A5a) that lies 0.22 eV below the physisorbed species ($\Delta E = -0.97$ eV with respect to the separated species). Even in this unlikely case, the conversion of the fully-relaxed monodentate intermediate to the chelate end-product is still kinetically accessible ($E_a = 0.40$ eV) at typical ALD temperatures even if with lower rates. Finally, based on the computed activation energies, the Arrhenius equation gives an estimate of $\sim 10^{25}$ -fold higher rate for Hacac binding on Al_2O_3 than on SiO_2 at the typical ALD temperature of 150 °C (assuming the pre-factor is similar in magnitude for both cases).

6.A3. Role of surface acidity on Hacac adsorption

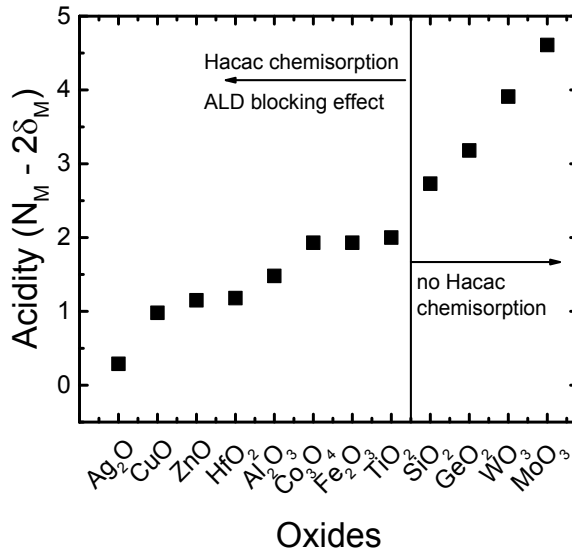


Figure 6.A8: Surface acidity as calculated following Ref. 39 for the different starting surfaces used in this work. The vertical line divides the materials depending on whether immediate growth or a nucleation delay is observed.

The acidity of a generic oxide with formula M_xO_y is calculated as the difference between the formal oxidation state of M and the Sanderson's partial charge on M in the compound. A good agreement was found between the calculated values and the experimental data except for MoO_3 . The MoO_3 surface is predicted to be the most acidic oxide among the calculated ones, but experimentally appears to allow for Hacac adsorption. Unfortunately, the Sanderson's electronegativity values for Pt, Pd and Ru are not reported in literature. According to Pauling's electronegativity however, one should expect the respective oxides to be slightly acidic and therefore allow for immediate growth of SiO_2 . This was experimentally proven to be the case for PdO whereas it does not hold for RuO_2 and PtO_2 . It should be noted that the calculated values are for ideal stoichiometric oxides and that in reality the surface acidity can be affected by the presence of a sub-stoichiometric oxide, degree of crystallinity, pre-treatments and deposition conditions (*e.g.* oxidation during the O_2 plasma step).⁴⁰

REFERENCES

- (1) Blöchl, P. E. Projector Augmented-Wave Method. *Phys. Rev. B* **1994**, *50*, 17953–17979.
- (2) Kresse, G. From Ultrasoft Pseudopotentials to the Projector Augmented-Wave Method. *Phys. Rev. B* **1999**, *59*, 1758–1775.
- (3) Kresse, G.; Hafner, J. *Ab Initio* Molecular Dynamics for Liquid Metals. *Phys. Rev. B* **1993**, *47*, 558–561.
- (4) Kresse, G.; Hafner, J. *Ab Initio* Molecular-Dynamics Simulation of the Liquid-Metal–amorphous-Semiconductor Transition in Germanium. *Phys. Rev. B* **1994**, *49*, 14251–14269.
- (5) Kresse, G.; Furthmüller, J. Efficiency of *Ab Initio* Total Energy Calculations for Metals and Semiconductors Using a Plane-Wave Basis Set. *Comput. Mater. Sci.* **1996**, *6*, 15–50.
- (6) Kresse, G. Efficient Iterative Schemes for *Ab Initio* Total-Energy Calculations Using a Plane-Wave Basis Set. *Phys. Rev. B* **1996**, *54*, 11169–11186.
- (7) Hohenberg, P. Inhomogeneous Electron Gas. *Phys. Rev.* **1964**, *136*, B864–B871.
- (8) Kohn, W.; Sham, L. J. Self-Consistent Equations Including Exchange and Correlation Effects. *Phys. Rev.* **1965**, *140*, A1133–A1138.
- (9) Perdew, J. P.; Burke, K.; Ernzerhof, M. Generalized Gradient Approximation Made Simple. *Phys. Rev. Lett.* **1996**, *77*, 3865–3868.
- (10) Perdew, J. P.; Burke, K.; Ernzerhof, M. Generalized Gradient Approximation Made Simple [Phys. Rev. Lett. *77*, 3865 (1996)]. *Phys. Rev. Lett.* **1997**, *78*, 1396–1396.
- (11) Grimme, S.; Antony, J.; Ehrlich, S.; Krieg, H. A Consistent and Accurate *Ab Initio* Parametrization of Density Functional Dispersion Correction (DFI-D) for the 94 Elements H–Pu. *J. Chem. Phys.* **2010**, *132*, 154104.
- (12) Henkelman, G.; Uberuaga, B. P.; Jónsson, H. A Climbing Image Nudged Elastic Band Method for Finding Saddle Points and Minimum Energy Paths. *J. Chem. Phys.* **2000**, *113*, 9901.
- (13) Nocedal, J. Updating Quasi-Newton Matrices with Limited Storage. *Math. Comput.* **1980**, *35*, 773–773.
- (14) VTST tool set for VASP.
- (15) Shapovalov, V.; Truong, T. N. *Ab Initio* Study of Water Adsorption on α -Al₂O₃ (0001) Crystal Surface. *J. Phys. Chem. B* **2000**, *104*, 9859–9863.
- (16) Kelber, J. A. Alumina Surfaces and Interfaces under Non-Ultrahigh Vacuum Conditions. *Surf. Sci. Rep.* **2007**, *62*, 271–303.
- (17) Felice, R. Di; Northrup, J. E. Theory of the Clean and Hydrogenated Al₂O₃ (0001)-(1×1) Surfaces. *Phys. Rev. B* **1999**, *60*, R16287–R16290.
- (18) Marmier, A.; Parker, S. C. *Ab Initio* Morphology and Surface Thermodynamics of α -Al₂O₃. *Phys. Rev. B* **2004**, *69*, 115409.
- (19) Lodziana, Z.; Norskov, J. K.; Stoltze, P. The Stability of the Hydroxylated (0001) Surface of α -Al₂O₃. *J. Chem. Phys.* **2003**, *118*, 11179–11188.
- (20) Hernández, N. C.; Graciani, J.; Márquez, A.; Sanz, J. F. Cu, Ag and Au Atoms Deposited on the α -Al₂O₃(0 0 0 1) Surface: A Comparative Density Functional Study. *Surf. Sci.* **2005**, *575*, 189–196.
- (21) Jensen, T. N.; Meinander, K.; Helveg, S.; Foster, A. S.; Kulju, S.; Musso, T.; Lauritsen, J. V. Atomic Structure of a Spinel-Like Transition Al₂O₃(100) Surface. *Phys. Rev. Lett.* **2014**, *113*, 106103-1-5.
- (22) Cruz Hernandez, N.; Marquez, A.; Sanz, J. F.; Gomes, J. R. B.; Illas, F. Density Functional Theory Study of Co, Rh, and Ir Atoms Deposited on the α -Al₂O₃ (0001) Surface. *J. Phys. Chem. B* **2004**, *108*, 15671–15678.
- (23) Guo, J.; Ellis, D. E.; Lam, D. J. Electronic Structure and Energetics of Sapphire (0001) and (11 $\bar{0}$ 2) Surfaces. *Phys. Rev. B* **1992**, *45*, 13647–13656.
- (24) Wang, X.-G.; Chaka, A.; Scheffler, M. Effect of the Environment on α -Al₂O₃ (0001) Surface Structures. *Phys. Rev. Lett.* **2000**, *84*, 3650–3653.
- (25) Weckman, T.; Laasonen, K. First Principles Study of the Atomic Layer Deposition of Alumina by TMA–H₂O-Process. *Phys. Chem. Chem. Phys.* **2015**, *17*, 17322–17334.
- (26) Ott, A. W.; Klaus, J. W.; Johnson, J. M.; George, S. M. Al₂O₃ Thin Film Growth on Si(100) Using Binary Reaction Sequence Chemistry. *Thin Solid Films* **1997**, *292*, 135–144.
- (27) Elliott, S. D.; Greer, J. C. Simulating the Atomic Layer Deposition of Alumina from First Principles.

- J. Mater. Chem.* **2004**, *14*, 3246.
- (28) Elliott, S. D.; Dey, G.; Maimaiti, Y.; Ablat, H.; Filatova, E. A.; Fomengia, G. N. Modeling Mechanism and Growth Reactions for New Nanofabrication Processes by Atomic Layer Deposition. *Adv. Mater.* **2016**, *28*, 5367–5380.
- (29) Elliott, S. D.; Pinto, H. P. Modelling the Deposition of High-K Dielectric Films by First Principles. *J. Electroceramics* **2004**, *13*, 117–120.
- (30) Elliott, S. D. Predictive Process Design: A Theoretical Model of Atomic Layer Deposition. *Comput. Mater. Sci.* **2005**, *33*, 20–25.
- (31) Shirazi, M.; Elliott, S. D. Cooperation between Adsorbates Accounts for the Activation of Atomic Layer Deposition Reactions. *Nanoscale* **2015**, *7*, 6311–6318.
- (32) Lager, G. A.; Jorgensen, J. D.; Rotella, F. J. Crystal Structure and Thermal Expansion of α -Quartz SiO₂ at Low Temperatures. *J. Appl. Phys.* **1982**, *53*, 6751–6756.
- (33) Goumans, T. P. M.; Wander, A.; Brown, W. A.; Catlow, C. R. A. Structure and Stability of the (001) α -Quartz Surface. *Phys. Chem. Chem. Phys.* **2007**, *9*, 2146–2152.
- (34) Mamei, A.; Kuang, Y.; Aghaee, M.; Ande, C. K.; Karasulu, B.; Creatore, M.; Mackus, A. J. M.; Kessels, W. M. M.; Roozeboom, F. Area-Selective Atomic Layer Deposition of In₂O₃:H Using a μ -Plasma Printer for Local Area Activation. *Chem. Mater.* **2017**, *29*, 921–925.
- (35) Kuang, Y.; Macco, B.; Karasulu, B.; Ande, C. K.; Bronsveld, P. C. P.; Verheijen, M. A.; Wu, Y.; Kessels, W. M. M.; Schropp, R. E. I. Towards the Implementation of Atomic Layer Deposited In₂O₃:H in Silicon Heterojunction Solar Cells. *Sol. Energy Mater. Sol. Cells* **2017**, *163*, 43–50.
- (36) Huang, L.; Han, B.; Han, B.; Derecskei-Kovacs, A.; Xiao, M.; Lei, X.; O'Neill, M. L.; Pearlstein, R. M.; Chandra, H.; Cheng, H. First-Principles Study of a Full Cycle of Atomic Layer Deposition of SiO₂ Thin Films with Di(sec-Butylamino)silane and Ozone. *J. Phys. Chem. C* **2013**, *117*, 19454–19463.
- (37) Han, B.; Zhang, Q.; Wu, J.; Han, B.; Karwacki, E. J.; Derecskei, A.; Xiao, M.; Lei, X.; O'Neill, M. L.; Cheng, H. On the Mechanisms of SiO₂ Thin-Film Growth by the Full Atomic Layer Deposition Process Using Bis(t-Butylamino)silane on the Hydroxylated SiO₂ (001) Surface. *J. Phys. Chem. C* **2012**, *116*, 947–952.
- (38) Kim, D. H.; Baek, S. Bin; Kim, Y. C. Energy Barriers for Trimethylaluminum Reaction with Varying Surface Hydroxyl Density. *Appl. Surf. Sci.* **2011**, *258*, 225–229.
- (39) Jeong, N. C.; Lee, J. S.; Tae, E. L.; Lee, Y. J.; Yoon, K. B. Acidity Scale for Metal Oxides and Sanderson's Electronegativities of Lanthanide Elements. *Angew. Chem. Int. Ed.* **2008**, *47*, 10128–10132.
- (40) Nortier, P.; Fourre, P.; Saad, A. B. M.; Saur, O.; Lavalley, J. C.; Mohammed, A. B.; Lavalley, J. C.; Saad, A. B. M.; Saur, O.; Lavalley, J. C. Effects of Crystallinity and Morphology on the Surface Properties of Alumina. *Appl. Catal.* **1990**, *61*, 141–160.

Chapter 7

Isotropic Atomic Layer Etching of ZnO Using Acetylacetone and O₂ Plasma*

Atomic layer etching (ALE) provides Ångström-level control over material removal and holds potential for addressing the challenges in nanomanufacturing faced by conventional etching techniques. Recent research has led to the development of two main classes of ALE: ion-driven plasma processes yielding anisotropic (or directional) etch profiles and thermally-driven processes for isotropic material removal. In this work, we extend the possibilities to obtain isotropic etching by introducing a plasma-based ALE process for ZnO which is radical-driven and utilizes acetylacetone (Hacac) and O₂ plasma as reactants. In-situ spectroscopic ellipsometry measurements indicate self-limiting half-reactions with etch rates ranging from 0.5 to 1.3 Å/cycle at temperatures between 100 and 250 °C. The ALE process was demonstrated on planar and 3D substrates consisting of a regular array of semiconductor nanowires conformally-covered by ALD-grown ZnO. Transmission electron microscopy studies conducted on the ZnO-covered nanowires before and after ALE proved the isotropic nature and the damage-free characteristics of the process. In-situ infrared spectroscopy measurements were used to elucidate the self-limiting nature of the ALE half-reactions and the reaction mechanism. During the Hacac etching reaction that is assumed to produce Zn(acac)₂, carbonaceous-species adsorbed on the ZnO surface are suggested as the cause of the self-limiting behavior. The subsequent O₂ plasma step resets the surface for the next ALE cycle. High etch selectivities (~80:1) over SiO₂ and HfO₂ were demonstrated. Preliminary results indicate that the etching process can be extended to other oxides such as Al₂O₃.

7.1 INTRODUCTION

Advanced nanodevice manufacturing requires atomic scale processing techniques with superior control of film thickness and material properties over challenging (3D) substrates.¹⁻⁴ In the past decade, atomic layer deposition (ALD) has become an established technique to provide unparalleled control over thin-film deposition, even on the high-aspect ratio structures that are increasingly used in semiconductor industry. On the other hand, its etching counterpart, i.e., atomic layer etching (ALE), has only recently re-gained considerable attention. ALE allows for layer-by-layer selective etching with Ångström-level control from planar and/or 3D substrates. As in ALD, this is achieved through the use of alternated and self-limiting half-reactions, that are interleaved by purge steps.⁵⁻⁹

*Mameli, A.; Verheijen, M.A.; Mackus, A. J. M.; Kessels, W. M. M.; Roozeboom, F. *submitted for publication*

ALE has been a research topic since its first conception by Yoder in 1988.¹⁰ The technique is now on the verge of being introduced in advanced manufacturing flows. So far, a large part of the plasma ALE processes reported in the literature makes use of alternate surface modification utilizing thermally-driven or plasma reactions during half-reaction A, and material removal by means of accelerated energetic species (e.g., ions or neutral beams) during half-reaction B.¹¹ In most of the cases, this is typically achieved by applying a bias voltage on the substrate table during plasma exposure, leading to *directional/anisotropic* removal of the modified layer.^{6,8,9} Figure 7.1a schematically depicts a directional/anisotropic ALE cycle and the resulting etch profile.

Recently, George and co-workers expanded the ALE toolset by introducing thermal ALE, which makes use of sequential and self-limiting thermochemical reactions.^{2,7,12–15} Thermal ALE can allow isotropic material removal. Figure 7.1b represents a schematic for an *isotropic* ALE cycle and the corresponding etch profile. During the half-reaction A, thermochemical reactions are used to modify the surface of the target material. During half-reaction B, the modified layer is removed by means of a suited co-reactant (Figure 7.1b).

Anisotropic and isotropic etch profiles are required for different applications, one of the most prototypical examples being: fin field effect transistors (FinFETs) for directional/anisotropic ALE (Figure 7.1a) and gate-all-around (GAA) field effect transistors for isotropic ALE (Figure 7.1b).¹⁶ The increasing demand for controlled etch processes and for novel functional materials requires the development of new ALE approaches to process a wider range of materials while meeting the stringent limitations in safety, etch selectivity, etch profile and process compatibility.^{16,17}

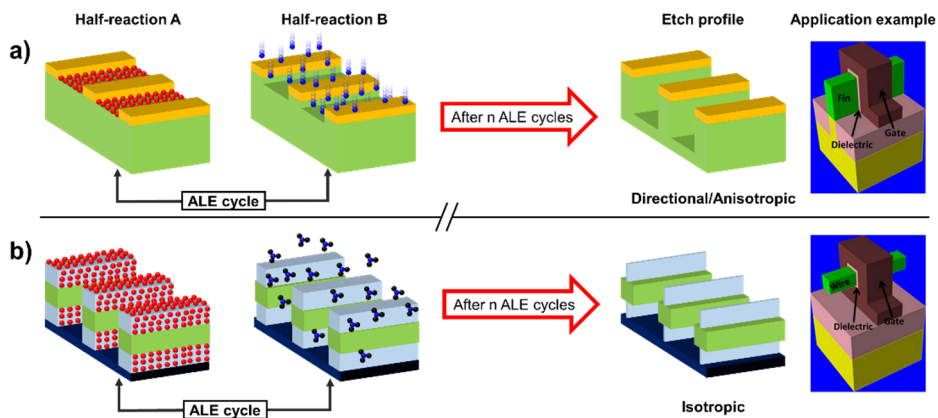


Figure 7.1: Schematics of a two-step **a)** directional/anisotropic and **b)** isotropic ALE cycle. During half-reaction A, the target material is modified by means of a self-limiting reaction. An anisotropic etch profile is obtained when using species that provide directionality during half-reaction B, for example ions that are accelerated perpendicularly to the substrate in the so-called plasma sheath before impinging on the substrate surface. Conversely, an isotropic etch profile is obtained when using non-directional species. For both processes, the control over the thickness of the etched material is accomplished by repeating half-reactions A and B in a cyclic fashion. Selective material removal is achieved by the appropriate choice of reactants. Application examples after Ref. 16 are provided (right side) for both directional ALE (Fin Field Effect Transistors) and isotropic ALE (gate-all-around Field Effect Transistors).

In this work, we introduce a novel approach for isotropic ALE by combining a thermochemical half-reaction with a plasma radical-driven half-reaction. In particular, a thermochemical reaction (half-reaction A) that employs acetylacetone (Hacac) is used to remove material. This reaction appears to be self-terminating due to the formation of a carbonaceous surface layer that inhibits further etching. Next, a radical-driven O₂ plasma pulse (half-reaction B) is used to restore the surface for the next ALE cycle. The process concept is inspired by the use of Sn(acac)₂ in thermal ALE,^{2,13,18} and β-diketones in organic vapor phase etching.^{19–24}

ALD-grown polycrystalline ZnO layers were chosen for demonstrating the feasibility of our process. This plasma-based ALE process can serve as an alternative approach to thermal ALE of ZnO using trimethylaluminum (TMA) and fluorine-based chemistry, which was recently conducted on planar substrates by Zywojko *et al.*¹⁴

We observed that alternating dosage of Hacac and O₂ plasma led to a reproducible etch per cycle (EPC) of 1.3 Å. Furthermore, the isotropic nature of the ALE process presented in this work was demonstrated by etching ZnO that was pre-deposited on an array of vertical nanowires (NWs). A reaction mechanism is proposed on the basis of *in-situ* Fourier transformed infrared (FTIR) measurements. Finally, we discuss the possibility of extending this process to other oxide films, such as Al₂O₃, and show high etch selectivities (~80:1) over SiO₂ and HfO₂.

7.2 Experimental section

7.2.A. ZnO preparation by ALD. ZnO thin films were deposited on 2 x 2 cm² c-Si wafer coupons using ALD in an OpAL reactor from Oxford Instruments equipped with a 200-mm substrate table. Diethylzinc (DEZ) and water (H₂O) were employed as the precursor and the co-reactant, respectively, at a substrate temperature of 250 °C. The recipe consisted of 40 ms of DEZ and 100 ms of H₂O exposure interleaved by 5 s argon purges. The same recipe was also employed to deposit conformal layers of ZnO on substrates with GaP nanowires (NWs), having a 7% Ge-doped Si (Si:Ge) shell.

From separate studies on the bare nanowires, it is known that these wires exhibit atomically flat sidewall facets, making them an excellent substrate for etch profile studies.²⁵ The temperature was 150 °C during the deposition on the NW samples.

7.2.B. ALE process of ZnO. The etching experiments were carried out in an Oxford Instruments FlexAL reactor, equipped with a remote inductively-coupled plasma (ICP) source (13.56 MHz), a 200-mm substrate table, a turbomolecular pump and a loadlock. Prior to all etching experiments the samples were subjected to a 3 minutes O₂ plasma cleaning step at a pressure of ~10 mTorr and a power of 200 W. Acetylacetone (Hacac, ≥ 99% ReagentPlus®; CAS 123-54-6) from Sigma-Aldrich was employed without further purification. The Hacac was kept at room temperature in a stainless steel container and vapor drawn into the chamber using multiple pulses of 2 s each and a 1 s hold step (~400 mTorr), interleaved by 5 s long Ar purges. The ALE cycle was

completed by a 5 s O₂ plasma step at a pressure of ~10 mTorr and an ICP power of 200 W, followed by a 5 s Ar purge. For a schematic of the cycle see the Appendix, Figure 7.A1. The etching experiments were conducted at substrate temperatures of 100, 150, 200 or 250 °C.

7.2.C. Analytical Methods. *In-situ* and *ex-situ* spectroscopic ellipsometry (SE) was performed using a J.A. Woollam M2000D ellipsometer. A Cauchy parametrization was used to model the Psi- and Delta-values measured by SE. X-ray photoelectron spectroscopy (XPS) measurements were carried out using a K-Alpha system from Thermo Scientific. To study the resulting etch profile of this ALE process, an array of NW was covered with ZnO layers using ALD (see above). Part of this array was subjected to the ALE process and compared with non-etched NWs samples using transmission electron microscopy (TEM). Several NWs were taken and analyzed using TEM to determine the ZnO thickness before and after ALE. The TEM measurements were conducted in high-angle annular dark-field (HAADF) scanning TEM (STEM) and high resolution TEM modes using a probe-corrected TEM (JEOL JEM ARM 200F). The ZnO thickness was measured at distinct regions along the length of each NW sample separated by 1 μm using ImageJ software.²⁶ Twenty thickness measurements were taken at each region and averaged to account for the ZnO surface roughness.

In-situ Fourier transform infrared (FTIR) transmission spectroscopy experiments were carried out in a home-built ALD setup (which is similar to the reactor used for the ALE experiments), using a Bruker Vector FTIR spectrometer with a mid-infrared light source (Globar ~10,000 – 50 cm⁻¹) and a liquid N₂-cooled mercury cadmium telluride (MCT) detector with a spectral range of 12,000 – 550 cm⁻¹. FTIR measurements were performed on ZnO nanopowder (< 100 nm particle size) that was pellet-pressed on a tungsten mesh. The powder was heated to 150 °C by passing a current through the mesh. The reaction chamber was pressurized with Hacac vapor and held at a constant pressure of ~1 Torr for 30 s to ensure adsorption of Hacac on the powder. The pressure during the plasma step was ~10 mTorr.

7.3. RESULTS AND DISCUSSION

7.3.A. ZnO ALE on planar substrates

The etching behavior was investigated using *in-situ* SE by monitoring the ZnO film thickness upon exposure to three different pulse sequences: **1**) alternated pulses of Hacac and O₂ gas, **2**) alternated pulses of Hacac and O₂ plasma, and **3**) multiple pulses of only O₂ plasma. The O₂ gas pulses in sequence **1** were included to keep the cycle time constant and as a control experiment to assess whether the O₂ plasma is necessary to achieve etching. Figure 7.2 shows the ZnO thickness variation for pulse sequences **1**, **2**, and **3**, for a process temperature of 250 °C. Pulsing sequences **1** and **3** resulted in no

significant ZnO thickness change (Figures 7.2a,c), while sequence **2** induced a linear thickness decrease (Figure 7.2b). An EPC value of $1.31 \pm 0.08 \text{ \AA}$ was calculated by linear regression of the data shown in Figure 7.2b. These results demonstrate that alternated doses of Hacac and O₂ plasma (sequence **2**) are required to achieve ZnO etching and that no significant ZnO etching is observed when dosing only one of the two reactants. As shown in Figure 7.2a, upon exposure to sequence **1**, an apparent thickness increase of $\sim 2 \text{ \AA}$ was observed after the first 10 cycles. Such an apparent thickness increase can be attributed to the adsorption of Hacac molecules on the ZnO surface, similarly to what was observed on Al₂O₃ substrates for the ABC-type area-selective ALD of SiO₂.²⁷ We note that the term “apparent thickness” is used here to reflect the fact that the SE modelling did not take the dielectric function of the adsorbed species into account. Therefore, the measured thickness might not directly correspond to the physical thickness.²⁸ After this initial increase, the thickness was observed to slowly decrease with a negligible formal value of $\sim 0.05 \text{ \AA/cycle}$. We note, however, that the measured thickness does not decrease below the starting ZnO thickness, indicating that no continuous etching occurs. The thickness decrease might be due to partial decomposition (and possibly desorption) of acac-species on the ZnO surface as it will be discussed below.

Upon exposure to sequence **3**, a negligible thickness decrease of $\sim 1 \text{ \AA}$ was measured over 40 O₂ plasma pulses (Figure 7.2c), revealing that no significant etching occurs during the O₂ plasma step ($\sim 0.03 \text{ \AA/cycle}$).

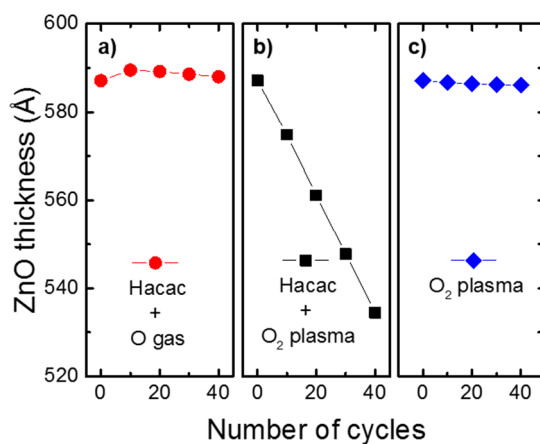


Figure 7.2: ZnO thickness evolution as a function of the number of cycles of: **a)** Hacac and O₂ gas (circles); **b)** Hacac and O₂ plasma (squares); **c)** O₂ plasma pulses (diamonds). Linear ZnO thickness decrease is observed only when alternating Hacac and O₂ plasma doses. All the experiments were carried out at a temperature of 250 °C.

To investigate the self-limiting nature of the ALE half-reactions, *in-situ* SE was used to measure the EPC at a fixed exposure time of the first half-reaction, while varying the exposure time of the second half-reaction, and *vice versa*. Figures 7.3(a,b) show the

measured EPC values as a function of the Hacac and O₂ plasma exposures, respectively. The EPC as a function of the Hacac exposure was observed to saturate at a value of $1.31 \pm 0.08 \text{ \AA}$, for a total Hacac exposure time of 27 s (including the hold steps as described in the experimental session). The EPC as a function of the O₂ plasma exposure time shows saturation already after 2 s. Longer O₂ plasma exposures result in EPC values that lie within the error range. Taken together, these data demonstrate the self-limiting nature of the two half-reactions employed.

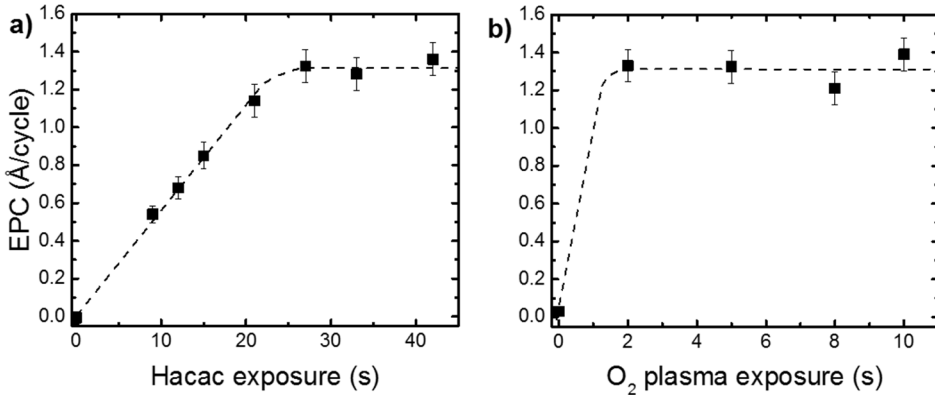


Figure 7.3: **a)** Etch per cycle (EPC) as a function of the Hacac exposure time for a fixed O₂ plasma step of 5 s. Saturation (self-limiting behavior) was reached for a total Hacac exposure of 27 s, resulting in an EPC of 1.31 \AA/cycle . **b)** EPC as a function of the O₂ plasma exposure time for a fixed Hacac dose of 27 s. A saturated EPC value was measured for all the investigated O₂ plasma exposure times (≥ 2 s). The processing temperature was 250 °C. The dashed lines serve as a guide to the eye.

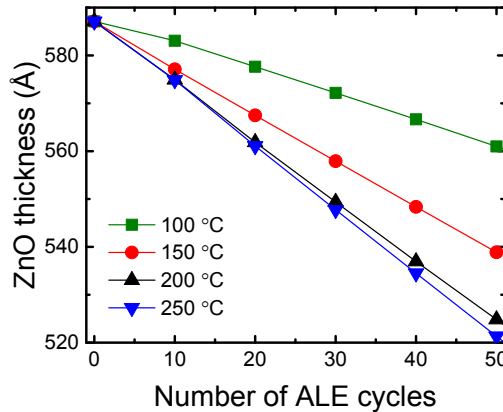


Figure 7.4: ZnO thickness as a function of the number of ALE cycles for temperatures between 100 and 250 °C, as measured by *in-situ* spectroscopic ellipsometry.

Figure 7.4 displays the ZnO thickness as a function of the number of ALE cycles for temperatures in a range of 100-250 °C. The ZnO thickness was found to decrease linearly with the number of ALE cycles for each temperature, in line with a layer-by-layer etching mechanism. The EPCs were determined to be 0.54 ± 0.05 , 0.97 ± 0.07 , 1.25 ± 0.08 and 1.31 ± 0.08 Å for processing temperatures of 100, 150, 200 and 250 °C, respectively.

The surface of the ZnO thin films, before and after ALE was investigated by *ex-situ* XPS to check for possible stoichiometry alterations and for the presence of surface contamination (see Appendix, Table A.I.). The stoichiometry, as in the ratio Zn/O, was found to be preserved over 100 ALE cycles. A comparable amount of carbon (12-13 at.%) was measured on both surfaces which can be attributed to adsorption of adventitious carbon on the sample upon exposure to atmosphere.

7.3.B. ZnO ALE on 3D substrates

The ALE process was also tested on a 3D substrate consisting of a regular array of vertical nanowires (NWs) (see Appendix, Figure 7.A2), conformally-covered with a 60 ± 2 nm thick polycrystalline ZnO layer. The NWs were then subjected to 120 cycles of the ALE process at 250 °C. Figures 7.5(a,b) show the TEM images of a pair of 7 μm long NWs, one before and one after ALE. For each of those NWs, high-magnification STEM images were acquired every 1 μm along the length of the NW. For the complete set of STEM images see the Appendix, Figure 7.A3. Figures 7.5(a,b) also display high-magnification STEM images recorded at the top, center and bottom regions of each NW. STEM images of an extra independent pair of NWs from the same array, before and after ALE, are shown in the Figure 7.A4, together with the measured ZnO thicknesses.

The STEM images reveal a decrease in ZnO thickness after the ALE process. The film thickness reduction (15 ± 2 nm) is comparable at all regions of the NW, as depicted in Figure 7.5c. From the STEM-measured thickness differences (before and after ALE), an averaged EPC of 1.3 ± 0.2 Å was obtained across the full length of the nanowire. This EPC value is in excellent agreement with the EPC measured by *in-situ* SE (i.e., 1.31 Å/cycle). The result clearly demonstrates the accurate etch control and the isotropic nature of the ALE process. Figure 7.5d shows a high-resolution TEM image of the top ZnO layers after the ALE process. Lattice fringes are visible up to the top surface layer, demonstrating that the ZnO surface retains its crystallinity upon ALE.²⁹ This result indicates that no significant damage or amorphization occurs during the ALE process. The observed isotropic etch profile and the fact that the ZnO surface is not damaged or amorphized is in line with a negligible role of ions in the ALE mechanism, illustrating that the O₂ plasma ALE half-reaction is predominantly driven by radicals. Indeed, for the employed plasma conditions described in the Experimental Section 7.2.B., ion energies of only ~20 eV can be expected,³⁰ which makes sputtering of ZnO through ion-induced collisions unlikely.

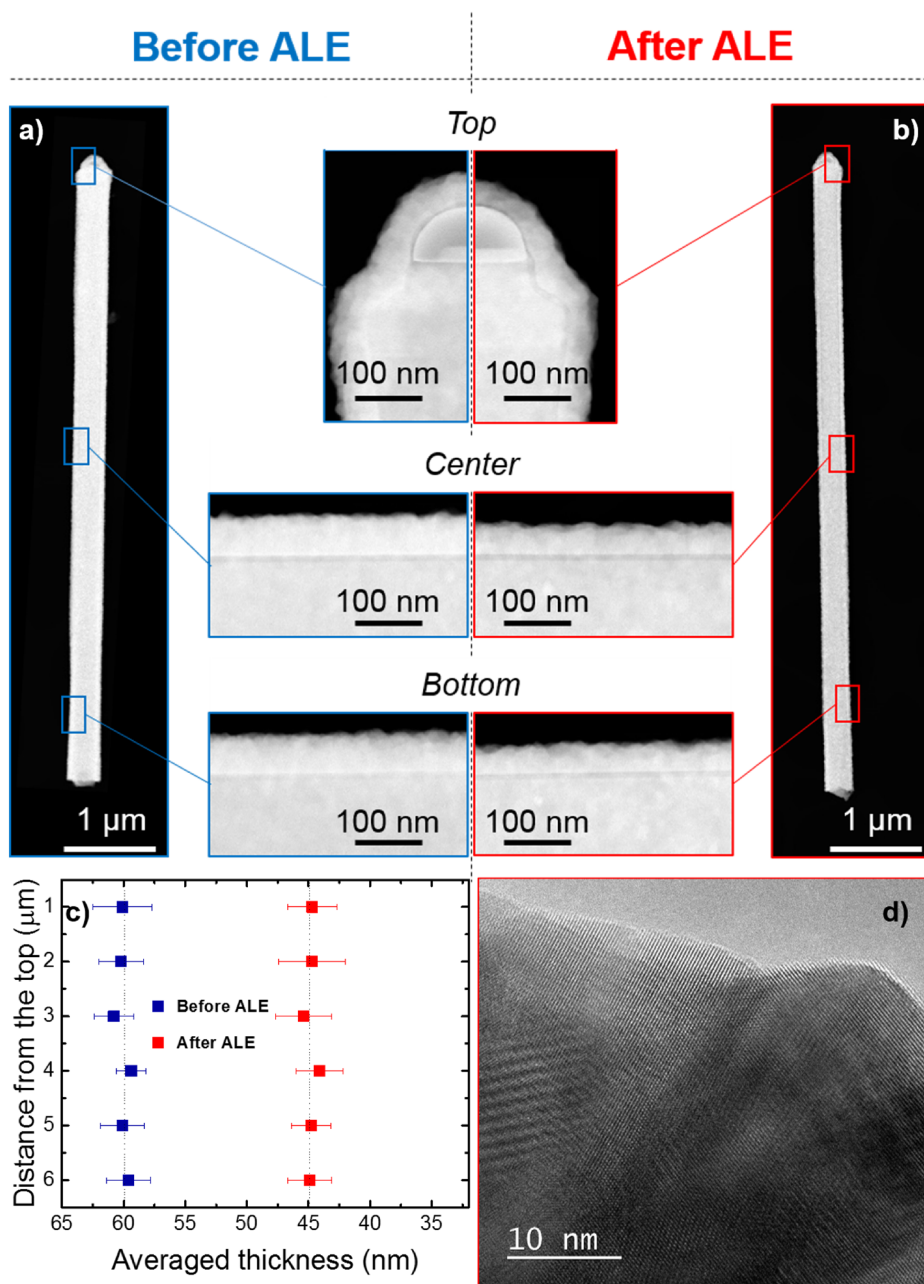


Figure 7.5: Low-magnification HAADF-STEM image of a ZnO-covered nanowire together with high-magnification images of the top, center and bottom regions **a)** before and **b)** after ALE. **c)** Averaged ZnO thicknesses as measured every μm along the nanowires before and after ALE. The standard deviation of the measurements is taken as the error. **d)** High-magnification TEM image of the ZnO layer after the ALE process. Lattice fringes are observable up to the top surface, indicating that no surface amorphization occurs during the ALE process.

7.3.C. Proposed reaction mechanism

In-situ FTIR spectroscopy was used to elucidate the self-limiting behavior of the ALE process. Figures 7.6(a,b) show the FTIR spectra after three consecutive Hacac or O₂ plasma exposures on pellet-pressed ZnO powder at a temperature of 150 °C. After the 1st Hacac dose, adsorption of Hacac is shown by the appearance of positive peaks between 900 and 1600 cm⁻¹ (Figure 7.6a). These peaks can be assigned to acac-species bonded to Zn²⁺ sites.^{31–33} Most likely, Hacac adsorbs through a proton transfer reaction.²⁷

Figure 7.6a shows that the peak intensities remain constant after the 1st exposure, indicating saturation behavior for the Hacac adsorption on ZnO. The ZnO stretching modes (~480 cm⁻¹) fall outside the detection range of the setup and could not be monitored during the *in-situ* measurements. Figure 7.6b reveals that upon O₂ plasma exposure, acac-species are removed from the ZnO surface. In this case, the spectra are referenced to the preceding Hacac exposure (3rd Hacac dose), therefore the same absorption features show up as negative peaks, pointing at the removal of acac-species from the surface. The removal most likely take place through combustion reactions. Prolonged O₂ plasma exposure caused a slight increase in the absorbance of the negative peaks, indicating further acac-species elimination. However, Figure 7.6c shows that complete removal is not achieved. This is probably due to the high surface area and complex topography of the ZnO powder that hamper the plasma reactions in the ‘bulk’ of the powder.

The *in-situ* FTIR data can be used to propose a reaction mechanism and hence an explanation for the self-limiting nature of the ALE process. As schematically depicted in Figure 7.7, volatile Zn(acac)₂ is assumed to be the etching product of the first half-reaction (A), i.e., ZnO starts to be etched. At the same time, the FTIR data in Figure 7.6a indicate that during this etching reaction, stable surface acac-species build up on the ZnO surface.

These acac-species may lead to surface site blocking and quench the etching reaction, thereby explaining the self-limiting nature of the process. Similar conclusions were also drawn by Lee *et al.* for the thermal ALE of AlF₃ using Sn(acac)₂ and HF.⁷ They also ascribe the self-limiting etching of AlF₃ to the presence of acac-containing surface species that inhibit the main etching reaction. In addition, Helms *et al.* have proposed that part of the Hacac may decompose on the metal oxide surfaces and form a carbonaceous layer that can also contribute to inhibiting the etching reaction.³⁴ In the second half-reaction (B), acac-groups/carbonaceous species are removed from the ZnO surface by the O₂ plasma step, as corroborated by the FTIR data in Figure 7.6b. Therefore, the half-reactions can be repeated in the following cycle.

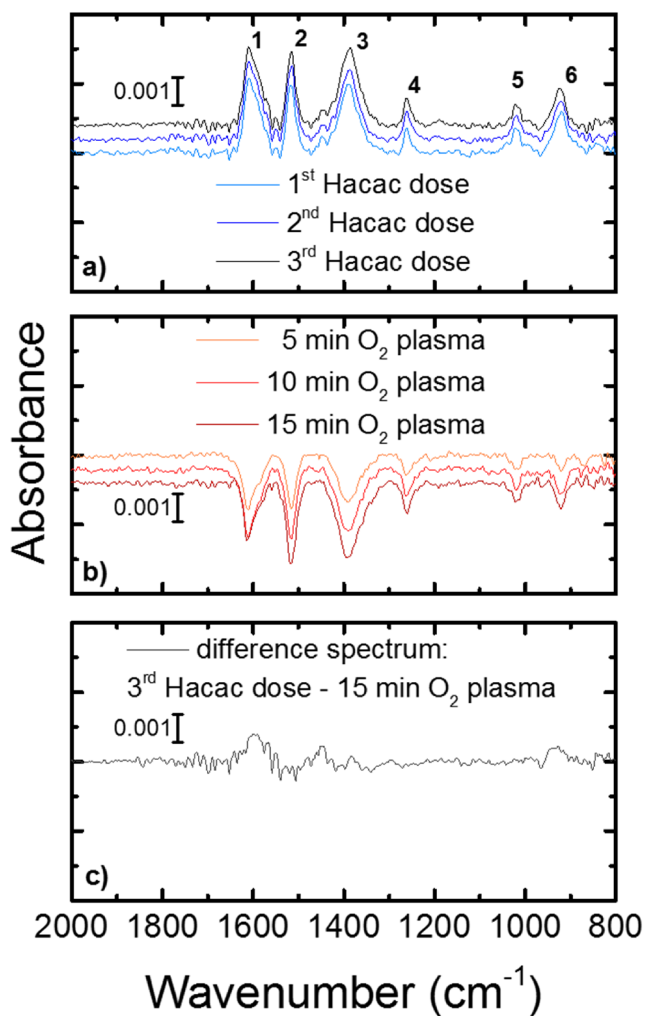


Figure 7.6: Difference infrared spectra for three consecutive exposures of **a)** Hacac and of **b)** O₂ plasma on ZnO powder at 150 °C. The reference spectrum for the Hacac doses was the bare ZnO powder. For the O₂ plasma pulses the spectra were referenced to the preceding Hacac exposure (3rd Hacac dose), therefore the removal of species shows up as negative peaks. The spectrum baselines have been equally shifted for clarity. **c)** Difference spectrum between the 3rd Hacac dose and the 15 min O₂ plasma exposure, indicating the presence of residual acac-species on the ZnO surface. Peak assignment, after Ref. ³³: **1** $\nu(\text{C}=\text{O})$; **2** $\nu(\text{C}=\text{C}) + \nu(\text{C}=\text{O})$, $\nu(\text{C}=\text{O}) + \delta(\text{C}-\text{H})$; **3** $\delta(\text{C}-\text{H}) + \delta(\text{CH}_3)$; **4** $\nu(\text{C}-\text{C}) + \nu(\text{C}-\text{CH}_3)$; **5** $\delta(\text{CH}_3)$; **6** $\delta(\text{C}-\text{CH}_3) + \nu(\text{C}=\text{O})$, where ν and δ indicate stretching and bending, respectively.

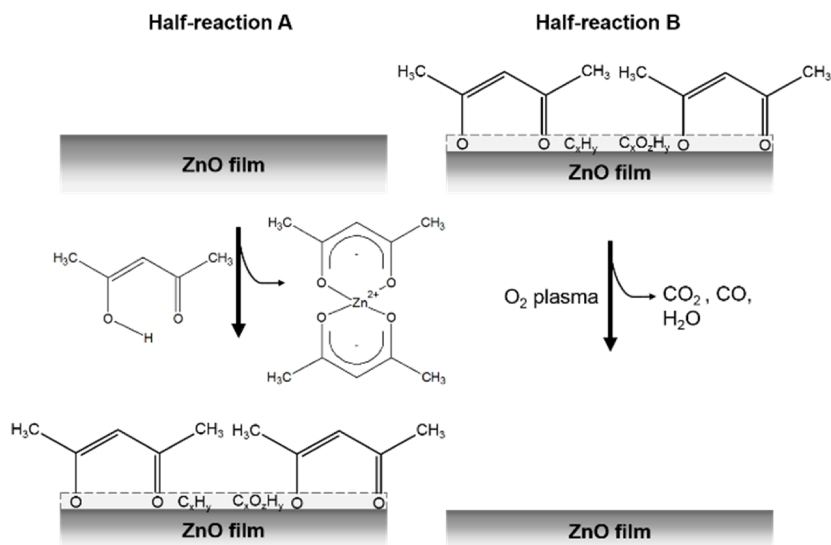


Figure 7.7: Schematic of the proposed reaction mechanism for ALE of ZnO. During half-reaction A, volatile $\text{Zn}(\text{acac})_2$ is assumed to form from Hacac and ZnO, while leaving residual acac-species and other possible carbonaceous fragments. During half-reaction B, an O_2 plasma combusts the carbonaceous surface-species and resets the ZnO surface for the next cycle.

7.3.D. Extension to other materials and etch selectivity

The possibilities of extending this ALE process to other materials were also explored. To this end, substrates with ALD-prepared ZnO, HfO_2 and Al_2O_3 thin films and a 90 nm thermally grown SiO_2 layer were subjected to 120 cycles of the ALE process at a temperature of 250 °C within the same run. Their thicknesses were measured by *ex-situ* SE, before and after ALE. Virtually no thickness reduction (~ 0.2 nm) was observed for SiO_2 and HfO_2 , while a decrease in thickness of 1.8 nm was observed for Al_2O_3 and ~ 16.0 nm for ZnO. These results translates into high etch selectivities ($\sim 80:1$) for ZnO over SiO_2 and HfO_2 , at 250 °C.

The absence of SiO_2 etching can be explained by density functional theory simulations that we performed for the chemisorption reaction of Hacac on SiO_2 .²⁷ On this surface, the Hacac chemisorption was found to be thermodynamically unfavorable, therefore SiO_2 etching was not expected. The etching of HfO_2 , on which Hacac does adsorb,²⁷ would require the formation of $\text{Hf}(\text{acac})_4$, which we believe is unlikely on a surface because of steric reasons.

On Al_2O_3 , the measured thickness difference translates into a formal EPC value of 0.15 Å. Similar EPC values between 0.14 and 0.61 Å (at 150 and 250 °C, respectively) have been reported for the thermal ALE of Al_2O_3 using $\text{Sn}(\text{acac})_2$ and HF.³ Our results indicate that the ALE process introduced in this work may be explored and optimized (temperature, dosing time, etc.) to enable the etching of materials other than ZnO.

Considering the proposed reaction mechanism (Figure 7.7), it can be inferred that metal oxides that coordinate up to three acac^- ligands may be etched using this process. As described by George *et al.*, Sc_2O_3 , Ga_2O_3 , Fe_2O_3 , Co_2O_3 , and Al_2O_3 can all form volatile compounds with Hacac having vapor pressures ranging from 1 to 4 Torr at 150 °C.^{2,35} Therefore, it should be possible to achieve etching of these materials. Conversely, no etching should be expected in the case of metal oxides in which the metal cation is in the 4⁺ oxidation state.

7.3.E. Merits and opportunities provided by the plasma approach

When comparing the plasma-based ALE process presented in this work with the complementary thermal ALE process of ZnO using TMA and HF,¹⁴ several differences can be highlighted. While the thermal ALE process was reported to leave residual Al and F impurities on the ZnO surface,¹⁴ this plasma-based ALE approach shows no significant surface contamination, thereby suggesting a cleaner etching chemistry. In the case of thermal ALE, no ZnO etching was observed for temperatures below 220 °C, conversely the plasma-based ALE can be used to etch ZnO at temperatures as low as 100 °C. Furthermore, the two ALE processes allow for different and complementary etch selectivities, thereby expanding the possibilities of ALE. For example, the thermal ALE process, using TMA and HF, can be used to achieve etching of ZnO, Al_2O_3 , SiO_2 and HfO_2 .^{14,36,37} Conversely, the plasma-based ALE process, using Hacac and O_2 plasma can be used to etch ZnO and Al_2O_3 , with high etch selectivities over SiO_2 and HfO_2 . This complementary difference in etch selectivity represents a valuable addition to the isotropic ALE toolbox.

In addition, the versatility of a plasma reactant can be used to tune the same etching chemistry from an isotropic to an anisotropic mode by carefully adjusting the plasma conditions.³⁸ During the plasma step, an external bias voltage can be applied to the substrate to provide directionality, if required. Alternatively, the ALE process can be extended by introducing a third step, consisting of a separate anisotropic plasma.

Finally, the use of different plasma chemistries can pave the way to the processing of other materials than oxides, e.g. nitrides, sulfides, etc.

7.4. CONCLUSIONS

A novel isotropic plasma-based approach for ALE of ZnO was demonstrated. This process employs alternating exposures of the ZnO surface to acetylacetone (Hacac) and O_2 plasma. The self-limiting behavior was verified for both half-reactions using *in-situ* spectroscopic ellipsometry measurements. Furthermore, the isotropic nature of this process was established by carrying out ALE on a ZnO-covered 3D-nanostructured substrate consisting of a vertical nanowire array. Controlled and uniform decrease of

the ZnO film thickness across the entire nanowire length was demonstrated. Damage-free (no amorphization) ALE was corroborated by showing that the uppermost ZnO layers remained crystalline after 120 cycles.

A reaction mechanism was proposed for the ZnO ALE process in which Hacac is assumed to produce volatile $\text{Zn}(\text{acac})_2$. In addition, the Hacac pulse also results in acac-species adsorbed on the ZnO surface and possibly other carbonaceous-species that quench the etching reaction. The O_2 plasma co-reactant removes the adsorbed organic species and resets the ZnO surface, allowing for subsequent etching in the next cycle. Furthermore, etching of Al_2O_3 and a high etch selectivity ($\sim 80:1$) over SiO_2 and HfO_2 were demonstrated.

When compared to isotropic thermal ALE processes in the literature, the isotropic plasma-based ALE process presented in this work exhibits different etch selectivities and a wider temperature window. Therefore, we believe that such plasma-based approach will provide additional pathways for achieving isotropic ALE.

REFERENCES

- (1) Fang, M.; Ho, J. C. Area-Selective Atomic Layer Deposition: Conformal Coating, Subnanometer Thickness Control, and Smart Positioning. *ACS Nano* **2015**, *9*, 8651–8654.
- (2) George, S. M.; Lee, Y. Prospects for Thermal Atomic Layer Etching Using Sequential, Self-Limiting Fluorination and Ligand-Exchange Reactions. *ACS Nano* **2016**, *10*, 4889–4894.
- (3) Lee, Y.; George, S. M. Atomic Layer Etching of Al₂O₃ Using Sequential, Self-Limiting Thermal Reactions with Sn(acac)₂ and Hydrogen Fluoride. *ACS Nano* **2015**, *9*, 2061–2070.
- (4) Kong, L.; Song, Y.; Kim, J. D.; Yu, L.; Wasserman, D.; Chim, W. K.; Chiam, S. Y.; Li, X. Damage-Free Smooth-Sidewall InGaAs Nanopillar Array by Metal-Assisted Chemical Etching. *ACS Nano* **2017**, *11*, 10193–10205.
- (5) Lill, T.; Kanarik, K. J.; Tan, S.; Shen, M.; Hudson, E.; Pan, Y.; Marks, J.; Vahedi, V.; Gottscho, R. A. Directional Atomic Layer Etching. *Encycl. Plasma Technol.* **2016**, 133–142.
- (6) Kanarik, K. J.; Lill, T.; Hudson, E. A.; Sriraman, S.; Tan, S.; Marks, J.; Vahedi, V.; Gottscho, R. A. Overview of Atomic Layer Etching in the Semiconductor Industry. *J. Vac. Sci. Technol. A Vacuum, Surfaces, Film.* **2015**, *33*, 20802.
- (7) Lee, Y.; Dumont, J. W.; George, S. M. Atomic Layer Etching of AlF₃ Using Sequential, Self-Limiting Thermal Reactions with Sn(acac)₂ and Hydrogen Fluoride. *J. Phys. Chem. C* **2015**, *119*, 25385–25393.
- (8) Faraz, T.; Roozeboom, F.; Knoops, H. C. M.; Kessels, W. M. M. Atomic Layer Etching□: What Can We Learn from Atomic Layer Deposition□? *ECS J. Solid State Sci. Technol.* **2015**, *4*, N5023–N5032.
- (9) Oehrlein, G. S.; Metzler, D.; Li, C. Atomic Layer Etching at the Tipping Point: An Overview. *ECS J. Solid State Sci. Technol.* **2015**, *4*, N5041–N5053.
- (10) Yoder, M. N. US Pat. 4,756,794 A **1988**.
- (11) Jhon, Y. I.; Min, K. S.; Yeom, G. Y.; Jhon, Y. M. Understanding Time-Resolved Processes in Atomic-Layer Etching of Ultra-Thin Al₂O₃ Film Using BCl₃ and Ar Neutral Beam. *Appl. Phys. Lett.* **2014**, *105*, 93104.
- (12) Lee, Y.; Dumont, J. W.; George, S. M. Trimethylaluminum as the Metal Precursor for the Atomic Layer Etching of Al₂O₃ Using Sequential, Self-Limiting Thermal Reactions. *Chem. Mater.* **2016**, *28*, 2994–3003.
- (13) Lee, Y.; DuMont, J. W.; George, S. M. Atomic Layer Etching of HfO₂ Using Sequential, Self-Limiting Thermal Reactions with Sn(acac)₂ and HF. *ECS J. Solid State Sci. Technol.* **2015**, *4*, N5013–N5022.
- (14) Zywojtko, D. R.; George, S. M. Thermal Atomic Layer Etching of ZnO by a “Conversion-Etch” Mechanism Using Sequential Exposures of Hydrogen Fluoride and Trimethylaluminum. *Chem. Mater.* **2017**, *29*, 1183–1191.
- (15) Johnson, N. R.; Sun, H.; Sharma, K.; George, S. M. Thermal Atomic Layer Etching of Crystalline Aluminum Nitride Using Sequential, Self-Limiting Hydrogen Fluoride and Sn(acac)₂ Reactions and Enhancement by H₂ and Ar Plasmas. *J. Vac. Sci. Technol. A Vacuum, Surfaces, Film.* **2016**, *34*, 50603.
- (16) Carver, C. T.; Plombon, J. J.; Romero, P. E.; Suri, S.; Tronic, T. A.; Turkot, R. B. J. Atomic Layer Etching: An Industry Perspective. *ECS J. Solid State Sci. Technol.* **2015**, *4*, N5005–N5009.
- (17) Lee, C. G. N.; Kanarik, K. J.; Gottscho, R. A. The Grand Challenges of Plasma Etching: A Manufacturing Perspective. *J. Phys. D. Appl. Phys.* **2014**, *47*, 273001.
- (18) Lee, Y.; DuMont, J. W.; George, S. M. Mechanism of Thermal Al₂O₃ Atomic Layer Etching Using Sequential Reactions with Sn(acac)₂ and HF. *Chem. Mater.* **2015**, *27*, 3648–3657.
- (19) Chen, J. K.-C.; Altieri, N. D.; Kim, T.; Chen, E.; Lill, T.; Shen, M.; Chang, J. P. Directional Etch of Magnetic and Noble Metals. I. Role of Surface Oxidation States. *J. Vac. Sci. Technol. A Vacuum, Surfaces, Film.* **2017**, *35*, 05C3041–05C3046.
- (20) Chen, J. K.-C.; Altieri, N. D.; Kim, T.; Chen, E.; Lill, T.; Shen, M.; Chang, J. P. Directional Etch of Magnetic and Noble Metals. II. Organic Chemical Vapor Etch. *J. Vac. Sci. Technol. A Vacuum, Surfaces, Film.* **2017**, *35*, 05C305.
- (21) Nigg, H. L.; Ford, L. P.; Masel, R. I. Surface-Mediated Reaction Pathways of 2,4-Pentanedione on Clean and Oxygen Covered Cu(210). *J. Vac. Sci. Technol.* **1998**, *A16*, 3064–3067.
- (22) Kytokivi, A.; Rautiainen, A.; Root, A. Reaction of Acetylacetone Vapour with γ -Alumina. *J. Chem. Soc. Faraday Trans.* **1997**, *93*, 4079–4084.
- (23) George, M. A.; Hess, D. W.; Beck, S. E.; Young, K.; Bohling, D. A.; Voloshin, G.; Lane, A. P. Reaction

- of 1,1,1,5,5,5-Hexafluoro-2,4-Pentanedione (H^+hfac) with Iron and Iron Oxide Thin Films. *J. Electrochem. Soc.* **1996**, *143*, 3257–3266.
- (24) Jain, A.; Kodas, T. T.; Hampden-Smith, M. J. Thermal Dry-Etching of Copper Using Hydrogen Peroxide and Hexafluoroacetylacetone. *Thin Solid Films* **1995**, *269*, 51–56.
- (25) Hauge, H. I. T.; Conesa-Boj, S.; Verheijen, M. A.; Koelling, S.; Bakkers, E. P. A. M. Single-Crystalline Hexagonal Silicon–Germanium. *Nano Lett.* **2017**, *17*, 85–90.
- (26) <https://imagej.nih.gov/ij/>.
- (27) Mameli, A.; Merckx, M. J. M.; Karasulu, B.; Roozeboom, F.; Kessels, W. M. M.; Mackus, A. J. M. Area-Selective Atomic Layer Deposition of SiO_2 Using Acetylacetone as a Chemoselective Inhibitor in an ABC-Type Cycle. *ACS Nano* **2017**, *11*, 9303–9311.
- (28) Langereis, E.; Heil, S. B. S.; Knoops, H. C. M.; Keuning, W. van de Sanden, M. C. M.; Kessels, W. M. M. In Situ Spectroscopic Ellipsometry as a Versatile Tool for Studying Atomic Layer Deposition. *J. Appl. Phys. D Appl. Phys.* **2009**, *42*, 073001–1/19.
- (29) Pécz, B.; Baji, Z.; Lábadi, Z.; Kovács, A. ZnO Layers Deposited by Atomic Layer Deposition. In *Journal of Physics: Conference Series in 18th Microscopy of Semiconducting Materials Conference (MSM XVIII)*; 2013; Vol. 471, p. 12015.
- (30) Profijt, H. B.; Kudlacek, P.; van de Sanden, M. C. M.; Kessels, W. M. M. Ion and Photon Surface Interaction during Remote Plasma ALD of Metal Oxides. *J. Electrochem. Soc.* **2011**, *158*, G88–G91.
- (31) National Institute of Standards and Technology. NIST Webbook. In *Chemistry WebBook, NIST Standard Reference Database Number 69, National Institute of Standards and Technology*; P.J. Linstrom and W.G. Mallard, Ed.; Gaithersburg MD, 20899.
- (32) Tayyari, S. F.; Milani-nejad, F. Vibrational Assignment of Acetylacetone. *Spectrochim. Acta - Part A Mol. Biomol. Spectrosc.* **2000**, *56*, 2679–2691.
- (33) Niven, M. L. ; Thornton, D. A. Band Assignment in the Infrared Spectrum of Zinc Acetylacetonate Monohydrate by ^{18}O , ^{68}Zn and ^{64}Zn -Labelling. *Spectrosc. Lett.* **1980**, *13*, 419–425.
- (34) Helms, A. B.; Burgess, J. S.; Street, S. C. Surface Studies of 2,4-Pentanedione on γ - Al_2O_3 /NiAl (100) and NiAl (100). *Surf. Sci.* **2009**, *603*, 3262–3266.
- (35) Lee, Y.; George, S. M. Atomic Layer Etching of Al_2O_3 Using Sequential, Self-Limiting Thermal Reactions with $Sn(acac)_2$. *ACS Nano* **2015**, *9*, 2061–2070.
- (36) Lee, Y.; Huffman, C.; George, S. M. Selectivity in Thermal Atomic Layer Etching Using Sequential, Self-Limiting Fluorination and Ligand-Exchange Reactions. *Chem. Mater.* **2016**, *28*, 7657–7665.
- (37) DuMont, J. W.; Marquardt, A. E.; Cano, A. M.; George, S. M. Thermal Atomic Layer Etching of SiO_2 by a “Conversion-Etch” Mechanism Using Sequential Reactions of Trimethylaluminum and Hydrogen Fluoride. *ACS Appl. Mater. Interfaces* **2017**, *9*, 10296–10307.
- (38) Sherpa, S. D.; Ventzek, P. L. G.; Ranjan, A. Quasiatomic Layer Etching of Silicon Nitride with Independent Control of Directionality and Selectivity. *J. Vac. Sci. Technol. A Vacuum, Surfaces, Film.* **2017**, *35*, 05C310.

Appendix

Isotropic Atomic Layer Etching of ZnO Using Acetylacetone and O₂ Plasma

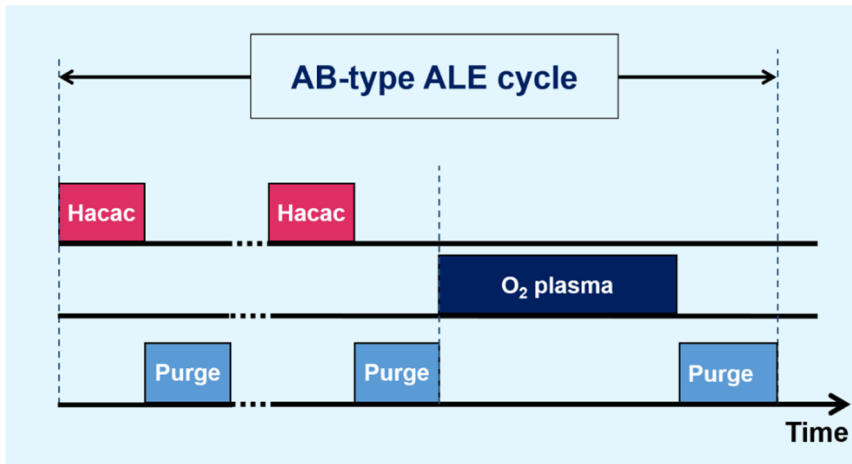
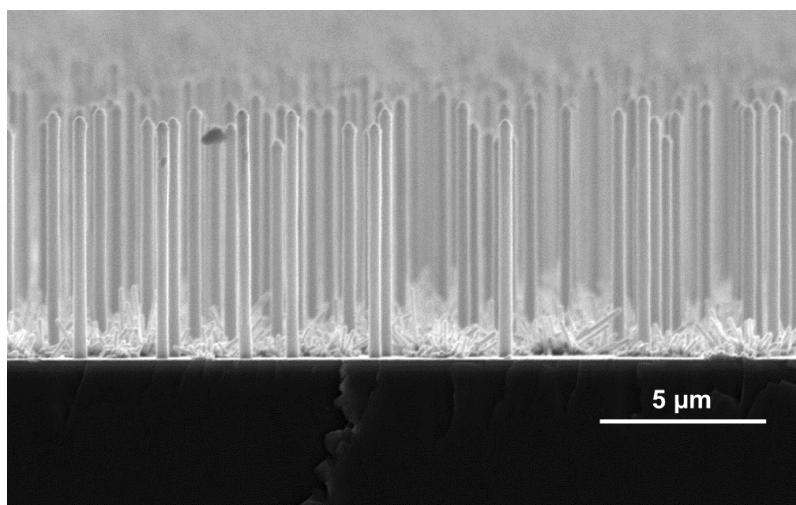


Figure 7.A1: Schematic of the ZnO ALE cycle developed in this work. The Hacac dose and the first argon purge have been repeated n times, with $1 < n < 14$ in order to avoid pressurizing of the reaction chamber during the Hacac dose. Saturation was achieved for $n = 9$. The O₂ plasma step follows the repeated Hacac/purge pulses, and the cycle is completed by another purge step.

Table A.I. XPS surface scans of ZnO samples before and after ALE.

	C at.%	Zn at.%	O at.%
Before ALE	13 ± 1	42 ± 1	45 ± 1
After ALE	12 ± 1	43 ± 1	46 ± 1

**Figure 7.A2:** SEM cross-sectional view of the GaP NW substrate, after ZnO ALD. The nanowires are 7.0 μm long and spaced 1.5 μm apart from each other, and designed in a regular honeycomb pattern.

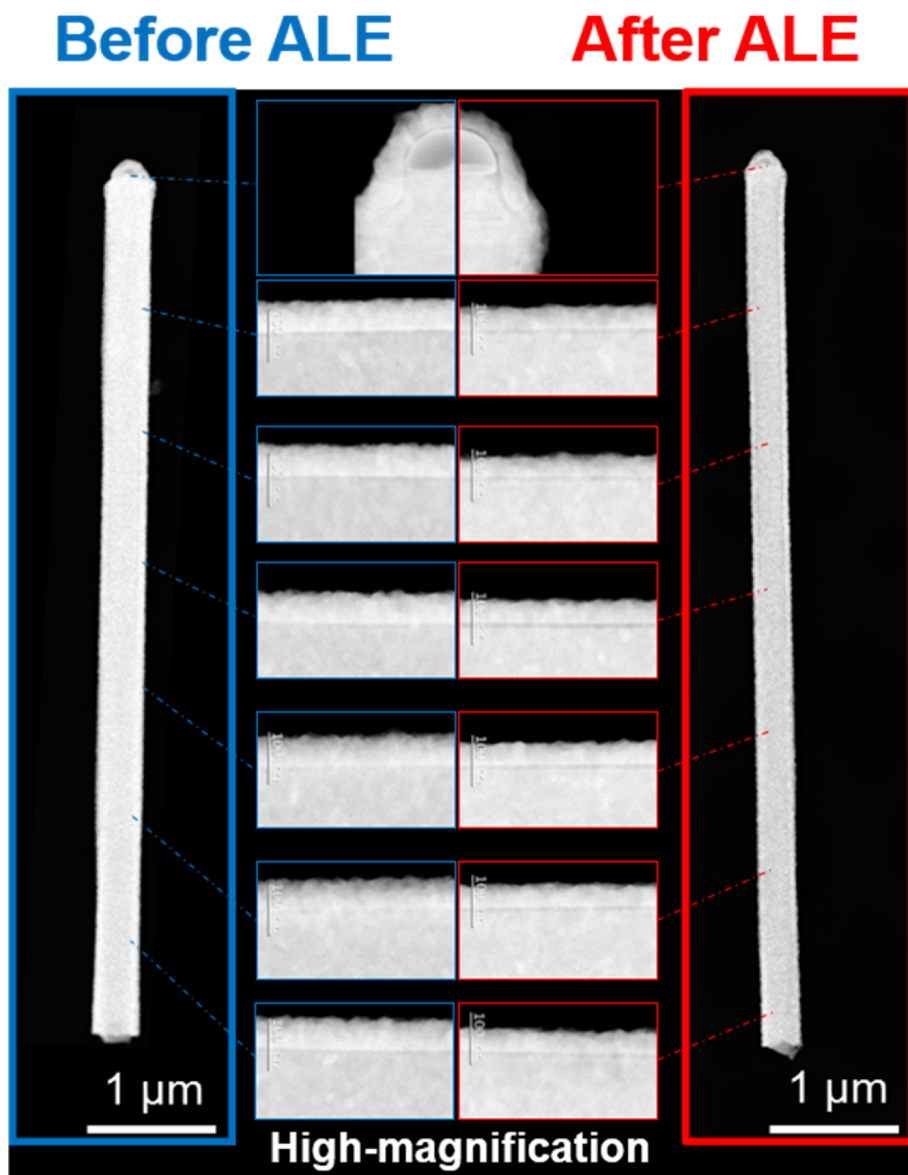


Figure 7.A3. Low-magnification HAADF-STEM image of the ZnO-covered nanowire also shown in Figure 7.5 of Chapter 7. High-magnification images of seven distinct regions separated by 1 μm along the vertical axis of the nanowire are shown in the middle. Note that the as-deposited ZnO is thinner on top of the gold (Au) nanoparticle used to make the NWs, indicating a nucleation delay for the ALD of ZnO on the Au surface. Yet, the thickness differences before and after ALE are comparable to those measured along the NWs. The consistent difference in ZnO thickness confirms the isotropic character of the ALE process.

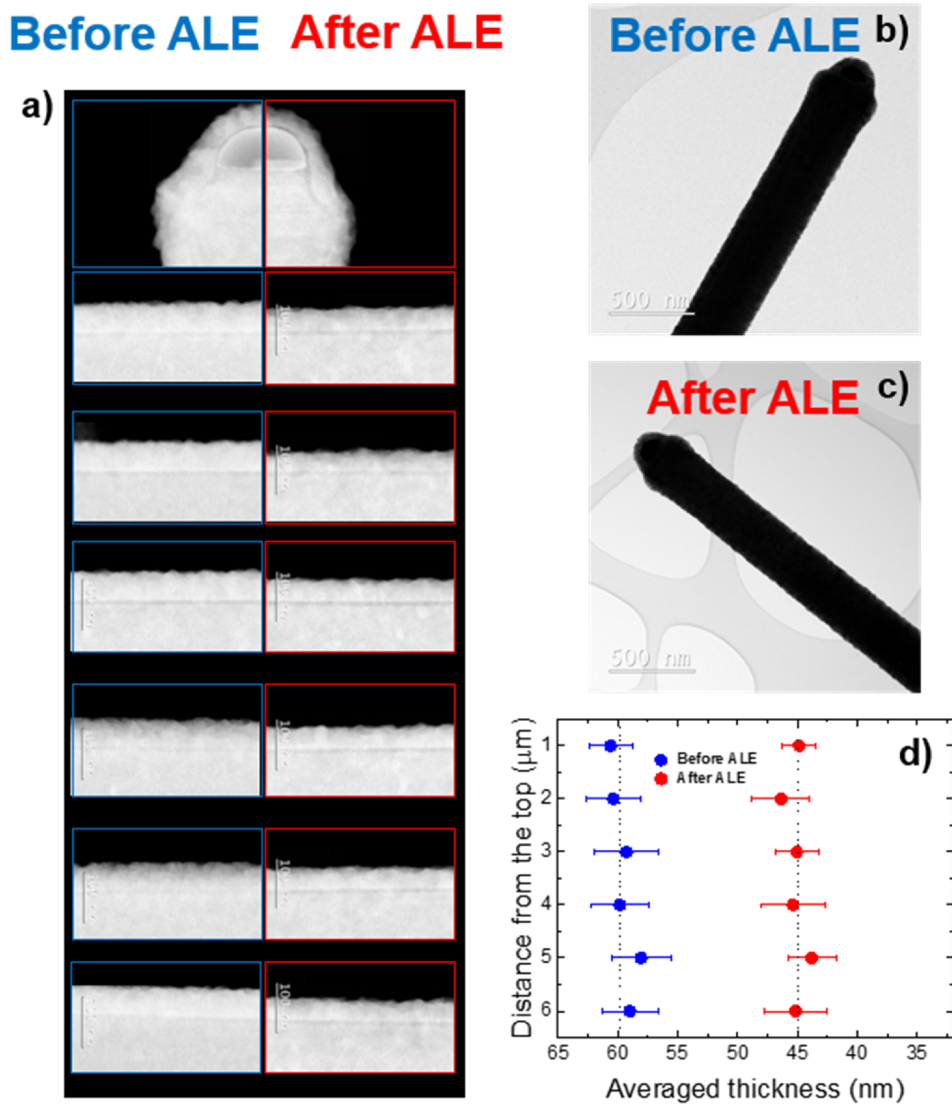


Figure 7.A4. **a)** High magnification HAADF-STEM images of a second set of ZnO-covered NWs, before and after ALE. **b-c)** Low-magnification bright-field TEM images of the same NWs shown in a). **d)** Averaged ZnO thicknesses as measured every μm along the nanowires before and after ALE. The standard deviation of the measurements is taken as the error.

Chapter 8

Conclusions and Outlook

Area-selective atomic layer deposition (ALD) and atomic layer etching (ALE) are emerging techniques that are highly relevant for next-generation devices both within and beyond the semiconductor industry.

The work described in this dissertation focuses on process development for area-selective ALD of several oxide materials such as In_2O_3 , ZnO and SiO_2 . In addition, a new approach for atomic layer etching (ALE) of ZnO was developed.

During this work, insights into the reaction mechanisms underlying atomic layer process techniques were obtained by employing both experimental and theoretical methods. These insights can be used for further optimization of present technology and extension to the selective processing of other materials.

From this thesis the following general conclusions can be drawn:

- Being inherently surface chemistry enabled, ALD allows to deposit films only on specific, pre-defined areas of a patterned substrate. Likewise, ALE enables the selective removal of a material in the presence of another. Both techniques rely on at least two time-separated half-reactions. Therefore, the selectivity will originate from the differences in thermodynamics or kinetics of the individual precursor or co-reactant half-reactions on the distinct surfaces of a patterned substrate. On this basis, we attempted to classify selective atomic layer process mechanisms into *chemoselective precursor* or *chemoselective co-reactant mechanisms*.

It is often challenging to obtain a sufficiently high selectivity for the deposition or removal of films in a highly controlled fashion. In order to increase the selectivity, several approaches could be adopted from more mature fields (area-selective chemical vapor deposition and conventional dry etching) regarding the factors and mechanisms that impart selectivity (adsorption, desorption, surface diffusion, reactions pathways, use of inhibitors, etc.). Besides these, the insights obtained by experimental and/or theoretical investigations can be used as a guide for tuning the reaction conditions in order to maximize the selectivity and minimize unwanted reactions. Finally, selectivity can also be further improved by using intermittent correction steps, such as etch-back steps during area-selective ALD or deposition steps during selective ALE.

- So-called *direct-write* process concepts were developed for the cases of $\text{In}_2\text{O}_3\text{:H}$ and ZnO , both exploiting the differences in film nucleation on OH-terminated SiO_2 and H-terminated Si. We used of a μ -plasma pre-activation step to locally convert H-terminated Si areas on a substrate into OH-terminated SiO_2 areas. We demonstrated the direct-write (i.e. maskless) deposition of $\text{In}_2\text{O}_3\text{:H}$ on $\sim 100\ \mu\text{m}$ sized patterns. This could open up new options in the manufacturing of flexible electronics and other devices (e.g., photovoltaics and displays) having pattern sizes of $\sim 100\ \mu\text{m}$. A further extension down to the $\sim 100\ \text{nm}$ scale was proven feasible for area-selective ALD of ZnO . Here, the substrate was pre-activated by the deposition of ultrathin SiO_2 seed layers (as thin as $\sim 1\ \text{nm}$), using electron beam induced deposition (EBID).

A major benefit of these approaches based on local surface pre-activation is that no resist patterning, etching or lift-off steps are required, thereby allowing for direct-write and *bottom-up* patterning and for reducing the number of manufacturing steps.

- The concepts summarized above have been based on *thermal* ALD processes. Another approach for area-selective ALD using a *plasma*-assisted process was demonstrated for SiO_2 , by using a three-step (ABC-type) ALD cycle. To this end, we selected a suitable chemoselective inhibitor molecule, acetylacetone (Hacac), that selectively adsorbs in step (A) on specific surfaces and inhibits the precursor chemisorption in the subsequent step (B). The ALD cycle is then completed in a third step (C) by an O_2 plasma that removes the inhibitor from the non-growth area and the precursor ligands from the growth area. In this way, area-selective deposition of SiO_2 proceeds only on those areas on which the inhibitor does not adsorb, thereby opening-up a possible route toward *self-aligned* fabrication relevant for mitigating *edge placement error* issues.

The role of the inhibitor in the reaction mechanism has been investigated using density functional theory (DFT) calculations, and experimentally using *in-situ* infrared spectroscopy measurements. These investigations yielded the insights on possible routes to improve the selectivity of the process, which are discussed in the recommendations below. The SiO_2 ABC-type process concept offers an exceptional substrate-selectivity, by distinguishing between different oxide starting surfaces. We expect that the compatibility of the approach with ozone-based or plasma-assisted ALD will extend the portfolio of materials deposited by area-selective ALD.

- The reaction mechanisms of the area-selective ALD processes presented herein have been investigated using DFT calculations and for the case of SiO_2 also by *in-situ* infrared spectroscopy. These calculations have proven to be very useful as a guide for understanding the mechanism underpinning area-selective ALD. DFT calculations indicated that the area-selective ALD processes presented in this work are enabled by the differences in *thermodynamics* and *kinetics* of the surface reactions that take place on the growth and the non-growth areas. Strong precursor physisorption was suggested as one of the stages in the full reaction path leading to selectivity loss during area-selective ALD of ZnO . Therefore, particular care should be paid to the energetics associated with all the elemental reaction steps (energetics

of: physisorption, activation and chemisorbed state, transition state to product, and desorption). Experimental investigations using *in-situ* infrared spectroscopy not only corroborated the DFT results to a large extent, but also highlighted small differences, which we suggest to be due to defects sites (contaminants, grain boundaries, dislocations) on the experimental surfaces that are not contemplated during DFT simulations.

- A novel process for the isotropic ALE of ZnO was introduced in this work, based on alternated dosing of Hacac and O₂ plasma. Microscopy studies on vertically aligned nanowire arrays showed that the process allows isotropic etch profiles with Ångstrom-level control over material removal. Typically plasma-based ALE is associated with anisotropic/directional etching, therefore a key achievement here is that plasma-based processes can also be used to obtain *isotropic* ALE. Based on *in-situ* infrared spectroscopic measurements we proposed a reaction mechanism in which the exposure of Hacac produces volatile Zn(acac)₂ while persistent acac-species on the surface inhibit further etching reactions. A radical-driven O₂ plasma step removes the acac species and resets the surface for the next cycle. High etch selectivity (80:1) over SiO₂ and HfO₂ and the possibility to extend the ALE process to other oxides (such as Al₂O₃) were demonstrated.

In summary, the work described in this dissertation demonstrates novel processes for achieving area-selective ALD and ALE. Furthermore, it highlights the importance of investigating the thermodynamics and kinetics of ALD and ALE surface reactions. The insights thus obtained are useful to understand and further develop novel selective atomic layer process.

Recommendations. Based on this work, the following recommendations for future research can be given:

- A deep understanding of the factors governing the selectivity loss may be gained by prolonged monitoring (for example using XPS) of the surface species as a function of: repeated precursor pulses (half-cycles), co-reactant pulses and full ALD cycles. For example, the non-growth area might be modified after a certain number of co-reactant pulses. Confronting that result with the one obtained for the full ALD cycles can shine light on the factors governing the selectivity loss.
- High aspect ratio structures require larger precursor and co-reactant doses to ensure conformal deposition. These circumstances may affect the selectivity and result in aspect ratio dependent area-selective deposition. Therefore, area-selective ALD should be investigated in detail for different material combinations and aspect ratios.

- To improve the selectivity further, AB or ABC-type ALD processes can be extended by adding extra steps (ABC or ABCD, etc.). A recent example that is currently being investigated in our group is the insertion of a fourth step consisting of an H₂ plasma step before the O₂ plasma, during the area-selective ALD of SiO₂. Such H₂ plasma step can be inserted to remove acac-species by re-forming volatile Hacac, thus avoiding the formation of carbonate species during the O₂ plasma step. These carbonates are thought to affect the adsorption of Hacac and thus the selectivity.
- The new concept investigated in this work for the ALE of oxide material can be extended to non-oxide materials by exploring different plasma chemistries, or by using multiple-step (ABC-type) approaches. Next, like in conventional etching, substrate biasing can be applied to provide additional processing freedom, e.g., by switching between directional/anisotropic and isotropic etch processes within the same tool or by switching the bias voltage on and off during the active half-cycle. Temperature modulation by pulsed lamp heating and cooling synchronized with the reactant gas pulsing can also be inserted to ‘activate’ reactions with a desired material and ‘de-activate’ undesired ones. In this way one could optimize the differential control over the kinetics of single reaction steps.
We note, that for many practical applications requiring so-called high fidelity etching profiles, *quasi-ALE* processes (not fully saturated, or not strictly layer-by-layer) may be sufficient as long as they are reproducible.
- Hybrid supercycles of area-selective ALD of ZnO and the corresponding ALE process can be used to improve the selectivity. Unwanted ZnO nucleation on the non-growth area (H-terminated Si) could be removed by inserting a few ALE cycles. For this approach to work, the ALE process needs to be adapted. An O₂ plasma step (used in the current ALE process) would oxidize the non-growth area (H-terminated Si) and lead to the formation of an OH-terminated SiO₂ layer on which ZnO deposition takes place. Thus novel plasma chemistry concepts need to be explored. For example, an Ar plasma could be used to remove adsorbed acac-species. Similar approaches can be extended to other oxides or material classes.
- Since ALD is an inherently isotropic deposition technique, side-effects such as *mushrooming* occur. This effect represents less of a problem for large patterns, however, it might represent an issue when the distance between two adjacent growth-areas is of the order of the layer thickness that needs to be selectively deposited. Process solutions to mitigate this effect should be investigated. The deposition could be laterally confined to a finite thickness using self-assembled monolayers, provided these can be applied in a cost- and time- effective manner. Alternatively, complementary area-selective ALD processes that lead to the deposition of two different materials on the two different surfaces need to be developed. Likely, novel and increasingly complex combinations of selective atomic level processes will be researched in the near future.

Summary

Selective Atomic Layer Deposition and Etching of Oxides

With the continuing downscaling of the physical sizes of critical components in modern 3D semiconductor devices beyond the 10-nm technology node, pattern misalignments are likely to reduce the device yield to unacceptable levels. This is due to the difficulties in the positioning and shape retention of the patterns on the sample during each processing step in the manufacturing flowchart. A figure of merit to quantify the misalignment is the so-called *edge placement error* (EPE). Severe EPEs can lead to shorts or misconnections, thus resulting in poor device performance or malfunctioning.

Meeting the ever stricter alignment specifications requires innovative solutions that can ensure *atomic scale fidelity* during material deposition or removal. Area-selective atomic layer deposition (ALD) provides Ångstrom level thickness control and can allow for *bottom-up* material deposition on pre-defined substrate areas. Atomic layer etching (ALE), permits in principle the same level of layer-by-layer control during the removal of a specific materials from certain substrate patterns with a high etch selectivity. Therefore, both techniques hold promises for reducing the number of manufacturing steps and for achieving (self-)aligned features or mitigating the EPE issues.

The work in this thesis focuses on the development of area-selective ALD and selective ALE processes for several oxide materials ($\text{In}_2\text{O}_3\text{:H}$, ZnO , SiO_2) and on gaining insights into the underlying reaction mechanisms. Chemoselective precursor or inhibitor chemisorption were exploited to achieve area-selective ALD of several oxides using thermal and also plasma-assisted ALD. Furthermore, the concept of chemoselectivity was also exploited to develop a novel method for isotropic ALE by making use of a plasma step.

Area-selective ALD of $\text{In}_2\text{O}_3\text{:H}$ (Chapter 4) and of ZnO (Chapter 5) was achieved on OH-terminated Si, in the presence of H-terminated Si substrate areas. Thermal ALD processes were employed in both cases. Micrometer-scale $\text{In}_2\text{O}_3\text{:H}$ patterns were obtained by using a microplasma printer to locally convert H-terminated Si areas of a substrate into OH-terminated SiO_2 areas, by local oxidation. This novel process could open up new options in the manufacturing flowcharts of flexible electronics and other devices (e.g., photovoltaics and displays) having pattern sizes in the order of $\sim 100\ \mu\text{m}$. In addition, area-selective ALD of ZnO was achieved by local deposition of OH-terminated SiO_2 seed layer patterns on H-terminated Si-based films, using e-beam induced deposition (EBID). In this way, the area-selective ALD of ZnO was proven feasible for pattern sizes down to $\sim 100\ \text{nm}$ scale. The nucleation of these films was

investigated by *in-situ* spectroscopic ellipsometry and the selectivity was demonstrated by means of chemical (X-ray spectroscopy methods) or structural (SEM and TEM) analyses.

A major benefit of the two approaches mentioned above is that no resist patterning, etching or lift-off steps are required, thereby allowing for direct-write *bottom-up* patterning and for reducing the number of manufacturing steps.

The underlying mechanisms enabling the selectivity were investigated using density functional theory (DFT) methods. Based on DFT results, it was suggested that the selectivity for In_2O_3 :H deposition originates from the differences in the *thermochemistry* of the precursor adsorption on the OH-terminated and H-terminated silicon surfaces. In contrast, the selectivity for ZnO deposition originates from the differences in *reaction kinetics* of the precursor on OH-terminated and on H-terminated silicon surfaces.

The area-selective ALD processes described above are based on thermal ALD recipes. However, some technologically relevant materials such as SiO_2 and Si_3N_4 can be deposited at low temperatures only by plasma-assisted ALD. A novel approach that allows plasma processes to be implemented in area-selective ALD techniques was developed for the case of SiO_2 , by using a three-step (ABC-type) ALD cycle (Chapter 6). To this end, a suitable chemoselective inhibitor molecule, acetylacetone (Hacac), was selected. Hacac selectively adsorbs in step (A) on specific surfaces and inhibits the bis(diethylamino)silane (BDEAS) precursor chemisorption in the subsequent step (B). The ALD cycle is then completed in a third step (C) by an O_2 plasma that removes the inhibitor and the precursor ligands.

The nucleation of SiO_2 using the ABC-type ALD process was investigated on 14 starting surfaces (e.g., direct deposition on SiO_2 and GeO_2 and nucleation delay on Al_2O_3 and HfO_2 were observed) using *in-situ* spectroscopic ellipsometry. The selectivity of this area-selective ALD process was demonstrated on a patterned sample consisting of Al_2O_3 and GeO_2 , using spectroscopy methods. The inhibitor reactions were investigated using DFT calculations on Al_2O_3 and SiO_2 starting surfaces. Based on these DFT results, it was made plausible that the selectivity originates from the difference in the thermochemistry of the Hacac adsorption: thermodynamically favorable on Al_2O_3 , and unfavorable on SiO_2 .

The ABC-type area-selective ALD process holds promise for realizing *self-aligned* fabrication schemes that are relevant for mitigating EPE issues. Furthermore, the ABC concept is fully compatible with plasma processing, thereby extending the portfolio of materials that can be selectively deposited.

Finally, a novel route for the isotropic ALE of ZnO was introduced in this work, using the alternated dosing of Hacac and O_2 plasma (Chapter 7). The process was investigated using *in-situ* spectroscopic ellipsometry on planar ZnO thin-films that were deposited on Si substrates. Using TEM inspection, the ALE process was demonstrated to enable isotropic layer-by-layer etching from 3D-topographies consisting of GaP nanowires that were coated with ZnO. High etch selectivity (80:1) over SiO_2 and HfO_2 and the possibility to extend the ALE process to other oxides (such as Al_2O_3) were also demonstrated. The etch selectivity of this process and the fact that it is a plasma-based

approach may provide additional possibilities for achieving isotropic and controlled removal of oxides with high etch selectivity.

In conclusion, area-selective ALD processes have been developed for several oxides, using thermal and plasma-assisted processing. The use of plasma radicals to achieve isotropic ALE has been demonstrated as well. The introduction of plasma process concepts in both area-selective ALD and isotropic ALE can enable novel processing options, thereby expanding the atomic layer processing toolbox. These results, together with the new insights into the surface chemistry reactions derived from DFT simulation, will contribute to mainstream industrial applications in advanced electronics, where single-digit nm process control is imperative. Other industries where dimensions are less critical can still benefit from the new selective atomic layer processing concepts. For example, in photovoltaics and displays, catalysis, energy-harvesting and optoelectronics, the manufacturing of superior-quality layers, the scaling and the reduction of manufacturing steps (i.e. cost) are essential.

Contributions of the author

The work presented in this thesis is the original work of the author (A. Mameli), with the following exceptions:

- The density functional theory calculations used in Chapter 4 were carried out by dr. B. Karasulu and dr. C. K. Ande. The density functional theory calculations in Chapters 5 and 6 were carried out by dr. B. Karasulu
- The micro-plasma printer used in Chapter 4 was operated by M. Aghaee
- Transmission electron microscopy and energy dispersive X-ray images in Chapters 5 and 7 were obtained by dr. M. A. Verheijen
- The *in-situ* FTIR measurements in Chapter 6 were carried out by M.J.M. Merkx
- A large part of the nucleation curves reported in Chapter 6 were collected by dr. A.J.M. Mackus
- The time of flight secondary ion mass spectroscopy measurements in Chapter 6 were conducted by dr. J. van Berkum

List of peer-reviewed publications

Related to this thesis

Area-selective atomic layer deposition of $\text{In}_2\text{O}_3\text{:H}$ using a μ -plasma printer for local area activation

Mameli, A.; Kuang, Y.; Aghaee, M.; Ande, C. K.; Karasulu, B.; Creatore, M.; Mackus, A. J. M.; Kessels, W. M. M.; Roozeboom, F.
Chem. Mater. **2017**, *29*, 921–925.

Area-selective atomic layer deposition of SiO_2 using acetylacetone as a chemoselective inhibitor in an ABC-type cycle

Mameli, A.; Merckx, M. J. M.; Karasulu, B.; Roozeboom, F.; Kessels, W. M. M.; Mackus, A. J. M.
ACS Nano **2017**, *11*, 9303–9311.

Area-selective Atomic Layer Deposition: role of surface chemistry

Mameli, A.; Karasulu, B.; Verheijen, M. A.; Mackus, A. J. M.; Kessels W.M.M.; Roozeboom F.
ECS Trans. **2017**, *80*, 39-48

Other work

Anti-stiction coating for mechanically tunable photonic crystal devices

Petruzzella, M.; Zobenica, Ž.; Cotrufo, M.; Zardetto, V.; Mameli, A.; Pagliano, F.; Koelling, S.; van Otten, F. W. M.; Roozeboom, F.; Kessels, W. M. M.; van der Heijden, R. W.; Fiore, A.
Optics Express **2018**, *26*, 3882-3891

Effect of reactor pressure on the conformal coating inside porous substrates by atomic layer deposition

Poodt, P.; Marni, A.; Schulpen, J.; Kessels, W.M.M.; Roozeboom, F.
Journal of Vacuum Science & Technology A: Vacuum, Surfaces, and Films **2017**, 35, 021502

On the growth, percolation and wetting of silver thin films grown by atmospheric-plasma enhanced spatial atomic layer deposition

Marni, A.; van den Bruele, F.; Ande, C.K.; Verheijen, M. A.; Kessels W.M.M.; Roozeboom F.
ECS Trans. **2016**, 75, 129-142

Acknowledgments

Here we are, the last few pages of my thesis and the end of my PhD...time to look back at the last four years. *'A PhD is a lonely journey'* (Daan Schram). It has definitely been a lonely *inner* journey, during which I have learned a lot about myself. On the other hand, the *outer* journey of my PhD has been enriched by so many people that for no apparent reason happened to be there at the right moments and with the right words. I would like to thank you all. Without you I could not have achieved my personal milestones during this journey.

First of all I would like to thank **Erwin** and **Fred** for giving me the opportunity to carry out my PhD project in PMP.

Thank you Erwin for being extremely critical with every single thing I did. Your approach has helped me a lot as a researcher, and has contributed in improving my writing and presentation skills. Thanks to you I have learned the importance of a good design of experiment what is needed and what not. I have to admit that it took me a while to understand your way of teaching but eventually it did work with me as well.

Fred, thank you for being friendly or I should say *Fredly!* Thank you for your guidance also throughout my *inner* journey. You have helped me overcome the hardest times of my PhD. I still remember when I received your phone-call for telling me that you were interested in interviewing me. Shortly after that I could choose between Leiden, DTU and TU/e. I choose TU/e because I felt a positive connection while talking with you in the ex-TNO building and now I do not regret that choice. Thank you for taking the time to have a coffee together once in a while and connect on a human level besides the professional (*atomic level*) one.

I have to admit that several times I thought this PhD would never work and I would have never completed it, even after having the first decent results...at the end I can say that I was lucky enough to have two completely different supervisors. I sincerely hope I took the best from both from you; anyhow I have learned a lot and hopefully you have learned something from me. That would be a great achievement.

Adrie although you joined after more than half of my PhD journey, your contribution has been really appreciated. I am grateful for your help and I have enjoyed working with you, especially at the beginning when you stepped into my office to discuss on which inhibitor could be used and on which surfaces. In retrospect it seems that I was able to make the right choice about the research on area-selective processing. That was one of the most inspiring and productive period of my PhD journey.

Marcel, thank you for being an excellent mentor and friend. I very much enjoyed discussing science with you and also annoying you with EDX requests while you were performing TEM on my samples. Thank you for your help and friendship. Without you this thesis would not be here! I very much admire your knowledge and personality. I sincerely hope I will have the chance to work with you again in future.

Special thanks to **Adriana**, who has also significantly contributed to my personal growth during these four years by discussing 'hard-core' technical details and by providing very useful suggestions as well as your beer tickets during the ALD2017. E comunque *Bari é sempre Bari...nan ste nudd da fè!* ☺

I would also like to thank all the committee members for dedicating their own time in reading and evaluating this thesis. Thanks to **Seán Barry, Stefan De Gendt, Regina Luttge,** and **Ingmar Swart**. I should particularly thank Seán Barry for giving a very positive feedback. I consider your appreciation of this thesis as a great personal achievement.

All the work done in these four years (within and beyond this thesis) would have never been possible without the help and support of all the technicians. Hartelijk bedankt aan **Cristian, Janneke, Jeroen, Caspar, Joris,** en **Martijn**. Thank you for training me, arranging and fixing everything that I needed. Cristian, thank you very much for being such a nice person and a good friend to me.

A big thanks also goes to the Nanolab technicians with whom I spent quite some time in the cleanroom: **Barry, Beatriz, René, Frank, Nando, Tjibbe** and **Erik**. Barry, it was very nice to get to know you and discuss with you about music while having a cigarette break. I have always been a fan of your emails and messages in the cleanroom, keep on rocking! I am extremely grateful to **Beatriz** for her infinite patience while training me on the dualbeam SEM and her help for the thousands of doubts I had while operating the tool. Thanks to **Sebastian** and **Nidhi** for helping me with the dualbeam when Beatriz was not available.

My sincere thank you to **Lianne** and **Jeanne**, you have heavily contributed in making my PhD journey easier by helping not only with bureaucratic matters but with every issue I could have.

A special thanks goes to **Chaitanya** '*Chai baba*', you gave me the best advice ever and it is thanks to that advice that I could start and complete my thesis: '*if you think your idea will work, do the experiments first and then discuss it*'. That is what I have been doing since that night. **Yinghuan** you taught me a lot during the short period we have been working closely together. I will always treasure the memories of the moments in which we obtained our best results and the subsequent celebration with beers in the office. **Bora** as you often says I have been one of your '*best customers*'. It was really great to discuss ideas with you and find out that you are crazy enough to believe and test them with your *magic* DFT. Thank you so much for the fruitful collaboration and solid friendship.

Another special thanks goes to my '*exotic words*' dealer and lucky charm: **Tahsin**. I was fortunate to have you as officemate and very close friend. We have shared a lot of stressful and very hilarious moments, discussed and influenced each other work and came-up with ideas for other 20 more small projects that will probably never see the light.

I am grateful to all my office-mates, **Morteza, Eldad, Leo, Patrick, Saravana, Claire, the other Bart** (PMP), **the other² Bart** (EPG), **Mark, Tijn, Tahsin, Akhil, Saurabh**. Thank you for tolerating me and my home-made drawer, together with my habit of whistling while listening to loud hard-rock music. Akhil '*Achille*' and Saurabh '*Sabino*' thank you for being my personal Hindish teachers and very good friends. Also thanks for teaching me Hindi *gaalis*, thanks to you I got to be the Hindi teacher of Saravana (the other Indian office-mate). I will always treasure the joyful and partying times we had until realizing we had to work much harder than that to get things done. All the best with your thesis and future job.

Thanks to all the PMP members that have voluntarily or accidentally contributed to this work and probably more importantly to shape the person I am today. Thanks to **Srinath**, the amazing **Yizhi, Shashank, Ben, Matthieu, Roger, Nick, Bart, Vincent, Harm, İlker, Sjoerd, Roy, Mahdi, Lachlan, Janne and Jimmy** for the useful discussion and for sharing your experience and knowledge with me. Thanks to **Dibya** for the discussions during my *sutta* break/and her SPAR-time. Thank you for being a good friend and for involving me in your work. All the best with your perovskites. Thanks to **Peter** from EPG for being a very kind and trustable person, thanks for helping and good luck with everything.

Thanks to the TNO collaborators for their help, the open discussion we had and the very much appreciated advices: **Paul, Andrea, Fieke, Yves, Ellis**.

I am grateful to my bachelor students, **Jeff** and **Maarten**. Working with you was a very formative experience for myself, and hopefully it has been the same for you. I wish you all the best with your careers.

A big thanks to the Italian crew that helped me throughout this journey: **Valentino** ‘tr-tr-tr’, **Valerio** ‘lo zio’ e **Sasa, Valerio Jr.** ‘il ragazzo chimico’ e **Serena, Alberto, Maria, Maurangelo** e **Luca**. Valentino, I will never forget our chess matches accompanied by good music, rum and obviously kapsalon...grazie mille per tutto! Lo zio, thank you for teaching me the secrets of XPS, but more importantly for telling me where to find a good Campari and Prosecco. Valerio Jr. you have been very resourceful for discussing our results from a chemistry perspective and in our own dialects. Ricordati: *la morte del platino è la cipolla!*

A special thanks goes to all my long-time and faraway friends, knowing that we can count on each other (and on several Campari Spritz per night) was very helpful. Grazie **Rino, Luca, Pamela, Paky, Peppe, Paolo, Stefania, Antonio** e il **direttivo alcolico**.

Un ringraziamento speciale ai miei genitori **Maria** e **Augusto**, grazie per l’aiuto e l’affetto che mi date ogni giorno. Grazie ai miei fratelli e alle loro famiglie: **Efisio** e **Marika, Marco** e **Rossella**, e i miei adorati nipotini: **Martina** e **Francesco**. Sapere di poter sempre contare su di voi anche se molto lontani è stato sempre di grande aiuto.

Un grazie infinito va a mia moglie **Anna** che mi ha spronato fin dall’inizio ad intraprendere questo percorso e mi ha sopportato durante tutto il PhD, soprattutto durante la fase di scrittura di questa tesi. Infine, alla mia piccola figlia, **Amelia Marie**, che non conosco ancora ma già adoro, grazie di avermi fatto il dono piu’ grande di tutti, se ho resistito all’ultimo periodo lo devo soprattutto a te.

My apologies to whom I might have forgotten to acknowledge, a big thank you to all of you!

Sincerely,

Alfredo Mameli

Curriculum Vitae

- November 3,
1986 Born in Barletta, Italy
- 2006 – 2010 Bachelor Degree in Materials Science
University of Bari, Italy
- 2011 – 2013 Master Degree in Materials Science and Technology
University of Bari, Italy
- 2014 – 2018 PhD Candidate in the Plasma & Materials Processing
group, Department of Applied Physics,
Eindhoven University of Technology, the Netherlands